A Multi-Wavelength Study of the Dwarf Galaxies NGC 2915 and NGC 1705:

Star Formation, Gas Dynamics and Dark Matter

E. C. Elson

Thesis Presented for the Degree of
Doctor of Philosophy

in the Department of Astronomy,
University of Cape Town

October, 2010

Supervisors:

Prof. W. J. G. de Blok, Prof. R. C. Kraan-Korteweg

Abstract

This thesis presents the results of a detailed multi-wavelength study of the nearby blue compact dwarf galaxies NGC 2915 and NGC 1705. The primary data set for each galaxy consists of new observations of the neutral hydrogen (H I) line obtained with the Australia Telescope Compact Array during the period October 2006 – May 2007. Nearly 100 hours of on-source data are accumulated for each galaxy. These new H I data are highly sensitive at both *low and high* spatial resolutions. Diffuse, low-level H I emission is traced in the very outskirts of the galaxies. In addition, the gaseous distribution is well-constrained on angular scales of $\sim 17''$. These H I data provide unprecedented views of the neutral gas components of these galaxies. The H I data are complemented with high-quality imaging from the *Spitzer* Nearby Galaxies Survey and the GALEX Nearby Galaxy Survey.

NGC 2915 has the optical characteristics of a late-type dwarf galaxy, yet its H I characteristics are those of a late-type spiral. Its large, rotating H I disk (extending out to ~ 20 B-band scale lengths) and apparent lack of stars in the outer H I disk make it a useful candidate for dark matter studies. The stellar disk of NGC 1705 is host to an intense star-bursting core which is rapidly depleting the galaxy's central H I reservoir. This galaxy can be used to rigorously test theories of star formation.

Detailed studies of the distribution and kinematics of the neutral inter-stellar medium (ISM) within each galaxy are carried out. A rotation curve is derived for each galaxy. These rotation curves probe the gravitational potential out to galactocentric radii of $\sim 4R_{25}$. *Spitzer* 3.6 μm imaging is used to separate the dynamical contribution of the stellar disk to the observed kinematics. Mass models are produced for each system in order to determine the radial distribution of dark matter. The dark matter halos are parameterised as pseudo-isothermal spheres and NFW halos. Neither galaxy's stellar potential can account for its observed kinematics. Both galaxies are dark-matter-dominated at all radii. At the last measured point of its rotation curve, the total mass to blue light ratio of NGC 2915 is $M_{tot}/L_B \sim 140$ $M_\odot/L_B$, making it one of the darkest galaxies known. The best-fitting pseudo-isothermal sphere parameters are

$\rho_0 \sim 0.17 \pm 0.03$ M$_\odot$ pc^{-3} and $r_c \sim 0.9 \pm 0.1$ kpc for NGC 2915, and $\rho_0 \sim 0.09 \pm 0.01$ M$_\odot$ pc^{-3} and $r_c \sim 1.2 \pm 0.1$ kpc for NGC 1705. The central dark matter cores of these galaxies are denser and more compact than those of typical late-type systems.

Three-dimensional models of the H I data cube are built in order to study the complex H I kinematics observed at the centre of NGC 2915. The observed kinematics are shown to be dictated by the input of kinetic energy from high-mass stars into the ISM. An inner disk radial outflow of ~ 30 km s^{-1} is required for the models to match the observations. The expanding gas stands essentially no chance of escaping into the inter-galactic medium due to the extreme nature of the dark matter halo of NGC 2915.

Neither NGC 2915 nor NGC 1705 are typical star-forming galaxies. A suite of star formation recipes and models are examined for each galaxy in order to quantify the relationship between the observed star formation activity and the distribution and kinematics of the ISM. These analyses fully utilise the complementarity of the various high-quality data sets. The star formation rate is estimated by combining the *Spitzer* and GALEX imaging. The H I synthesis data are used to measure the distribution and kinematics of the neutral ISM. A velocity dispersion of 4.9 km s^{-1} is determined for the cold phase of the neutral ISM. It is shown that the star formation threshold in each galaxy is not a purely local phenomenon. Global kinematics as well as the stellar and dark matter potentials play a role in regulating the star formation activity. Treating $\sim 4.9 \times 10^9$ M$_\odot$ and $\sim 9.0 \times 10^8$ M$_\odot$ of dark matter as being distributed within the H I disks of NGC 2915 and NGC 1705 respectively, leads to gravitational instabilities that are consistent with observations. Alternatively, adopting the rotational shear as a characterisation of the global kinematics allows for accurate descriptions of the star-forming cores of the galaxies.

Disclaimer

I herewith declare that this thesis embodies my own original work, both in concept and execution, and that apart from the normal guidance from my supervisors, I have received no assistance. Where pertinent, extracts from the work of others is acknowledged.

The NGC 2915 H I data products presented in Chapter 2, as well as the tilted ring and mass-modeling results presented in Chapter 3, have been published as a paper in the Monthly Notices of the Royal Astronomical Society: Elson E. C., de Blok W. J. G., Kraan-Korteweg R. C., 2010, MNRAS, 404, 2061.

The NGC 2915 H I data products have also appeared in the PoS electronic journal as part of a conference proceedings: Elson E. C., de Blok W. J. G., Kraan-Korteweg R. C., 2009, PoS(PRA2009)051.

The results of the harmonic decomposition of the H I velocity field of NGC 2915 presented in Chapter 3 have been accepted for publication in the Monthly Notices of the Royal Astronomical Society (eprint arXiv:1009.1753).

E. C. Elson
October, 2010

Acknowledgements

My deepest gratitude is extended first and foremost to my parents who have always supported me wholeheartedly in my scientific endeavours. The completion of this thesis would have been burdensome and even more arduous without your constant understanding and encouragement. To my sisters, of whom I am always extremely proud, thank you for always keeping me well-grounded and for your constant support. Special thanks are also extended to my grandparents who, from undergraduate days, have always helped me in every way that they could.

I am sincerely grateful to my supervisors, Erwin and Renée, for all their help, guidance and advice over the past three years. You have imparted to me your knowledge and have allowed me the freedom to explore and discover the joys of independent research. This project could not have been completed without the two of you. Similarly, I appreciate all the selfless support that I've received from the UCT postdocs. Prof. R. Sancisi is thanked for his enthusiasm and endless patience in discussing various aspects of the H I data presented in this thesis.

To my friends and the people closest to me, who have soldiered on with me throughout my postgraduate studies, I am deeply thankful. Cornelia, I'm sincerely grateful for all of your comfort and encouragement, without which I could not have achieved my goal. Special thanks are extended to Paul for literally being there from day one. I appreciate all the support over the years, we've really come a long way. To my office mates, Ihab and Viral, thank you for putting up with me over the past few months that I've been writing up. To Nikki, Tana, Brad and Roger, I hope that we can all be together again later in our careers. Finally, to Leigh, you've helped me in more ways than you can know, I'll care for you always.

I am deeply indebted to the South African Square Kilometre Array project for generous funding throughout my Ph.D. It has been my pleasure to be able to participate in the MeerKAT initiative and to be part of the South African radio astronomy community.

Contents

List of Figures

List of Tables

Chapter 1

Introduction

The universe contains billions of galaxies. A typical galaxy is a complex collection of stars, gas and dark matter, with the evolutionary interplay between these mass components determining the time-dependent observable properties of the galaxy. Historically, it has been the class of high surface brightness galaxies that have been most extensively studied. These are usually the grand design spirals or the extremely massive ellipticals. High-mass systems, however, constitute only a small fraction of the total number of galaxies. Most of the galaxies in the universe are low-mass dwarf systems (Springel et al., 2005; Sandage et al., 1985; Mateo, 1998). Our local group, for example, consists of only two large spiral galaxies, our own Milky Way and the Andromeda Galaxy, as well as a less massive and less luminous spiral, M33. Besides the large Magellanic Cloud, the rest of the local group is constituted by at least 38 dwarf galaxies. Indeed, dwarf galaxies are thought to dominate the cosmic scenery in terms of number density and are therefore crucial to the overall evolution of the universe. Dwarfs have been shown in numerical simulations to seed the growth of more massive, more majestic spiral and elliptical galaxies (Springel et al., 2005). It is therefore important to clearly understand all that we can about these building blocks of the universe.

This thesis serves as a detailed study of two nearby dwarf galaxies, NGC 2915 and NGC 1705. Each of these galaxies is unique in its own right. A multi-wavelength approach is adopted to study the various mass components within these systems. The complex interplay between the components is investigated and interpreted in the overall context of the dynamics and evolution of the galaxies.

1.1 Dark matter

A significant component of this thesis is dedicated to the study of the dark matter content of NGC 2915 and NGC 1705. In the following section, the standard ΛCDM cosmological model is described together with the practical problems that are encountered when attempting to reconcile its predictions with observations.

Our present understanding of the universe is one in which all that we can see constitutes less that 5% of all that we know to be out there (Riess et al., 1998; Perlmutter et al., 1999; Spergel et al., 2003). The best working model for the universe, the ΛCDM cosmological model, tells us that almost three quarters of the mass/energy budget is made up of some mysterious form of energy, the dark energy, which accelerates the observed cosmological expansion. Another one quarter or so of the mass/energy budget is the dark matter, an unknown type of matter which is the dominant mass component within and outside galaxies. The dark matter occurs in two varieties: baryonic and non-baryonic. Observations of the cosmic microwave background, the remnant radiation of the Big-Bang, suggest that the vast majority of the dark matter in the universe is non-baryonic (Spergel et al., 2003). Numerical simulations of the formation of the observed large-scale structure of the universe require large fractions of non-baryonic dark matter to seed the hierarchical galaxy formation (Springel et al., 2005). Indeed, the majority of cosmological and astrophysical observations cannot be easily understood without the invocation of a significant dark matter component of the mass/energy budget of the universe.

1.1.1 Observing the dark matter

Our modern view of a typical galaxy is one in which the gaseous and stellar components are completely embedded in a large dark matter halo. Since dark matter cannot be directly observed, its properties need to be inferred via the gravitational influence they have on directly observable matter. A galaxy's rotation curve is used to trace the distribution of its dark matter. Knowing the rotation velocity of a tracer particle at a given galactocentric radius, the question to answer is "How much of the rotation velocity *cannot* be accounted for by the observable mass components?". Direct measures of the gaseous and stellar distributions allow the contributions of these components to the total rotation velocity to be determined. The "missing" velocity is then the dark-matter-induced rotation velocity which can be linked to the dark mass distribution via Newton's second law of motion.

1.1.2 Dark matter in dwarf galaxies

Dwarf galaxies serve as ideal laboratories in which to study the properties of dark matter. Dwarfs are usually low-mass systems, generally treated as having absolute B-band magnitudes larger that $M_B \sim -17$. Compared to high-mass spiral galaxies, late-type dwarfs are relatively simple dynamical systems, generally consisting of a bulge-less exponential stellar disk as well as a gaseous disk. Their dark matter properties are thus easier to trace than those of more complex high-mass systems. The late-type dwarfs are usually gas rich, meaning that their kinematics can be studied out to large galactocentric radii using radio telescopes. It has been known since the 1970's that dark matter is the dominant mass component of high-mass galaxies such as late-type spirals (Rubin & Ford, 1970). A major effort in modern observational astrophysics is to accurately trace the distribution of dark matter within late-type galaxies, including high-mass spirals and low-mass dwarfs. Several large surveys have been dedicated to this task:

- Swaters (1999) was the first to study the dark matter properties of a large representative sample of H I-rich late-type galaxies as part of the 'Westerbork H I Survey of Spiral and Irregular Galaxies' (WHISP, Swaters et al., 2002). From the entire WHISP sample, late-type dwarfs were selected as being those galaxies with Hubble type later than Sd, as well as earlier-type galaxies with absolute magnitudes fainter than $M_B = -17$. Of all the WHISP galaxies, 73 were treated as late-type dwarfs.

- 'The Local Volume H I survey' (LVHIS[‡], PI: B. Koribalski) has used the Australia Telescope Compact Array (ATCA[§]) to carry out deep H I line and continuum observations of gas-rich galaxies within 10 Mpc. The H I interferometric measurements will provide a better understanding of the baryonic and non-baryonic matter distribution within the local volume.

- A morphologically diverse sample of nearby galaxies, including dwarf systems, was observed using the NRAO[†] Very Large Array (VLA) as part of 'The H I Nearby Galaxy Survey' (THINGS, Walter et al., 2008). The survey aim was to investigate key characteristics related to galaxy mass content, mass distribution, and star formation processes across the Hubble sequence. The survey targeted 34 nearby ($D < 15$ Mpc) galaxies ranging from massive, early-type spirals to low-mass late-type dwarfs.

- The 'LITTLE THINGS Survey'[¶] (LITTLE = Local Irregulars That Trace Luminosity Ex-

[‡]http://www.atnf.csiro.au/research/LVHIS/

[§]The Australia Telescope Compact Array is part of the Australia Telescope which is funded by the Commonwealth of Australia for operation as a National Facility managed by CSIRO.

[†]The National Radio Astronomy Observatory is a facility of the National Science Foundation operated under co-operative agreement by Associated Universities, Inc.

[¶]http://www.lowell.edu/users/dah/littlethings/

tremes, THINGS = The H I Nearby Galaxy Survey, PI: D. Hunter) used the VLA to obtain deep, high-resolution H I line maps of 42 dwarf irregular and blue compact dwarf galaxies. The galaxy sample spans a V-band absolute magnitude range of $-18.7 < M_V < -9.4$ and an H I mass range of $1.1 \times 10^5 < M_{HI} < 1.1 \times 10^9$ $M_\odot$.

- In order to provide a comprehensive understanding of the H I in faint dwarf galaxies, the Faint Irregular Galaxies GMRT Survey (FIGGS, Begum et al., 2008) has imaged the H I in a sample of 65 extremely faint nearby low-mass systems. The FIGGS galaxies represent the extreme low-mass end of the dIrr population, with a median absolute magnitude in the B-band of $M_B \sim -13$ and a median H I mass of $M_{HI} \sim 3 \times 10^7$ $M_\odot$.
- The VLA-ANGST (ACS Nearby Galaxy Survey Treasury) survey[†] (PI: J. Ott) is an ambitious multi-wavelength program to map the stellar content of all galaxies within 3.5 Mpc with the Hubble Space Telescope, and to observe their H I distribution and kinematics with the VLA. A main scientific goal of the program is to study star formation triggering and stellar feedback processes in a galaxy evolution context.

These cumulative efforts have led to an understanding that dark matter plays an important role in the dynamics and evolution of dwarf galaxies.

1.1.3 The dark matter cusp-core discrepancy

Dwarf galaxies, with their high dark matter fractions and relatively simple dynamics, serve as ideal candidates for studying the distribution of dark matter on galactic length-scales. Observational studies of their mass distributions have shown their dark matter halos to be well-modelled by a pseudo iso-thermal sphere with an approximately constant-density core, i.e. $\rho(r) = \text{const}$ (Begeman et al., 1991; Broeils, 1992; de Blok et al., 1996; Côté et al., 2000; de Blok et al., 2008). These observations are, however, inconsistent with theoretical expectations. Theoretically, the study of the properties of dark matter halos in a hierarchical clustering context is carried out mainly in the form of cold dark matter numerical simulations (e.g. Navarro et al., 1996; Moore et al., 1999; Springel et al., 2008). The equilibrium density profile of simulated dark matter halos is found to vary with radius as $\rho(r) \propto r^\alpha$ with $\alpha \approx -1$ (Navarro et al., 1997), thereby predicting extremely steep inner density profiles. Present-day state-of-the-art cold dark matter numerical simulations are able to simulate $\sim 10^{12}$ $M_\odot$ halos with up to $\sim 1.1 \times 10^9$ particles within the viral radius (Navarro et al., 2010). These simulations continue to predict very steep inner density profiles. This discrepancy between the observed shapes of dark matter halos and the predictions from numerical simulations has become known as the "cusp/core problem", and

[†] http://www.cv.nrao.edu/ jott/VLA-ANGST/Welcome.html

has plagued both theoretical and observational astronomers for almost two decades. Attempts at reconciling observations with theoretical predictions depend crucially on: (1) accurate dynamical analyses of nearby galaxies and (2) the correct implementation of baryonic physics in numerical simulations. As an example, Governato et al. (2010) have recently reported on hydrodynamical simulations in which the inhomogeneous interstellar medium (ISM) is resolved. The authors show that strong gas outflows at the centres of galaxies caused by supernovae explosions are able to remove sufficient amounts of low-angular-momentum gas, which inhibits the formation of bulges and decreases the central densities of dark matter halos. Results such as these are beginning to suggest that dark matter halos with central *core-like* properties can, in fact, arise naturally from simulations, thereby reconciling theory with observations of present-day dwarfs. Quite ironically, it is therefore the dwarfs, the smallest galaxies in the universe, that can provide an answer to one of the biggest outstanding questions of modern astrophysics.

1.2 Star formation

Star formation is one of the main drivers of galaxy evolution. A galaxy's luminosity, colours, metallicity and gas content are all controlled by its star formation activity. The gas reservoir of a galaxy serves as its fuel for star formation. A large component of this thesis focuses on the links between the star formation activity and the properties of the neutral ISM in NGC 2915 and NGC 1705. These are not typical star-forming galaxies and therefore serve as extreme tests of various star formation recipes and models. NGC 2915 contains a small stellar disk embedded in a much larger, extended H I disk with well-defined spiral structure. It is not obvious why there should be no widespread star formation activity occurring in the outer H I disk. NGC 1705 also has a small stellar disk embedded in a larger H I disk, yet its stellar disk is host to an intense starburst which is rapidly depleting that galaxy's central H I fuel supply.

Star formation recipes generally describe how efficiently a galaxy is converting its gas into stars (e.g. Kennicutt, 1983, 1989, 1998; Hunter et al., 1998; Leroy et al., 2008). Star formation models on the other hand are designed to determine exactly which regions within a galaxy are likely to be forming stars (e.g. Toomre, 1964; Hunter et al., 1998; Leroy et al., 2008). The ability of these models to accurately characterise the star-forming properties of a galaxy sheds light on the interplay between the key properties of the ISM that regulate the star formation activity.

Star formation largely dictates the kinematics of the ISM. Dwarf galaxies are unique laboratories in which to study the complex interplay between the effects of star formation and the induced dynamics of the ISM. Stellar winds from high-mass stars as well as supernova explosions will set up expanding shells within the ISM and excavate the gas from actively star-forming re-

gions (e.g. Mac Low & Ferrara, 1999). Because dwarfs often rotate in a solid-body-like manner as $V(R) \propto R$ over their entire gaseous disk, kinematic signatures within the gas distribution are less likely to be dissolved by differential rotation, thereby allowing their long-lived effects to be studied.

1.3 THINGS: The HI Nearby Galaxy Survey

In recent years, entire galaxy surveys have been dedicated to studying the mass content and star-forming properties of nearby galaxies. One such survey was THINGS. This survey used the H I spectral line to carry out high-resolution ($\sim 6''$) interferometric observations of a morphologically diverse sample of nearby galaxies ($D \lesssim 15$ Mpc). The northern hemisphere survey consisted of 34 galaxies ranging from massive spirals to low surface brightness dwarfs. All of these galaxies were observed with the VLA. A southern hemisphere extension of THINGS has included a further six galaxies that were observed with the ATCA. NGC 2915 and NGC 1705 form part of THINGS south.

THINGS was designed to have its targets overlap with those of the *Spitzer* Nearby Galaxies Survey (SINGS, Kennicutt et al., 2003) and the GALEX Nearby Galaxy Survey (NGS, Gil de Paz et al., 2007). The goal of THINGS is to combine these high-quality multi-wavelength data sets in order to study various properties and characteristics of the galaxies on sub-kiloparsec length-scales.

1.4 In this thesis

In this thesis, the new ATCA observations of the dwarf galaxies NGC 2915 and NGC 1705 are combined with high-quality imaging from the Spitzer Nearby Galaxies Survey and the GALEX Nearby Galaxy Survey. These complementary data sets are used to carry out detailed analyses of these unusual galaxies in order to: (1) study the mass content and distribution, (2) quantify the complex ISM kinematics, and (3) understand the observed star formation activity.

The high spatial and spectral resolution of the THINGS data allow the distribution and kinematics of the H I to be accurately studied from the dynamical centres of the galaxies all the way out to $\sim 4R_{25}$. Using the H I as a tracer of the gravitational potential, accurate rotation curves are derived for each galaxy. The *Spitzer* 3.6 μm imaging is used to constrain the contribution of the stellar potential to the observed rotation curve. Mass models are produced for each galaxy, describing the radial distribution of dark matter.

The quantitative relationship between the star formation rate and the properties of the neutral ISM is investigated. By combining the *Spitzer* and GALEX imaging with the THINGS data, the star formation efficiency of each galaxy is measured on sub-kiloparsec length-scales. The results are compared with the expectations from a set of proposed star formations recipes and models in order to better quantify the complex process that regulate the star formation activity.

1.4.1 Thesis outline

- Chapter 2 of this thesis provides a detailed description of the H I data acquisition and reduction methods for NGC 2915. The final H I data products are presented and the quality of the H I data tested for the degrading effects of beam smearing.
- In Chapter 3, the H I data are used to carry out a full kinematic study of NGC 2915. A tilted ring model is fitted to the H I velocity field in order to generate a rotation curve for the system. This rotation curve is used as mass-modelling input to determine the distribution of dark matter within the galaxy. Separate studies of the non-circular velocity components within the system's inner and outer gaseous disks are conducted. Three-dimensional models of the inner disk are built to link its H I dynamics to the effects of the star-formation activity. An harmonic decomposition of the outer H I velocity field is carried out, the results of which are interpreted in the context of non-axisymmetric perturbations to the galaxy's gravitational potential.
- Chapter 4 presents the NGC 1705 H I data products and the results of dynamical analyses. A tilted ring model is constructed for the galaxy, yet is shown to yield a rotation curve that is inconsistent with the observations. An alternative approach to determining the rotation curve is adopted and the resulting rotation curve used as mass-modelling input.
- Chapter 5 focuses on the star formation activity in NGC 2915 and NGC 1705. The observed star-forming properties of each galaxy are linked to the properties of the H I , stellar and dark matter mass components on sub-kiloparsec length-scales. This is done in an attempt to understand the processes that govern the observed star formation activity.
- Chapter 6 provides a summary of the results presented in this thesis as well as future research prospects.

Chapter 2

HI observations of NGC 2915

NGC 2915 was observed using the Australia Telescope Compact Array (ATCA) as part of the southern-hemisphere extension of The H I Nearby Galaxy Survey (THINGS, Walter et al., 2008). The resulting 21 cm interferometric data are some of the best ever obtained for this galaxy. Their high spatial resolution ($\sim 17''$) and excellent sensitivity ($\sigma \sim 0.6$ mJy beam^{-1}) allow the galaxy to be studied in unprecedented detail. This chapter is dedicated to a description of the NGC 2915 H I data acquisition methods and reduction techniques as well as the various H I data products.

A brief general introduction to NGC 2915 is provided, followed by a full description of the H I data acquisition and reduction procedures. The various H I data products are presented in the latter half of the chapter together with detailed descriptions of the channel maps, global profile, total-intensity map, velocity field and second-order moment map. The final part of the chapter deals with an investigation of the systematic effects that possibly degrade the quality of the H I data. Thereafter, the justification is made to adopt a Gauss-Hermite polynomial parameterisation of the H I line profiles of NGC 2915 in order to construct an H I velocity field.

2.1 Introduction to NGC 2915

2.1.1 Optical properties

This first of the two galaxies presented in this thesis is NGC 2915. This galaxy is unusual in the sense that is has the optical properties of a late-type dwarf, yet the H I properties of a late-type

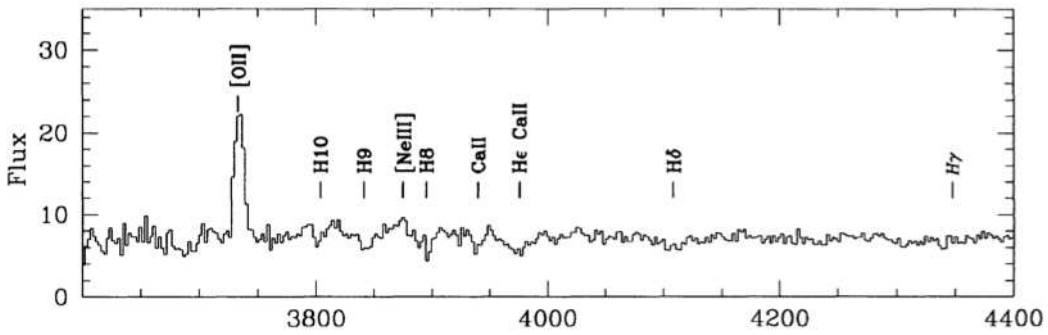

Figure 2.1: Blue portion of a large aperture spectrum of NGC 2915, taken from Meurer et al. (1994). The slit dimensions are $4'' \times 72''$. Flux units are 10^{-14} erg cm^{-2} s^{-1} and the x-axis represents wavelength in units of Å.

spiral. It has been targeted by previous investigators for dark matter and star formation studies.

NGC 2915 has celestial coordinates $\alpha_{2000} = 09^{h}\ 26^{m}\ 11.53^{s}$, $\delta_{2000} = -76^{\circ}\ 37'\ 34.80''$ (Skrutskie et al., 2006). Its most recent distance determination is $D = 4.1 \pm 0.3$ Mpc, provided by Meurer et al. (2003) who resolved the brightest red giant stars within the galaxy. The first modern study of NGC 2915 was carried out by Sersic et al. (1977). The galaxy was then subsequently studied by Sersic & Donzelli (1992) and Meurer et al. (1994) among others. Optically, NGC 2915 is a typical blue compact dwarf with some high-mass star formation occurring at the centre of an otherwise old, diffuse stellar disk with an R-band R_{25} radius of $\sim 98''$ (Meurer et al., 1994). The blue compact dwarfs form a specific dwarf sub-class and appear to be experiencing a burst of star formation. These galaxies have relatively low intrinsic luminosities ($M_B \gtrsim -18$) and a blue spectrum with narrow emission lines (Thuan & Martin, 1981). NGC 2915 meets these two criteria, having a B-band absolute magnitude of $M_B = -15.90$ (Meurer et al., 1994) and exhibiting various emission lines in the blue portion of its large-aperture spectrum (Fig. 2.1). At a Galactic latitude of -18.357°, NGC 2915 suffers a Galactic extinction of $A_B = 0.^{m}275$ at optical wavelengths.

2.1.2 HI properties

Late-type dwarf galaxies are generally gas rich and NGC 2915 is no exception. An entirely different view of the galaxy is obtained when it is observed at 21 cm. The small stellar disk is seen to be completely embedded in a huge H I disk ($M_{HI}/L_B \sim 1.8$ M$_{\odot}$/L$_{\odot}$) extending out to ~ 22 B-band scale-lengths. The size of this gaseous disk relative to that of the stellar disk is what sets NGC 2915 apart from other dwarfs. Becker et al. (1988) were the first to draw

attention to the extended H I disk of NGC 2915, assuming a Gaussian distribution for which, they determined a full-width-at-half-maximum of 9.5′. For their sample of 33 bright southern galaxies, NGC 2915 was found to have the largest H I extent relative to that of its optical when adopting a photometric diameter of $D_{25} = 1.5'$ (de Vaucouleurs & de Vaucouleurs, 1964). It was also shown to have a clear double-horned H I profile, indicative of a disk that is rotating with constant velocity in its outer parts.

The observations of Becker et al. (1988) were carried out using the 64 m radio telescope at Parkes, Australia. The half-power-beam-width for their observations was 15 arcmin, meaning that they could not discern any detailed structure within the H I disk of NGC 2915. Meurer et al. (1996) carried out the first H I synthesis observations of NGC 2915's gaseous disk using the Australia Telescope Compact Array. With these data, the authors were able to obtain $27'' \times 23''$ images of the galaxy's H I disk, a factor of ~ 30 improvement in spatial resolution as compared to the single dish observations. These observations showed evidence for well-defined spiral structure within the H I disk (Fig. 2.2). No significant star-formation is observed in the outer parts of the gas disk. Only a few faint HII regions have been detected by carrying out deep Hα imaging of the disk (Werk et al., 2010; Meurer et al., 1999).

2.1.3 Properties of the extended HI disk

Regardless of its formation history, the cause of the observed H I spiral structure and the mechanism by which it is sustained is not clear. Several investigators have attempted to explain the observed H I distribution of NGC 2915. Bureau et al. (1999) studied the dynamics of the H I within the optical disk, and the spiral pattern of the outer H I disk. For both they calculated a common, slow pattern speed of $\Omega_p = 8.0 \pm 2.4$ km s^{-1} kpc^{-1} which they associated with the figure rotation of a tri-axial dark matter halo. They also proposed that some dark matter is distributed in the disk of NGC 2915, thereby making it gravitationally unstable to the formation of the observed spiral structure. Masset & Bureau (2003), using hydrodynamical simulations, further explored the ideas of Bureau et al. (1999). They showed that the observed spiral structure can be accounted for by either an unseen bar or a rotating tri-axial dark matter halo. However, the mass of the required bar, $M_{bar} \sim 5 \times 10^9$ M$_\odot$, is very large in comparison to the total stellar mass, thereby making the nature of such a bar problematic. The required pattern speed of the tri-axial dark matter halo is significantly larger than those from numerical simulations. Masset & Bureau (2003) disfavoured the external perturber scenario. They also found that while a heavy disk is able to account for the main features of the observed H I morphology, it fails to match the observed gas dynamics.

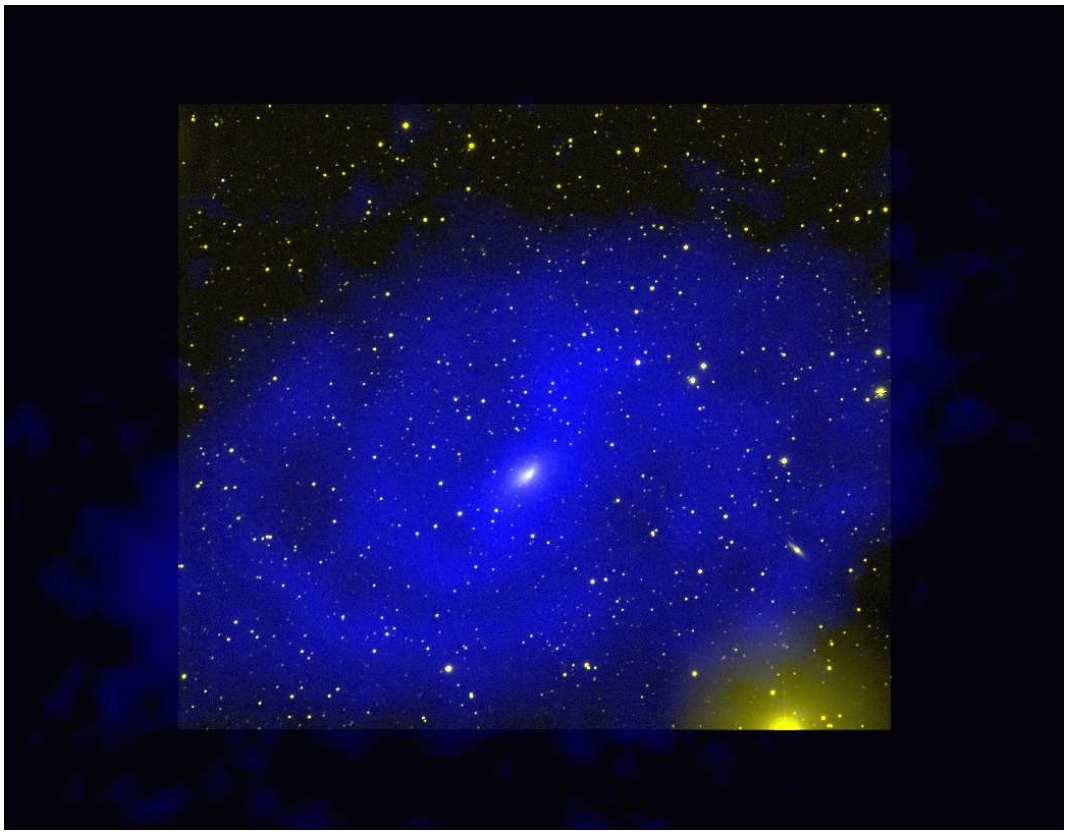

Figure 2.2: Composite optical (yellow) and H I (blue) image of NGC 2915 from Meurer et al. (1996).

2.1.4 Local environment

NGC 2915 is located in a very low-density environment, with seemingly no nearby interaction partners or companion galaxies. A careful search through the H I data cube used in this thesis reveals no obvious faint companions. This does not, however, rule out the possibility of a recent interaction. The size of the ATCA field of view at 21 cm is $\sim 0.54^\circ$ which, at the distance of NGC 2915 (4.1 Mpc), translates to ~ 41.9 kpc. An interaction partner moving with a velocity of 300 km s^{-1}, say, could traverse this distance in roughly 140 Myr, a short time period in a cosmological context, thereby placing it beyond the field of view. A search of the NASA/IPAC Extragalactic Database (NED[†]) for possible companions within 5° (~ 330 kpc) of NGC 2915's photometric centre yields only one nearby object, the radio source SUMSS J092558-763832. This object, separated from NGC 2915 by an angular distance 1.22 arcmin, has an integrated

[†]The NASA/IPAC Extragalactic Database is operated by the Jet Propulsion Laboratory, California Institute of Technology, under contract with the National Aeronautics and Space Administration.

radio flux at 843 MHz of only 9.8 ± 1.6 mJy (Mauch et al., 2003) and has no measured redshift. It is most likely a distant quasar and cannot be treated as an interaction partner.

By carrying out a similar search of the NASA/IPAC Extragalactic Database, Meurer et al. (1996) identified a single object, SCG 0938.1-7623, as a possible interaction partner to NGC 2915. It is not certain whether this object is a nearby low surface brightness galaxy or diffuse nebulosity associated with the Galaxy. Meurer et al. (1996) obtained a Parkes 64 m radio telescope H I spectrum in the direction of SCG 0938.1-7623. Despite the H I observations covering the radial velocity range -1000 km s^{-1} to 4000 km s^{-1}, no obvious H I features in the spectrum could be linked to SCG 0938.1-7623. There is therefore now clear evidence that SCG 0938.1-7623 is interacting with NGC 2915, yet the possibility cannot be conclusively ruled out.

2.2 Acquisition of HI aperture synthesis data

NGC 2915 was observed between 23 October 2006 and 2 May 2007 (project number C 1629) with six different ATCA configurations using all six antennas. The EW-352 array was used to build up sensitivity of low-level, spatially extended emission. The intermediate 750D, 1.5B and 1.5C array configurations further extended the *uv* coverage while the 6A array configuration maximised the spatial resolution of the observations. A single run consisted of a primary calibrator observation, regular secondary calibrator observations and source observations. Each of the EW-352, 750D, 1.5B and 1.5C runs was approximately 12 hours long. Since higher resolution observations are less sensitive to low surface brightness emission, 24 hours were spent in the 6A configuration. Table 2.1 lists all of the information specific to each of the THINGS observing runs. Besides these data, archival data were also incorporated. These data were obtained by Meurer et al. (1996) (project number C191) using 3 different ATCA configurations with all 6 antennas. The archival data were obtained in their raw *uv* format, and were reduced in the same manner as our new H I data (discussed in Sec. 2.3). Following Meurer et al. (1996), baselines including antenna 6 were discarded due to them producing insignificant correlation amplitudes. A summary of the Meurer et al. (1996) observing run is provided in Table 2.2.

From their naturally-weighted data cube, Meurer et al. (1996) determined the H I diameter of NGC 2915 to be $\sim 0.32^\circ$. The HI extent of the galaxy therefore falls well within the $\sim 0.54^\circ$ field-of-view of the ATCA dishes when observing at 21 cm. For our observations, the telescope pointing centres were set to the optical centre of NGC 2915 ($\alpha_{2000} = 09^{\rm h}\ 26^{\rm m}\ 11.5^{\rm s}$, $\delta_{2000} = -76^\circ\ 37'\ 35''$) with no mosaicking required. The correlator was set to use 512 channels with a bandwidth of 8 MHz centered at 1418 MHz. The resulting velocity range is -335 km s^{-1} to 1353 km s^{-1} with an approximate channel spacing of 3.2 km s^{-1}. The archival data from Meurer et al. (1996)

Table 2.1: Summary of NGC 2915 THINGS observing setups

1 Conf.	2 Date (yy-mm-dd)	3 Start (hh-mm-ss)	4 End (hh-mm-ss)	5 Dur. (hrs)	6 Amp. Cal	7 Flux (Jy)	8 Phase Cal.	9 Flux (Jy)
EW352	2006-10-23	11:28:55.0	23:17:45.0	10.39	1934-638	14.88 ± 0.12	1036-697	2.33 ± 0.8
750D	2007-03-14	04:58:45.0	15:56:10.0	9.64	1934-638	14.91 ± 0.10	1036-697	2.36 ± 0.06
1.5B	2006-11-24	19:29:05.0	06:51:35.0	9.95	0823-500	5.59 ± 0.08	1036-697	2.05 ± 0.07
1.5C	2007-05-02	04:37:25.0	15:36:05.0	9.64	0823-500	5.59 ± 0.11	1036-697	2.05 ± 0.05
6A	2007-02-10	10:34:35.0	21:32:25.0	9.64	1934-638	14.87 ± 0.11	1036-697	2.39 ± 0.06
6A	2007-02-16	05:12:35.0	00:42:15.0	17.06	1934-638	14.88 ± 0.12	1036-697	2.39 ± 0.07

Comments on columns: Column 1: ATCA configuration used; Column 2: start date of observation (UT); Column 3/4: start/end of observations (UT); Column 5: time on source; Column 6/7: name of amplitude calibrator and its flux density; Column 8/9: name of phase calibrator and its flux density.

Table 2.2: Summary of Meurer et al. (1996) NGC 2915 observing setups

1 Conf.	2 UT date	3 Baseline range[1] (m)	4 Dur. (hrs)
375	3 May 1992	31-459	11.34
750C	22 Jan 1993	46-750	10.52
1.5D	12 March 1993	107-1439	10.80

Comments on columns: Column 1: ATCA configuration used; Column 2: date of observation (UT); Column 3: baseline range in meters, excluding baselines with antenna 6; Column 4: time on source.

were generated using 256 channels with a 4 MHz bandwidth, thereby yielding the same velocity resolution as the THINGS data. Their velocity range spans 87 km s^{-1} to 928 km s^{-1}.

The absolute flux scale for the data was determined by observing a standard primary calibrator. Such a calibrator should be compact, unpolarised and must have constant flux density. The primary calibrator was also used to make bandpass corrections. Two primary calibrators were used during the THINGS observations of NGC 2915. The most commonly used, PKS B1934-638, is a galaxy with a Seyfert 2 nucleus (Fosbury et al., 1987). At 21 cm its mean flux density is 14.95 Jy $beam^{-1}$ with no significant flux variation observed in recent years. The other primary calibrator was PKS B0823-500 with a mean flux density of 6.45 Jy $beam^{-1}$. PKS B0823-500 has been reported to have a $\sim$ 10% variation in flux over recent years and has also been found to be significantly circularly polarised. In order to correct for temporal changes in gain and phase, periodic observations of a nearby secondary calibrator were made. For the THINGS observations this was always PKS B1036-697. This source has an average flux density of 2.46 Jy $beam^{-1}$. The ATCA website[2] shows the flux variation and also provides further information for these calibrator sources.

2.3 HI data reduction

2.3.1 Importing the data

The MIRIAD software package (Sault et al., 1995) was used to take the raw *uv* data (for our new H I observations of NGC 2915 as well as the Meurer et al. (1996) archival data) from the correlator through to the image analysis stage. For a single run, all of the raw *uv* data were converted from the ATCA RPFITS file format to MIRIAD format using the ATLOD task. When making spectral line observations with the ATCA, two frequency bands may be observed simultaneously. For THINGS observations, only the first band, always centered at 1418 MHz, was used. All velocities were measured relative to the barycentre rest frame.

2.3.2 Data flagging

Once the data were read in, the first and last five correlator channels were flagged using UVFLAG. This was done to ensure that only channels over which the bandpass was relatively constant and well-behaved were used in the reduction process. The data were then split into 3 parts using UVSPLIT: (1) the primary calibrator, (2) the secondary calibrator, and (3) the source. Bad

[2]http://www.narrabri.atnf.csiro.au/

data needed to be removed. Bad data may be caused by radio frequency interference or may be correlator specific. Most such data irregularities were easily detected using the TVFLAG task which for each run produces a time vs. channel plot of the data. The anomalous data, constituting $\lesssim 3\%$ of all the on-source data for a particular run, were flagged and excluded from further use.

2.3.3 Data calibration

Next the data were calibrated. The task MFCAL determined the required corrections to the antenna gains, delay terms and bandpass shapes. The task BLFLAG was used to further check and refine the primary calibrator data by flagging any clearly deviant *uv* points. After each such modification of the data using BLFLAG, new average correction terms were derived using MFCAL. As an example of the small phase-amplitude scatter in the primary calibrator *uv* data, the calibrated PKS B1934-638 data from the EW352 run had an r.m.s. scatter of ~ 0.17 Jy beam^{-1} about the mean *uv* amplitude. The scatter about 0° of the *uv* phases was $\sim 1.2^\circ$. The task GPCAL calibrated the time-varying phases and antenna gains based on the observations of the secondary calibrator. Again, BLFLAG was used to flag deviant visibilities in order to further refine the data. The GPBOOT task applied the corrections to the secondary calibrator flux density measurements based on the primary calibrator gain corrections. Typical scaling factors were ~ 1.2. The corrections applied to the secondary calibrator were applied to the source data using the GPCOPY task.

2.3.4 Data deconvolution and restoring

The calibrated source data were continuum-subtracted by fitting and subtracting a first-order polynomial to the line-free channels which, for our observations, were channels 50 – 150 and 350 – 460. This was carried out in the *uv* plane by the UVLIN task. Having isolated the H I signal, image cubes were produced from the continuum-subtracted *uv* data using the INVERT task.

The weighting scheme applied to the *uv* data when inverting determines various image properties. Various weighting schemes are used in practice. Natural weighting assigns equal weights to all *uv* points. Since the *uv* data will most densely fill the central region of the the *uv* plane, natural weighting emphasises short baseline spacings and tends to produce a broader dirty beam. This has the effect of increasing the signal to noise of extended, low-level emission. The scheme in which each *uv* point is weighted according to the inverse of the number of visibilities within a small region centered on that point is known as uniform weighting since it has the effect of making the sampling of the *uv* plane appear more uniform. Such a scheme, however, yields an

image with lower signal to noise. Super-uniform weighting simply increases the uv cell size used for uniform weighting, thereby giving comparable weights to sparsely-sampled and well-sampled regions of the uv plane. Finally, robust weighting is a sort of hybrid of uniform and natural weighting resulting from minimising the power contained within the side lobes of the dirty beam. For this work, data cubes were produced using natural weighting as well as robust weighting with a Briggs' visibility weighting robustness parameter of 0.2. For reasons described in Sec. 2.4.3 and Sec. 3.1.2 of Chapter 3, only the naturally-weighted data cube is used to carry out analyses of the H I distribution and kinematics in NGC 2915. Unless otherwise specified, all H I-related results, figures and discussions pertain to the naturally-weighted H I data cube.

The INVERT task produces (1) a dirty beam, B_{dirty}, which is the Fourier transform of the sampling function describing the coverage of the uv plane, and (2) a dirty image, I_{dirty}, which is the brightness distribution of the source convolved with the dirty beam.

The dirty image was deconvolved using a Steer CLEAN algorithm (Steer et al., 1984). CLEAN is a non-linear deconvolution process which reduces the effects of prominent and extended side-lobe patterns induced by incomplete sampling of the uv plane. The general "CLEANing" steps carried out for each velocity channel are briefly summarised:

1. Determine the position (x_P, y_P) of the pixel containing the highest flux. Call the amplitude of this pixel A_P.

2. Subtract a scaled version, $G \times B_{dirty}$, of the dirty beam, where $G < 1$, by centering $G \times B_{dirty}$ on (x_P, y_P).

3. Add $G \times A_P$ to the CLEAN table containing all the CLEAN components.

4. Repeat the above steps until a user-specified number of CLEAN components are produced or until a user-specified intensity cut-off is reached.

An intensity cut-off of 2.5 times the r.m.s. of the flux in a line free channel was used. This cut-off was typically reached within $\sim$ 50 000 iterations of the above steps. After the deconvolution process, each of the CLEAN components was convolved with a Gaussian approximation of the dirty beam. This process was carried out by the RESTOR task. The full width at half maximum of the beam was $17'' \times 18.2''$ and $10.2'' \times 10.2''$ for the naturally-weighted (NA) and robust-weighted (RW) data cubes respectively while the channel widths were set to $dV = 3.49$ km s^{-1} and $dV = 3.28$ km s^{-1} respectively. No Hanning smoothing was applied to either data cube.

Table 2.3: Summary of NGC 2915 H I data cube properties

Quantity	NA value	RW value	Units
image size	$512 \times 512 \times 84$	$512 \times 512 \times 84$	pixels
pixel size	$2.5 \times 2.5 \times 3.49$	$2.0 \times 2.0 \times 3.28$	arcsec×arcsec×km s^{-1}
beam	17.0×18.2	10.3×10.2	arcsec×arcsec
noise/pixel	0.6	0.58	mJy beam^{-1}

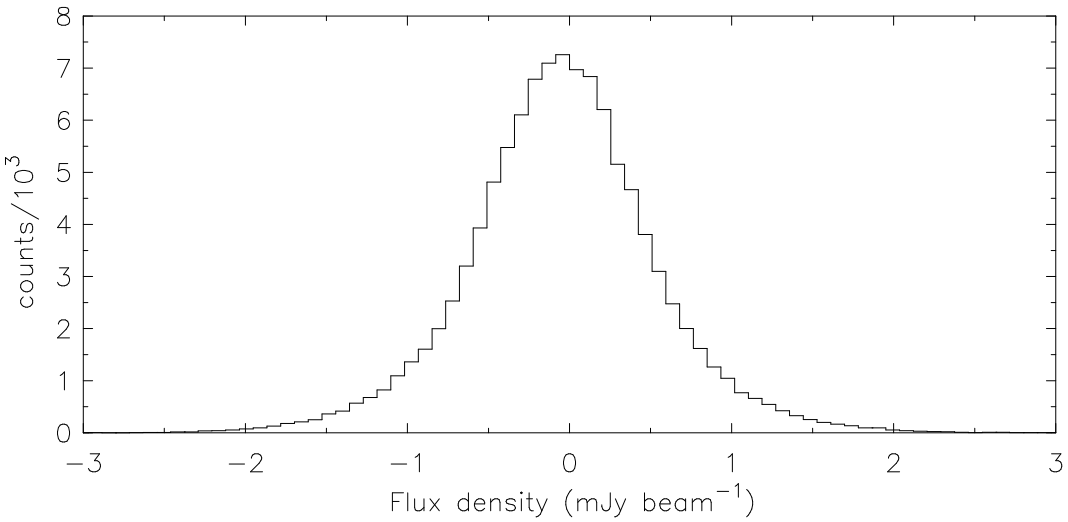

Figure 2.3: Noise histogram for all 512×512 pixels in a single channel of the NA data cube containing no galaxy emission. The data are Gaussian distributed with a mean of -0.02 mJy beam^{-1} and a standard deviation of 0.60 mJy beam^{-1}.

For each cube, the noise in a line-free channel is Gaussian distributed with a standard deviation of $\sigma \sim 0.60$ mJy beam^{-1} for the NA cube, while $\sigma \sim 0.58$ mJy beam^{-1} for the RW cube (see Fig.2.3 for a graphical representation of the NA cube noise properties). The main properties of each data cube are summarised in Table 2.3.

2.3.5 HI moment maps

All H I moment maps were generated using the Groningen Image Processing System (GIPSY, van der Hulst et al. 1992). The entire H I data cube was smoothed down to a resolution of $34'' \times 36.4''$ using a Gaussian convolving function. A flux cut-off was applied to the smoothed cube at 2.5σ. For each channel of the smoothed data cube, any flux that was clearly not spatially connected to or associated with the galaxy emission was flagged and removed. The selectively-blanked, smoothed cube was then applied as a mask to the original $17'' \times 18.2''$ cube.

Given a line profile for which S_i is the flux density in Jy beam^{-1} contained in channel i and ΔV is the channel width in km s^{-1}, the zeroth-order moment is the summed emission of all the channels:

$$M_0 = \Sigma S_i \times \Delta V. \tag{2.1}$$

M_0 has units of Jy beam^{-1} km s^{-1}. If V_i is the velocity in km s^{-1} of channel i, then the first-order moment of the line profile is given by

$$M_1 = \frac{\Sigma_i (S_i \times V_i)}{\Sigma_i S i}. \tag{2.2}$$

M_1 has units of km s^{-1}. The second-order moment is

$$M_2 = \sqrt{\frac{\Sigma_i [S_i \times (V_i - M_1)^2]}{\Sigma_i S_i}}. \tag{2.3}$$

M_2 also has units of km s^{-1}.

The H I total intensity and velocity dispersion maps were constructed from the zeroth- and second-order moments of the data cube respectively. A map in which each pixel is equal to $\sigma\sqrt{N}$, where N is the number of un-blanked channels in the data cube that would contribute to a particular resolution element in the moment maps, was created. Such a construction is permitted for a data cube with independent channels. Dividing each pixel in a map of the summed flux densities by $\sigma\sqrt{N}$ produced a dimensionless signal-to-noise (S/N) map. The average flux density of all the pixels in the summed flux density map that had a corresponding signal-to-noise ratio in the range $2.75 \leq \mathrm{S/N} \leq 3.25$ was used as an intensity cut-off (after being scaled by the channel width) for the total intensity map. This removed, in a robust manner, pixels from the outer disk that had low S/N values. This new H I total intensity map was then used as a mask on other H I maps.

The method of using Gauss-Hermite polynomials to parameterise line profiles of galaxies was introduced by van der Marel & Franx (1993). While Gaussians are reasonable approximations to many realistic line profiles, higher order Gauss-Hermite polynomials are able to better capture profile asymmetries and non-Gaussian deviations. The Hermite method has already been

successfully implemented by various authors (van der Marel & Franx, 1993; Noordermeer et al., 2007; de Blok et al., 2008). A third-order Gauss-Hermite polynomial was fitted to each data cube line profile to generate a so-called Gauss-Hermite H I velocity field. Three filters were used simultaneously when fitting the profiles: (1) profiles with fitted peak fluxes less than 2.5σ were discarded; (2) profiles with a fitted line width less than the channel width were excluded; and (3) fitted profile peaks had to be within the velocity range of the data cube. The benefits of adopting the Gauss-Hermite parameterisation as opposed to other standard parameterisations are discussed further in Sec. 2.7.

2.4 HI data products

2.4.1 Channel maps

A grey-scale representation of the $17'' \times 18.2''$ resolution channel maps is shown in Fig. 2.4. H I structures are visible at large and small scales. At large scales, the emission clearly exhibits the usual pattern of a rotating disk. The H I disk of NGC 2915 exhibits clear spiral structure (c.f. H I total intensity map, Fig. 2.6). On small scales the gas in the central parts of the galaxy forms two dominant over-densities in nearly all of the channels with fainter emission in-between them.

2.4.2 Global profile

A global H I profile, extracted from the selectively-blanked H I data cube by summing the H I emission in each velocity channel, is presented in Fig. 2.5. Using a synthesis array to estimate the total H I flux of a galaxy can result in an underestimate due to missing short base lines. The shortest baseline used for our observations was 31 m (as part of the EW352 antenna configuration), implying that the observations are less sensitive to structures larger than $\sim 23'$. Meurer et al. (1996), however, estimated the H I extent of NGC 2915 to be $\sim 19'$. The amount of H I missed in the global H I profile is therefore expected to be small. In Fig. 2.5 we compare our determination of the global H I profile for NGC 2915 to the HIPASS global H I profile from Koribalski et al. (2004). The HIPASS data are calibrated with $8'$ spatial binning and 13 km s^{-1} channel width. Due to the large HIPASS beam, as well as the fact that the Parkes telescope is a single dish telescope, one would expect the amount of flux missed in the HIPASS observations to be negligible. Figure 2.5 shows, however, that our ATCA spectrum lies above the HIPASS spectrum. This is because all HIPASS-detected sources were treated as being unresolved. This

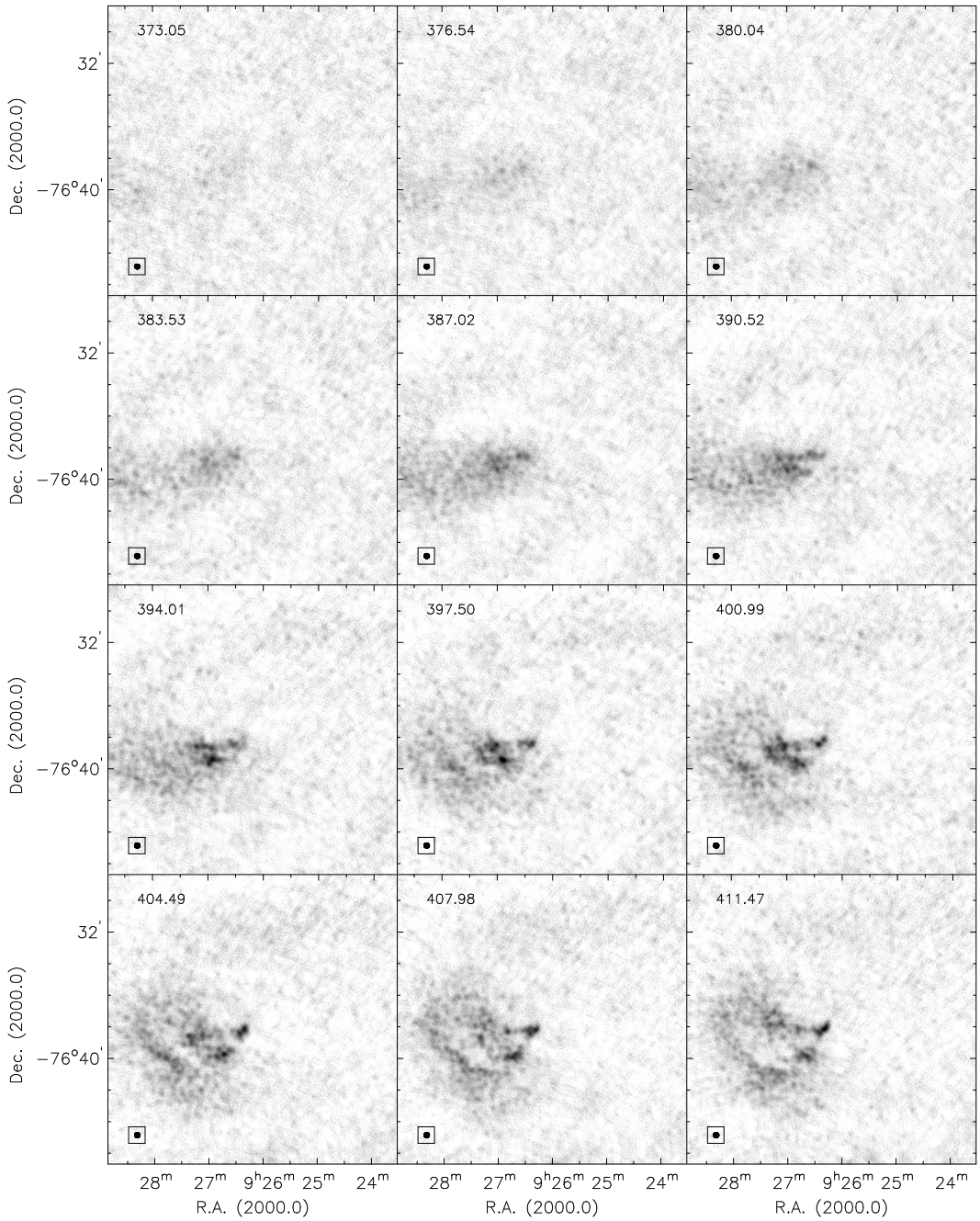

Figure 2.4: Channel maps of the naturally-weighted H I data cube of NGC 2915. The heliocentric radial velocity (km s^{-1}) of each channel is shown in the upper left corner. The half-power-beam-width is shown in the bottom left corner. Grayscale range is from -0.6 mJy $beam^{-1}$ to 10.0 mJy $beam^{-1}$. The r.m.s. noise in a channel is $\sim$ 0.6 mJy $beam^{-1}$.

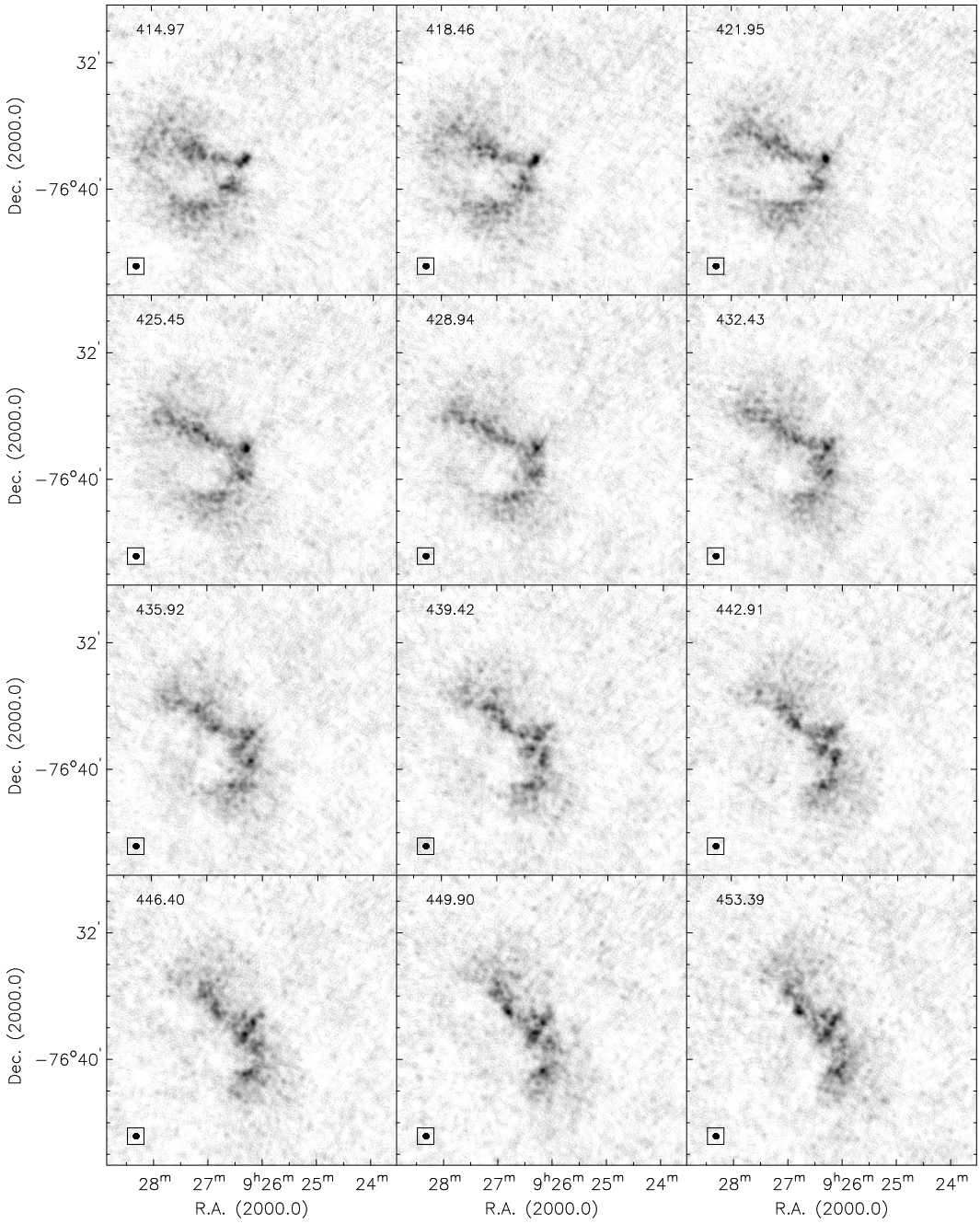

Figure 2.4: Continued.

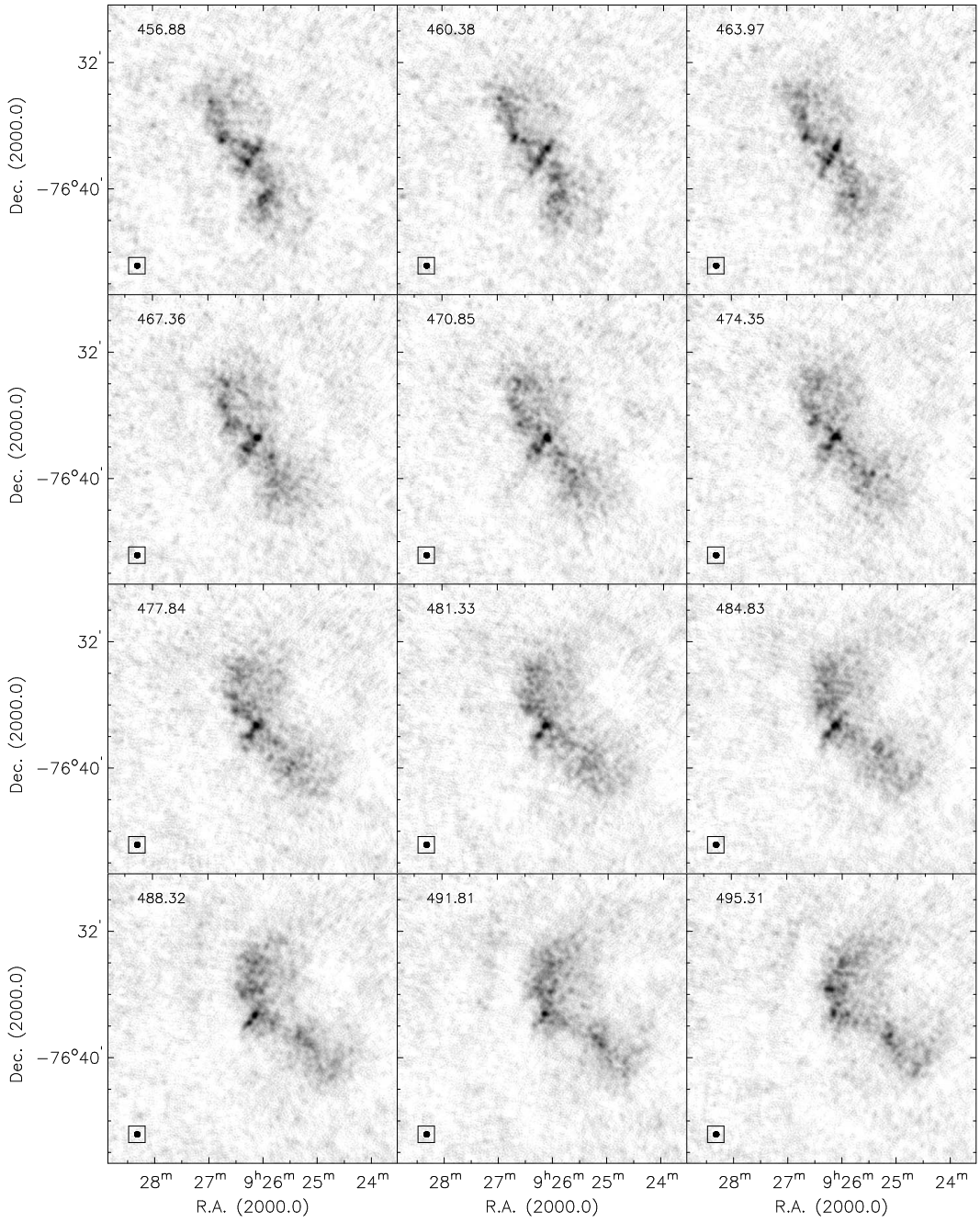

Figure 2.4: Continued.

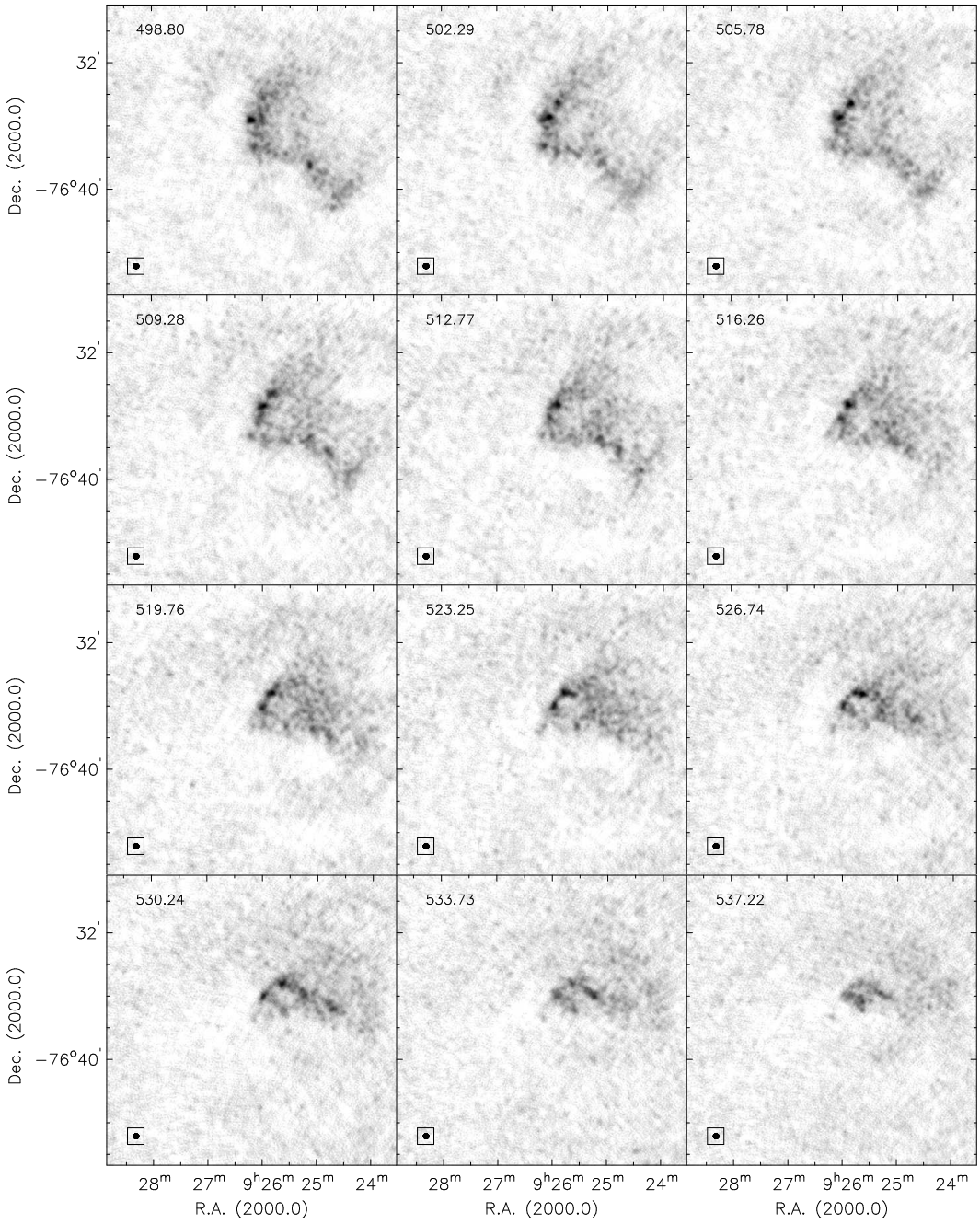

Figure 2.4: Continued.

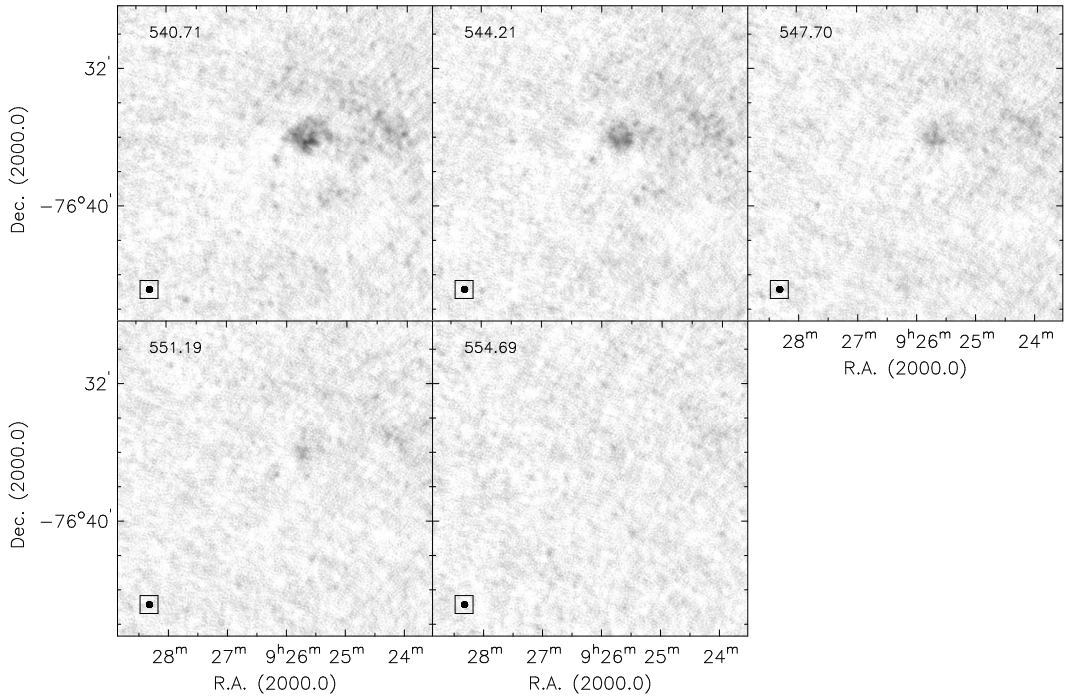

Figure 2.4: Continued.

means that for a galaxy with an H I extent of $\sim 19'$, some of the emission from the outskirts of the galaxy will be incorrectly subtracted. For an ideal single-dish observation, the single-dish H I global profile should never drop below the interferometer global profile.

The resulting global H I profile is double-horned and asymmetric. From this profile we derived the profile widths, the systemic velocity, and the total H I mass. The profile widths were calculated as the differences between the high and low velocities of the galaxy at 20% and 50% of the peak flux density ($V^{20\%}_{high}$, $V^{20\%}_{low}$, $V^{50\%}_{high}$, $V^{50\%}_{low}$ respectively). The profile widths were not corrected for inclination. Two systemic velocity estimates were determined: the first from the midpoint of the two velocities at the 50% level in the global H I profile, and the second from the equation

$$V_{sys} = 0.25 \times (V^{20\%}_{high} + V^{20\%}_{low} + V^{50\%}_{high} + V^{50\%}_{low}). \tag{2.4}$$

The total H I mass was calculated as

$$M_{HI} = 2.36 \times 10^5 \times D^2 \times \int F dV, \tag{2.5}$$

where D is the distance to the galaxy in units of Mpc and $\int F dV$ is the total H I line flux in units of Jy km s^{-1}. This determination of the total H I mass assumes that the H I is optically thin. There is no evidence of optically thick H I from absorption or continuum sources lying

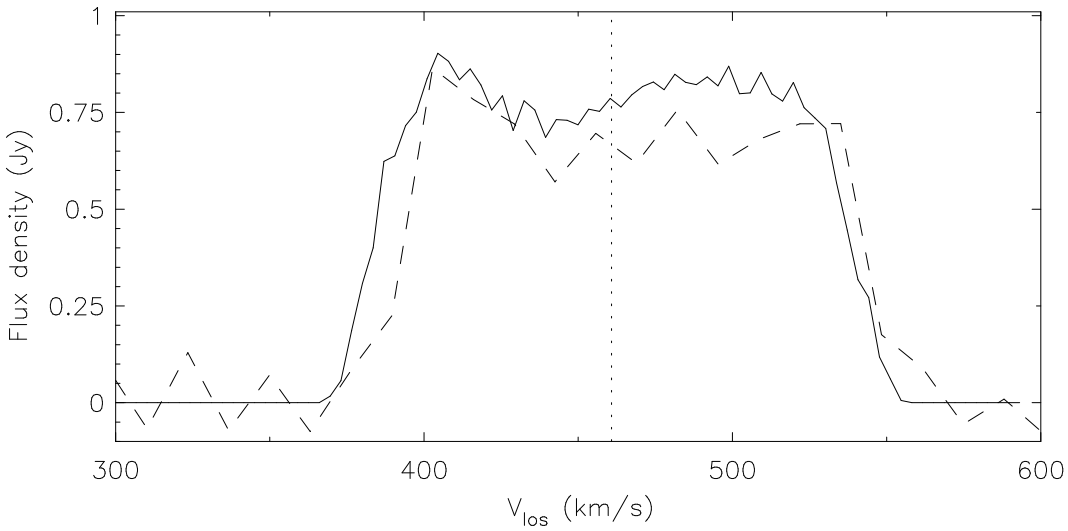

Figure 2.5: Global H I profile of NGC 2915 extracted from the masked H I data cube (solid curve) together with the HIPASS global H I profile (dashed curve). The dotted vertical line shows the systemic velocity as calculated using Eqn 2.4.

behind or within the extended H I disk. Throughout this work we adopt the $D = 4.1 \pm 0.3$ Mpc determination of Meurer et al. (2003). Table 2.4 lists our determinations of the above mentioned quantities. Meurer et al. (1996) measured a total mass of 1.27×10^9 $M_\odot$ assuming a distance of 5.1 Mpc. Using a distance of 4.1 Mpc, their total mass estimate reduces to $\sim 8.2 \times 10^8$ $M_\odot$, similar to our mass estimate of $\sim 6.4 \pm 1.7 \times 10^8$ $M_\odot$.

Table 2.4: Quantities derived from the global H I profile of NGC 2915.

1	2	3	4	5
M_{HI}	W_{50}	W_{20}	V_{sys}^{50}	$V_{sys}^{Eqn.1}$
(10^8 $M_\odot$)	(km s^{-1})	(km s^{-1})	(km s^{-1})	(km s^{-1})
6.4 ± 1.7	186.8 ± 4.9	170.0 ± 6.1	460.5 ± 4.9	460.8 ± 7.1

Comments on columns: Column 1: total H I mass; Column 2: velocity width at 50% of the peak flux; Column 3: velocity width at 20% of the peak flux; Column 4: systemic velocity from W_{50} midpoint; Column 5: systemic velocity from Eqn. 2.4.

2.4.3 Total intensity map

The full H I total intensity map extracted from the NA H I data cube is shown in the upper panel of Fig. 2.6. The edge of the H I disk (the outer-most contour level) lies at $\sim 510''$ and therefore extends out to $R \sim 20$ B-band scale lengths. For comparative purposes the IRAC 3.6 μm image of the stellar disk is shown in Fig 2.7. To determine the photometric centre, we fitted ellipses to three 3.6 μm flux density annuli near the edge of the old stellar disk. A 3.6 μm flux density contour at a level of 1.2 MJy ster^{-1}, the average flux density of the second annulus, is shown in Fig. 2.7. The average flux densities of the other two annuli are 0.8 and 1.7 MJy ster^{-1}. The average centre position of the ellipses fitted to the flux density annuli, $\alpha_{2000} = 09^{h}\ 26^{m}\ 12.611^{s}$, $\delta_{2000} = -76^{\circ}\ 37'\ 37.80''$, was used to estimate the position of the photometric centre (shown as a cross in Fig. 2.7). For comparison, the 2MASS determination of the centre of the system is $\alpha_{2000} = 09^{h}\ 26^{m}\ 11.53^{s}$, $\delta_{2000} = -76^{\circ}\ 37'\ 34.80''$ (Skrutskie et al., 2006). To facilitate length-scale comparisons between IR and H I images, an ellipse with semi-major axis length $a = 98''$, the R-band R_{25} radius determined by Meurer et al. (1994), is included in the figures. In their study of the H I content of 73 late-type dwarf galaxies, Swaters et al. (2002) found that the ratio of the H I extent to the optical diameter, defined as 6.4 disk scale lengths, is 1.8 ± 0.8 on average. The same ratio for NGC 2915 is ~ 3.4, close to double that value.

Our observations resolve the central regions of NGC 2915 into two distinct H I concentrations (Fig. 2.6, lower panel). Their centres are separated by a distance of $\sim 60''$ (1.2 kpc) and have a combined mass of $\sim 2.2 \times 10^{7}$ M$_{\odot}$. The central H I concentrations are located close to the stellar core. They have approximately the same orientation and are roughly the same size as the stellar core, as demonstrated in Fig. 2.8. Several authors (Meurer et al., 1996; Masset & Bureau, 2003; Bureau et al., 1999) have treated this central H I morphology as an H I bar. Although our new, high-resolution H I observations partly detract from such a scenario, it could of course be the case that molecular hydrogen (H_2) fills the regions between the H I concentrations. In Sec. 5.3.5 of Chapter 5, the measured total star formation rate surface densities of NGC 2915 are used to infer the mass distribution of a possible molecular gas component at its centre. A total molecular gas mass of $M_{H2} = 5.7^{+3.4}_{-2.1} \times 10^{7}$ M$_{\odot}$ is inferred for NGC 2915. This amount of molecular gas is conceivably sufficient to fill the region between the central H I concentrations. Also visible in the H I total intensity map is a plume-like feature to the north-west of these central H I concentrations with a mass of $\sim 3.3 \times 10^{7}$ M$_{\odot}$.

The observed spiral structure of the outer disk is asymmetric: the arm beginning at the north-western central H I concentration can be traced over $\sim 200^{\circ}$ in azimuthal angle while the arm beginning at the south-eastern H I concentration can be traced for only $\sim 120^{\circ}$. The logarithmic spiral morphology of the H I disk is more clearly seen in a $\log_{10} R - \theta$ plot of the de-projected H I

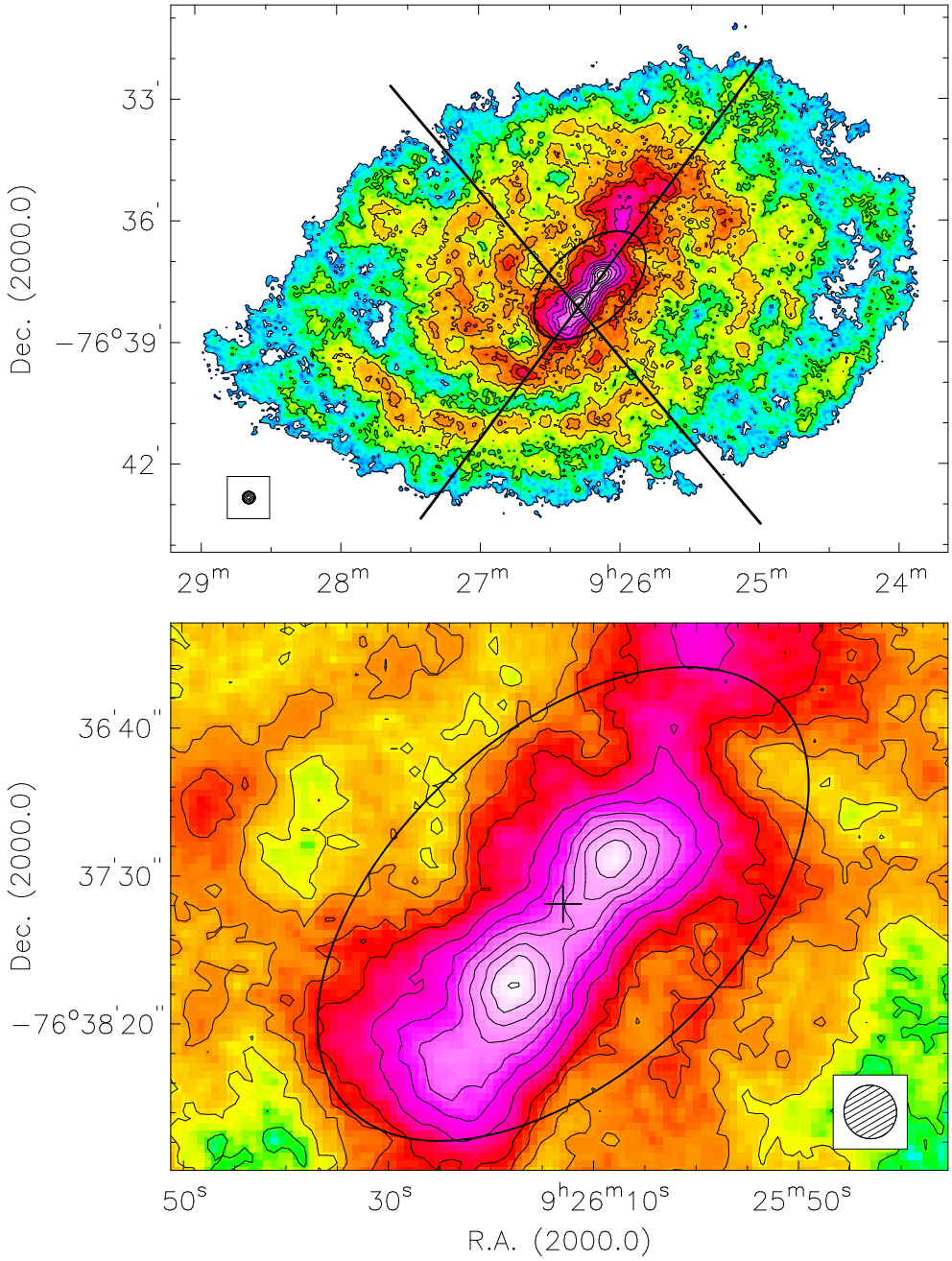

Figure 2.6: **Top panel:** H I total-intensity map for NGC 2915. Contour levels run from 10 - 60 mJy beam^{-1} km s^{-1} in steps of 10 mJy beam^{-1} km s^{-1} and from 80 - 230 mJy beam^{-1} km s^{-1} in steps of 20 mJy beam^{-1} km s^{-1}. **Bottom panel:** A zoom-in of the central region. The photometric centre from the 3.6 μm image is marked with a cross. The hatched circles in the lower corners represent the half power beam width of the synthesised beam. The black ellipse has a semi-major axis length of 98". The solid black lines represent the position-velocity slices shown in Fig. 2.14.

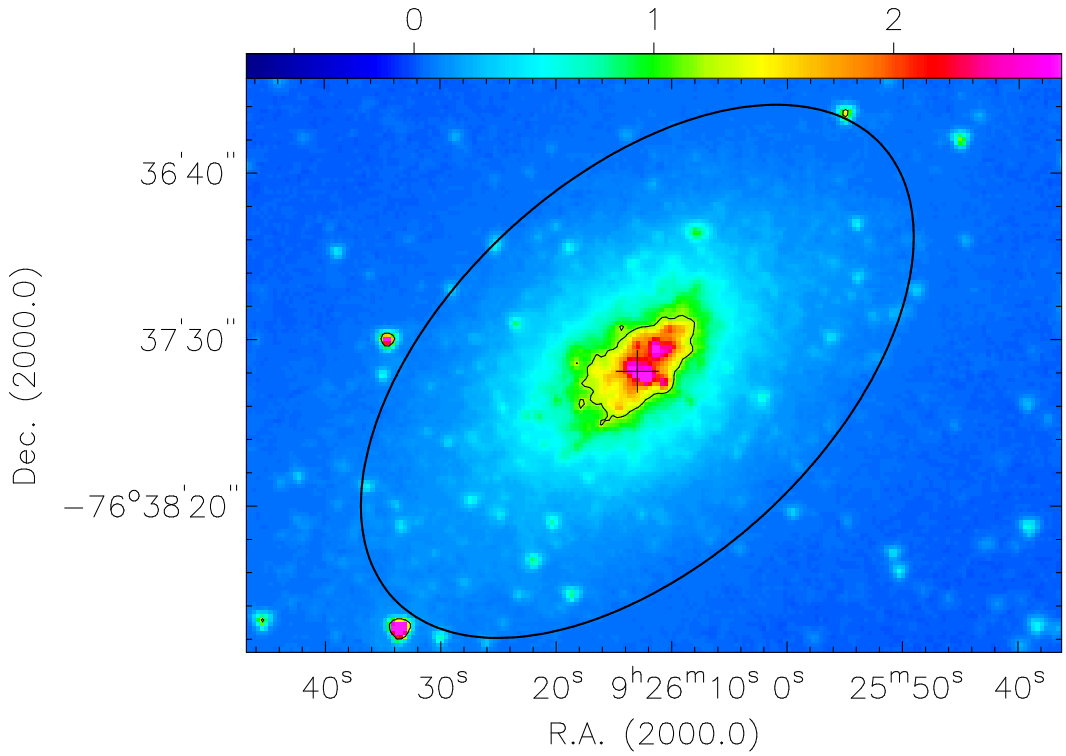

Figure 2.7: 3.6 μm IRAC *Spitzer* map of NGC 2915. The intensity scale is specified in units of MJy ster^{-1} by the colour bar. The single black contour is at a level of 1.2 MJy ster^{-1} and represents the average flux of one of three flux annuli used to estimate the position of the photometric centre. The estimated photometric centre is marked with a cross. The black ellipse is the same as that shown in Fig. 2.6

surface densities (assuming a constant inclination of 55° for the H I disk) as shown in Fig. 2.9. Each de-projected H I surface density was scaled by a factor 1.37 to account for helium and other metals. When the gas distribution is plotted using these modified coordinates, the spiral arms appear as linear features. Clearly visible in the figure is a main spiral feature at $2.0 \lesssim \theta \lesssim 4.0$, $0.55 \lesssim \log_{10} R \lesssim 0.7$ as well as an inner spiral feature at $1.7 \lesssim \theta \lesssim 2.6$, $0.43 \lesssim \log_{10} R \lesssim 0.48$ and an outer spiral feature at $3.5 \lesssim \theta \lesssim 5.0$, $0.74 \lesssim \log_{10} R \lesssim 0.8$. These features are marked by dashed lines in Fig. 2.9.

From the H I total intensity map, an H I surface density radial profile was constructed. This was done using the GIPSY task ELLINT which breaks the H I disk up into a set of user-specified concentric ellipses. A constant position angle[3] and inclination of 285° and 55° respectively were used. These values were determined by fitting ellipses to constant flux-density contours in the

[3]Measured anti-clockwise from north to the receding major axis.

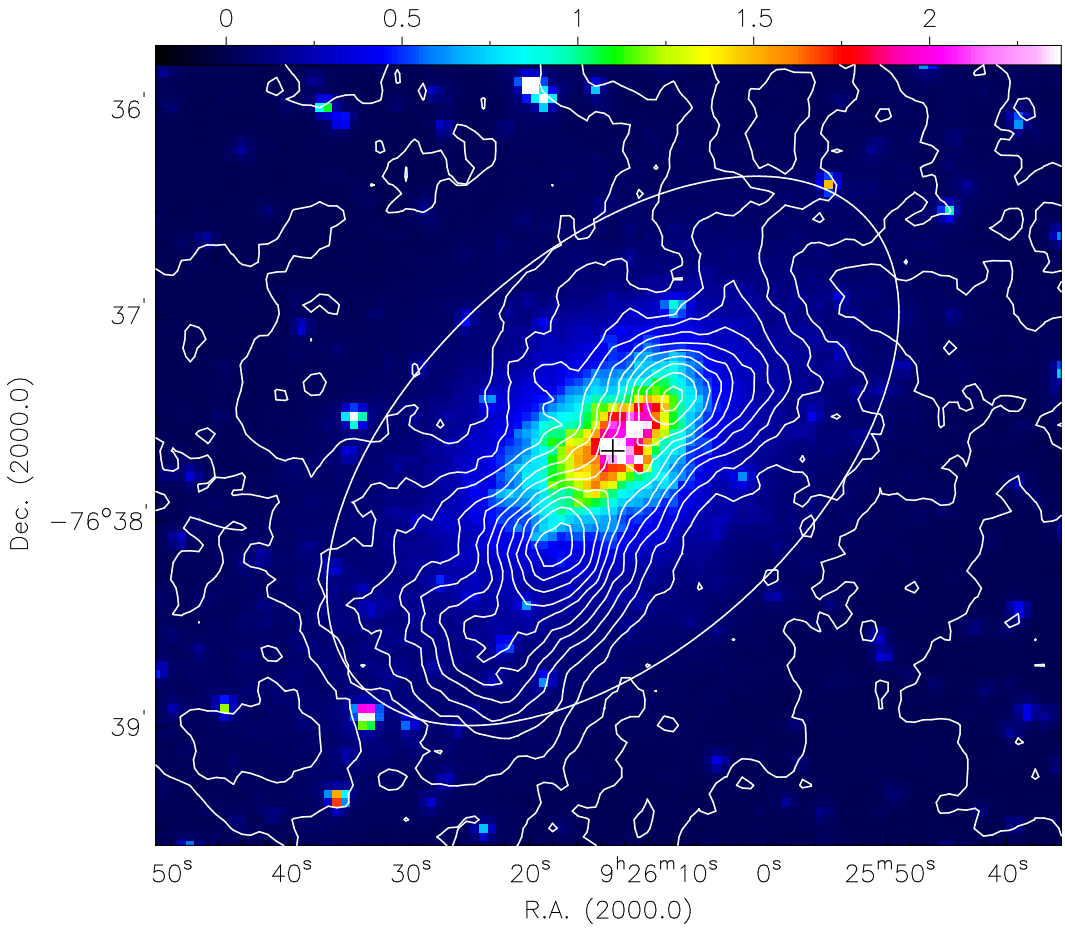

Figure 2.8: 3.6 μm IRAC *Spitzer* map of NGC 2915 with H I total intensity contours overlaid. The central H I over-densities are seen to correspond in position, orientation and size to the stellar core. The intensity scale is specified in units of MJy ster^{-1} by the colour bar. The H I total intensity contour levels run from 10 - 200 mJy beam^{-1} km s^{-1} in steps of 15 mJy beam^{-1} km s^{-1}. The white ellipse is the same as that shown in Fig. 2.6. The black cross marks the photometric centre.

H I outer disk. The ELLINT output is the average flux density in units of Jy beam^{-1} for each ring. These flux densities were then converted to H I column densities using the prescription from Walter et al. (2008):

$$N_{HI} = 1.823 \times 10^{18} \times \sum_i T_{B,i} \Delta V, \tag{2.6}$$

where $T_{B,i}\Delta V$ is the velocity-integrated surface brightness temperature in units of K km s^{-1} and ΔV is the channel width in km s^{-1}. The resulting column densities have units of atoms cm^{-2}.

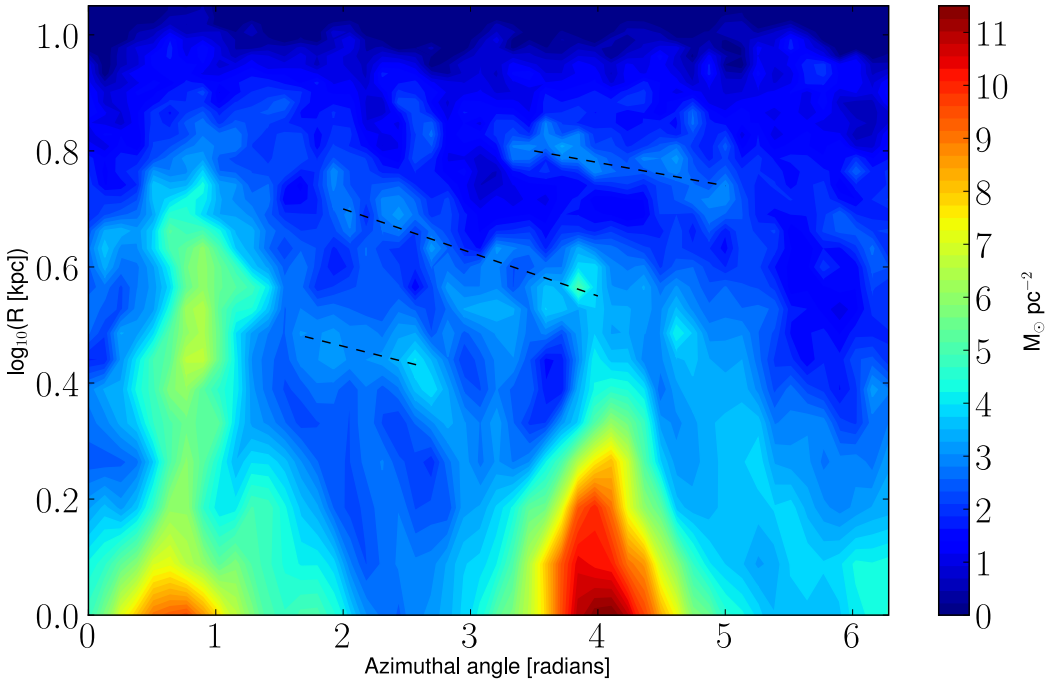

Figure 2.9: Gas surface density distribution of NGC 2915 in $\log_{10} R$ - θ coordinates, obtained by assuming an inclination of 55° and scaling the de-projected H I surface densities by 1.37. The dashed lines mark the spiral features in the H I distribution.

Finally, each azimuthally averaged column density was inclination-corrected and converted to a surface density in units of solar masses per square parsec. The resulting H I surface density profile is shown in Fig. 2.10.

In an attempt to better constrain the H I distribution of NGC 2915, an H I total intensity map was extracted from the RW H I data cube. For the sake of brevity this map is not shown here, yet it suffices to say that the higher spatial resolution confirms the above-mentioned nature of the central H I concentrations. However, the very low S/N ratios in the outer parts of this map yield it unsuitable for the study of low column density H I features, with only the central-most H I features standing out above the noise. This map does not allow for a more accurate study of the H I distribution and is therefore not discussed further.

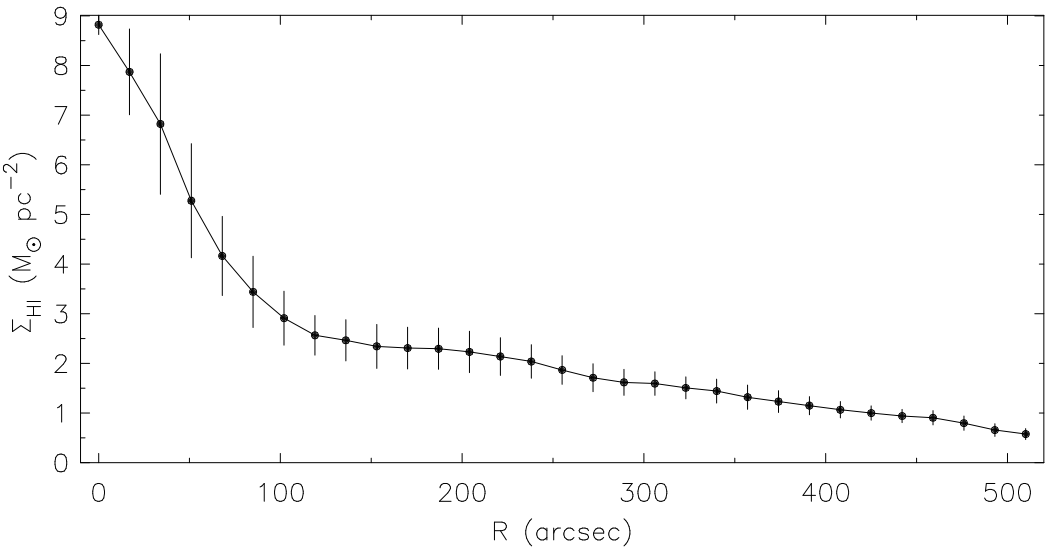

Figure 2.10: NGC 2915 H I surface density radial profile. All surface densities have been inclination-corrected. Error bars represent the r.m.s spread of the surface densities in each azimuthally-averaged ring.

2.4.4 Velocity field

The third-order Gauss-Hermite velocity field is shown in Fig. 2.11. The blank pixels in this map are those that were rejected by the fitting routine according to the criteria mentioned in Sec. 2.3.5. de Blok et al. (2008) showed that the Gauss-Hermite parameterisation of a line profile gives a robust estimate of the peak of the profile. Inner contours roughly parallel to the kinematic minor axis are caused by $V(R) \propto R$ rotation while the outer contours running radially away from the centre are due to a constant rotation speed. The overall "S-shaped" distortion of the contours is indicative of a kinematic warp within the disk. Small wiggles along the outer contours are caused by streaming gas motions. The sharp kinks at inner radii suggest the presence of non-circular velocity components within the gas. Finally, differences in the shapes of the iso-velocity contours on the receding and approaching halves of the galaxy are indicative of a degree of kinematic lopsidedness within the galaxy.

A third-order Gauss-Hermite velocity field was also extracted from the RW H I data cube. Due to the high noise levels in the RW H I cube, most line profiles were rejected by the fitting filters and hence not fitted. The general characteristics of the fitted peaks of the remaining profiles are very similar to those of the NA velocity field, differing on average by ~ 3 km s^{-1}. Rather than showing this H I velocity field here, a tilted ring model is fitted to it in Sec. 3.1.2

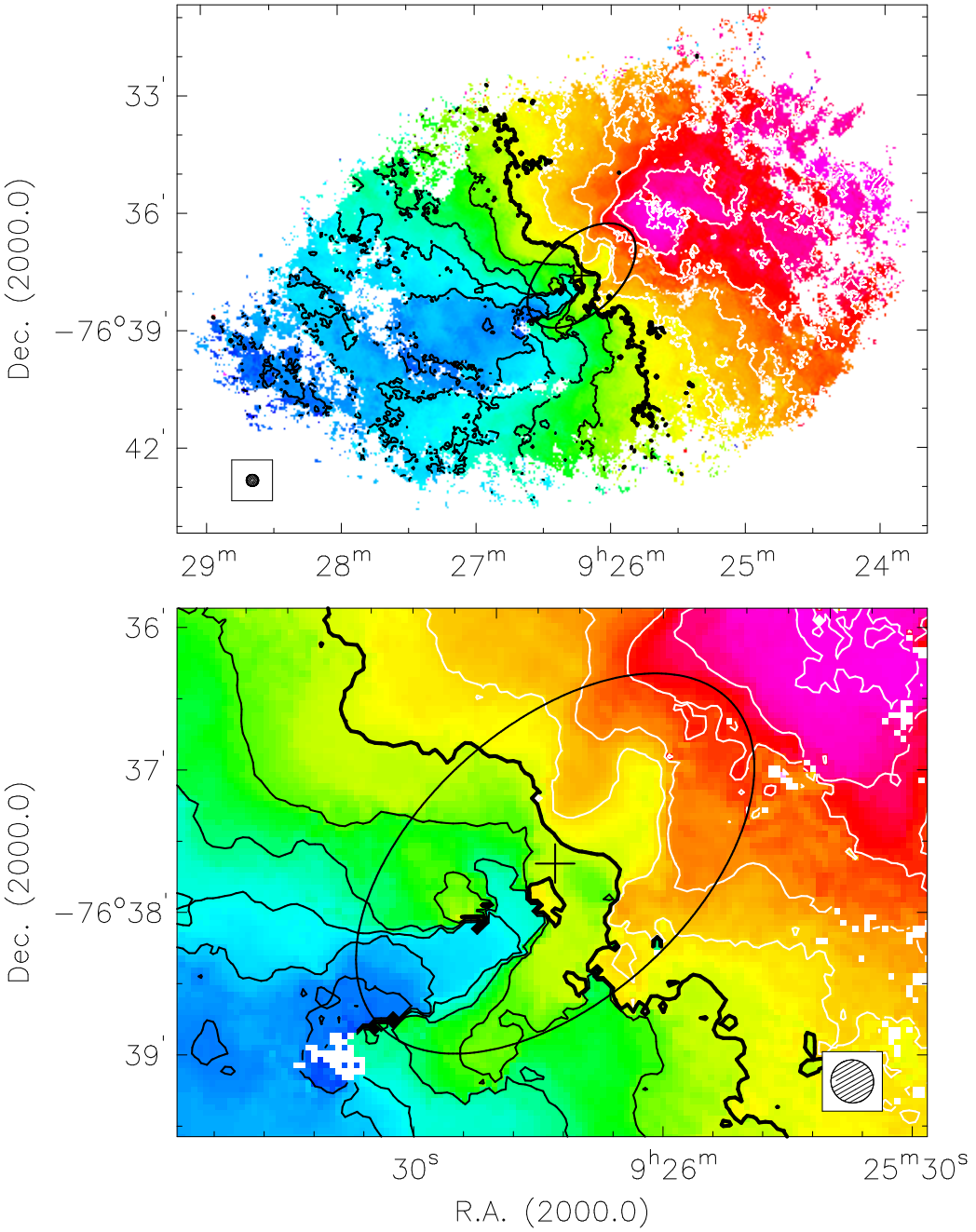

Figure 2.11: **Top panel:** Third-order Gauss-Hermite H I velocity field of NGC 2915. **Bottom panel:** A zoom-in of the central region. Contours are separated by 15 km s^{-1}, with the thick contour marking the systemic velocity at 465 km s^{-1}. White and black contours represent receding and approaching halves of the galaxy respectively. The hatched circles in the lower corners represent the half power beam width of the synthesised beam. The ellipse is the same as that shown in Fig. 2.6.

to demonstrate that the resulting rotation curve is very similar to the one derived using the NA third-order Gauss-Hermite velocity field. Motivated by this result is the decision to use only the NA velocity field for our kinematic analyses.

2.4.5 Second-order moment map

The second-order H I moment map extracted from the NA cube is shown in Fig. 2.12. The highest second-order moments are found near the stellar core of the galaxy. The radial profile of the second-order moment map is shown in Fig. 2.13. If the second-order moments are interpreted as a measure of the gas velocity dispersion, then the average outer disk dispersion of ~ 10 km s^{-1} is close to the constant gas velocity dispersion value of 11 km s^{-1} found by Leroy et al. (2008) for a sample of THINGS late-type galaxies.

2.5 Non-Gaussian line profiles

Position-velocity slices taken though the centre of NGC 2915 betray the presence of broad and multi-component line profiles at inner radii. Figure 2.14 shows two position-velocity slices, the positions of which are shown in the H I total intensity map (Fig. 2.6, top panel). The first slice is taken at a position angle of 322°, through both of the central H I concentrations. This slice suggests that the galaxy contains a fast-rotating gas component near its centre, clearly manifesting itself as a sharp velocity spike with a peak velocity of ~ 550 km s^{-1}. Line profiles near the centre of the galaxy show significant departures from Gaussianity.

This position-velocity slice also reveals asymmetric line profiles on the receding side of the galaxy, seen in the upper-left quadrant ($V > V_{sys} = 465$ km s^{-1}, angular offset $< 0''$) as an "H I beard" that is lagging in velocity relative to the main disk. To better distinguish this "beard emission", zeroth- and first-order moment maps were generated of residual emission after subtracting single-component Gaussian fits to the H I line profiles. The zeroth-moment map (top right panel in Fig. 2.15) exhibits a clear residual excess near the position of the plume-like H I feature seen in the H I total intensity map (delimited by a black rectangle in the top left panel of Fig. 2.15), thereby linking this feature of the H I distribution with the "beard" emission. The excess residual is caused by the long, non-Gaussian low-velocity tails of the H I line profiles clearly seen in the position velocity slice. Strong residual also appears in the vicinity of the central H I concentrations seen in the H I total intensity map. Many line profiles in this region of the galaxy are double-peaked, and hence poorly approximated by a single-component Gaussian. The first-order moment map shows a large fraction of the residual in the region of the plume-like

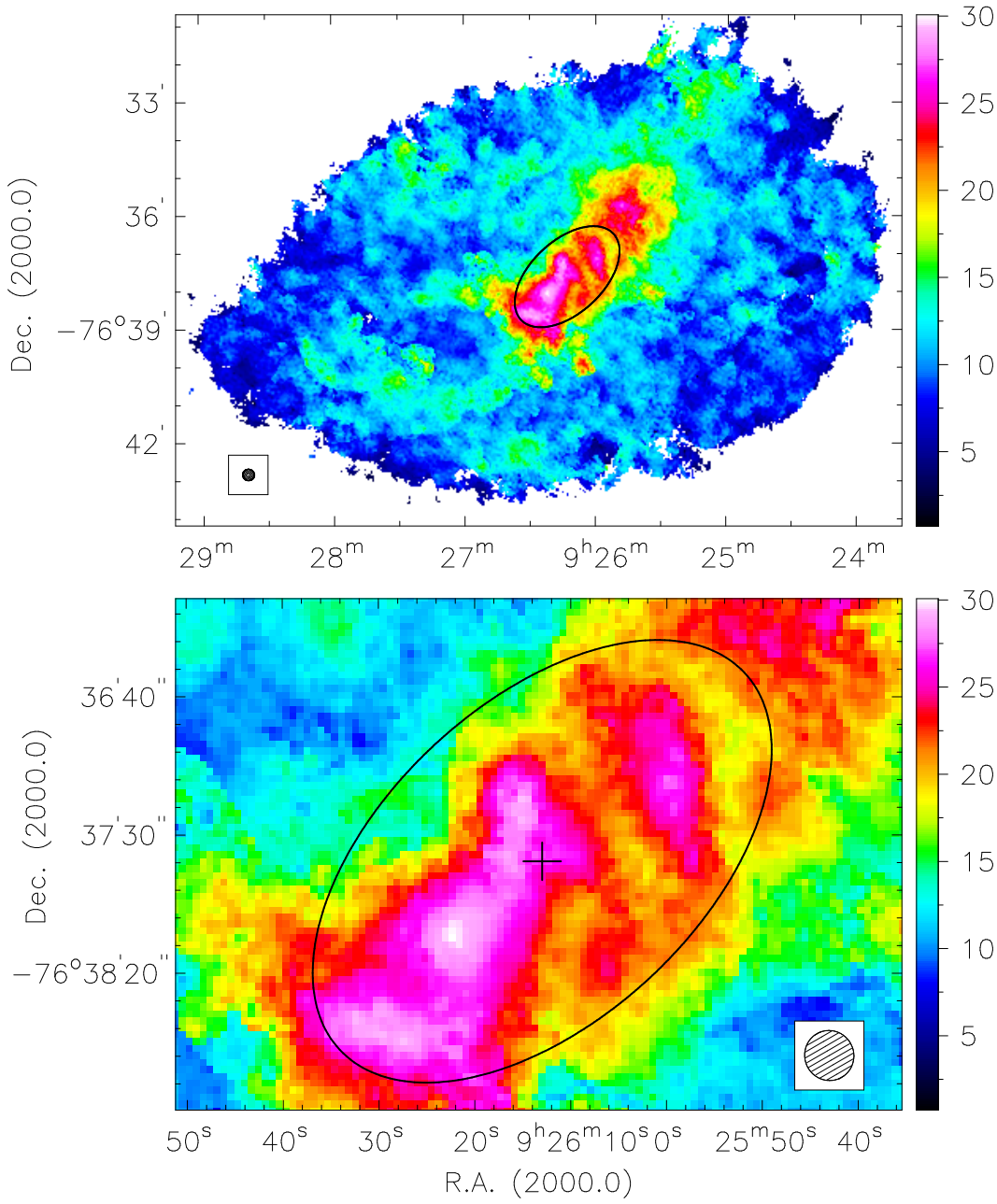

Figure 2.12: **Top panel:** Second-order H I moment map of NGC 2915. **Bottom panel:** A zoom-in of the central region. The intensity scale is specified in units of km s^{-1} by the colour bars. The hatched circles in the lower corners represent the half power beam width of the synthesised beam. The black ellipse is the same as that shown in Fig. 2.6.

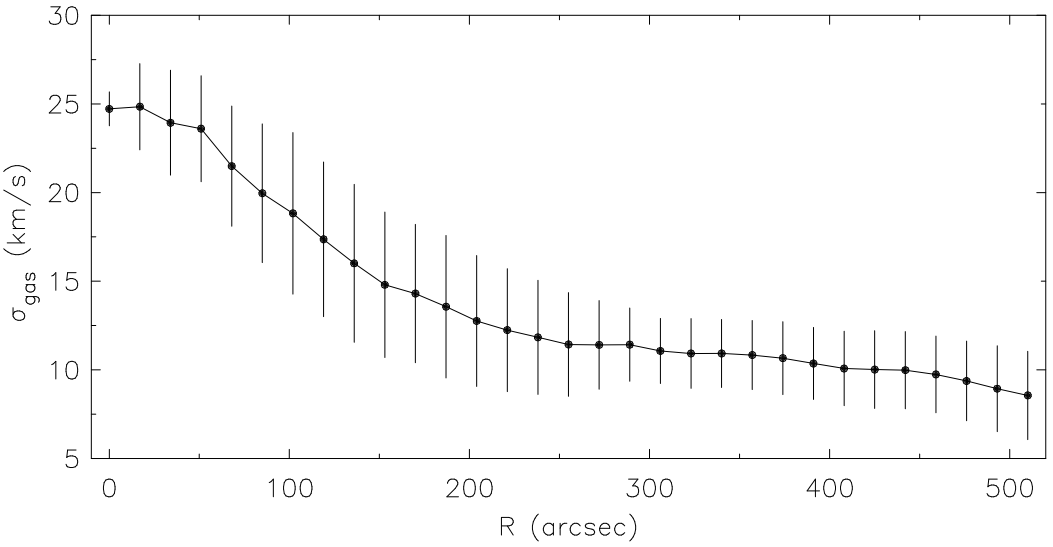

Figure 2.13: NGC 2915 second-order H I moment map radial profile. Error bars represent the r.m.s. spread of the second-order moments in each azimuthally averaged ring.

H I feature to lie close to the systemic velocity of NGC 2915 ($\sim$ 460 km s^{-1}), thereby providing further evidence of the kinematic separation of the "beard emission" from the regular circular kinematics of the underlying H I disk. Treating the "beard emission" as being associated with the plume-like H I feature of the H I distribution, its approximate mass is $\sim 3.3 \times 10^7$ M$_\odot$, 5.6% of the total H I mass of NGC 2915.

The second position-velocity slice is extracted almost parallel to the minor axis, through the south eastern central H I concentration which contains many double-component profiles. Line profiles in this central region are split by $\sim$ 30 km s^{-1} on average. The sharp rise seen toward the centre of the second-order H I moment map radial profile (Fig. 2.13) over-estimates the true H I velocity dispersions of the inner disk of NGC 2915. Since the disturbed H I line profiles are located within $\sim 150''$ of the centre of NGC 2915, it is plausible that the central gas dynamics of the galaxy are largely dictated by the stellar winds of its young stellar population. This possibility is examined in detail in Sec. 3.7

2.6 Systematic effects

Observing a gaseous disk with a beam of finite size results in any pointing at a particular position containing information from the nearby surrounding H I. This effect is commonly known as beam

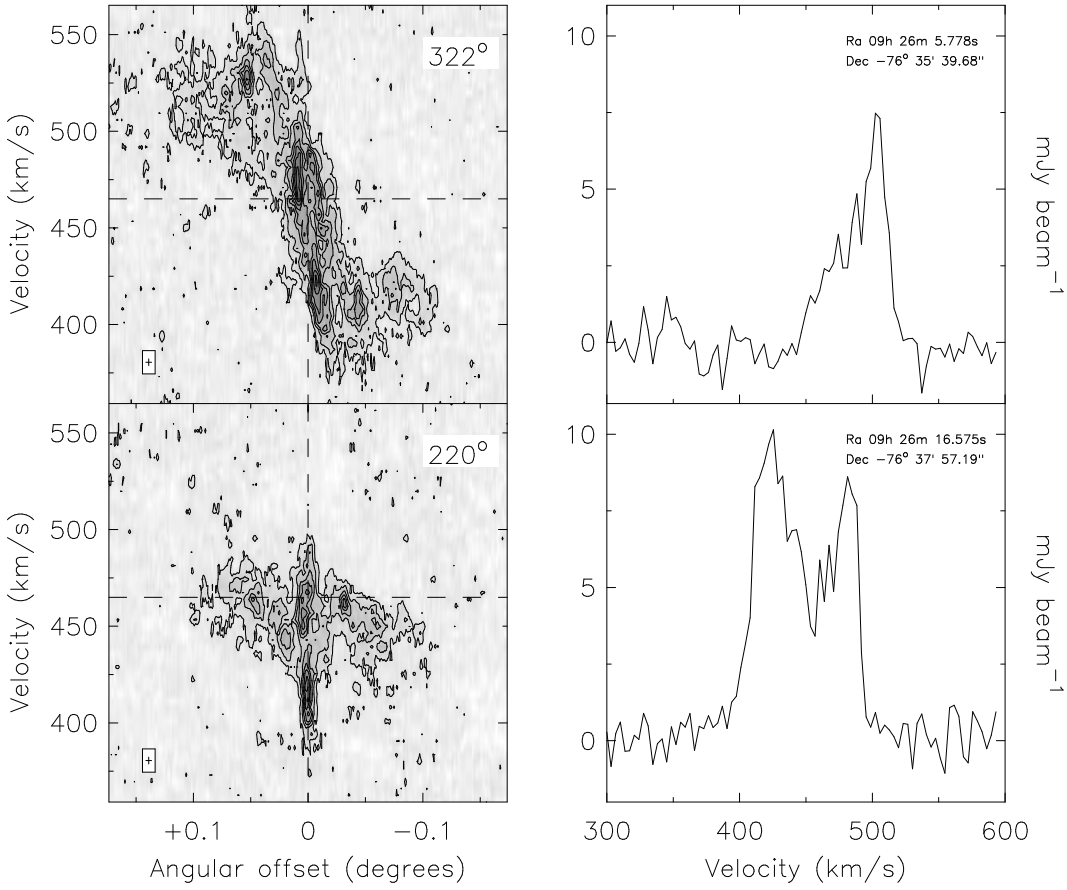

Figure 2.14: Position-velocity diagrams extracted along (1) a position angle of 322° (**top left**) and (2) a position angle of 220° (**bottom left**). The slice positions are shown in the H I total intensity map (Fig. 2.6). The thickness of the slices is that of a single pixel in the data cube (2.5″) and the velocity resolution is 3.5 km s^{-1}. The intensity scale runs from -3σ to (white) 40σ (black). Contours start at 2σ in steps of 3σ. Also presented are typical broad (**top right**) and split (**bottom right**) line profiles extracted from the plume-like H I region and south-eastern central H I over-density seen in the H I total intensity map. Exact profile positions are given in each panel.

smearing and is an effect suffered by all H I observations. Both the observed spatial distribution of the H I and the observed H I kinematics are affected. Compact, high column density features in the total intensity map will appear smeared while intrinsically under-dense regions in the disk (holes, inter-arm clearings) will appear filled. The outer disk will also appear slightly larger in spatial extent. Line profiles will be artificially broadened towards the systemic velocity and sharp velocity gradients intrinsic to the gas will be hidden.

The main factor determining the extent of the beam smearing effects is the size and shape of the beam relative to the size of the observed H I distribution. However, the inclination of the disk of a galaxy can also lead to uncertainties in measurements of the H I distribution and kinematics. If the galaxy is highly inclined, several line-of-sight velocities will contribute to a velocity measurement at a particular disk position. If, on the other hand, the disk is at too low an inclination, the random three-dimensional motions of the gas that are not associated with the global circular rotation of the disk begin to dominate over the projected circular velocities, again generating uncertainties. An intermediate inclination of $\sim 60^\circ$ is largely accepted as the optimal inclination that minimises the combination of these effects.

In this section the effects of beam smearing on our new NGC 2915 H I observations are quantified. The size of the synthesised beam is small relative to the extent of the H I disk of NGC 2915. The half-power-beam-width is $\sim 17''$ while the H I disk at this resolution extends further than $510''$. A single pointing will therefore only cover a small portion of the entire disk and the effects of beam smearing in this sense are expected to be small. The potential problem, however, lies in the fact that the inner portion of the rotation curve (derived in Sec. 3.1.2) rises very sharply. It rises as $V(R) \propto R$ from $V \sim 9.5$ km s^{-1} at $R \sim 17''$ and reaches its maximum rotation velocity of $V \sim 82$ km s^{-1} within $R \sim 150''$ from the centre of the disk. This is an average velocity gradient of 0.55 km s^{-1} arcsec^{-1} or, equivalently, 9.4 km s^{-1} per half-power-beam-width. Thus, despite the high spatial resolution of our observations, line profiles (i.e. the observed kinematics) can still be affected by the steeply rising inner rotation curve.

Quantifying the effects of beam smearing is often best done through modeling. Bosma (1978) was the first to do this by producing model data cubes which he smoothed using progressively larger beams. From the smoothed cubes he constructed velocity fields in order to derive rotation curves. He compared each of these rotation curves to the rotation curve used to create the original cube. He concluded that beam smearing can seriously affect the inner, steeply rising portion of the rotation curve if less than ~ 7 half-power-beam-widths are contained within the Holmberg radius.

We follow Bosma's procedure by producing two model data cubes which differ only in the rotation curves used to produce them. The cubes were produced using the GIPSY task GALMOD. The routine assumes axisymmetry and distributes many "H I clouds" into a set of tilted rings. For each ring the inclination, position angle, and rotation velocity must be provided as well as a velocity dispersion, column density and scale height perpendicular to the plane. The routine then proceeds to select random positions at which to distribute H I clouds within each ring. A more detailed description of this procedure is given in Sec. 3.7.3. A scale height of 486 pc, corresponding to $\sim 22.5''$ at a distance of $D = 4.1$ Mpc was used for all rings in each cube. Again, a detailed derivation of this value is presented in Sec. 3.7.3. To allow the model cubes

to be similar to the H I data cube of NGC 2915, we used our derived H I surface density radial profile (Sec. 2.4.3) and a constant velocity dispersion of 9 km s^{-1}. The inclinations and position angles of all the rings in each cube were set to 55° and 285° respectively. For the rotation curves we used modified versions of the circular rotation curve derived from our tilted ring modeling (Sec. 3.1.2). The input rotation curves had the same shape as the observed rotation curve but rose more steeply in their inner portions: the first curve reached a maximum velocity of 83.6 km s^{-1} within 102″ while the second curve reached this velocity within 51″. For comparison, the observed rotation curve of NGC 2915 rises as $V(R) \propto R$ from the centre of the galaxy and reaches a maximum rotation speed at $R \sim 150''$. The radial profiles of the above-mentioned input parameters used to generate each of the two model cubes are shown in Fig. 2.16.

The model cubes were smoothed down to a resolution of 17″ to match the resolution of the H I data. From each of these model cubes a third-order Gauss-Hermite velocity field was extracted using the method outlined in Sec. 2.3.5. To each of the two model velocity fields, a tilted ring model (described in detail in Sec. 3.1) was fitted using the GIPSY task ROTCUR. All of the ring parameters, except for the expansion velocity which was fixed to zero, were allowed to freely vary in ROTCUR.

Figure 2.16 shows the results of the tilted ring fitting. For the sake of clarity only parameters over the radial range $0'' \leq R \leq 300''$ are shown. It is only within the steeply rising portions of the rotation curves that the fitted tilted ring parameters differ from the input values. The differences are, however, small. The fitted centres of the rings deviate at most by half a pixel from the input centre position. Some of the fitted position angles differ by $\sim 5°$ but this is within a beam-width of the centre of the galaxy where beam smearing is unavoidable. The fitted inclinations differ from the 55° input value by $\sim 5°$ for $0'' \lesssim R \lesssim 80''$. The differences between the fitted systemic velocities and the input value of 465 km s^{-1} are negligible. These beam smearing effects which are small, yet clearly present, are best seen in the fitted rotation curves which differ slightly from the input rotation curves. To highlight the differences between the input and the fitted rotation curves, the absolute velocity differences are shown in the lower right panel of Fig. 2.16. Within 17″ from the centre of the galaxy, the absolute velocity differences are as large as 30 km s^{-1}. This is to be expected since a beam centred on the dynamical centre of the galaxy will sample many different lines of sight. Beyond $R = 17''$, however, the differences between the steeply rising portions of the input and fitted rotation curves are less than 5 km s^{-1} and are essentially zero beyond the knees of the input rotation curves. Clear spikes in the absolute velocity differences are visible but these are at the unrealistically sharp knees of the input rotation curves.

In summary, although beam smearing effects are present in our model data cubes and velocity

fields, they are generally very small. They are relatively large only within one beam-width of the galaxy centre and at the very sharp knees of the input rotation curves. Since the velocity gradient of the steeply rising portion of the observed NGC 2915 rotation curve is shallower than the model velocity gradients, we do not expect the observed kinematics to be significantly affected by beam smearing. The rotation curve of NGC 1705, derived in Sec. 4.5.2, varies with radius roughly as $V(R) \propto R$ over the extent of its H I disk. Its rotational gradient is shallower than that of the inner portion of NGC 2915's observed rotation curve. Beam smearing effects of NGC 1705's observed kinematics are thus also expected to be negligible. Furthermore, as mentioned above, since our data are well resolved, we expect the observed spatial distribution of the H I to be an accurate representation of the true H I distribution. Based on these results we do not make any corrections for beam smearing effects in the analyses that follow.

2.7 HI line profile parameterisations

An H I velocity field is essentially a 2-dimensional compression of a full 3-dimensional data cube. To create a velocity field, a typical velocity that is representative of a particular kinematic component of interest needs to be generated for each line profile. This velocity is then assigned as the line-of-sight velocity to the corresponding resolution element in the velocity field. A line profile's peak-associated velocity is usually adopted as being representative of the typical rotational motion along the line of sight. Thus, in the case that a galaxy is regularly rotating at all radii; its symmetric, high signal-to-noise line profiles allow for the trivial construction of a so-called "peak-amplitude" velocity field that accurately represents the typical rotational velocity along each line of sight.

Line profiles shapes are not always neat and symmetric. The shapes of H I line profiles are affected by various systematic and random effects, each of which in turn affect the determination of a representative profile velocity. A common instrumental effect is beam smearing which, in practice, results in systematically asymmetric line profiles with "long velocity tails" in the direction of the systemic velocity. Beam smearing effects can be particularly severe in the case of low-resolution observations, especially of small dwarf galaxies, in which a single pointing of the telescope will sample a large portion of the galaxy. It was shown in the previous section, however, that beam smearing effects are expected to be negligible for the H I data presented in this thesis. In addition to systematic effects, randomly-induced departures of profile shapes from Gaussianity also need to be contended with. The presence of non-circular velocity components within a galaxy's rotating gaseous disk will affect the shapes of H I line profiles. Random asymmetric as well as symmetric deviations of the line profile shapes from Gaussianity will be present, with such deviations being potentially difficult to identify and correct for.

In the case that a line profile's peak-associated velocity does not accurately represent the typical rotational motion along the line of sight, the manner in which the typical rotation velocity is alternatively determined can significantly affect the structure and properties of the velocity field. Appearing below are descriptions of some standard profile parameterisations used to create H I velocity fields, as well as a further discussion of the peak velocity field. The pros and cons of each parameterisation are discussed and the resulting peak-associated velocity estimates compared to one another in the bottom-panels of Fig. 2.17.

In the sections appearing below, individual line profiles were fitted with single- and double-component Gaussians as well as third-order Gauss-Hermite polynomials using the GIPSY task XGAUFIT. The task implements a non-weighted least-squares fitting routine, described in Marquardt (1963), to determine the optimal parameters for a line profile. An important component of the XGAUFIT task is dedicated to finding good initial estimates for the fitted parameters. It does this by fitting second-order polynomials to the line profiles, using a predetermined number of data points around the profile maximum. The fitted coefficient of the quadratic term is then used as an approximation of the second derivative of the line profile. A moments method is then used to estimate the centre and dispersion of the profile. The profile amplitude is simply derived from the actual line profile. The iterative fitting routine is halted when successive fits fail to produce a decrement in the reduced χ^2 statistic less than a specified tolerance level. The default tolerance level of 0.001 was used for all fits, yielding good fit results. For further details see the online XGAUFIT documentation*.

Intensity-weighted mean

The most common method of generating a velocity field involves calculating an intensity-weighted-mean (IWM) velocity, V_{IWM}, for each line profile:

$$V_{IWM} = \int I(V)\ V\ dV / \int I(V)\ dV, \tag{2.7}$$

where $I(V)$ is the intensity amplitude of a line profile at a line-of-sight velocity V. A benefit of the method is that it is simple and computationally inexpensive to implement. In the case that a line profile is reasonably symmetric and represents a single kinematic component, the IWM velocity estimate will closely match the peak-associated profile velocity. By construction, however, an IWM velocity determination is susceptible to the effects of profile asymmetries, with the more extended side of the profile holding more weight than the less extended side. This effect is illustrated in the bottom-left panel of Fig. 2.17 where, because of the extended high-velocity portion of the profile, the IWM velocity of $V_{IWM} = 9.4$ km s^{-1} is significantly larger than the

*http://www.astro.rug.nl/ gipsy/tsk/xgaufit.dc1

peak-associated velocity of $V \sim 7.2$ km s^{-1}.

The IWM velocity of a double-peaked profile will lie between the two profile peaks, representing the peak-associated velocity of neither component satisfactorily, regardless of which component may be of more interest. This is demonstrated in the bottom-right panel of Fig. 2.17 in which the IWM velocity of $V_{IWM} = 9.6$ km s^{-1} inaccurately represents either of the $V \sim 8.0$ km s^{-1} and $V \sim 11.5$ km s^{-1} peak-associated velocities. The IWM velocity field of NGC 2915 is shown in the top-left panel of Fig. 2.18. No additional smoothing or blanking was applied to the H I data cube in order to produce this map, i.e. it is the same map as shown in Fig. 2.11.

Peak amplitude

As stated by Sofue & Rubin (2001), in the outer parts of galactic disks, where line profiles can be treated as being symmetric about the peak, the IWM velocity estimate of a profile can be approximated by its peak-associated velocity. This method of assigning velocities to profiles is appealing since it is independent of the profile shape and is the most computationally inexpensive profile parameterisation method. Besides the expected shortcomings of the technique in the case of non-Gaussian line profiles, the method produces inaccurate velocity estimates in low signal to noise regions of a galaxy. This is clearly illustrated in the peak-amplitude velocity field of NGC 2915 (middle-left panel of Fig. 2.18) in which anomalous line-of-sight velocities are scattered along the edge of the H I disk. The lower-left panel of Fig. 2.17 shows how, because not all of the velocities along a line of sight are used to determine the typical rotational velocity, the peak-amplitude velocity is less affected by profile asymmetries. Furthermore, in the case of a double-peaked line profile in which the profile peaks have a large signal-to-noise ratio (lower-right panel of Fig. 2.17), the the peak-amplitude velocity will not lie in the middle of the two profile peaks as will the IWM velocity.

Single Gaussian

Line profiles extracted from a regularly rotating, moderately inclined gaseous disk are expected to be approximately Gaussian-shaped. Fitting single-component Gaussians to a galaxy's line profiles is a method often used to estimate the peak-associated velocities. A benefit of fitting the entire line profile is that the estimated velocity is less affected by noise and moderate profile asymmetries. Sufficiently strong profile asymmetries will, however, degrade the quality of fit. This is shown in the top left panel of Fig. 2.17 in which the peak of the fitted Gaussian has been "dragged" towards the extended portion of the profile. Double-peaked profiles stand the chance of having neither component satisfactorily represented by a fitted single component Gaussian,

as demonstrated in the top right panel of Fig. 2.17. The single-component Gaussian velocity field for NGC 2915 is shown in the top-right panel of Fig. 2.18. The white patches represent blank pixels whose corresponding line profiles were rejected by the fitting filters used to select the profiles suitable for parameterisation. For the single-component Gaussian, double-component Gaussian, and Gauss-Hermite h_3 velocity fields, three filters were used simultaneously when fitting the profiles: 1) profiles with fitted peak fluxes below 2.5σ were excluded, 2) profiles with a fitted line width less than the channel width were rejected, and 3) fitted profile peaks had to be within the velocity range of the data cube.

Double Gaussian

An extension of the single-component Gaussian parameterisation method is to simultaneously fit two Gaussians to each line profile, i.e. a double-component Gaussian. Depending on the spectral resolution of the data cube, a given line profile stands the chance of containing relatively few independent data points that are sufficiently above the noise for fitting purposes. When this occurs, fitting a double-component Gaussian can yield spurious results. Once the fit is made, the investigator is tasked with having to decide which of the two fitted Gaussian components best describes the typical rotation velocity along the line of sight. Furthermore, because both Gaussian components are fitted *simultaneously*, potentially close correlations exist between the errors in the fitted free parameters.

The left-most panel of the second row in Fig. 2.17 demonstrates how the the double-component Gaussian parameterisation is able to handle profile asymmetries, with the velocity associated with fitted peak of the larger-amplitude component, $V_{2G_1} = 7.0$ km s^{-1}, closely matching the profile peak at $V \sim 7.2$ km s^{-1}. By virtue of its construction, the double-component Gaussian accurately fits both component peaks of a typical double-peaked profile (right-hand panel in the second row of Fig. 2.17) as well as the profile minimum between the two profile peaks, which can provide a measure of the systemic velocity. The middle-right panel of Fig. 2.18 shows the H I velocity field constructed using the peak-associated velocity of the larger-amplitude component of a double Gaussian fitted to each line profile in the data cube. As expected, the structure of this velocity field is similar to that of the single-component Gaussian velocity field presented above it.

Gauss-Hermite h_3 polynomial

van der Marel & Franx (1993) introduced the method of using a sum of orthogonal components in a Gauss-Hermite series to parameterise line profiles of elliptical galaxies. A low order Gauss-

Hermite polynomial is well-approximated by a Gaussian while at higher orders it is parameterised by h_3 and h_4 parameters describing asymmetric and symmetric deviations from a Gaussian respectively. Furthermore, using a sum of orthogonal functions reduces correlations between fitted parameter errors. The Gauss-Hermite polynomials up to forth order are

$$\phi(x) = ae^{y^2/2}\left[1 + \frac{h_3}{\sqrt{6}}(2\sqrt{2}y^3 - 3\sqrt{2}y) + \frac{h_4}{\sqrt{24}}(4y^4 - 12y^2 + 3)\right], \tag{2.8}$$

where $y \equiv (x-b)/c$ (van der Marel & Franx, 1993). In the case that $h_3 = h_4 = 0$, the function is a Gaussian of amplitude a, mean b and centre c. If $h_3 \neq 0$ the profile is asymmetric, and if $h_4 \neq 0$, it has either a more pointed ($h_4 > 0$) or flatter ($h_4 < 0$) top than a Gaussian. As Young et al. (2003) point out, the disadvantage of the Gauss-Hermite formulation is that there is no simple physical interpretation of the magnitudes of h_3 and h_4.

A benefit of using the Gauss-Hermite formulation is that it contains fewer free parameters to be simultaneously fitted than the double-component Gaussian parameterisation. The left-hand panel in row 3 of Fig. 2.17 demonstrates how, with these fewer free parameters, a third-order Gauss-Hermite polynomial is able to accurately match the peak-associated velocity of an asymmetric profile. The figure below compares the Gauss-Hermite-estimated peak with that of the larger-amplitude component of a fitted double Gaussian. The right-hand panel of row 3 in Fig. 2.18 demonstrates that even a double-peaked profile is accurately fitted by a third-order Gauss-Hermite polynomial. de Blok et al. (2008) claim that including the h_4 term leads to less stable fits. While in high signal-to-noise profiles, the derived velocities will be close to the peak-amplitude velocities, Gauss-Hermite velocity fields are more stable in low signal-to-noise regions. For this as well as the above-mentioned regions we favour the third-order Gauss-Hermite profile parameterisation over the other above-mentioned parameterisations. The third-order Gauss-hermite velocity field is reproduced in the lower-right panel of Fig. 2.18 and it is this velocity field that is used to study the H I dynamics of NGC 2915 in Sec. 3.1.

2.8 Chapter summary

We have obtained new deep, high-resolution H I synthesis observations of NGC 2915 and have used them to conduct a detailed study of its H I distribution as well as a cursory examination of its H I kinematics. We estimate the total mass of the H I disk to be $M_{HI} \sim 5.4 \times 10^8$ $M_\odot$. Our high resolution, high sensitivity observations clearly resolve the inner H I distribution of NGC 2915 into two H I concentrations separated by $\sim$ 1.1 kpc. This observation discredits the claim by previous investigators that the central gas disk of the system is made up of a massive H I bar. We have shown the shapes of H I line profiles to be significantly non-Gaussian in the vicinity of

these central H I over-densities, being split by $\sim$ 30 km s^{-1} on average over the spatial extent of the lower H I concentration. These profiles are indicative of non-circular velocity components within the gas near the centre of NGC 2915. In Sec. 3.7 of Chapter 3, a detailed investigation of the central gas dynamics of this system is presented.

In terms of kinematics, a third-order Gauss-Hermite parameterisation of the H I line profiles was shown to sufficiently capture line profile asymmetries and departures from Gaussianity. The justification was made for adopting this form of the H I velocity field for subsequent analyses of the system's H I kinematics. Systematic beam smearing effects within the H I data were quantified and shown to be small relative the corresponding circular velocities. The observed spatial distribution of the H I is expected to be an accurate representation of the true distribution.

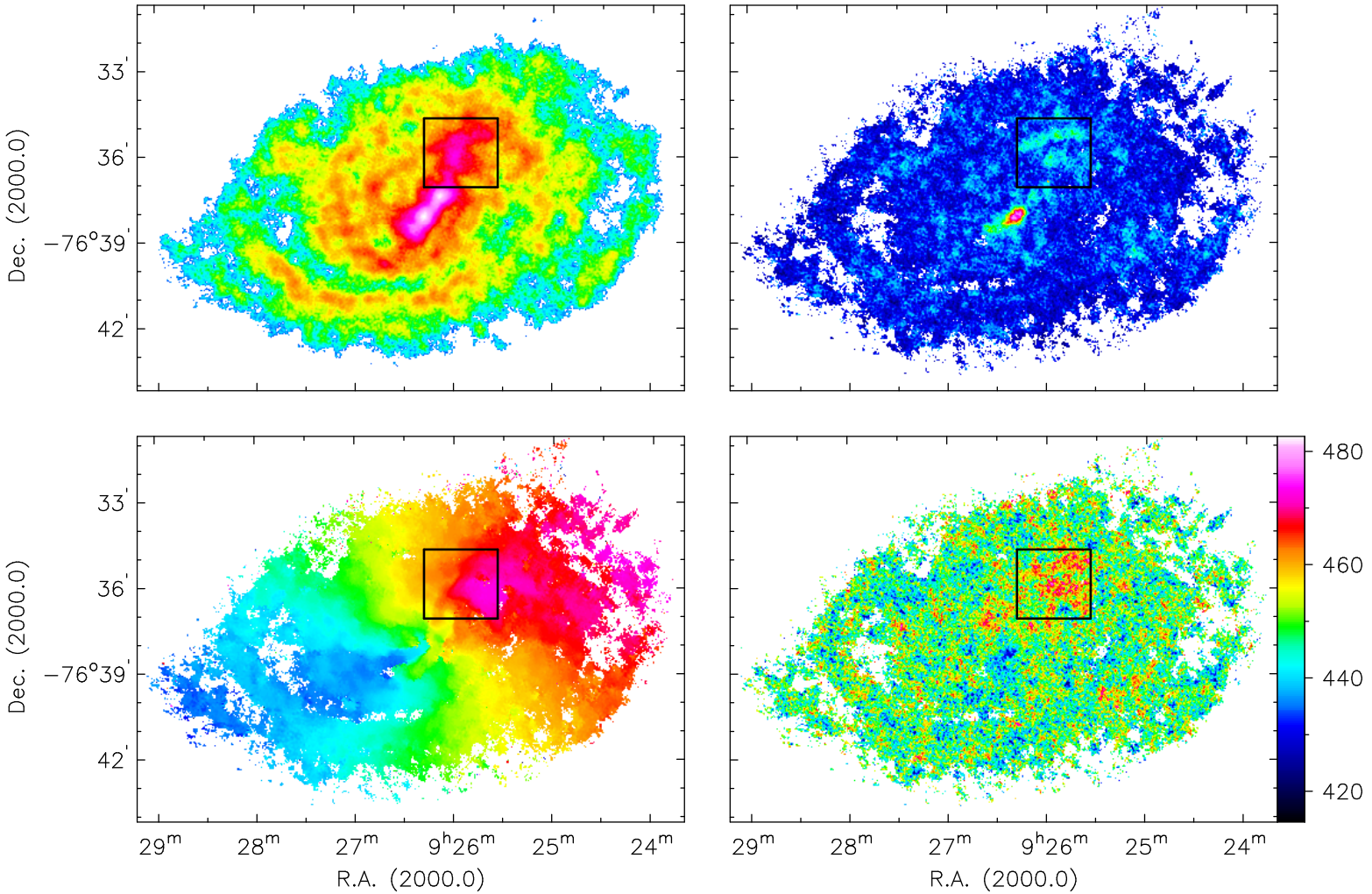

Figure 2.15: Zeroth- and first-order moment maps (top and bottom right panels respectively) generated of residual emission after subtracting single-component Gaussian fits to the line profiles in the H I data cube. The H I total intensity map and velocity field extracted from the H I data cube are shown in the top and bottom left panels respectively for comparison. In each panel the position of the plume-like feature seen in the H I total intensity map is delimited by a black rectangle. The position of this feature coincides with an excess of residual emission that lies close to the systemic velocity of ~ 460 km s^{-1}. A different intensity scale is used for all panels, with the intensity scale for the bottom right panel specified in km s^{-1} by the adjacent colour bar.

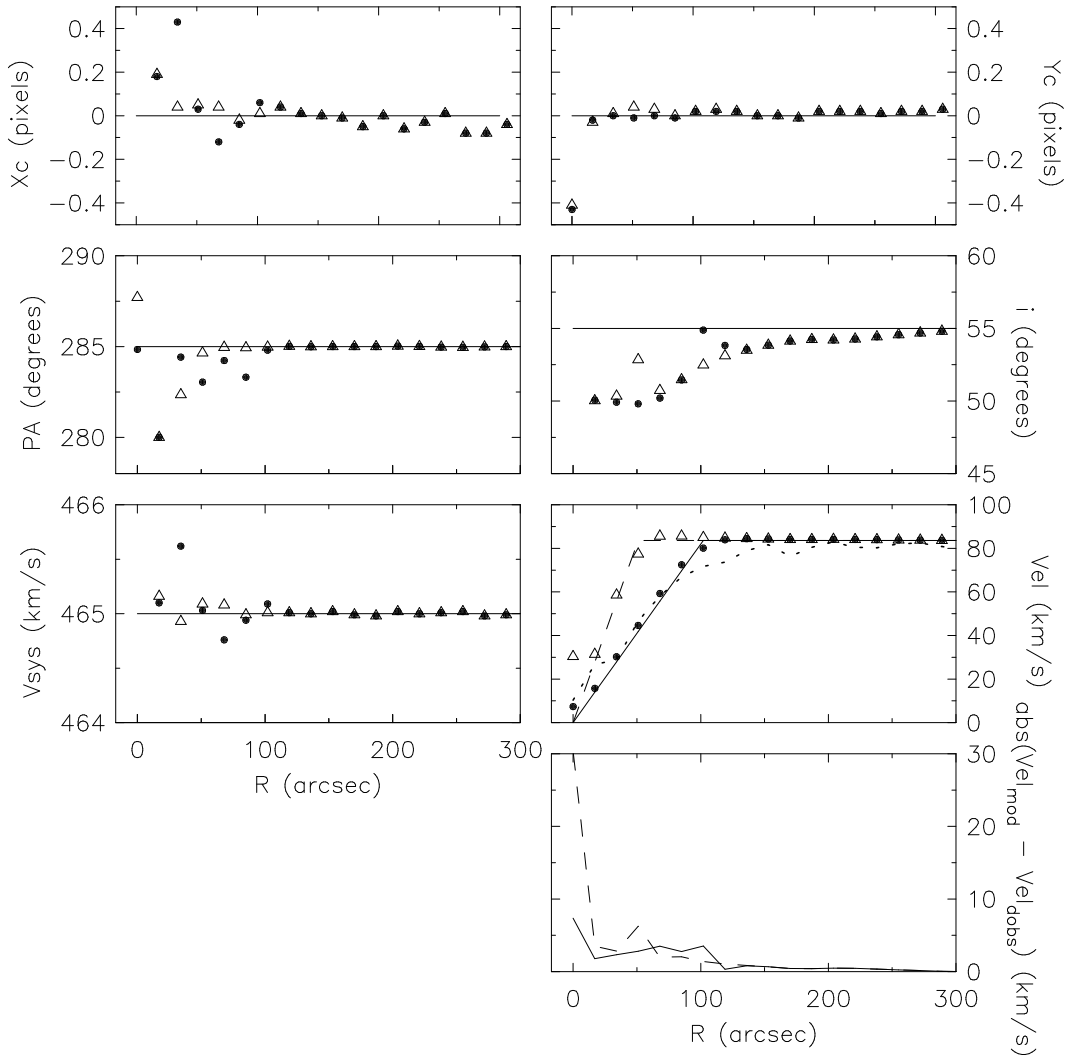

Figure 2.16: Tilted ring models fitted to model data cubes. In each panel the parameter input values used to construct the model cubes are represented by solid and dashed curves. Note that in the cases of X_c, Y_c, PA, i and V_{sys} the inputs for the two models are identical. The open triangles and filled circles in each panel represent the ROTCUR-fitted parameters. The dotted curve in the right-hand panel second from the bottom represents the observed rotation curve (derived in Sec. 3.1.2). The solid and dashed curves in the bottom panel represent the absolute velocity difference between the input and the fitted rotation curves.

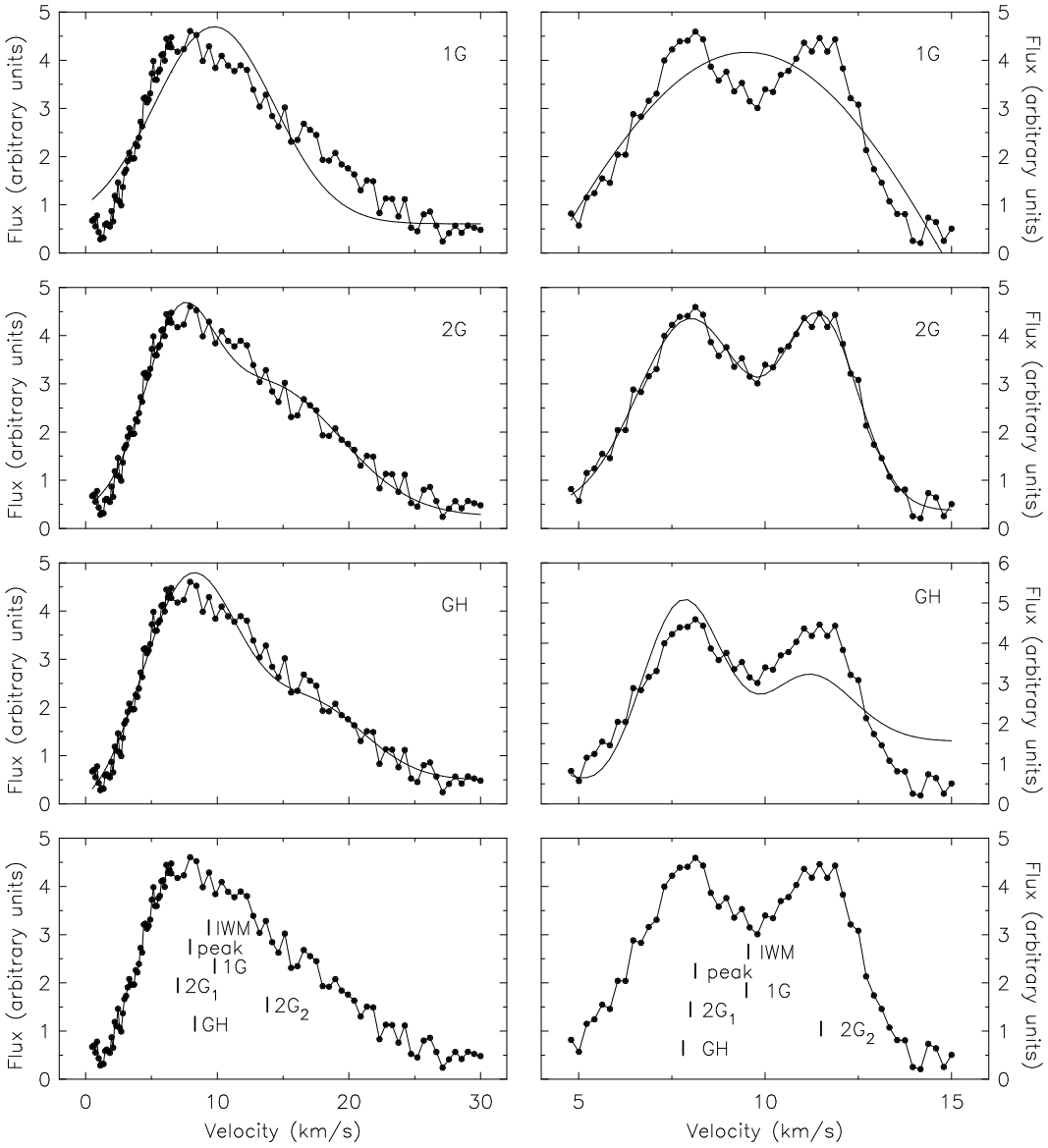

Figure 2.17: Various H I line profile parameterisations. In each panel the black filled circles represent the line profile extracted from the H I data cube. The solid black curves represent the fitted profiles. The left- and right-hand columns represent typical asymmetric and double-peaked line profiles. The profile parameterisations in rows 1–3 are single-Gaussian, double-Gaussian and third-order gauss-Hermite polynomial parameterisations respectively. The six short vertical lines in each of the bottom panels indicate the derived velocities using each of profile parameterisations. For the profile shown in the bottom left panel, the velocities are $V_{IWM} = 9.4$ km s^{-1}, $V_{peak} = 7.9$ km s^{-1}, $V_G = 9.8$ km s^{-1}, $V_{2G_1} = 7.0$ km s^{-1}, $V_{2G_2} = 13.8$km s^{-1} and $V_{GH} = 8.3$ km s^{-1}. For the profile shown in the bottom right panel, the velocities are $V_{IWM} = 9.6$ km s^{-1}, $V_{peak} = 8.1$ km s^{-1}, $V_G = 9.5$ km s^{-1}, $V_{2G_1} = 8.0$ km s^{-1}, $V_{2G_2} = 11.5$ km s^{-1} and $V_{GH} = 7.8$ km s^{-1}. An arbitrary velocity offset is used for the x-axis of each panel.

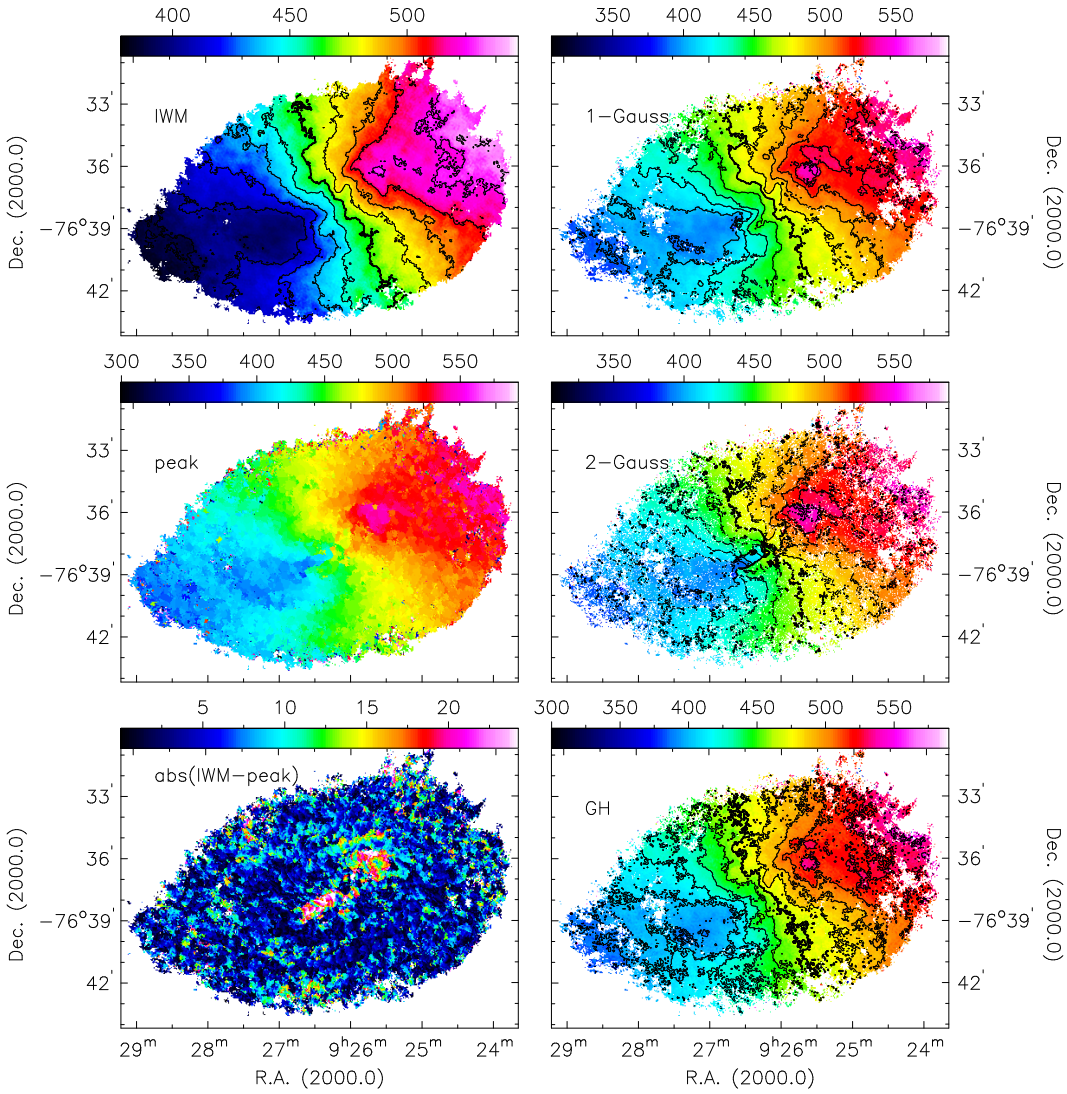

Figure 2.18: Various NGC 2915 velocity fields generated using the H I data cube. In the left column are shown, from top to bottom, the intensity-weighted-mean **(IWM)**, peak amplitude **(peak)** and the absolute difference between the IWM and peak **(abs(IWM-peak))** velocity fields. In the right column are shown, from top to bottom, the single Gaussian **(1-Gauss)**, the larger amplitude component of the double Gaussian **(2-Gauss)** and the third-order Gauss-Hermite **(GH)** velocity fields. The intensity scale of each figure is specified in units of km s^{-1} by the colour bar at the top of the panel. Iso-velocity contours are separated by 15 km s^{-1} with the systemic velocity of V_{sys} = 465 km s^{-1} marked by the thick contour. For the sake of clarity, iso-velocity contours are not included in some of the velocity fields.

Chapter 3

A dynamical HI study of NGC 2915

While the previous chapter focused mainly on presenting the various NGC 2915 H I data products, this chapter serves as a detailed study of its H I kinematics. A tilted ring model is fitted to the H I velocity field of the system's extended H I disk in order to constrain its kinematic parameters. In this manner a rotation curve is produced. The extended H I disk of NGC 2915 is an ideal tracer of the gravitational potential out to radii of $R \sim 10$ kpc, far beyond the visible radial extent of the stellar disk. Due to the apparent lack of stars in its outer parts, the dynamics of the H I disk are an almost direct tracer of the dark matter distribution. The main focus of this chapter is the construction and interpretation of various mass models describing, among other things, the distribution of mass within the galaxy's large dark matter halo. NGC 2915 was the first blue compact dwarf to have its dark matter properties accurately quantified by means of mass modeling (Meurer et al., 1996). The galaxy is known to be dark-matter-dominated at nearly all radii with a very dense dark matter core. In terms of dark matter, NGC 2915 is one of the most extreme galaxies known.

The latter part of the chapter is dedicated to a study of the non-circular velocity components within the H I disk of NGC 2915. To quantify the non-circular motions of the outer disk, an harmonic decomposition of the observed H I velocity field is carried out, the results of which are interpreted in the context of non-axisymmetric perturbations to the gravitational potential. To study the complex dynamics of the inner H I disk, full three-dimensional models are built and compared to the H I data. The modeling results are interpreted in the context of the effects of stellar winds from high-mass stars on the ISM kinematics.

3.1 Tilted ring model

The H I line data allow the H I gas dynamics of NGC 2915 to be studied. In this section a rotation curve for the galaxy is derived.

The standard method of producing a rotation curve involves fitting a tilted ring model to a velocity field (Begeman, 1987). NGC 2915's intermediate inclination of $i \sim 55^\circ$ makes it an ideal candidate for such an analysis. The method involves modeling the galaxy as a set of concentric rings within which the gas orbits about the kinematic centre of the galaxy. Each ring has a set of defining parameters: central coordinates X_c and Y_c, inclination i, systemic velocity V_{sys}, position angle PA (in the sky plane[1]), and the rotation velocity V_{rot} of the material within the ring. In the case that expansion velocities within the disk are ignored, the standard algorithm carries out a least squares fit to

$$V_{los}(x, y) = V_{sys} + V_{rot} \sin(i) \cos(\theta), \tag{3.1}$$

where V_{los} is the line-of-sight velocity, x and y are rectangular coordinates on the sky and θ is the angle from the major axis in the galaxy plane. θ is related to the position angle PA in the sky plane by

$$\cos(\theta) = \frac{-(x - X_c)\sin(PA) + (y - Y_c)\cos(PA)}{R}, \tag{3.2}$$

$$\sin(\theta) = \frac{-(x - X_c)\cos(PA) + (y - Y_c)\sin(PA)}{R\cos(i)}, \tag{3.3}$$

where R is the radius of the ring in the galaxy plane.

The GIPSY task ROTCUR (Begeman, 1987) was used to fit tilted ring models to the third order Gauss-Hermite H I velocity field extracted from the NA H I data cube. Rings of width $dR = 17''$ were used to ensure that adjacent rings were largely independent of one another. When fitting Eqn. 3.1 to the data, each datum was weighted by $|\cos(\theta)|$ so that points closer to the major axes held more weight. All points within 10° of either side of the minor axes were excluded from the fit. Both sides of the galaxy were used for the fitting.

3.1.1 Fitting procedure

Each tilted ring should be centred on the dynamical centre of the galaxy, assuming it is constant, which is usually estimated by the least-squares fitting algorithm together with the other tilted ring parameters. In the case of NGC 2915, however, the kinematic centre determinations from

[1] Measured anti-clockwise from North to the receding semi-major axis.

ROTCUR varied with radius in a non-systematic manner. We therefore used the photometric centre of the 3.6 μm emission as the kinematic centre. Using the photometric and kinematic centres interchangeably is reasonable if one assumes that the stars lie at the bottom of the gravitational potential. We carried out a single ROTCUR iteration with all parameters allowed to vary freely. The resulting X_c and Y_c values are shown as black-filled circles in panels A and B respectively of Fig. 3.1. These fitted X_c and Y_c positions deviate on average by $8.3'' \pm 0.3''$ and $7.2'' \pm 0.25''$ (179 pc and $\sim$ 155 pc) respectively from the photometric centre, thereby placing them well within a single half power beam width. This average deviation is consistent with the results of Trachternach et al. (2008) who found that approximately 50% of their kinematic centres derived for $\sim$ 1000 individual tilted rings fitted to the THINGS H I velocity fields differed by less than a beam width from their best centre estimates. In the case of the THINGS sample, one beam width corresponds to $\sim$ 200 pc on average. Throughout the tilted ring fitting procedure, X_c and Y_c were therefore each fixed to the position of the photometric centre (solid lines in panels A and B of Fig. 3.1)

The remaining tilted ring parameters (V_{sys}, PA, i, V_{rot}) were derived iteratively. We first allowed all parameters to vary freely. This gave a general feel for the parameter behaviour with R. Little scatter was seen in the radial run of V_{sys}, which was then fixed to the average value of 465 km s^{-1} in subsequent iterations (compare with the estimate of $V_{sys} = 460.8$ km s^{-1} derived from the global H I profile using Eqn. 2.4). The PA, i, and V_{rot} parameters were allowed to vary freely in the subsequent iterations. The PA and i runs showed relatively little scatter except for a clear change from inner to outer disk. The inner disk inclination remained approximately constant at $\sim 75^\circ$ out to a radius of $\sim 150''$ beyond which it dropped steeply to $\sim 55^\circ$ at $R \sim 250''$, remaining approximately constant out to the edge of the disk. Our kinematically-derived position angles are consistent with the position angles of ellipses fitted to flux contours in the H I total intensity map. Several more iterations with various combinations of fixed and free parameters were carried out in order to check the stability of the radial parameter profiles. The sharp drop in i for $R \gtrsim 150''$ always remained with little scatter.

For the final iteration, the X_C, Y_C and V_{sys} parameters were fixed to values that were constant with R while the inclination and position angle radial profiles were smoothed and then fixed. The smoothed versions of the profiles are shown as solid curves in panels A-E in Fig. 3.1. The filled circles represent the parameter values just before they were smoothed and fixed. Smoothing the PA and i radial profiles did not affect the final rotation curve in any noticeable manner. As de Blok et al. (2008) point out, the smoothing only affects the point-to-point scatter of the profiles and in no way affects the resolution of the radial distributions. To derive the final rotation curve, only V_{rot} was allowed to vary. One of the main sources of uncertainty in the derivation of the inner rotation curve is the rise in inclination of $\sim 20^\circ$ towards inner radii preferred by the tilted

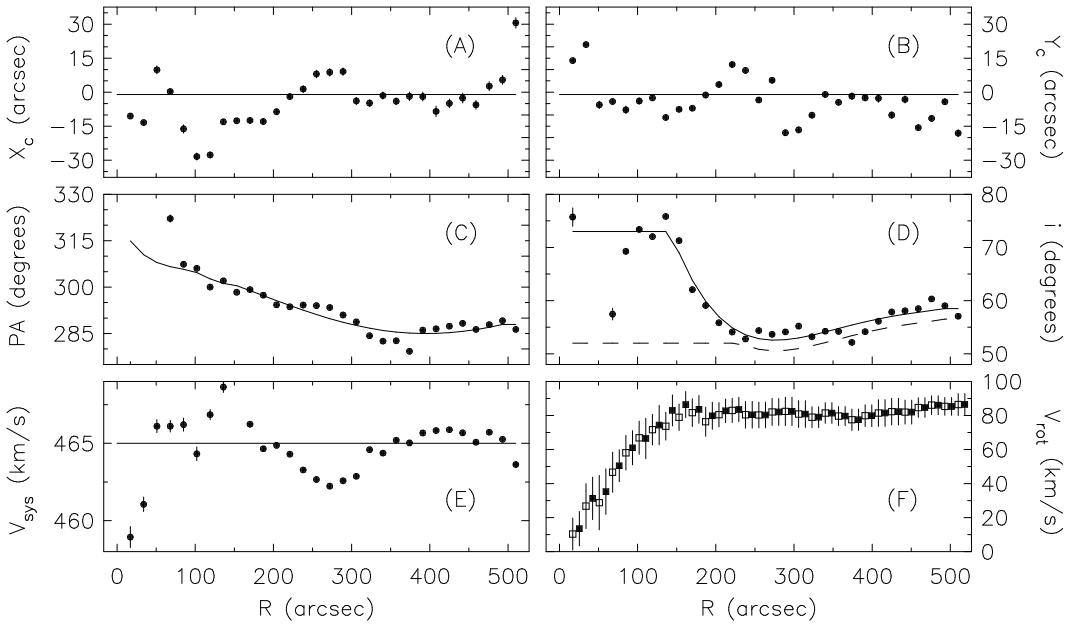

Figure 3.1: Radial variations of tilted ring parameters fitted to the third order Gauss-Hermite velocity field. Panels are A: central X positions, B: central Y positions, C: position angles, D: inclinations, E: systemic velocities, and F: circular rotation velocities. Filled circles show the radial variations just before the parameter profiles were smoothed and fixed in order to derive the final rotation curves. The smoothed profiles used to construct models SI and CI are shown as solid curves except for the model CI inclination profile which appears as a dashed curve (offset by -2° for the sake of clarity). Panel F shows the final rotation curves derived for models SI and CI (open and filled squares respectively). For the sake of clarity the model CI rotation curve has been offset by 8.5″. Error bars represent the r.m.s. spread of the velocities in a given ring.

ring models. It is not clear whether this rise is due to a genuine kinematic warp, or whether it is merely an artefact of the non-Gaussian line profiles near the galaxy's centre. We therefore derived two final tilted ring models, one with and one without the rise in inclination (solid and dashed curves in panel D of Fig. 3.1 respectively). Both models used the same X_c, Y_c, V_{sys} and PA radial profiles. We hereafter refer to these two tilted ring models as models SI (Steep Inclination) and CI (Constant Inclination). In panel F of Fig. 3.1, the rotation curves of both models are presented. The rotation curves are also shown separately in Fig. 3.2. In each of the panels A - E in Fig. 3.1, the error bars represent the formal least-squares errors from the ROTCUR fitting routine. In panel F, the error bars represent the r.m.s. spread of the velocities in a single ring.

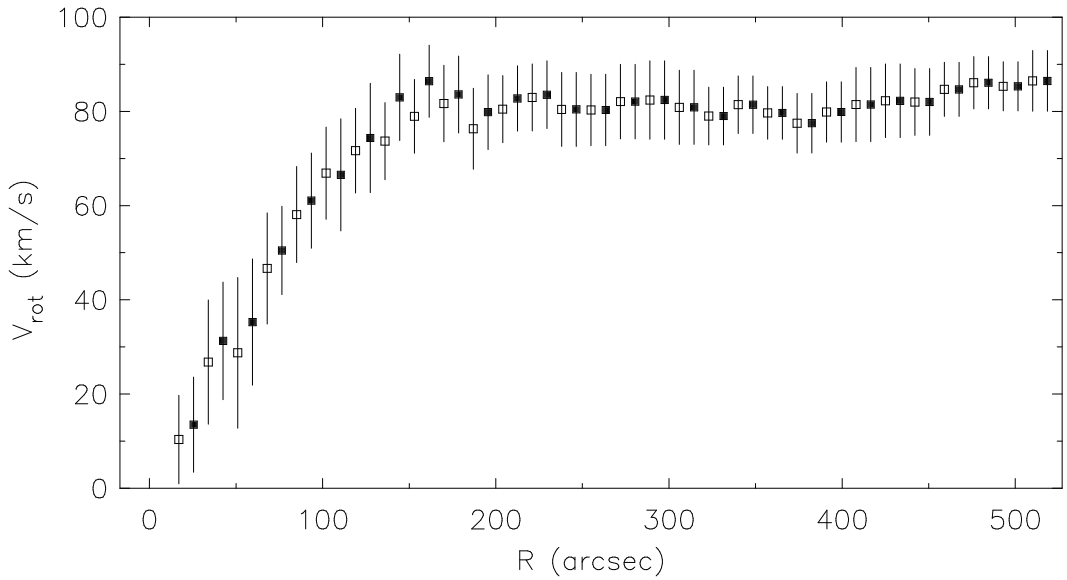

Figure 3.2: Tilted ring models SI and CI rotation curves (open and filled squares respectively). For the sake of clarity the model CI rotation curve has been offset by 8.5″. Error bars represent the r.m.s. spread of the velocities in a given ring.

3.1.2 Rotation curve

The final tilted ring models fitted to the third order Gauss-Hermite velocity field are presented in Fig. 3.1. While the stellar disk seen in the 3.6 μm image (Fig. 2.7) extends as far as $R \sim 100''$, the inner portion of the rotation curve rises as $V(R) \propto R$ out to $R \sim 150''$. Beyond this radius the rotation velocity remains almost constant. For model SI, the average rotation velocity for $R \geq 187''$ is $V = 81.9 \pm 1.6$ km s^{-1}. Despite using different inclination profiles to derive the two final rotation curves, the maximum absolute difference between them is $V = 9.3 \pm 12.2$ km s^{-1} at $R = 136''$. The average absolute difference for $R \leq 187''$ is $V = 4.3 \pm 4.8$km s^{-1}. The resulting two rotation curves are thus very similar to one another. For each tilted ring model we constructed separate rotation curves for the approaching and receding sides of the galaxy. In the case of model SI (Fig. 3.3), the rotation curve differs significantly between the two sides of the galaxy. Within the steeply rising portion, differences of ~ 20 km s^{-1} are observed as well as at $R \sim 290''$. The same is true in the case of model CI.

To check that the two tilted ring models are consistent with the data, we used the smoothed radial parameter profiles to project the rotation curves onto various position-velocity slices extracted from the H I data cube. The overlays for tilted ring model SI are presented in Fig 3.4 which demonstrates that model SI fits well the high-intensity regions of the position-velocity

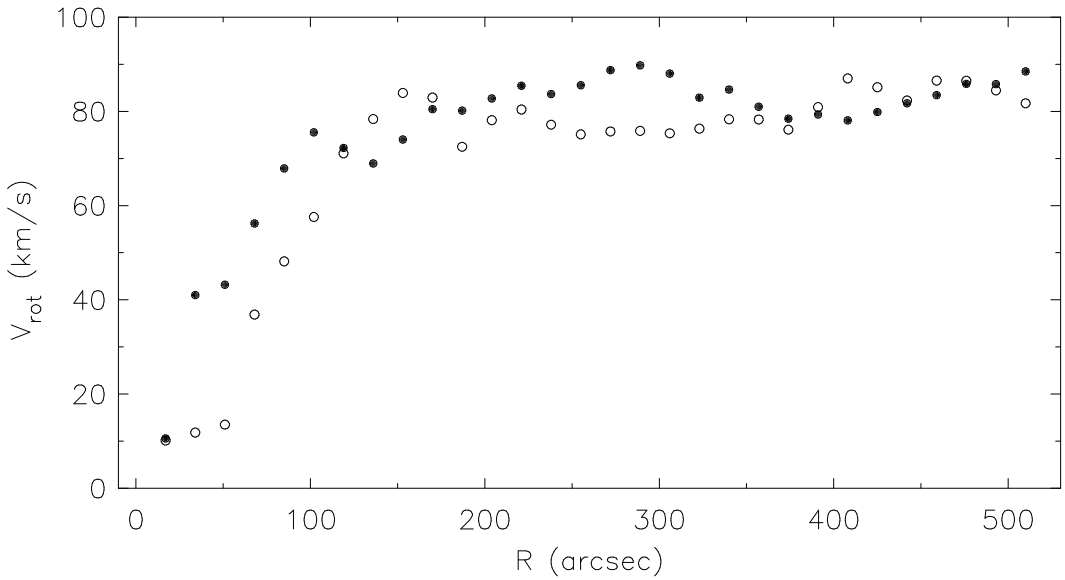

Figure 3.3: Rotation curves from tilted ring model SI derived separately for the approaching (filled circles) and receding (open circles) sides of NGC 2915. For the sake of clarity error bars are omitted.

slices. For the sake of brevity, the projected rotation curve of tilted ring model CI is not shown, yet it suffices to say that it is almost identical to that of model SI. Given a set of fixed radial profiles, the ROTCUR routine will adjust the rotation curve so that the *line-of-sight* velocities best match the data. Thus, although the circular rotation curves of tilted ring models CI and SI differ (i.e. panel F of Fig. 3.1), the good agreement between the projected rotation curves is not surprising. Meurer et al. (1994) obtained two-dimensional spectroscopy of the stellar disk of NGC 2915. Their slit had an east-west orientation, and was 4″ wide. Their reduced spectra cover a wavelength range 3510-7006 . Figure 3.5 shows the Meurer et al. (1994) velocity measurements along the slit over-plotted on the relevant east-west position velocity slice from the H I data cube of NGC 2915. Despite the H I kinematics near the centre of NGC 2915 being non-viralized and hence irregular, it is clear that the the H I and H II components of the ISM share similar velocity fields.

Using the smoothed, fixed radial parameter profiles of model SI and ring widths of $dR = 10''$, a tilted ring model was also fitted to the third order Gauss-Hermite velocity field extracted from the RW H I cube. The resulting rotation curve is compared to the rotation curve of model SI in Fig. 3.6. The figure demonstrates that for $R \lesssim 250''$, the derived rotation curves are very similar to one another. Beyond $R \sim 250''$ the filling factor of the RW H I velocity field becomes too low for meaningful derivations of the rotation velocity. For these reasons, only the rotation

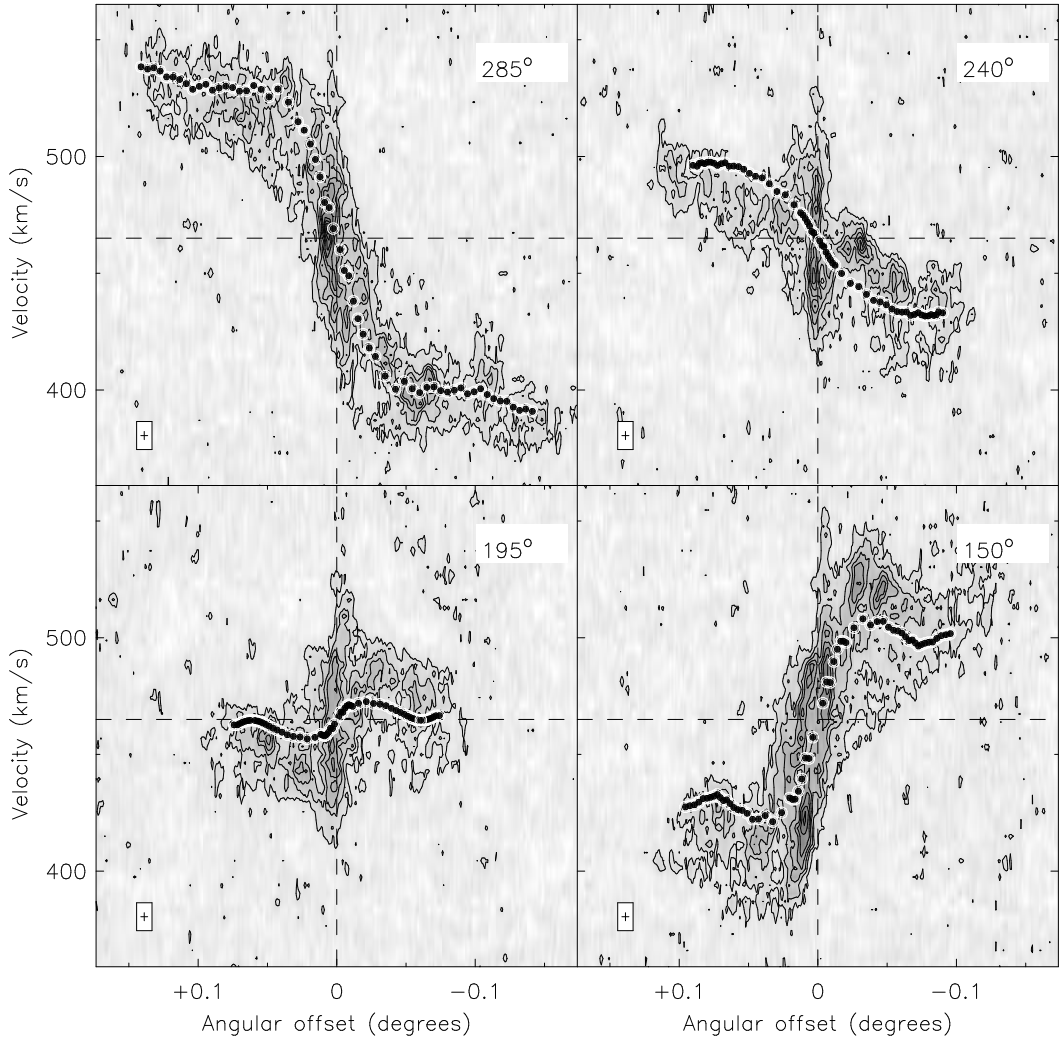

Figure 3.4: Position-velocity slices through the kinematic centre of NGC 2915 at various position angles. Overlaid on each slice is the rotation curve of tilted ring model SI, projected using the smoothed parameter radial profiles as shown in Fig. 3.1. The thickness of the position-velocity slices is that of a single pixel in the data cube (2.5″) and the velocity resolution is 3.5 km s^{-1}. The dashed horizontal line shows the systemic velocity at 465 km s^{-1} adopted for our kinematic analyses. Contours start at 2σ in steps of 2.5σ, with $\sigma = 0.6$ mJy beam^{-1}.

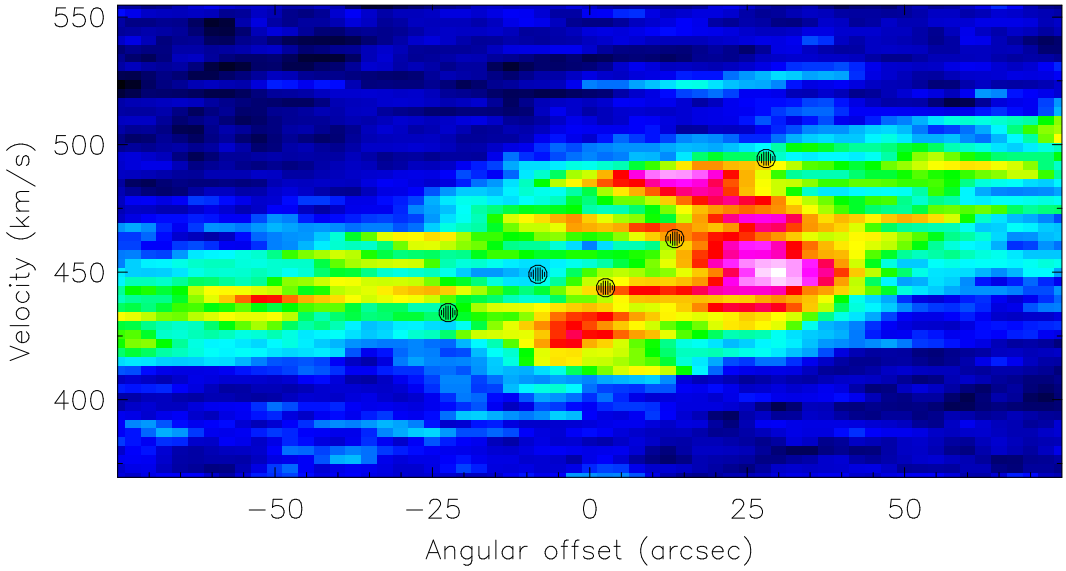

Figure 3.5: Spectroscopically-determined H II line-of-sight velocities from Meurer et al. (1994) over-plotted on an east-west position velocity slice through the NGC 2915 H I data cube.

curves of tilted ring models CI and SI are used as mass model inputs in Sec. 3.2.

3.1.3 Asymmetric drift correction to rotation curve

In long-lived gaseous disks, the rotational motion of the gas together with pressure gradients within it provide dynamical support against the self-gravity which would otherwise lead to gravitational collapse. In the case that non-circular velocity components and random motions are small, the observed rotation velocity of the gas is a good approximation of the circular velocity, and it's this circular motion that provides the required dynamical support. H I line profiles near the centre of NGC 2915 are observed to be very broad and often double-peaked, suggesting that large random motions are present with the ISM in this portion of the galaxy. These random motions can significantly contribute to the dynamical support of the gaseous disk, thereby causing the observed rotation velocities to differ from the true circular velocities.

In this section an asymmetric drift correction (Binney & Tremaine, 1987) is applied to the observed rotation velocities (V_{rot}) in order to derive the corresponding true circular velocities (V_c). Assuming a constant scale height for the gaseous disk, this correction is

$$\sigma_D^2 = -R\sigma_{gas}^2 \left(\frac{\partial \ln \Sigma_{gas}}{\partial R} + 2\frac{\partial \ln \sigma_{gas}}{\partial R} \right) \tag{3.4}$$

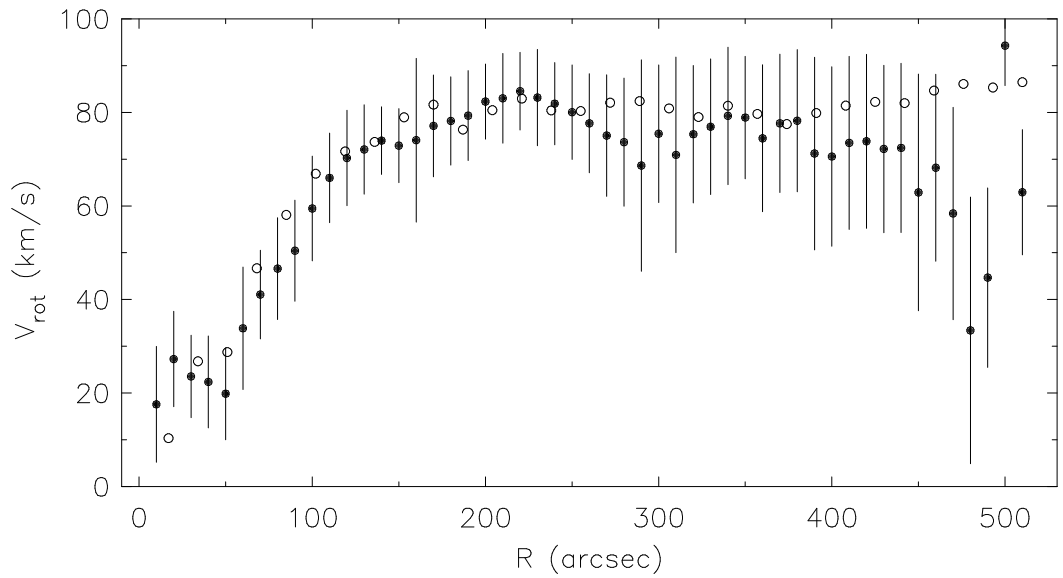

Figure 3.6: Tilted ring model SI rotation curve (open circles) compared to the rotation curve derived by fitting a tilted ring model to the H I velocity field extracted from the RW H I data cube (black filled circles). For the sake of clarity, error bars are not shown for the model SI rotation curve, yet it suffices to say that they are generally significantly smaller than those for the RW velocity field for $R \gtrsim 200''$ (see Fig. 3.2).

so that

$$V_c^2 = V_{rot}^2 + \sigma_D^2. \tag{3.5}$$

In Sec. 2.5 of the previous chapter, the possibility that the large second-order moments of the H I line profiles near the centre of NGC 2915 could be linked to the effects of stellar feedback on the ISM was briefly discussed. In Sec. 3.7.3, it is shown by means of three-dimensional modelling that an ISM with a very high velocity dispersion ($\sigma_{gas} \sim 25$ km s^{-1}, as suggested by the second-order moments of the H I line profiles) is in fact inconsistent with the H I observations. For these reasons a constant H I velocity dispersion of $\sigma_{gas} = 8$ km s^{-1} is adopted for the asymmetric drift correction, thereby setting the second term on the right hand side of equation 3.4 to zero. To determine the remaining $\frac{\partial \ln \Sigma_{gas}}{\partial R}$ term, the H I surface density radial profile presented in Sec. 2.4.3 was fitted with a fifth-order polynomial:

$$f(x) = -4.98\times10^{-12}x^5 + 7.95\times10^{-9}x^4 - 4.84\times10^{-6}x^3 + 1.40\times10^{-3}x^2 - 1.98\times10^{-1}x + 14.13. \tag{3.6}$$

The un-weighted fit has an r.m.s. residual of 0.15 M$_\odot$ pc^{-2}. Figure 3.7 shows the fitted H I surface density radial profile (upper panel) scaled by a factor of 1.37 to account for the presence

of helium and other metals. The resulting asymmetric drift correction is shown in the bottom panel of Fig. 3.7. Figure 3.8 (upper panel) shows the corrected circular velocities for NGC 2915 derived by combining via Eqn. 3.4 the σ_D radial profile with the tilted ring model SI rotation curve. The V_{rot} and V_c velocity profiles are clearly similar in shape, with their inner portions having nearly equivalent velocity gradients. The two velocity profiles are also similar in magnitude for a given galactocentric radius, differing by $\lesssim$ 10 km s^{-1} over the entire H I disk (bottom panel of Fig. 3.8) and differing by $\sim$ 6.0 km s^{-1} on average. In the sections that follow, the circular velocity radial profile is also used as mass modeling input together with the observed rotation velocity radial profiles from the tilted ring models.

3.2 Mass modeling

Dwarf galaxies such as NGC 2915 serve as useful probes of dark matter (DM). In this section, two mass models are derived for NGC 2915, one for each of the tilted ring models CI and SI.

The gravitational potential within a galaxy is determined by the combined gravitational potentials of all the mass components. The derived 3.6 μm surface brightness profile of NGC 2915 shows little deviation from an exponential light distribution at any radius. It was therefore concluded that the galaxy does not contain a significant central stellar bulge. The total mass was treated as the sum of the masses of the stellar and gaseous disks as well as the DM halo. Since $M \propto V^2$ at a given R, the rotation curves of the individual mass components, when summed in quadrature, will yield the square of total rotation curve, V_{tot}:

$$V_{tot}^2 = \alpha_{gas} V_{gas}^2 + \Upsilon_* V_*^2 + V_{DM}^2, \tag{3.7}$$

where V_{gas}, V_*, and V_{DM} are the contributions to the total rotation curve of the gas, the stars and the DM respectively. V_{tot} should match the observed rotation curve. Υ_* is the stellar mass-to-light ratio used to convert the observed distribution of star light to a stellar mass distribution. $\alpha_{gas} = 1.37$ is the scaling factor used for all mass models to take into account the contribution of helium to the gaseous mass.

3.2.1 Gas and stellar distributions

The GIPSY task ROTMOD (Casertano, 1983) was used to convert the observed mass distributions into rotation curves. Each of the fitted tilted ring models (Sec. 3.1.2) was used together with the H I total intensity map to yield an H I surface density profile. These profiles were used as ROTMOD input which, assuming an infinitesimally thin gas disk, yielded two different H I

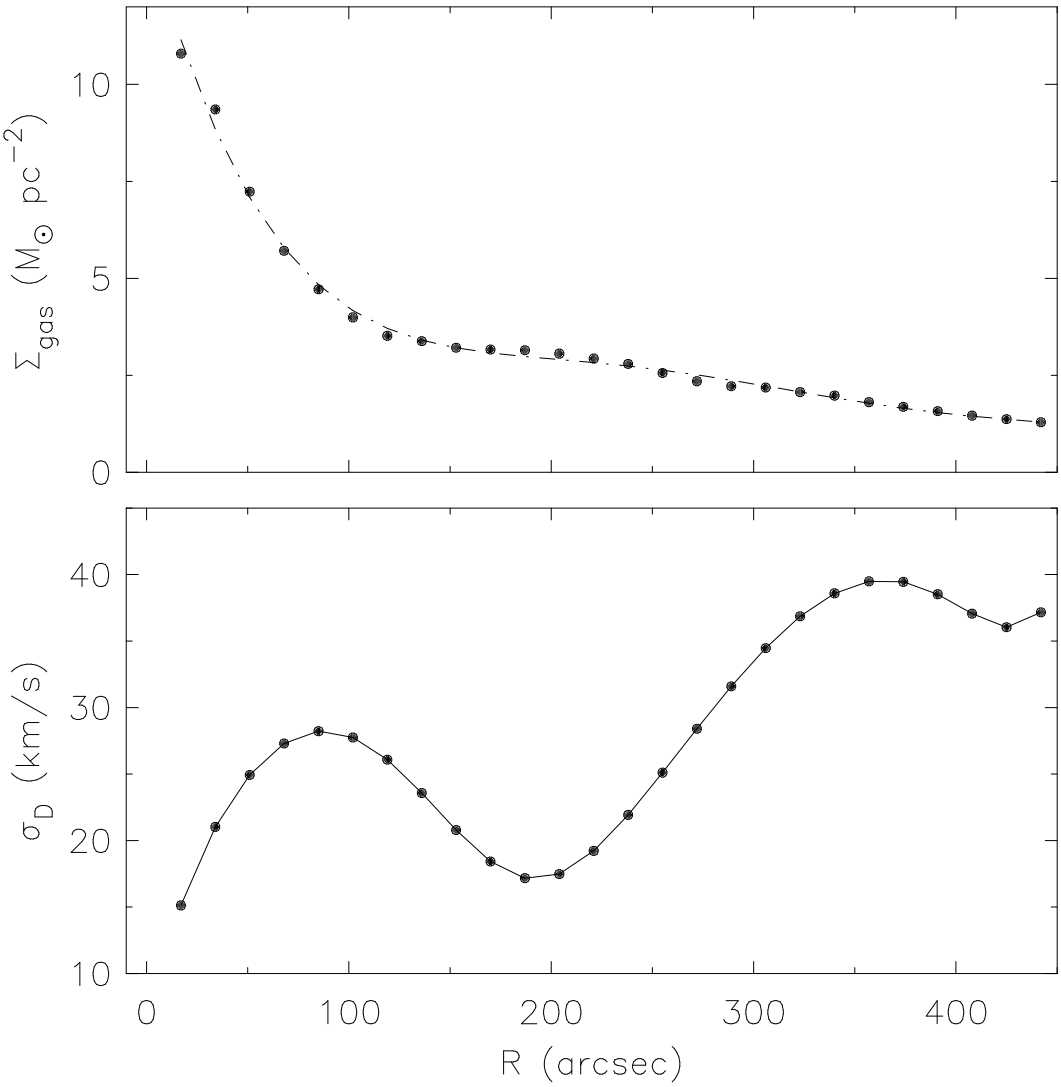

Figure 3.7: **Top panel:** Fifth-order polynomial (dot-dash curve) fitted to the gas surface density radial profile of NGC 2915 (black circles). **Bottom panel:** Asymmetric drift correction (black circles) for the derived rotation velocities. The solid curve simply joins the data points, it *is not* a fit to the data.

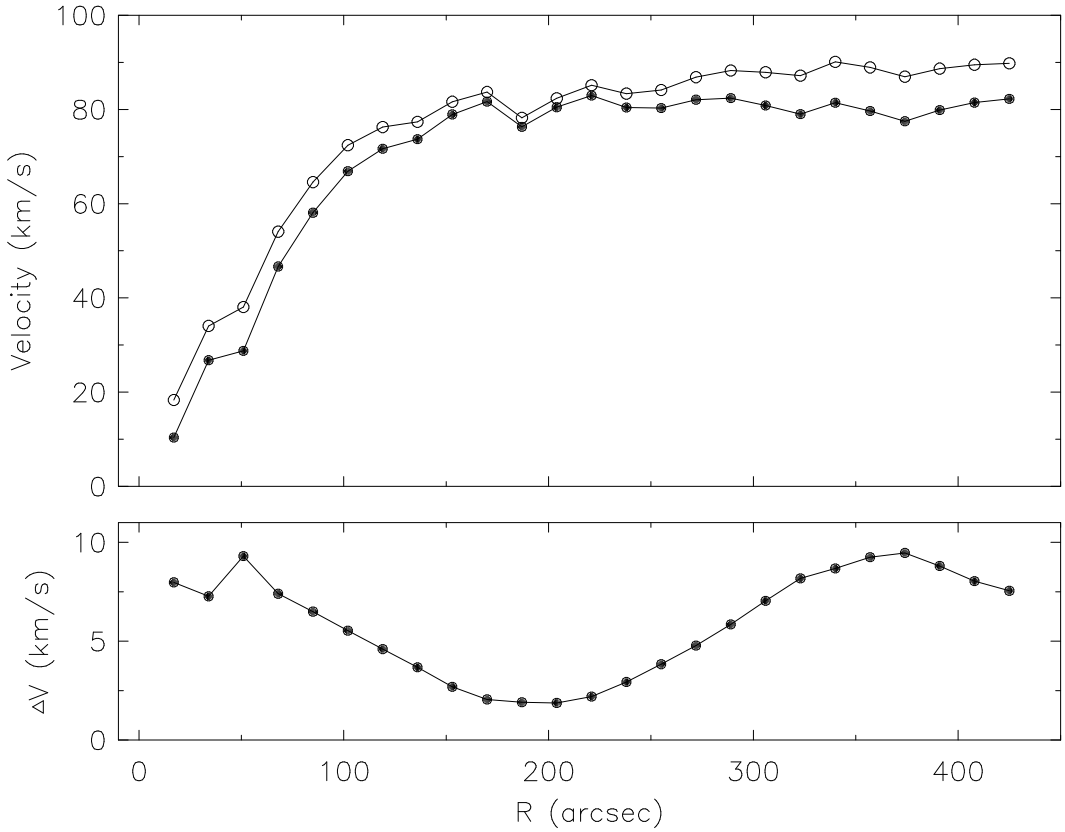

Figure 3.8: Comparison between observed rotation velocities and circular velocities for NGC 2915. **Top panel:** Circular velocity radial profile (open circles) derived by applying an asymmetric drift correction to the observed rotation velocity radial profile (filled circles) from tilted ring model SI. **Bottom panel:** Absolute difference between the two velocity profiles.

rotation curves. Ellipses fitted to 3.6 μm surface brightness isophotes suggest a constant inclination of $i \sim 55°$ for the old stellar population. Using this inclination and a position angle of 306°, a single surface density profile for the stellar disk was derived, shown in Fig. 3.9. This surface density profile was extrapolated out to $R = 510''$ to match the radial extent of the observed rotation curve, and then converted into a stellar rotation curve assuming a sech^2 vertical distribution (van der Kruit, 1981) and $h/z_0 = 5$, yielding $z_0 = 0.12$ kpc. It may be the case that NGC 2915 contains a molecular gas components near its centre, the associated gravitational potential of which could significantly contribute to the observed rotational properties of the galaxy. In Sec. 5.3.5 of Chapter 5, the measured total star formation rate surface densities of NGC 2915 are used to determine the distribution of a possible H_2 component. The total molecular gas mass is estimated to be $M_{H2} = 5.7^{+3.4}_{-2.1} \times 10^7$ M$_\odot$. The azimuthally-averaged distribution of

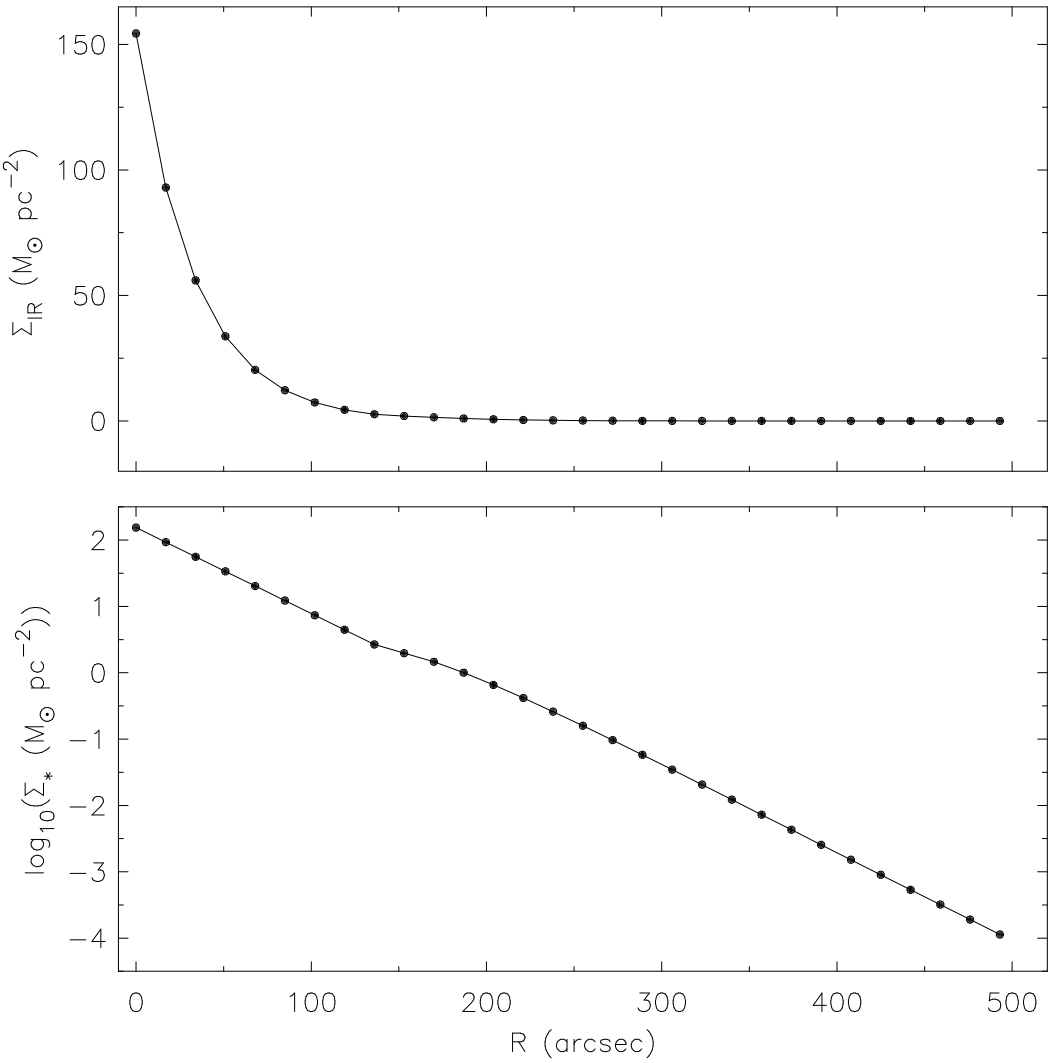

Figure 3.9: Observed stellar density radial profile for NGC 2915. Upper and lower panels present linear and logarithmic versions respectively.

the H_2 surface densities is shown in Fig. 3.10 which shows that the H_2 is contained within the central $\sim 50''$ of the galaxy. From the tilted ring model SI rotation curve, a total (dynamical) mass of $\sim 5.1 \times 10^7$ $M_\odot$ is contained within $17''$ of the centre of the galaxy. Since this amount of total mass, which equals the inferred H_2 mass, is contained well within the radial extent of the H_2 component, we do not expect the associated H_2 potential to significantly contribute to the overall potential. We therefore do not include an H_2 rotation curve in our mass models.

In principle the DM density distribution of a suitably rotating system can be determined

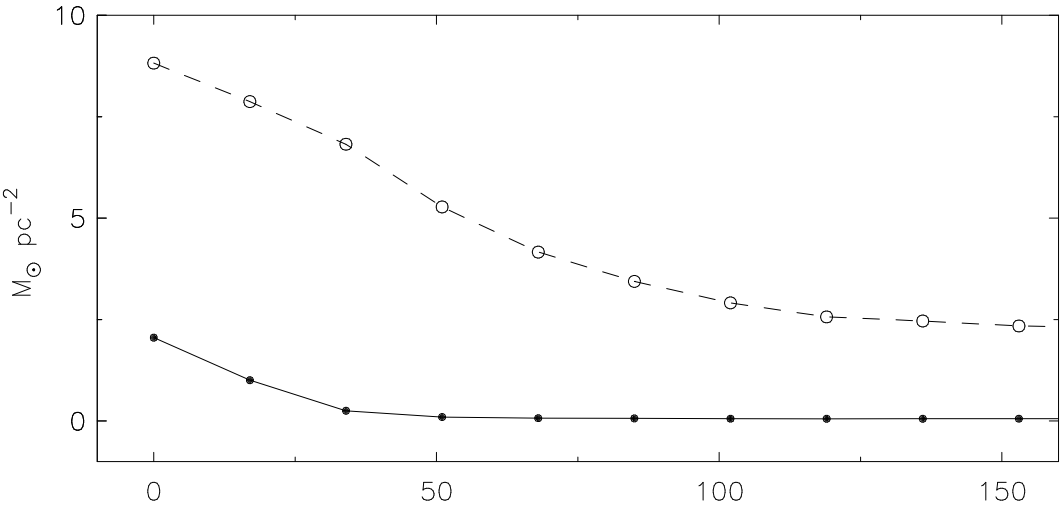

Figure 3.10: H_2 surface density radial profile (filled circles) derived from the star formation rate surface density map in Sec. 5.3.5 of Chapter 5. For comparison, the H I surface density profile is also shown (open circles). Both sets of surface densities are inclination-corrected to their face-on values.

knowing the contributions to the observed rotation curve from the gas and the stars. The H I rotation curve is directly related to the observed H I distribution, assuming that the H I is optically thin. The situation is not as simple for the stellar component of a galaxy, however, since a stellar mass-to-light ratio is needed to link the stellar light and mass distributions. Determining the stellar mass-to-light ratio from the rotation curve alone is problematic. Given an observed rotation curve, equally well-fitted mass models can be obtained for a range of stellar mass-to-light ratios (e.g. van Albada et al., 1985; Swaters, 1999). This degeneracy therefore leads to uncertainties in stellar mass-to-light ratios determined solely by rotation curves.

Bell & de Jong (2001) used spectroscopic and photometric spiral galaxy evolution models to show that a reasonable correlation exists between the optical and infrared stellar mass-to-light ratios and the colours of integrated stellar populations. They further showed that the relative trends between model stellar mass-to-light ratios and colours are fairly insensitive to uncertainties in stellar population and galaxy evolution modeling. Oh et al. (2008) used stellar population synthesis models (together with a scaled Salpeter 1955 IMF) to determine a relationship between the stellar mass-to-light ratio in the 3.6 μm and K bands ($\Upsilon_*^{3.6}$ and Υ_*^K respectively):

$$\Upsilon_*^{3.6} = 0.92 \times \Upsilon_*^K - 0.05. \tag{3.8}$$

From Bell & de Jong (2001), the relation between the $B-V$ colours and the K-band mass-to-

light ratio is

$$\log_{10}\left(\Upsilon_*^K\right) = b^K \times (B-V) + a^k, \tag{3.9}$$

where a^K and b^k for varying colours and metallicities are provided in their Table 4. By combining these two equations, the stellar mass-to-light ratio at 3.6 μm can be estimated. We use $a^K = -0.59$ and $b^K = 0.60$ for $B-V$ colours as used by Oh et al. (2008) for IC 2574, the justification being that IC 2574 is also a low metallicity, star-forming dwarf galaxy with $B-V \sim 0.6$, much like NGC 2915. $B-V \sim 0.3 \pm 0.2$ for NGC 2915 (de Vaucouleurs et al., 1991; Schlegel et al., 1998) thereby yielding (from Eqn. 3.9) $\Upsilon_*^K \approx 0.39$. Substituting this value into Eqn. 3.8 yields $\Upsilon_*^{3.6} \approx 0.3$ $M_\odot/L_\odot$. Leroy et al. (2008), applying the Bell et al. (2003) relation between $B-V$ colour and Υ_*^K and assuming a Kroupa (2001) IMF, found $\Upsilon_*^K = 0.48 - 0.60$ $M_\odot/L_\odot$ for the $K-$band stellar mass-to-light ratios of all of the THINGS galaxies in their sample.

3.2.2 Dark matter halos

The way in which dark matter is distributed on galactic length-scales has been a topic of much debate. Over the past decade, the constant increase in computational power has allowed detailed N-body simulations of the clustering properties of cold dark matter particles to be carried out. One of the first large-scale studies was carried out by Navarro et al. (1996) in which they studied the equilibrium density profiles of dark matter halos in a hierarchical galaxy clustering scenario. Their results suggested the existence of a "universal dark matter density profile" (Navarro et al., 1997) which is independent of clustering scale, mass or size as well as the power spectrum of initial fluctuations. Their parameterisation of this universal profile is

$$\frac{\rho(r)_{NFW}}{\rho_{crit}} = \frac{\delta_c}{(r/r_s)(1+r/r_s)^2} \tag{3.10}$$

where δ_c is a measure of the density of the universe at the time of collapse of the DM halo, r_s is the characteristic scale radius and $\rho_{crit} = 3H^2/8\pi G$ is the critical density required for closure. This profile scales as r^α, with $\alpha = -3$ and $\alpha = -1$ at large and small radii respectively, thereby predicting extremely steep inner density profiles of DM halos, known as central cusps.

The Aquarius Project (Springel et al., 2008) recently completed a set of high-resolution numerical simulations to study the formation and structure of galaxy-sized DM halos in the standard ΛCDM cosmology. Navarro et al. (2010) reported that the spherically-averaged density profile of the six different-sized simulated galaxy halos becomes progressively shallower inwards and, at the innermost resolved radius, has a logarithmic slope $\alpha = \mathrm{d}\ln\rho/\mathrm{d}\ln r \gtrsim -1$. These predictions of cuspy inner DM density profiles can be tested against real, dark matter dominated galaxies. If cuspy NFW halos are found, constraints can be put on halo concentrations and

cosmological parameters. From Navarro et al. (1997), the rotation curve resulting from an NFW DM density profile is

$$\left(\frac{V_{NFW}}{V_{200}}\right)^2 = \frac{\ln(1+cx) - cx/(1+cx)}{x\ln(1+cx) - c/(1+c)}, \tag{3.11}$$

where V_{200} is the circular rotation speed at r_{200}, the radius at which the density of the DM halo equals 200 times the critical density, ρ_{crit}; $x = r/r_{200}$ is the radius in units of the virial radius and $c = r_{200}/r_s$ is the "concentration" parameter of the halo.

Low surface brightness dwarf galaxies are thought to be dark-matter-dominated down to small radii (de Blok & McGaugh, 1997a). The inner structure of their dark matter halos can therefore be accurately probed. It is often the case that the density profiles of dwarf galaxies are shallower at inner radii than those of simulated DM halos (Moore, 1994; Flores & Primack, 1994; de Blok & McGaugh, 1997a; Marchesini et al., 2002). The distribution of the DM in these dwarfs is consistent with approximately constant inner dark matter densities. A particular dark matter density profile that well describes the DM distribution of dwarf systems is that of the pseudo-isothermal sphere (Binney & Tremaine, 1987):

$$\rho(r)_{ISO} = \rho_0 \left(1 + \left[\frac{r}{r_c}\right]^2\right)^{-1}, \tag{3.12}$$

where ρ_0 is the central DM density and r_c is the core radius. This parameterisation, which has no particular physical justification, has a constant density core. The rotation curve resulting from such a DM density profile is

$$V_{ISO} = \left(4\pi G\rho_0 r_c^2 \left[1 - \frac{r_c}{r}\arctan\left(\frac{r}{r_c}\right)\right]\right)^{1/2}. \tag{3.13}$$

3.2.3 Fitted models

The GIPSY task ROTMAS was used to fit DM halos to the observed rotation curve of NGC 2915. The task subtracts from the observed rotation curve the scaled rotation curves of the stellar and gaseous disks. It then fits to the residuals a rotation curve corresponding to a particular parameterisation of the DM halo. When matching the total and observed rotation curves, the points were uniformly weighted to ensure that each point in the rotation curve contributed equally to the fit. This essentially reduced the fitting procedure to a non-weighted least-squares fitting method.

As previously mentioned, the rotation curves from each of the tilted ring models fitted to the H I velocity field were used as mass modeling input. For each of these mass models, fits were carried out for a pseudo-isothermal sphere and an NFW halo. Models were created using three different mass-to-light ratios:

- Under the so-called "maximum disk assumption", the stellar rotation curve is scaled up to contribute maximally to the observed rotation curve at inner radii. Such a scaling usually allows the stellar disk to account for most of the inner rotation curve (van Albada et al., 1985; Swaters, 1999). For the maximum disk cases, regardless of the DM halo parameterisation, Υ_* was fixed to 0.64 $M_\odot/L_\odot$ and 0.44 $M_\odot/L_\odot$ for mass models SI and CI respectively.
- Under the "minimum disk assumption", the contribution of the stellar disk is made as low as possible (often zero) while still allowing for a good fit of the total rotation curve to the observed rotation curve. For the minimum disk cases, Υ_* was fixed to zero (no contribution from the stellar disk to the observed rotation curve).
- The final set of models used a mass-to-light ratio of $\Upsilon_* = 0.3\ M_\odot/L_\odot$, our pre-determined value from Sec. 3.2.1.

In all models, α_{gas} was fixed to 1.37. Thus, six mass models were fitted to each of the rotation curves derived from the tilted ring modeling.

3.2.4 Results

The fitted parameters for all of the mass models are summarised in Table 3.1. The results for mass model SI are also presented in Fig. 3.11. This figure shows that NGC 2915 is dark-matter-dominated at nearly all radii (depending on modeling assumptions). Mass ratios as well as the total mass to B-band light ratio at the last measured point of each fitted total rotation curve are calculated. For mass models SI and CI, DM constitutes, on average, 92.8% of the dynamical mass. This dark-matter-dominance leads to very high total-mass-to-light ratios: 141 $M_\odot/L_\odot$ and 129 $M_\odot/L_\odot$ on average for mass models SI and CI respectively. These estimates are almost double that of the 76 $M_\odot/L_\odot$ upper limit set by Meurer et al. (1996), thereby making NGC 2915 one of the most dark-matter-dominated late-type galaxies known.

The second main mass-modeling result that Fig. 3.11 demonstrates is that, for either parameterisation of the DM halo, the steeply rising portion of the observed rotation curve is poorly matched by the total rotation curve. It is usually the stellar rotation curve that is used to match the inner observed rotation curve (Swaters, 1999), yet no such scaling is useful in the case of NGC 2915 due to the intrinsically different shapes of the stellar and observed rotation curves. The stellar disk is clearly contained well within the steeply rising portion of the observed rotation curve which continues to rise as $V(R) \propto R$ out to $R \sim 3$ kpc (150″). The best-fitting mass models are those in which the stellar rotation curve contributes zero to the observed total rotation curve. Figure 3.11 shows that when the fitting routine attempts to fit the inner observed

Table 3.1: NGC 2915 mass modeling results for the observed rotation velocities

		1	2	3	4	5	6
	DM halo	*ISO*	ISO_{max}	ISO_{min}	*NFW*	NFW_{max}	NFW_{min}
	Model SI						
1	χ^2_{red}	38.1	59.8	28.2	62.5	93.4	44.7
2	r.m.s. (km s^{-1})	0.56	1.30	0.79	0.75	1.37	0.40
3	Υ_* ($M_\odot/L_\odot$)	0.3	0.64	0.0	0.3	0.64	0.0
4	ρ_0 (10^{-3} $M_\odot$ pc^{-3})	100.6 $\pm$ 23.3	56.9 $\pm$ 17.8	178.7 $\pm$ 33.0	...	...	...
5	R_c (kpc)	1.3 $\pm$ 0.2	1.7 $\pm$ 0.4	0.9 $\pm$ 0.1	...	...	...
6	V_{200} (km s^{-1})	...	...	...	69.6 $\pm$ 7.9	83.5 $\pm$ 20.1	62.7 $\pm$ 4.1
7	*C*	...	...	...	11.7 $\pm$ 2.2	7.9 $\pm$ 2.7	15.6 $\pm$ 2.0
	At last measured pt:						
8	M_{tot} (10^8 $M_\odot$)	151.4	151.3	151.6	151.1	154.2	148.3
9	M_{HI}/M_{tot} (10^{-3})	43.84	43.85	43.79	43.92	43.03	44.76
10	M_{DM}/M_{tot} (10^{-2})	92.94	89.91	95.62	92.93	90.10	95.52
11	M_{DM}/M_{lum}	6.68	4.47	21.84	6.67	4.57	21.34
12	M_{tot}/L_B ($M_\odot/L_\odot$)	140.72	140.69	140.91	140.47	143.37	137.9
	Model CI						
1	χ^2_{red}	46.7	53.6	37.5	78.1	89.1	61.2
2	r.m.s. (km s^{-1})	0.74	1.00	0.27	1.03	1.28	0.66
3	Υ_* ($M_\odot/L_\odot$)	0.3	0.44	0.0	0.3	0.44	0.0
4	ρ_0 (10^{-3} $M_\odot$ pc^{-3})	127.9 $\pm$ 34.9	103.2 $\pm$ 31.1	227.6 $\pm$ 50.1	...	...	...
5	R_c (kpc)	1.10 $\pm$ 0.2	1.2 $\pm$ 0.2	0.8 $\pm$ 0.1	...	...	...
6	V_{200} (km s^{-1})	...	...	...	66.4 $\pm$ 8.3	70.3 $\pm$ 11.5	60.7 $\pm$ 4.7
7	*C*	...	...	...	12.9 $\pm$ 2.8	11.2 $\pm$ 2.9	17.0 $\pm$ 2.5
	At last measured pt:						
8	M_{tot} (10^8 $M_\odot$)	138.8	138.3	139.8	137.6	138.4	136.3
9	M_{HI}/M_{tot} (10^{-3})	47.29	47.43	46.92	47.66	47.42	48.16
10	M_{DM}/M_{tot} (10^{-2})	92.34	91.13	95.31	92.28	90.92	95.18
11	M_{DM}/M_{lum}	6.11	5.15	20.31	6.06	5.01	19.77
12	M_{tot}/L_B ($M_\odot/L_\odot$)	129.00	128.62	130.01	127.99	128.64	126.68

Comments on rows: Row 1: Reduced χ^2 goodness-of-fit statistic; Row 2: r.m.s. of the difference between the observed and total rotation curves; Row 3: stellar mass-to-light ratio; Row 4: central density for pseudo-isothermal sphere; Row 5: core radius for pseudo-isothermal sphere, Row 6: circular rotation speed at virial radius for NFW halo; Row 7: concentration parameter for NFW halo; Row 8: dynamical mass; Row 9: H I to total mass ratio; Row 10: Dark to total mass ratio; Row 11: Dark to luminous mass ratio; Row 12: Total mass to *B*-band light ratio.

Comments on columns: For each model, columns 1 and 4 show the results for the case in which Υ_* is fixed to the predetermined value of 0.3 and α_{gas} is fixed to 1.37. Columns 2 and 5 show the results for the maximum disk case while columns 3 and 6 are for the minimum disk case.

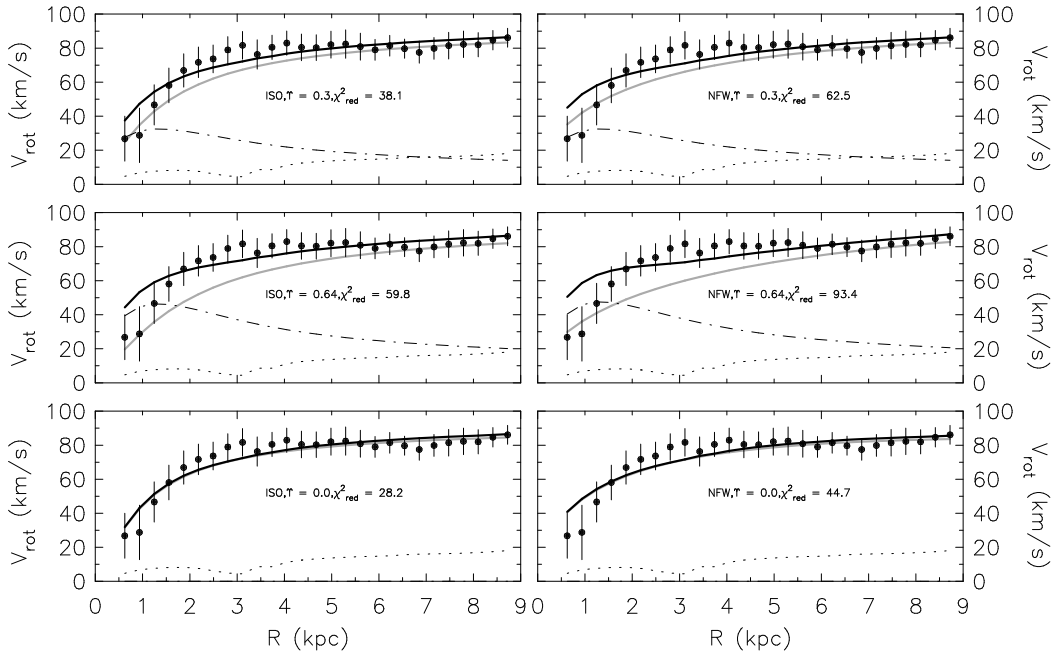

Figure 3.11: Pseudo-isothermal sphere (ISO) and NFW mass models for NGC 2915, constructed using the radial parameter profiles of tilted ring model SI. The observed rotation curve is also from tilted ring model SI. The panels on the left show the fits using the pseudo-isothermal sphere while the panels on the right show the fits using an NFW halo. The top panels show the fits when the stellar rotation curve is scaled by the predetermined value of $\Upsilon_* = 0.3\ M_\odot/L_\odot$. The middle and bottom panels show the fits for the maximum and minimum disk cases respectively. In all panels the black filled circles represent the observed rotation curve while the error bars represent the r.m.s. spread of velocities in a given ring. The black dot-dash curve shows the rotation curve of the stellar disk while the black dotted curve shows the rotation curve of the gaseous disk. The solid grey curve shows the resulting rotation curve of the DM halo. Finally, the solid black curve represents the total rotation curve resulting from the best-fit model. In each panel the reduced χ^2 goodness-of-fit statistic is presented. At the distance of NGC 2915, 1 kpc $\approx 50''$.

rotation curve with the DM rotation curve, the result is an over-estimation of the observed rotation velocities for $R \lesssim 2$ kpc (110″) and an under-estimation for radii 2 kpc $\lesssim R \lesssim 5.5$ kpc. The poor matches between the total and observed inner rotation curves do not allow a particular DM halo parameterisation to be confidently ruled out or confirmed. Furthermore, the observed non-Gaussian line profiles near the centre of NGC 2915 (Sec. 2.5) suggest the H I to be non-virialised within this portion of the galaxy, leading to uncertainty in the shape of the inner portion of the observed rotation curve. Possible radial velocity components within the H I (associated with the bar-like feature seen in the H I distribution) will lead to further uncertainty in the shape of the inner rotation curve. These uncertainties, in turn, lead to associated uncertainties in the shapes of the inner portions of the fitted DM halos. Assuming the stellar kinematics to be virialised, spectroscopic observations of the stellar disk would have to be carried out to better constrain the inner rotation curve.

What is the explanation for the discrepancy between the observed and total rotation curves? Have we failed to include a significant mass component during the decomposition process? The surface brightness profile obtained from the 3.6 μm imaging provides no evidence for a central stellar bulge. A significant mass of molecular gas at inner radii is a possibility, yet as demonstrated in Sec. 3.2.1, the inferred molecular gas component of NGC 2915 ($M_{H2} = 5.7^{+3.4}_{-2.1} \times 10^7$ M$_\odot$) is very unlikely to significantly contribute to the overall potential of the galaxy.

If we consider the mass-modeling results as they appear in Table 3.1, then the pseudo-isothermal sphere allows for the best match to the observed rotation curve. The fitted pseudo-isothermal sphere, under the minimum disk assumption, has a core density and a core radius of $\rho_0 = 0.17 \pm 0.03\ M_\odot$ pc^{-3} and $r_c = 0.9 \pm 0.1$ kpc for model SI. These results are similar to those of Meurer et al. (1996) who, for their favoured mass model, estimated $\rho_0 = 0.10 \pm 0.02$ M$_\odot$ pc^{-3} and $r_c = 1.23 \pm 0.15$ kpc. Mass models with Υ_* as a free parameter were also fitted. The best-fitting value of Υ_* was always found to be negative, consistent with the mass modeling results of Meurer et al. (1996).

In Fig. 3.12 the derived pseudo-isothermal halo parameters for NGC 2915 are compared to those derived for the THINGS sample of de Blok et al. (2008). The infrared stellar mass-to-light ratios used in their mass models were derived from the 3.6 μm images in combination with stellar population synthesis arguments. Our models for the minimum disk and $\Upsilon_* = 0.3$ M$_\odot$/L$_\odot$ cases for both models SI and CI are shown in Fig. 3.12. This comparison suggests that NGC 2915 has a central DM core that is much more compact and dense compared to most other dwarfs and late-type systems.

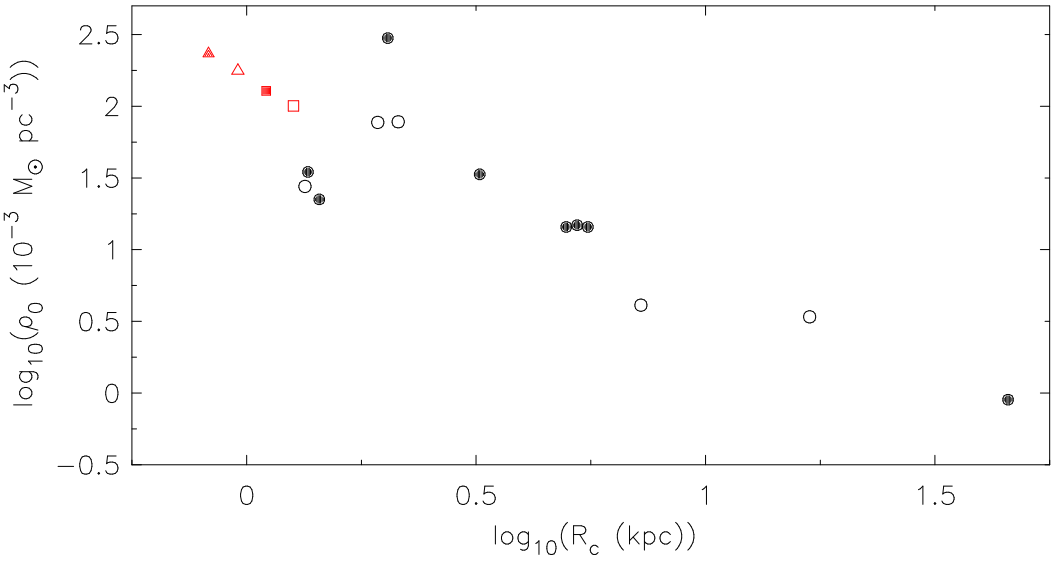

Figure 3.12: Mass modeling results for the minimum disk and $\Upsilon_* = 0.3$ $M_\odot/L_\odot$ cases in which the DM halo of NGC 2915 is modelled as a pseudo-isothermal sphere, compared to the mass modeling results of the THINGS sample of de Blok et al. (2008). The red-filled and open triangles correspond to the minimum disk results for models SI and CI respectively while the red-filled and open squares correspond to the $\Upsilon_* = 0.3$ $M_\odot/L_\odot$ results for models SI and CI respectively. The mass modeling results from THINGS are shown as open circles for dwarf galaxies and filled circles for all other galaxies.

3.2.5 Asymmetric drift correction to mass models

This section presents mass models that use the circular velocity radial profile generated in Sec. 3.1.3 as input. These circular velocities were generated by applying an asymmetric-drift correction to the observed rotation velocities from tilted ring model SI. A direct comparison of these two velocity profiles (Fig. 3.8) shows them to be very similar to one another, however, the effects of the asymmetric drift correction on the inferred dark matter halo properties of NGC 2915 needs to be tested explicitly by producing mass models using the circular velocities.

To produce the corresponding mass models, the ROTMOD-generated H I and stellar rotation curves for tilted ring model SI (Sec. 3.2.1) were used together with the circular velocity radial profile from Sec. 3.1.3. The maximum and minimum disk assumptions used for mass model SI in Sec. 3.2.3 were incorporated (i.e. $\Upsilon_* = 0.64$ and $\Upsilon_* = 0.0$ $M_\odot/L_\odot$ respectively). Models were also generated using $\Upsilon_* = \Upsilon_*^{3.6} = 0.3$ $M_\odot/L_\odot$, our estimate of the stellar mass ratio for NGC 2915 in the 3.6 μm IRAC band (Sec. 3.2.1). Pseudo-isothermal sphere and NFW halo mass

models were fitted.

The mass modeling results are summarised in Table 3.2 and presented graphically in Fig. 3.13. For all but the pseudo-isothermal sphere case incorporating a minimum disk assumption, the r.m.s. residuals for these new mass models based on the circular velocity profile are larger than those based on the model SI rotation curve, albeit by a factor $\lesssim 2$. More importantly, the best-fitting dark matter halo parameters for the circular velocities are generally consistent (within error) with those for the model SI rotation curve (i.e. the results presented in the top half of Table 3.1). This is certainly true for the pseudo-isothermal sphere R_c parameter estimates and for the NFW halo V_{200} and C parameter estimates. The models are inconsistent within error, however, for the pseudo-isothermal sphere ρ_0 parameter estimates which are higher by a factor of ~ 1.6. Nevertheless, it would seem that applying an asymmetric drift correction to the observed rotation velocities does not significantly impact on the inferred dark matter halo properties of NGC 2915. This result, together with the fact that asymmetric drift corrections are themselves generally only accurate to within $\sim 25\%$, leads us to adopt the mass modeling results for tilted ring model SI as our favoured set of results. We used the mass modeling results presented in Table 3.1 for subsequent analyses presented in this work.

3.3 Kinematic warp

The preferred kinematic warp of the tilted ring models is consistent with the fact that warps in spiral disks are ubiquitous, both optically (Sanchez-Saavedra et al., 1990; Reshetnikov & Combes, 1998) and at radio wavelengths (Sancisi, 1976; García-Ruiz et al., 2002). Warps are often thought to be long-lived phenomena. For their sample of 26 edge-on galaxies, García-Ruiz et al. (2002) find that all systems that have an H I disk that is more extended than the optical disk, are warped. The measured amplitudes of their warps vary considerably from galaxy to galaxy, with typical warp amplitudes $\lesssim 15°$. Three galaxies in their sample[†] do, however, have warp amplitudes between 20 - 25°. This is approximately the amplitude of the kinematic warp in NGC 2915 inferred from the tilted ring modeling.

The sample studied by García-Ruiz et al. (2002) consisted of edge-on systems in which the warps were directly observable. Since NGC 2915 is inclined at $\sim 55°$, its warp is inferred from models of its H I kinematics. Using a tilted ring model to infer the presence of a warp assumes a certain degree of axisymmetry and circularity of gas orbits, assumptions that we know probably do not hold true within the central regions of NGC 2915. The warping suggested by the tilted ring modeling cannot be treated as conclusive evidence for a true warp in the H I disk.

[†]One of which was identified as an interacting system.

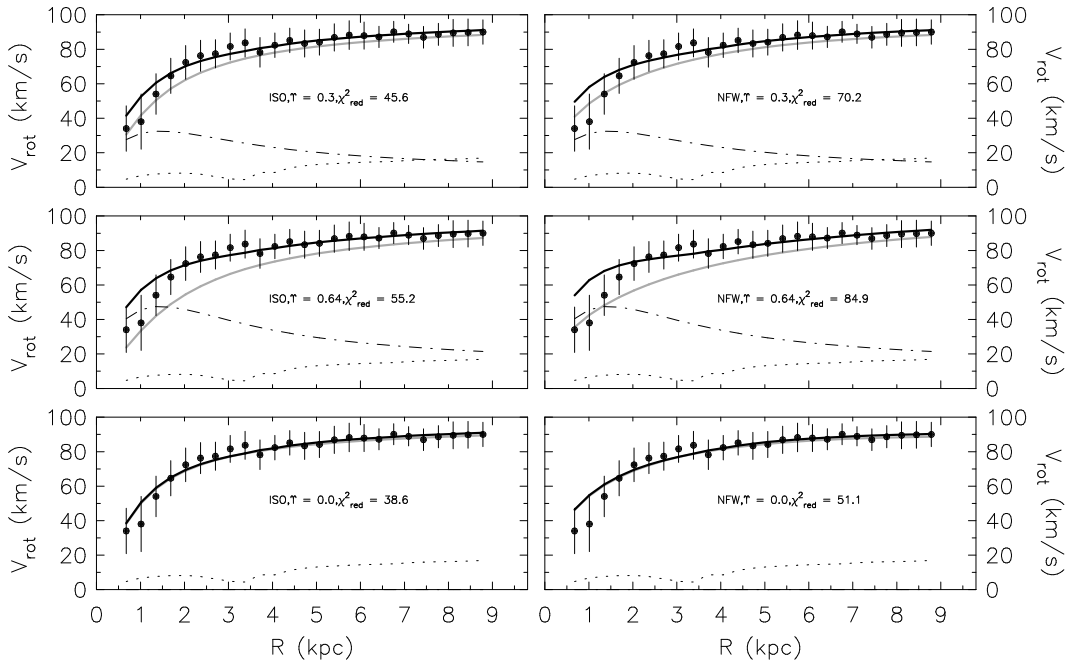

Figure 3.13: Pseudo-isothermal sphere (ISO) and NFW mass models for NGC 2915, constructed using the radial parameter profiles of tilted ring model SI. The "observed" rotation curve is the tilted ring model SI rotation curve that has had an asymmetric drift correction applied to it. The panels on the left show the fits using the pseudo-isothermal sphere while the panels on the right show the fits using an NFW halo. The top panels show the fits when the stellar rotation curve is scaled by the predetermined value of $\Upsilon_* = 0.3$. The middle and bottom panels show the fits for the maximum and minimum disk cases respectively. In all panels the black filled circles represent the observed rotation curve while the error bars represent the r.m.s. spread of velocities in a given ring. The black dot-dash curve shows the rotation curve of the stellar disk while the black dotted curve shows the rotation curve of the gaseous disk. The solid grey curve shows the resulting rotation curve of the DM halo. Finally, the solid black curve represents the total rotation curve resulting from the best-fit model. In each panel the reduced χ^2 goodness-of-fit statistic is presented.

Table 3.2: NGC 2915 mass modeling results for an asymmetric drift correction applied to the observed rotation velocities

		1	2	3	4	5	6
	DM halo	ISO	ISO_{max}	ISO_{min}	NFW	NFW_{max}	NFW_{min}
1	χ^2_{red}	45.6	55.2	38.6	70.2	84.9	51.1
2	r.m.s. (km s^{-1})	0.79	1.40	0.50	1.39	2.04	0.97
3	Υ_* ($M_\odot/L_\odot$)	0.3	0.64	0.0	0.3	0.64	0.0
4	ρ_0 (10^{-3} $M_\odot$ pc^{-3})	160.2 $\pm$ 21.3	89.1 $\pm$ 14.2	284.0 $\pm$ 35.9	...	...	...
5	R_c (kpc)	1.1 $\pm$ 0.1	1.4 $\pm$ 0.1	0.8 $\pm$ 0.1	...	...	...
6	V_{200} (km s^{-1})	...	...	...	68.3 $\pm$ 3.4	77.8 $\pm$ 7.3	63.0 $\pm$ 2.0
7	C	...	...	...	14.7 $\pm$ 1.4	10.8 $\pm$ 1.6	18.8 $\pm$ 1.3
	At last measured pt:						
8	M_{tot} (10^8 M$_\odot$)	156.3	157.4	155.9	156.1	159.3	153.4
9	M_{HI}/M_{tot} (10^{-3})	34.56	34.33	34.66	34.61	33.91	35.21
10	M_{DM}/M_{tot} (10^{-2})	93.94	91.05	96.53	93.93	91.16	96.47
11	M_{DM}/M_{lum}	7.79	5.16	27.84	7.78	5.23	27.39
12	M_{tot}/L_B ($M_\odot/L_\odot$)	145.35	146.36	144.94	145.15	148.14	142.65

Comments on rows: Row 1: Reduced χ^2 goodness-of-fit statistic; Row 2: r.m.s. of the difference between the observed (circular) and total rotation curves; Row 3: stellar mass-to-light ratio; Row 4: central density for pseudo-isothermal sphere; Row 5: core radius for pseudo-isothermal sphere, Row 6: circular rotation speed at virial radius for NFW halo; Row 7: concentration parameter for NFW halo; Row 8: dynamical mass; Row 9: H I to total mass ratio; Row 10: Dark to total mass ratio; Row 11: Dark to luminous mass ratio; Row 12: Total mass to B-band light ratio.
Comments on columns: For each model, columns 1 and 4 show the results for the case in which Υ_* is fixed to the predetermined value of 0.3 and α_{gas} is fixed to 1.37. Columns 2 and 5 show the results for the maximum disk case while columns 3 and 6 are for the minimum disk case.

Nevertheless, treating the inferred warp as being real, the inclination of the H I disk varies largely with radius for $130'' \lesssim R \lesssim 240''$ (2.5 kpc $\lesssim R \lesssim$ 4.7 kpc) . Beyond $R \sim 240''$ the inclination remains fairly constant. That the disk inclination varies over this radial range is consistent with the statements made by García-Ruiz et al. (2002) and Briggs (1990) that H I warps usually start at or beyond the edge of the optical disk. The R-band R_{25} radius of this galaxy is $\sim 98''$ (1.9 kpc) (Meurer et al., 1996). The change in inclination therefore begins $\sim 30''$ beyond the edge of the stellar disk. Although the non-circular motions present within the central regions of the H I disk lead to uncertainties in the fitted tilted ring parameters, the main features of the kinematic warp are consistent with those that have been directly observed in other galaxies.

3.4 Lopsided kinematics

Asymmetry in the H I distribution and kinematics of disk galaxies is a common phenomenon. Baldwin et al. (1980) were the first to draw attention to H I asymmetries in a number of nearby galaxies. Since then several investigators have attempted to determine how common such asymmetries are (e.g. Richter & Sancisi, 1994; Haynes et al., 1998; Swaters et al., 2002) and have set a lower limit of about 50% for the fraction of such galaxies.

Richter & Sancisi (1994) suggested that galaxy lopsidedness is a long-lived phenomenon. The structural lopsidedness affects the whole disk and is sustained in some way to prevent it from being dissolved by differential rotation within a few orbital periods. They state further that "such common deviations from circularity (in the H I distributions), if also present in light distributions, induce significant errors into many standard reduction techniques". Indeed, Rix & Zaritsky (1995) and Zaritsky & Rix (1997) found that $\sim 30\%$ of face-on spirals observed in the I and K' bands exhibit significant lopsidedness.

It is not known exactly what causes lopsidedness in galaxies. Short-lived gravitational interactions or minor mergers may play a role (Zaritsky & Rix, 1997), yet most lopsided galaxies are observed to be isolated. Numerical simulations carried out by Bournaud et al. (2005) showed that such events can trigger strong lopsidedness, yet cannot explain several other statistical properties of the lopsided galaxies. Gas accretion has long since been proposed (Zaritsky & Rix, 1997; Bournaud et al., 2005; Sancisi et al., 2008) as a possible cause yet, again, such a mechanism would lead to transient as opposed to long-lived asymmetries. Swaters et al. (1999) suggested that kinematic lopsidedness is related to a lopsided gravitational potential and that even small deviations from axisymmetry in the potential can produce significant kinematic effects.

Is NGC 2915 a lopsided galaxy? The new high resolution H I data allow this question to be addressed. The global H I profile of NGC 2915 (Fig. 2.5) is not neatly symmetric. The red-shifted H I is spread over a larger range of velocities than the blue-shifted H I , which is closely centered about $V_{los} \sim 405$ km s^{-1}. The dip in the profile is skewed toward the lower-velocity horn rather than being close to the midpoint of the two horns. Richter & Sancisi (1994) showed that asymmetric gas density distributions generally lead to asymmetric global H I profiles. The H I disk of NGC 2915 does not, however, exhibit large-scale deviation from circular symmetry.

A galaxy's lopsidedness is often betrayed by its kinematics and NGC 2915 is no exception in this regard. A position-velocity slice through the kinematic centre of the galaxy at a position angle of 327° (Fig. 3.14) reveals asymmetric line profiles on the receding side of the galaxy. The profiles are contained with the region $1' \leqslant \Delta\alpha \leqslant 4'$ and 460 km s^{-1} $\leqslant V \leqslant$ 500 km s^{-1}, and appear as an "H I beard" that is lagging in velocity relative to the main disk. The beard emission

spatially coincides with the plume-like H I feature seen in the H I total intensity map. The mass of this feature is estimated to be $\sim 0.34 \times 10^8$ $M_\odot$ which is 5.6% of total H I mass estimated from global H I profile. This kinematically anomalous gas component could therefore be evidence of gas being accreted from the nearby inter-galactic space onto the outer disk of NGC 2915.

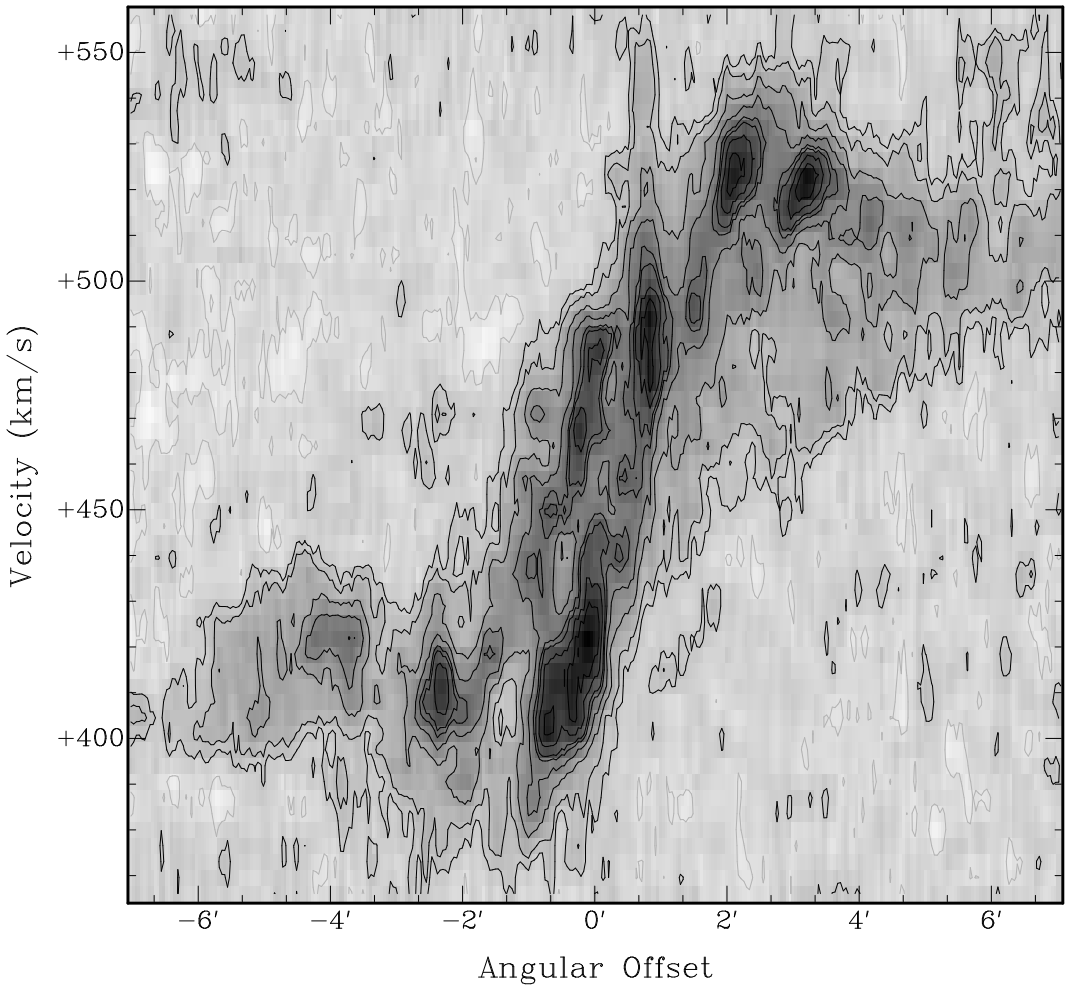

Figure 3.14: Position-velocity slice extracted along a position angle of 327° through the kinematic centre of the galaxy. The thickness of the slice is that of a single pixel in the data cube (2.5″) and the velocity resolution is 3.5 km s^{-1}. Contours levels are -1, 1, 2, 4, 6, 8, 9, 11, 13σ ($\sigma = 0.6$ mJy), with negative and positive contours coloured grey and black respectively.

Further evidence of kinematic lopsidedness in NGC 2915 comes from the rotation curve. In Sec. 3.1.2 the rotation curve was separately derived for the approaching and receding halves of the galaxy. The two rotation curves differ significantly within their steeply rising portions. Swaters et al. (1999) state that galaxies with asymmetric global profiles often have rotation curves that

are more slowly rising on one side of the galaxy than the other. Additionally, the rotation curve of the receding half of the galaxy drops below the rotation curve of the approaching half for $200'' \lesssim R \lesssim 400''$ (Fig. 3.3)-the radial range over which the "beard" emission is observed.

3.5 Harmonic decomposition of HI velocity field

Observed velocity fields of late-type galaxies are often treated as being consistent with a purely circular flow pattern. However, the intrinsic, and therefore also the observed, properties of a galaxy's kinematics will be affected by the presence of non-circular velocity components within the orbits of observable test particles. These non-circular motions are caused in various ways, and can be either systematic or random in nature. On small length scales ($\lesssim$ 0.5 kpc) for example, stellar feedback can significantly disrupt gas dynamics, setting up expanding shells within a galaxy's inter-stellar medium (ISM) (e.g. Walter & Brinks, 1999). On larger scales, stellar feedback can drive galactic outflows in systems of sufficiently low dynamical mass (Meurer et al., 1992; Martin, 1996; Mac Low & Ferrara, 1999; van Eymeren et al., 2009). Globally, a non-axisymmetric gravitational potential will force orbits to be intrinsically elliptical rather than circular (Binney, 1978; Bosma, 1978).

Given an observed velocity field, it is the task of the investigator to determine what information the observed flow pattern contains about the mass distribution and other properties of the system. In the case where the orbits of tracer particles are significantly affected by non-circular motions, a careful characterisation of the non-circular signatures present within the velocity field is required. Several authors (e.g. Franx et al., 1994; Schoenmakers et al., 1997; Canzian & Allen, 1997; Spekkens & Sellwood, 2007) have developed methods for investigating and interpreting complex, non-circular velocity fields of galaxies in the context of perturbations of the potential. These methods allow further insight into the fundamental nature of the processes responsible for generating the non-circular components, as well as the non-circular components themselves. As an example, Wong et al. (2004) used the CO and H I velocity fields of seven nearby spirals to search for evidence of radial gas flows. They found deviations from pure circular rotation at the level of 20-60 km s^{-1} and attributed them to the effects of bar streaming, inflows and warps. More recently, Trachternach et al. (2008) quantified the non-circular motions in a sample of 19 galaxies from the The H I Nearby Galaxy Survey (THINGS, Walter et al., 2008). They found a median absolute amplitude of the non-circular motions, averaged over their entire sample, of 6.7 km s^{-1}. From the measured non-circular velocity components they determined the mean elongation of the gravitational potential to be 0.017 ± 0.020, consistent with a round potential.

In this section we search for non-circular flows in the extended H I disk of NGC 2915. We

carry out a Fourier decomposition of the line-of-sight velocities in order to search for non-ciecular velocity components. The method of Franx et al. (1994) and Schoenmakers et al. (1997) is used to interpret the harmonic decomposition results of the observed velocity field in the context of time-varying perturbations to an axisymmetric potential.

3.5.1 Residual velocity field

Non-circular motions are known to be present within the inner H I disk of NGC 2915 (Sec. 2.5). To estimate how much they deviate from regular circular motion, the observed velocity field is compared to purely-circular model velocity fields. Two model fields were constructed using the GIPSY task VELFI along with the radial parameter profiles from tilted ring models CI and SI. These two model fields are presented in the middle panels of Fig. 3.15.

The two model fields are very similar to one another; of the pixels that actually differ between the two fields, less than 3.5% differ by more than 5 km s^{-1}. The model fields (Fig 3.15, middle panels) were subtracted from the the third-order Gauss-Hermite velocity field (Fig. 3.15, top panel) to yield residual velocity fields (Fig. 3.15, bottom panels). These residual fields provide a measure of the deviation from pure circular rotation of the gas at various positions within the galaxy. The distribution of absolute residuals for tilted ring model SI is shown in the left-hand panel of Fig. 3.16. The right-hand panel of the figure shows the relative percentage of resolution elements in the residual map with a corresponding residual larger or smaller than a given absolute velocity. 68% of the non-blank resolution elements in the residual velocity field are less than $\sim$ 10 km s^{-1}, the approximate velocity dispersion of the outer H I disk. This suggests that a significant fraction of the H I is regularly rotating in circular orbits about the kinematic centre of the galaxy. However, almost 10% of the residuals are larger than 15 km s^{-1}, with some as high as $20 - 25$ km s^{-1}, clearly indicative of significant non-circular H I components.

3.5.2 Measuring the non-circular velocity components

To better quantify the non-circular gas motions in NGC 2915, an harmonic decomposition (i.e. a Fourier expansion) of the observed (Gauss-Hermite) velocity field was carried out. Following Schoenmakers et al. (1997) (hereafter Sch1997b), the line-of-sight velocity was expressed as

$$V_{los}(R) = V_{sys}(R) + \sum_{m=1}^{N} c_m(R) \cos m\psi + s_m(R) \sin m\psi, \tag{3.14}$$

where N is the order of the fit, R the radial distance from the kinematic centre, c_m and s_m represent the magnitudes of the non-circular velocity components, and ψ is the azimuthal angle

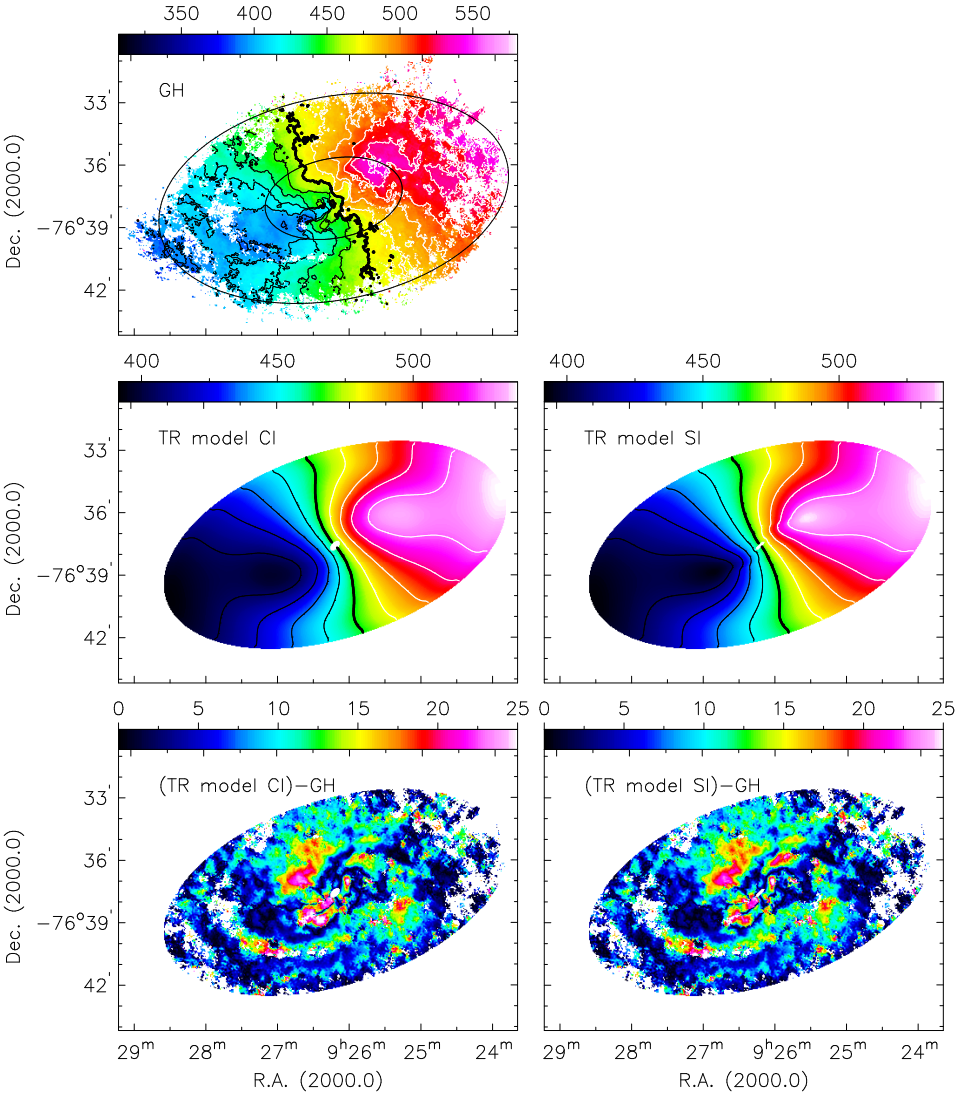

Figure 3.15: **Top panel:** 3rd order Gauss-Hermite velocity field; **Middle panels:** Model circular velocity fields constructing using tilted ring models CI and SI. **Bottom panels:** Absolute residual velocity fields obtained by subtracting the model fields CI and SI from the Gauss-Hermite velocity field. Contours are separated by 15 km s^{-1} with the thick contour marking the systemic velocity at 465 km s^{-1}. White and black contours represent approaching and receding halves of the galaxy respectively. The intensity scale is specified in units of km s^{-1} by the colour bar above each panel. All panels show the same area. The black ellipses in the top panel have semi-major axes of 200″ and 510″. These ellipses delimit the portion of the H I disk for which the harmonic decomposition is carried out.

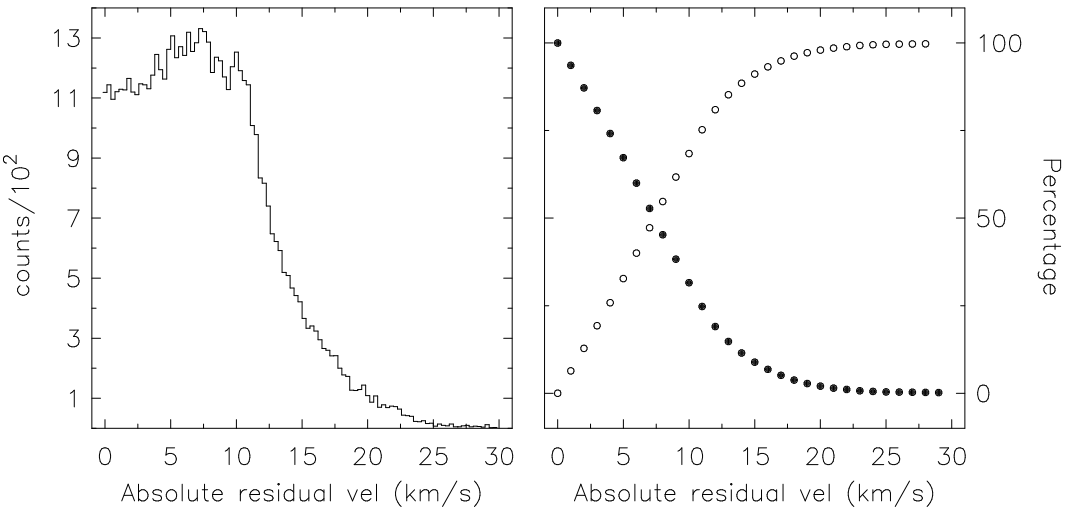

Figure 3.16: Left-hand panel: Distribution of the absolute residuals constituting the residual velocity field shown in the bottom right panel of Fig. 3.15. Right-hand panel: Relative percentage of residual field resolution elements with a corresponding residual greater than (filled circles) and less than (open circles) a given absolute velocity

in the plane of the galaxy.

The GIPSY task RESWRI was used to fit equation 3.14 to concentric rings in the velocity field. Following Trachternach et al. (2008), the line-of-sight velocities were expanded up to order $N = 3$. Including the $N = 3$ harmonics in the expansion allows for more precise classifications of the non-circular velocity components. As part of the decomposition process, RESWRI first fits a circular tilted ring model to the velocity field to obtain a measure of the orientation parameters as well as the kinematic centre for each ring. RESWRI then subtracts the circular rotation model from the observed velocity field and determines the non-circular components of the residual field. Both Franx et al. (1994) and Sch1997b caution that the centre position of the tilted ring model should always be kept fixed when running RESWRI. If allowed to vary, the centre will drift so as to make real c_2 and s_2 harmonics disappear. The centres of the rings were therefore fixed to the position of the photometric centre (α_{2000} = 09^h 26^m 12.611^s, $\delta_{2000} = -76^\circ$ 37′ 37.80″). The tilted ring model orientation parameters were allowed to vary freely, since incorrectly fixing them would lead to incorrect measures of the harmonic components. The default uniform weighting was used during the fitting procedure to ensure that points along the minor axis contributed equally to the measured harmonics. These points contain the most information about non-circular motions. Ring widths of 17″ were used to ensure that adjacent rings were independent of one another.

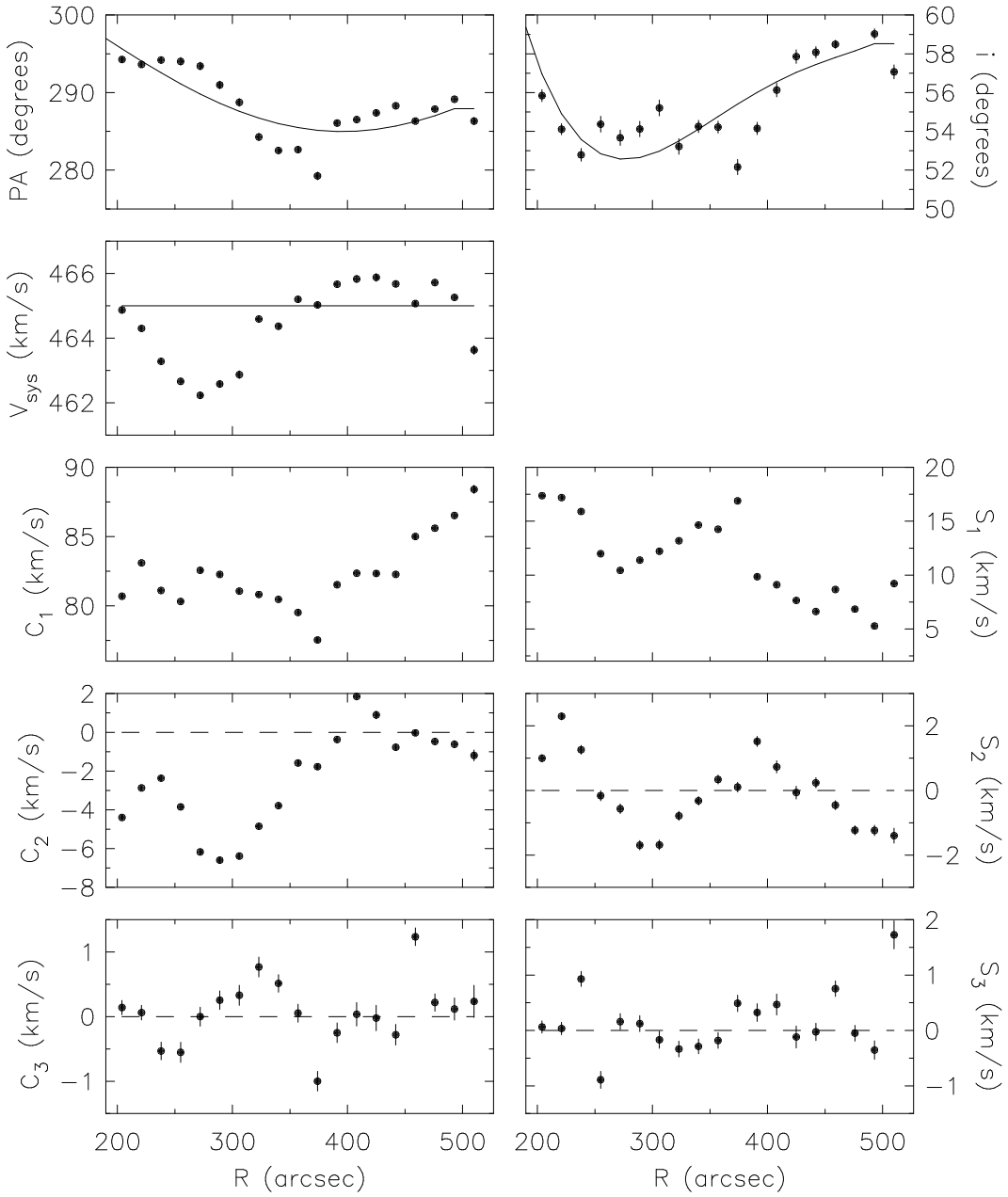

Figure 3.17: Harmonic decomposition results. Rows 1 and 2 show the circular tilted ring model parameters fitted by RESWRI to the velocity field. Rows 3 - 5 show the amplitudes of the harmonic components fitted to the residual velocity. Error bars represent the formal least-squares errors. The solid curves in rows 1 and 2 represent the smoothed parameter profiles from tilted ring model SI. In each panel of rows 4 and 5, the dashed line marks 0 km s^{-1}. The harmonic decomposition was only carried out for radii $R \geq 200''$.

Rings with radius $R < 200''$ were not included in the harmonic decomposition. The complex gas dynamics within this region are most likely dictated by the ongoing high-mass star formation at the centre of NGC 2915 and therefore cannot be meaningfully interpreted in terms of an axisymmetric potential. Furthermore, the magnitudes of these non-circular motions are expected to be a significant fraction of the circular velocity component. The approach developed by Franx et al. (1994) and Sch1997b to interpret the results is only valid for small departures from circular motion, since it is based on epicyclic theory. Finally, Sch1997b caution that errors in the tilted ring fits are expected to be large in regions where $V(R) \propto R$, thereby preventing a reliable measure of the harmonic components of the velocity field. For these reasons, only the region $R > 200''$ of the velocity field was used in the harmonic decomposition. Additionally, to prevent having to work with rings near the edge of the H I disk that would have a low filling factor, the harmonic expansion was only carried out as far as $R = 510''$. The portion of the H I disk that is analysed is delimited by the solid ellipses shown in the top panel of Fig. 3.15.

Figure 3.17 shows the results of the harmonic decomposition. The top 3 panels show the position angles, inclinations, and systemic velocities from the circular tilted ring model fitted to the velocity field by RESWRI. The radial profiles for these parameters are consistent with those of tilted ring model SI (shown as solid curves). RESWRI creates a second residual field by subtracting the fitted harmonic components of each ring from the observed velocity field. This residual field therefore provides a measure of the signal that was not captured by the harmonic expansion. For all radii larger than $200''$, a mean absolute residual of 3.6 km s^{-1} is found, suggesting that an harmonic expansion up to third order is capable of capturing most of the non-circular motions. Trachternach et al. (2008) found an average value of 2.9 km s^{-1} for the absolute residual of the 19 THINGS galaxies in their sample. The average amplitude of the non-circular velocity components for their entire sample is 6.7 $\pm$ 5.9 km s^{-1}. For NGC 2915 the corresponding average is 11.7 km s^{-1} with an r.m.s. spread of 4.0 km s^{-1} about the mean value.

3.5.3 Interpretation of results

In this sub section, the approach developed by Franx et al. (1994) and Sch1997b is used to interpret the harmonic decomposition results in the context of a non-axisymmetric potential. Sch1997b expanded on the work of Franx et al. (1994) (see also Canzian & Allen, 1997) by connecting the measured harmonics of a velocity field to the rotating perturbations of the potential. By solving the equations of motion for the case of a slightly disturbed potential and then calculating the resulting line-of-sight velocities, these authors showed that a potential with a perturbation of order m will yield an observed velocity field with $m + 1$ and $m - 1$ harmonic

terms (their Appendix A1, Eqn. A12). Their results therefore allow for an interpretation of the harmonic decomposition results in the context of a time-varying, axisymmetric potential. Within such a framework, c_0 and c_1 correspond to the systemic and circular velocities of each ring while the higher order terms measure the non-circular velocity components.

A cursory examination of the harmonic decomposition results shows that the c_3 term is approximately zero over the full radial range indicating, according to Sch1997b, that the correct inclinations were fitted by RESWRI. Sch1997b do caution, however, that in the case of an $m = 2$ spiral arm, this inclination is not necessarily equal to the true inclination. Perhaps the most striking result from the harmonic decomposition is the large amount of power seen in the s_1 component ($s_1 \gtrsim$ 10km s^{-1} for $R \lesssim 400''$ and then generally $s_1 \gtrsim$ 5 km s^{-1} thereafter). A strong s_1 harmonic in the velocity field suggests the presence of an $m = 2$ term in the H I field which is often associated with a tri-axial halo. The problem, however, is that $m = 2$ spiral structure, which is clearly present in the H I distribution, will also result in a significant s_1 term in the observed velocity field. Wong et al. (2004), using the linearised equations of Canzian & Allen (1997) for the velocity perturbations caused by a two-armed spiral density wave, pointed out that a characteristic kinematic signature in the velocity field due to such a perturbation is a sinusoidal variation with radius of the s_1 and s_3 harmonic components. While it may be argued that some sinusoidal variation is present in the s_1 and s_3 terms, the power in the s_3 component is negligible ($\lesssim$ 1 km s^{-1}) at all radii, thereby providing evidence against any significant perturbational effects of a two-armed spiral density wave to the observed velocity field.

Another interpretation of the strong s_1 term is that of an axisymmetric radial flow. In their description of the kinematic signatures of different types of non-circular motions, Wong et al. (2004) state that a significant s_1 term together with a negligible s_3 term can be caused by radial gas inflow. This behaviour is indeed seen in the harmonic terms of NGC 2915. Wong et al. (2004) go on to list $|ds_3/ds_1| \lesssim 0.1$ over a significant radial range as a further kinematic signature of radial flow. By plotting the s_3 and s_1 values of NGC 2915 against one another and then fitting a straight line through the data (Fig. 3.18), an average absolute gradient of $|ds_3/ds_1| \approx 5.8 \times 10^{-4}$ is measured for the outer disk. This value is therefore consistent with the radial flow scenario. A further kinematic signature of radial flow is non-orthogonality of the kinematic major and minor axes. From the circular tilted ring model fitted by RESWRI to the GH velocity field, the position angle of the kinematic major axis is estimated to be $\sim 287^\circ$. From the iso-velocity contours in the GH H I velocity field, the position angle of the kinematic minor axis is estimated as $\sim 212^\circ$. The two kinematic axes thus appear to be non-orthogonal, differing in position angle by only $\sim 75^\circ$, thereby further supporting the possibility of radial flow.

Wong et al. (2004) mention that if the s_1 term is interpreted as evidence for radial flow, then in a counter-clockwise rotating galaxy, a positive s_1 term implies outflow. Assuming that a

galaxy's spiral arms are always trailing, NGC 2915 is rotating counter-clockwise, thereby implying the strong s_1 term to be indicative of a radial outflow of the order of $5-17$ km s^{-1}. This result is similar to that of Gentile et al. (2007) who inferred the presence of radial inflows of the order of $5-13$ km s^{-1} in the H I disk of the nearby dwarf irregular galaxy NGC 3741. Sancisi et al. (2008) hypothesise the existence of NGC 2915's extended H I disk to be as a result of the accumulation of in-fallen pristine gas from the surrounding inter-galactic medium. This gas, they say, forms "a reservoir of fresh gas for fuelling star formation in the inner regions". The physical process of gas moving from the outer to the inner disk would, however, be associated with an axisymmetric radial *inflow*, and is hence difficult to reconcile with our kinematic evidence for a radial outflow. Werk et al. (2010) have recently reported on lower- and higher-than-expected oxygen abundances for the respective inner and outer portions of NGC 2915's H I disk. The authors showed that the few isolated regions of low-level star formation within the outer disk cannot account for the measured oxygen abundance. They propose a metal-mixing scenario in which metals produced by the star forming core are radially redistributed towards the outer disk. Such a scenario is consistent with our kinematic evidence for radial outflows. Furthermore, several authors (e.g., Bureau et al., 1999; Masset & Bureau, 2003) strongly advocate the presence of a bar within NGC 2915's co-rotation radius. If mass is able to flow along this bar towards the centre of the galaxy, conservation of angular momentum dictates that some mass must also be sent outwards, away from the centre of the system. Our inferred outward radial motions are consistent with this physical scenario which could perhaps go some way in explaining the existence of NGC 2915's very extended H I disk.

A major flaw in the radial flow argument is that the velocity field of a stationary bar potential resembles axisymmetric inflow or outflow. This, according to Wong et al. (2004), is because for a flat rotation curve the s_3 and c_3 terms are expected to vanish in the case of a stationary perturbation to the potential (demonstrated by Franx et al. 1994). Bars are indeed thought to be the most effective mechanism for transporting gas to the centre of a galaxy (Combes, 1999), and so the kinematics alone cannot distinguish between the stationary bar potential and the radial flow scenarios. Wong et al. (2004) carried out harmonic decompositions of the CO and H I velocity fields of seven nearby spiral galaxies in order to search for evidence of radial gas flows. They found no unambiguous evidence for radial flows, concluding that "the inherent non-axisymmetry of spiral galaxies is the greatest limitation to the direct detection of radial flows". Thus, although the s_1 term provides very suggestive evidence for gas outflow, it should not be treated as conclusive evidence for such gas kinematics. Elliptical streaming of the gas in a bar-like potential can still contribute significantly to the observed non-circular motions. Andersen et al. (2001) demonstrated that high-quality H_α velocity fields and I-band imaging of nearly face-on galaxies can be used to exclude the hypothesis that galaxy disks are intrinsically free of $m = 2$ (elliptical) distortions. The various perturbations to the potential described in this section are

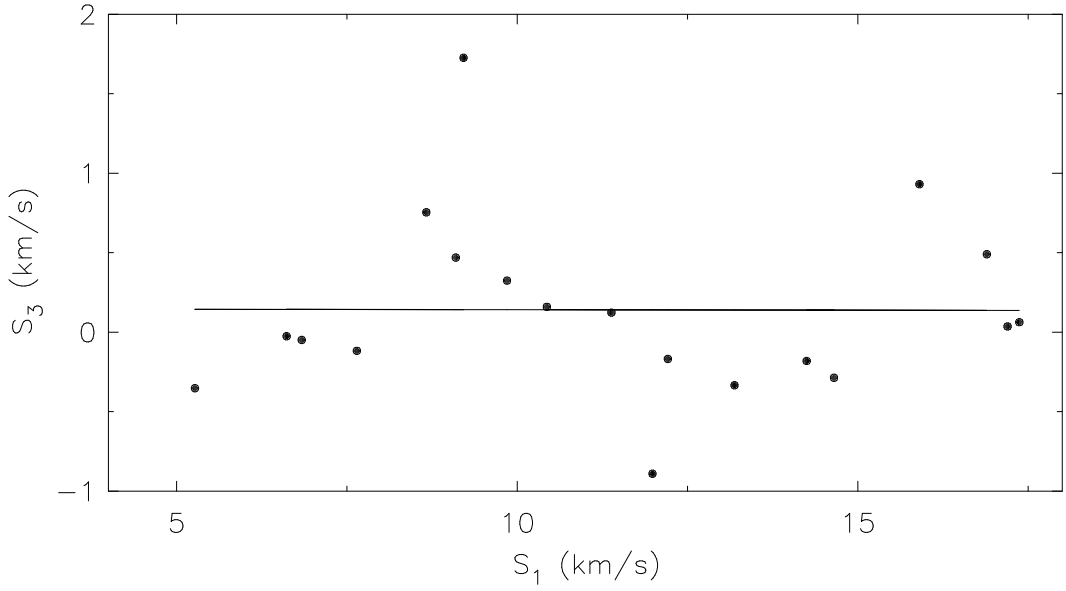

Figure 3.18: Scatter plot of fitted S_3 and S_1 components for the outer disk of NGC 2915. The solid curve is the un-weighted best-fit line with an average absolute gradient of $\sim 5.8 \times 10^{-4}$.

summarised in Table 3.3, together with a list of evidence for and against each perturbation type.

3.6 Elongation of the potential

NGC 2915 is known to be extremely dark-matter-dominated with a total mass to B-band light ratio of $\sim 140\ M_\odot/L_\odot$ (Sec. 3.2.4). If the non-circular components measured in the velocity field are treated as being due to a tri-axial dark matter halo, then the elongation of the potential, according to Sch1997b, can be estimated using the measured s_1 and s_3 via the equation

$$\epsilon_{pot} \sin(2\varphi_2) = (s_3 - s_1)\frac{(1 + 2q^2 + 5q^4)}{c_1(1 - q^4)}, \tag{3.15}$$

where $q \equiv \cos i$, ϵ_{pot} is the ellipticity of the potential, φ_2 is the unknown angle in the plane of the ring between the minor axis of the elongated ring and the observer. φ_2 cannot be measured separately, and so only the combination of the global ellipticity and the viewing angle can be measured as opposed to ϵ_{pot} on its own. Non-circular velocities induced by a global elongation of the potential will result in a constant offset from 0 in $\epsilon_{pot} \sin 2\varphi_2$ while similar such velocities induced by spiral arms occur on small scales and therefore lead to wiggles in $\epsilon_{pot} \sin 2\varphi_2$. Figure 3.19 shows that $\epsilon_{pot} \sin 2\varphi_2$ is negative for all values of $R > 200''$. This is due to the large s_1 term in the harmonic expansion of the velocity field. The error-weighted-mean of the ellipticities

Table 3.3: Summary of H I velocity field harmonic decomposition results for NGC 2915.

Perturber type	Evidence for	Evidence against
$m = 2$ spiral density wave	Strong s_1 term	s_3 term does not vary sinusoidally
Tri-axial halo	Strong s_1 term	Contributions from radial flow and $m = 2$ perturbation
Axisymmetric radial flow	Strong $s1$ term *and* weak s_3 term, $\lvert ds_3/ds_1\rvert \approx 0$, Non-orthogonal kinematic axes	Indistinguishable from elliptical streaming in a stationary bar potential

is -0.41 and is shown as a solid line in Fig. 3.19. Trachternach et al. (2008) measured a mean elongation of 0.011 for their sample of 19 THINGS galaxies. Our estimate of the elongation of the potential of NGC 2915 is an order of magnitude larger than the elongation of -0.067 that Trachternach et al. (2008) measured for NGC 7793, the galaxy in their sample with the most elongated halo. The point is stressed, however, that in the case of NGC 2915, the measured $\epsilon_{pot} \sin 2\varphi_2$ values should not be treated as accurate measures of the elongation of the potential. The observable signatures of a possible radial outflow *and* an $m = 2$ perturbation to the potential from the two-armed spiral density wave will couple significantly with the those of an elongated potential.

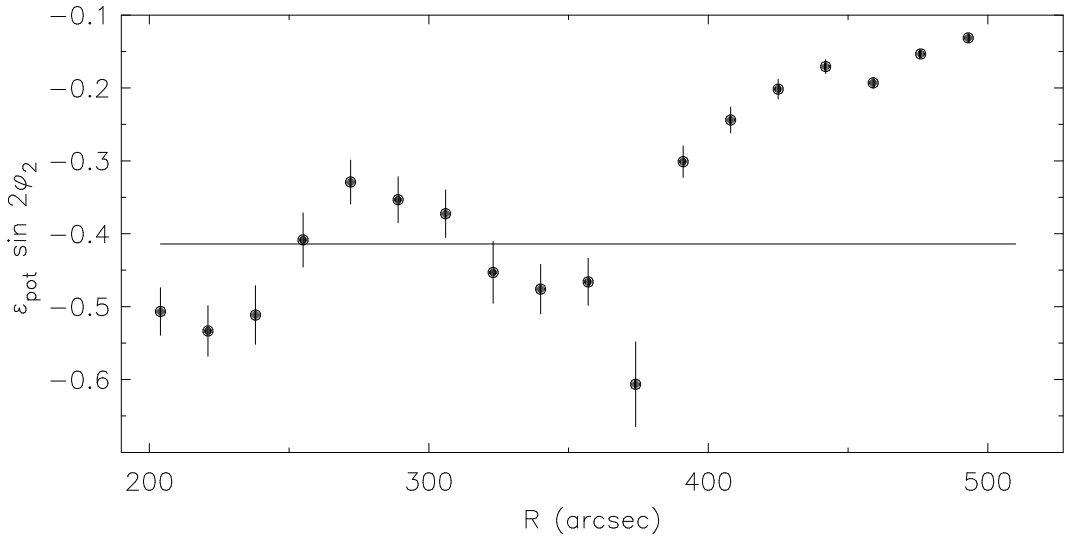

Figure 3.19: Radial distribution of the elongation of the potential of NGC 2915. Error bars were estimated using Gaussian error propagation of the formal least-squares errors of the harmonic components. The solid line represents the error-weighted mean of all the measured elongations.

3.7 Central gas dynamics

Stellar feedback plays an important role in the formation and evolution of galaxies. Dwarf galaxies generally have shallow gravitational potential wells, meaning that the input of kinetic energy into the inter-stellar medium (ISM) from high-mass star formation and supernova explosions can significantly affect the gas dynamics. In the so-called "galactic fountain scenario" (Shapiro & Field, 1976; Bregman, 1980), the ISM is heated and pushed out of the galaxy by stellar winds and supernova explosions. The ejected material moves into the halo of the galaxy, expands, cools and falls back onto the disk. In the case that the ejected gas is accelerated to velocities larger than the escape velocity of the galaxy, significant fractions of the ISM will escape into the inter-galactic medium (IGM) (Mac Low & Ferrara, 1999). In this sense, stellar winds play an important role in determining the chemical evolution of galaxies and the IGM. Within the disk, stellar winds can dictate the gas dynamics by setting up expanding gas shells and holes within the ISM, typically with diameters of $D \lesssim 0.5$ kpc (e.g. Walter & Brinks, 1999; Brinks & Bajaja, 1986; Kamphuis, 1993, for the cases of IC 2574; M31; M101 and NGC 6946 respectively).

The inner H I distribution and kinematics of NGC 2915 are complex. The sharp kinks and wiggles at inner radii seen in the iso-velocity contours of the third order Gauss-Hermite H I velocity field (Fig. 2.11) are indicative of a non-virialised H I component. Direct evidence of broad and multi-component line profiles is provided by position-velocity slices extracted from the

central regions of the galaxy (Fig. 2.14). These non-Gaussian line profiles are in the immediate vicinity of the star-forming core of NGC 2915, and could therefore be due to the effects of stellar winds from the young stellar population. In this section, a detailed study of the central H I properties of NGC 2915 is carried out. A simple physical scenario that links the high-mass star formation at the centre of the galaxy to the observed H I kinematics is proposed and tested.

3.7.1 Double-component line profiles

In Sec. 2.5 it was demonstrated that multi-component and broad H I line profiles exist within the central regions of NGC 2915's H I disk. In order to classify a particular line profile as being either single- or double-component in nature, the reduced χ^2 goodness-of-fit statistics of fitted single- and double-component Gaussians were compared to one another. A line profile with a double Gaussian goodness-of-fit statistic, χ^2_d, that was less than 85% of the corresponding single Gaussian goodness-of-fit statistic, χ^2_s (i.e. $\chi^2_d < 0.85\chi^2_s$) was classified as being double-peaked. Profiles for which $\chi^2_d > 0.85\chi^2_s$ were classified as consisting of a single component. The H I data cube was re-gridded to a pixel size of $10'' \times 10''$ in order to increase the level of independence between adjacent line profiles. Three filters were used simultaneously when fitting the line profiles with single- and double-component Gaussians: (1) only data above 4σ were used for the fit; (2) line profiles with a fitted line-width less than the channel width were rejected; and (3) fitted profile peaks had to be within the velocity range of the data cube. An example of a fitted double-peaked profile is shown in Fig. 3.20.

A comparison between the reduced χ^2 goodness-of-fit statistics of both sets of fits showed that of the 2571 fitted profiles, 561 have $\chi^2_d < 0.85\chi^2_s$, i.e. they were significantly better fitted by a double-component Gaussian than by a single-component Gaussian. These profiles are shown as black-filled squares in Fig. 3.21 while the profiles for which $\chi^2_d > 0.85\chi^2_s$ appear in grey. It is evident that the double-peaked H I profiles are most prevalent within the immediate vicinity of the galaxy's star-forming core. Double-peaked profiles also occur within the general vicinity of the plume-like H I feature seen in the H I total intensity map (delimited by a rectangle in Fig. 3.21). Also evident from Fig. 3.21 is the fact that most of the double-peaked line profiles near the centre of the galaxy are associated with the south-eastern central H I concentration seen in the H I total intensity map. The double-peaked line profiles also correspond to the tip of one of two Hα bubbles identified by Meurer et al. (1994) who also showed that star clusters in this region of the galaxy have tendrils or tails, suggestive of radial inflows. For each of the identified double-peaked H I line profiles within $98''$ of the dynamical centre (i.e. within the black ellipse shown in Fig. 3.21), the absolute difference between the two fitted peak velocities was determined. The average velocity separation for the profiles is $\Delta V = 59$ km s^{-1}, roughly 72%

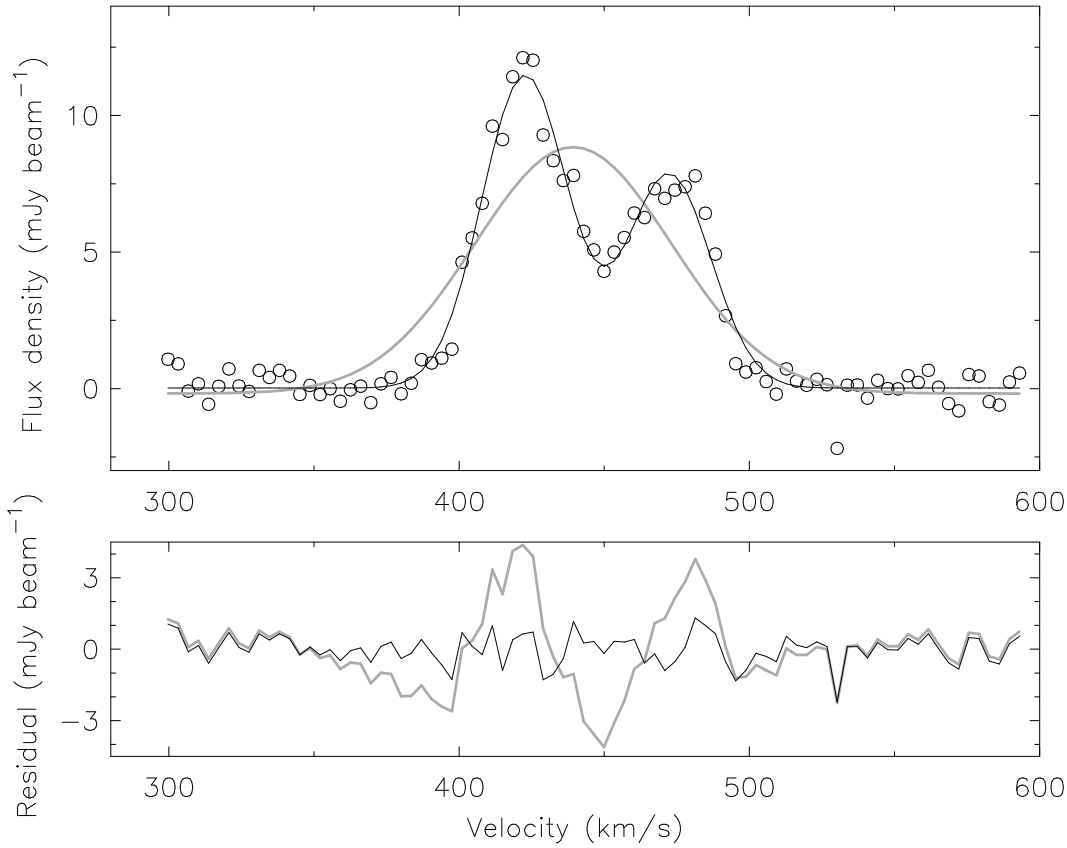

Figure 3.20: Example of a double-peaked line profile extracted from position $\alpha_{2000} = 09^{h}\ 26^{m}\ 12.6^{s}$, $\delta_{2000} = -76^{\circ}\ 37'\ 37.8''$ in the re-gridded H I data cube of NGC 2915. This position is marked by a black cross in Fig. 3.21. In the top panel, open circles represent the data, the solid grey and black curves represent best-fitting single- and double-component Gaussians respectively. The solid grey and black curves in the lower panel represent the residuals for the fitted single- and double-component Gaussians respectively.

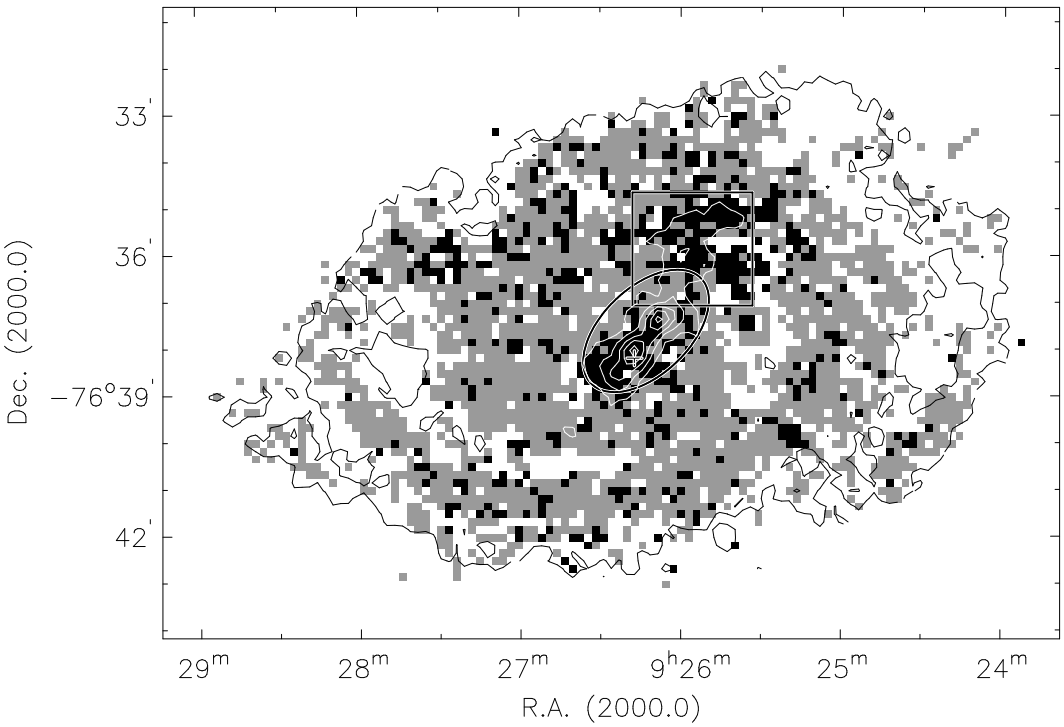

Figure 3.21: Comparison of the quality of single- and double-component Gaussian fits to the H I line profiles. Black-filled squares denote the positions at which the reduced χ^2 statistic of the fitted double Gaussian is less than 85% of the corresponding statistic for the fitted single Gaussian, i.e. $\chi^2_d < 0.85\chi^2_s$. Grey-filled squares represent profiles for which $\chi^2_d > 0.85\chi^2_s$. White-filled squares represent line profiles that were rejected by the fitting filters and which were therefore not parameterised. The angular size of each coloured square is $10'' \times 10''$, corresponding to ≈ 183 pc $\times$ 183 pc. The single contour is at a column density level of 1.6×10^{20} cm^{-2}, and is arbitrarily selected to represent the approximate edge of the outer H I disk. The white contours run from $4.4 \times 10^{20} - 1.3 \times 10^{21}$ cm^{-2} in steps of 2.2×10^{20} cm^{-2}. The ellipse represents the edge of the old stellar disk and has a semi-major axis length of $98''$. The rectangle delimits the plume-like H I feature seen in the H I total intensity map. The cross at $\alpha_{2000} = 09^h\ 26^m\ 12.6^s$, $\delta_{2000} = -76^\circ\ 37'\ 37.8''$ marks the position of the H I profile shown in Fig. 3.20.

of the galaxy's asymptotic circular velocity of 81.9 ± 1.6 km s^{-1}.

3.7.2 Central energetics

Are the effects of stellar winds and/or supernovae explosions the cause of the double-peaked H I line profiles observed near the centre of NGC 2915? Several authors have linked the effects of stellar feedback to radially expanding gas components in nearby galaxies. For example, by carrying out a kinematic study of the irregular dwarf galaxy NGC 4816 using H I and Hα observations, van Eymeren et al. (2009) detected prominent H I and Hα outflows with expansion velocities of $V_{exp} \sim 25$ km s^{-1} and $V_{exp} \sim 30$ km s^{-1} respectively. They associated these outflows with a fast-expanding supergiant gas shell, set up by the injection of mechanical energy from massive stars into the ISM. Walter & Brinks (1999), in their study of the holes and shells in the ISM of the dwarf galaxy IC 2574, determined the expansion velocity of the gas around each of 40 identified HII regions. They found expansion velocities of $V_{exp} \sim 6-25$ km s^{-1}. One of their main findings was that the energy requirements for "the formation of the holes can be understood in terms of the combined effects of stellar winds and multiple supernova explosions of the most massive stars formed during a recent phase of active star formation". Young et al. (2003) used VLA observations of three dwarf galaxies to analyse their H I line profile widths and shapes. The authors found a trend between the fraction of asymmetric profiles in a galaxy and its Hα luminosity, with galaxies having greater star formation rates also having a greater fraction of asymmetric, double-peaked line profiles. They interpret the result as being indicative of the star formation activity and its associated injection of kinetic energy into the ISM that is responsible for stirring the surrounding H I .

Gas energetics

Supposing that the double-peaked H I line profiles observed in the central regions of NGC 2915 are due to an expanding gas component, could the young stellar core be supplying the energy required to drive such an expansion? To begin answering this question, an estimate of the energy associated with the expanding gas is required. Following Meurer et al. (1996), the central energetics are quantified by estimating the kinetic energy associated with an expanding gas component as

$$E_k = \frac{1}{8} M_g \Delta V^2, \tag{3.16}$$

where M_g is the mass of the expanding gas and ΔV is the observed velocity separation between the peaks of a double-peaked H I line profile. The observed velocity separation is related to the expansion velocity by $V_{exp} = \frac{1}{2}\Delta V$. For the sake of brevity, the term "splitting" is henceforth used to denote the velocity separation between the fitted peaks of a double-peaked H I line profile. Considering only the split line profiles within 100″ of the centre of NGC 2915 (i.e. black-filled resolution elements within the ellipse shown in Fig. 3.21), the associated flux density of each

profile (obtained from the corresponding resolution element in the re-gridded H I total intensity map) was converted to a mass estimate, all of which were summed to yield $M_g \sim 2.6 \times 10^6$ M$_\odot$. The average splitting of $\Delta V = 59$ km s^{-1} for the central double-peaked line profiles suggests an expansion velocity of $V_{exp} \sim 30$ km s^{-1}. These M_g and ΔV values yield $E_k \sim 5.6 \times 10^{44}$ J for the amount of kinetic energy associated with an expanding central gas component.

Meurer et al. (1996), using $M_g = 10^8$ M$_\odot$ and $\Delta V = 40$ km s^{-1}, estimated $E_k \sim 4 \times 10^{46}$ J for NGC 2915 assuming a distance of 5.1 Mpc. At a distance of 4.1 Mpc, their energy estimate reduces to $E_k \sim 2.6 \times 10^{46}$ J. It is stressed that our estimate of M_g is a lower limit for the mass of expanding gas. Only the masses associated with identified split profiles were considered, as opposed to all of the mass within a specified central region. For this reason, our E_k estimate is lower than that of Meurer et al. (1996). The expanding gas mass $M_g = 10^8$ M$_\odot$ used by Meurer et al. (1996) to estimate E_k is almost as large as the total H I mass of NGC 2915 derived in Sec. 2.4.2 from the global H I profile of the high-resolution H I data cube. We therefore treat the $E_k \sim 2.6 \times 10^{46}$ J estimate of Meurer et al. (1996) as an upper limit for the kinetic energy of the expanding neutral ISM.

Stellar energetics

The amount of kinetic energy associated with the expanding gas component needs to be compared to the mechanical energy output of the central stellar population. Hα emission is observed near the centre of NGC 2915. Importantly, it *only* occurs at inner radii where a large fraction of the split H I line profiles are observed. An Hα image, produced using the data of Gil de Paz et al. (2003), is shown in Fig. 3.22 (upper panel) together with the GALEX near ultra-violet image (sub panel). The location of the Hα emission relative to the H I emission is also shown in Fig. 3.22 (bottom panel). The Hα emission is clearly contained between the two central H I concentrations seen in the H I total intensity map. The filamentary structure of the Hα emission (Fig. 3.22, top panel) is indeed testament to the perturbing effects that the high-mass star formation has on the distribution of the ISM.

While the intense ultra-voilet radiation energy produced by young, massive O- and B-type stars is capable of ionising the neutral ISM, it is not expected to play a significant role in redistributing it. Rather, it is the mechanical energy injected by stars via stellar winds and supernova explosions that is expected to set up shock-heated (T $\gtrsim 10^6$ K) gas and expanding structures within the ISM. Chu (2005) neatly demonstrates that the total amount of mechanical wind energy output during the entire lifetime of an O-type star, including the high-mass-loss-rate Wolf-Rayet phase, is $\sim 4 \times 10^{43}$ J. The author further points out that this energy is more than a factor of 2 lower than the mechanical explosion energy of a supernova, $\sim 10^{44}$ J. In this work

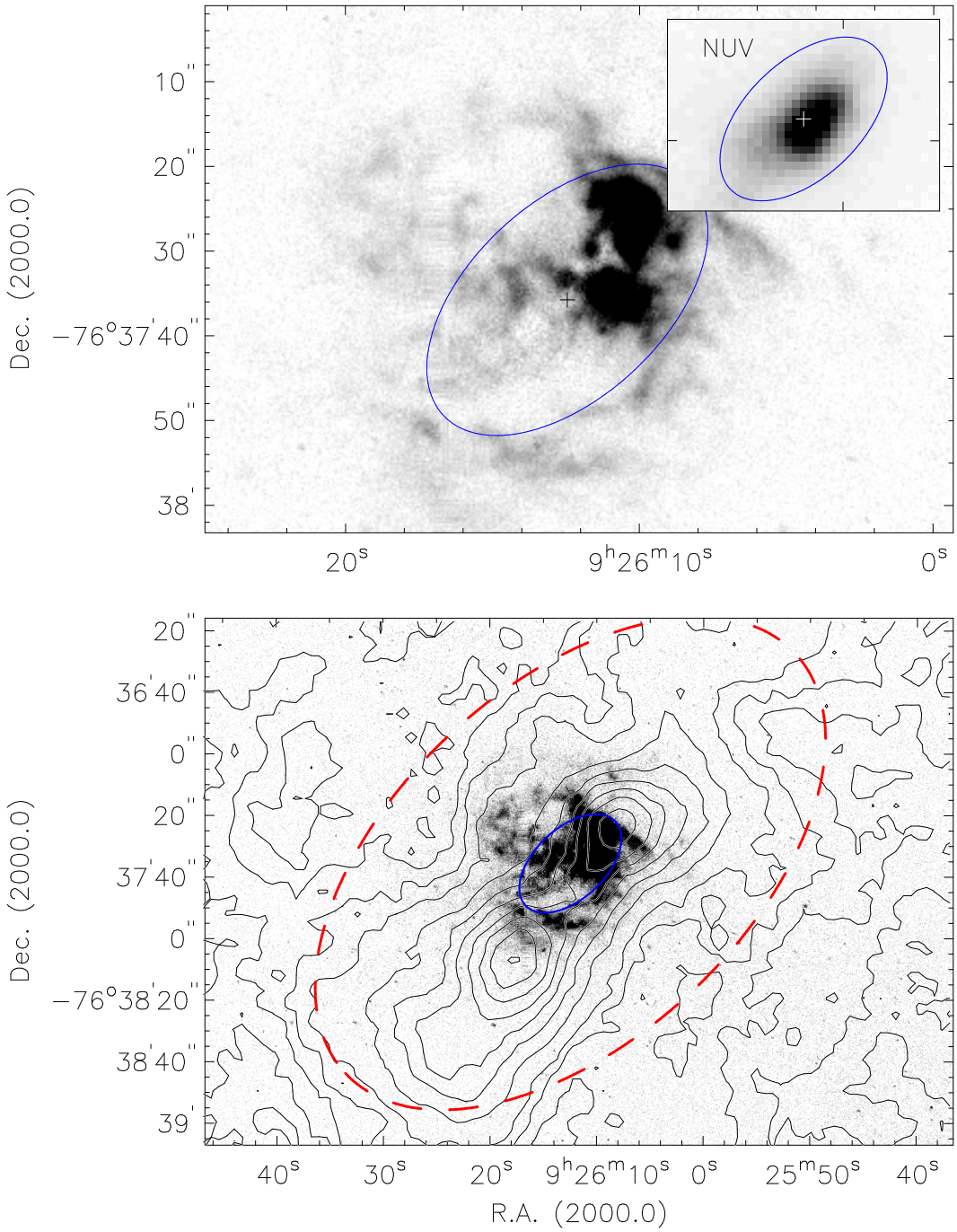

Figure 3.22: Top panel: Hα greyscale image produced using the data from Gil de Paz et al. (2003). In both panels the Hα intensity scale is arbitrary since the Hα data are un-calibrated. The sub-panel shows the GALEX near ultra-violet image. The blue ellipses, included to facilitate length-scale comparisons between the images, have a semi-major axis of length 20''. Bottom panel: Hα greyscale image with H I flux density contours overlaid. H I contour levels run from 10 - 60 mJy beam^{-1} km s^{-1} in steps of 10 mJy beam^{-1} and from 60 - 230 mJy beam^{-1} in steps of 20 mJy beam^{-1} km s^{-1}. The red dashed ellipse is the same ellipse shown in Fig. 3.21, and represents the approximate edge of the old stellar disk. The black cross in the top panel represents the photometric centre.

we therefore consider the mechanical energy produced by supernova explosions, and the effects is has on the distribution and kinematics of the neutral ISM. In the remainder of this section we estimate the time-scales over which mechanical energy deposition from stars into the ISM can account for the $E_k \sim 5.6 \times 10^{44}$ J and $E_k \sim 2.6 \times 10^{46}$ J estimates presented above for the ISM kinetic energy.

Leitherer & Heckman (1995) show that the equilibrium ratio of the mechanical luminosity from supernova explosions to a galaxy's Hα luminosity is $L^{SNe}_{mech}/L_{H\alpha} = 1.8$. This, they say, is the case for a Salpeter IMF (Salpeter, 1955) stellar population having formed at a constant rate. Using this relation together with the $L_{H\alpha} = 10^{32.5}$ J s^{-1} measurement of Gil de Paz et al. (2003) yields an estimate of $L^{SNe}_{mech} = 1.8 \times 10^{48}$ J s^{-1} for the total mechanical luminosity of NGC 2915's supernova population. However, not all of this mechanical energy will be deposited into the ISM as kinetic energy. For example, Mori et al. (2002) treat only 30% of the mechanical energy from supernovae as being converted into ISM kinetic energy. Adopting the same conversion factor, we estimate $L^{ISM}_{mech} = 0.3 L^{SNe}_{mech} = 1.7 \times 10^{32}$ J s^{-1} to be the rate at which mechanical energy from supernovae is injected into NGC 2915's ISM. At this rate, the central H I energetics of NGC 2915 could be accounted for within $\sim 1.0 \times 10^5$ to 4.8×10^6 yr for $E_k \sim 5.6 \times 10^{44}$ to 2.6×10^{46} J.

A second estimate for the timescale required by NGC 2915's supernovae population to energise the central HI component of the galaxy can be obtained by considering the expected total supernova mass and supernova rate. Treating a single supernova event as depositing 0.3×10^{44} J of mechanical energy into the ISM, roughly 20 - 860 supernovae are needed to account for an amount of kinetic energy $E_k \sim 5.6 \times 10^{44}$ - 2.6×10^{46} J associated with the expanding central H I component of NGC 2915. By randomly sampling stellar masses between 0.08 $M_\odot$ and 120 $M_\odot$ from a Salpeter IMF, and then identifying supernova progenitors as those stars more massive than 8 $M_\odot$, we find 860 supernovae to correspond to a stellar mass of $\sim 6.9 \times 10^4$ $M_\odot$. The corresponding stellar mass for a Kroupa IMF (Kroupa, 2001) is almost identical. This stellar mass is much less than that of the blue stellar population of NGC 2915. Adopting a B-band extinction-corrected apparent magnitude of $m_B = 12.0$ (Helmboldt et al., 2004; Schlegel et al., 1998) together with the 4.1 Mpc distance estimate of Meurer et al. (2003), the total B-band luminosity of NGC 2915 is determined to be 3.2×10^8 $L_\odot$. Even for a B-band stellar mass-to-light ratio as low as 0.1 $M_\odot/L_\odot$, the total mass of the blue stellar population is still at least two orders of magnitude larger than that required for ~ 860 type-II supernovae to form.

The supernova rate of a galaxy is often found to be of the order of one percent of the total star formation rate (Boomsma, 2007). Kennicutt (1983) determined the relation

$$SFR_{tot} = 3.42 \times 10^{-8} L_{H_\alpha}, \tag{3.17}$$

where SFR_{tot} is the total star formation rate of a galaxy in units of $M_\odot$ yr^{-1} and $L_{H\alpha}$ its total Hα luminosity in solar units. Using this relation together with the $L_{H\alpha} = 10^{32.5}$ J s^{-1} measurement of Gil de Paz et al. (2003) yields an estimate of $SFR_{tot} = 2.8 \times 10^{-2}$ $M_\odot$ yr^{-1} for the total star formation rate of NGC 2915. The supernova rate is thus expected to be of the order of 10^{-4} $M_\odot$ yr^{-1}. Considering only type-II supernovae events, a lower supernova mass limit for 860 supernovae is $M_{SN} = 860 \times 8 \approx 6.8 \times 10^3$ $M_\odot$, since core collapse supernovae events only occur for stars at least as massive as 8 $M_\odot$. The ratio of this supernova mass to the supernova rate yields a formation timescale of $\sim 6.8 \times 10^7$ yr. The corresponding timescale for 20 supernovae is ~ 1.6 Myr.

These estimated time-scales of $\sim 10^5 - 10^7$ yr match the typical main sequence lifetimes of high-mass O- or B-type stars. These are exactly the types of stars expected to constitute NGC 2915's blue stellar core, thereby implicating them as a mechanical energy source responsible for the anomalous central H I kinematics. In the sections that follow, the central H I component of NGC 2915 is modelled as being radially expanding due to the input of kinetic energy from the high-mass stars into the ISM. The kinematic models that we produce are not expected to precisely match the complex features of the H I data. Instead, they allow us to generally identify the constituent disk properties and processes that may be responsible for the observed H I distribution and kinematics.

3.7.3 Modelling the central HI dynamics

A radially expanding inner gas component should exhibit distinct kinematic signatures as seen in a three-dimensional data cube. To check whether such a scenario is consistent with the observed H I kinematics of NGC 2915, various model cubes were constructed and compared to the observations. The model cubes differ in the radial profiles of some of their orientation parameters as well as their kinematics.

Modeling routine

The model cubes were generated using the GIPSY task HALOMODGAL[‡], a modified version of the standard GIPSY task GALMOD. The routine assumes axisymmetry and distributes many "H I clouds" into a set of tilted rings. For each ring the inclination, position angle, and rotation velocity must be provided; as well as a velocity dispersion, column density and scale height perpendicular to the plane. Unlike the standard GALMOD routine, the user can additionally specify non-circular velocities parallel and perpendicular to the plane for each ring using HALOMODGAL.

[‡]Kindly provided by Filippo Fraternali.

The routine selects random positions at which to distribute H I clouds within each ring. Having placed a cloud, the routine uses the systemic and rotation velocities of the tilted ring to build a velocity profile around the position of the cloud. For this purpose, the cloud is divided into sub-clouds and each sub-cloud assigned a velocity equal to the central velocity of the cloud[§] plus a random increment extracted from a Gaussian. This Gaussian has a mean equal to the central velocity and a width equal to the velocity dispersion of the ring. Finally, the routine uses the position and velocity of the sub-cloud to place it at the corresponding pixel position within the data cube.

Gas disk scale height

The HALOMODGAL routine requires an estimate of the H I disk scale height. To obtain an estimate, the method outlined by Walter & Brinks (1999) was used. They state that for a density distribution given by $\rho(z, R) = 2\rho(0, R)\ \mathrm{sech}(z/z_0)$ (Kellman, 1972; van der Kruit, 1981), the scale height is

$$z_0(R) = \frac{\sigma_{gas}}{\sqrt{2\pi G \rho(0, R)}}, \tag{3.18}$$

where σ_{gas} is the velocity dispersion of the gas in quiescent regions of the galaxy, and $\rho(0, R)$ is the total volume density of the galaxy in the disk plane. Under this approximation, the H I disk scale height is proportional to the H I velocity dispersion and inversely proportional to the total mass density in the disk. Assuming a Gaussian distribution of the H I disk in the z-direction, the 1σ scale height is approximately $h = z_0/\sqrt{2}$.

A constant value of 10 km s^{-1} was used for σ_{gas}, chosen in accordance with the typical azimuthally-averaged second-order moments of the H I line profiles of the outer H I disk of NGC 2915. Following Walter & Brinks (1999) to calculate the average mass density for all the mass (i.e. stars, gas and dark matter) in the plane of the gas disk, it was assumed that the total mass of the galaxy can be estimated from the last measured point (with radius R_{last}) of the observed rotation curve, V_{last}. This mass was treated as being distributed over a spherical volume of radius R_{last}. The results of the tilted ring models fitted to the H I velocity field were used: $R_{last} = 8.7$ kpc and $V_{last} = 86$ km s^{-1}. These values yield an average density of $\rho = 0.005\ \mathrm{M}_\odot\ \mathrm{pc}^{-3}$ at the radius R_{last}. Since this is only the mean density of the galaxy, and the density near the plane is certainly higher, Walter & Brinks (1999) suggest that twice the derived value should be used to approximate the mid-plane density. The mid-plane density is thus approximated as $\rho(0, R) = 0.01\ \mathrm{M}_\odot\ \mathrm{pc}^{-3}$. In Sec. 3.2.4, under a minimum disk assumption, a central dark matter density of $\rho_0 = 0.17 \pm 0.03\ \mathrm{M}_\odot\ \mathrm{pc}^{-3}$ and a core radius of $R_c = 0.9 \pm 0.1$ kpc was estimated for NGC 2915. Our estimate for the mid-plane dark matter density is therefore

[§]The sum of the cloud's systemic and rotation velocities.

roughly a tenth of the core density, and matches the halo volume density at a galactocentric radius of 3.6 kpc. Using these σ_{gas} and $\rho(0, R)$ estimates, together with Eqn. 3.18 and $h = z_0/\sqrt{2}$, yields $h = 413$ pc as the approximate scale height of the gaseous disk NGC 2915. This puffy H I layer is attributed to the relatively low gravitational potential of this low mass system and the H I velocity dispersion of $\sigma_{gas} \sim 10$ km s^{-1}. For reference, high surface brightness spirals have typical H I disk scale heights of $\sim 1 - 2$ kpc (Kregel et al., 2004).

Tested models

Several models were generated to study the H I kinematics of NGC 2915. To create these models, the tilted ring modeling results were used. Specifically, the inclination and position angle radial profiles as well as the rotation curves of tilted ring models CI and SI were incorporated. The two tilted ring models differ mainly in their inclination profiles, and very slightly in their rotation curves. Model CI has an almost constant inclination of $i \sim 55°$ for all radii. The inclination profile of model SI rises from $i \sim 55°$ to $i \sim 75°$ when moving from the outer to the inner disk, beginning at a galactocentric radius of $\sim 240''$. For all model cubes, the systemic velocity was always kept constant at 465 km s^{-1}. The kinematic centre was set equal to the photometric centre. The H I column density profile presented in Sec. 2.4.3 was inclination-corrected using each of the inclination radial profiles, yielding two face-on column density radial profiles. Each of the model cubes was smoothed down to a resolution of $17.0'' \times 18.2''$, the resolution of the actual data cube. Various position-velocity slices were extracted from the model cubes and compared directly to the corresponding slices from the H I data cube. The locations and orientations of these slices in the H I total intensity map are shown in Fig. 3.23. All of the position-velocity data are shown in Fig. 3.24.

Six different model cubes were constructed in total. The first two are purely circular models, and were made using the radial parameter profiles of tilted ring models CI and SI together with a constant H I velocity dispersion of 10 km s^{-1}. These two model cubes, henceforth referred to as cubes CI and SI, served as the "base" models. They were manipulated in order to construct the rest of the model cubes. Cubes CI and SI are shown in columns 1 and 2 of Fig. 3.24. Slice 1 (row 1) demonstrates how these purely circular model are capable of reproducing the observed H I kinematics of the outer disk where non-circular gas motions are negligible. Slice 1 also shows that, by construction, all six models reduce to models CI and SI in the outer disk. Slices 2, 3 and 4, however, show that simple, purely circular models such as cubes CI and SI are unable to reproduce the inner-disk H I kinematics of NGC 2915 which are dominated by non-circular velocity components.

Is a neutral ISM with a high velocity dispersion responsible for the non-Gaussian line profiles

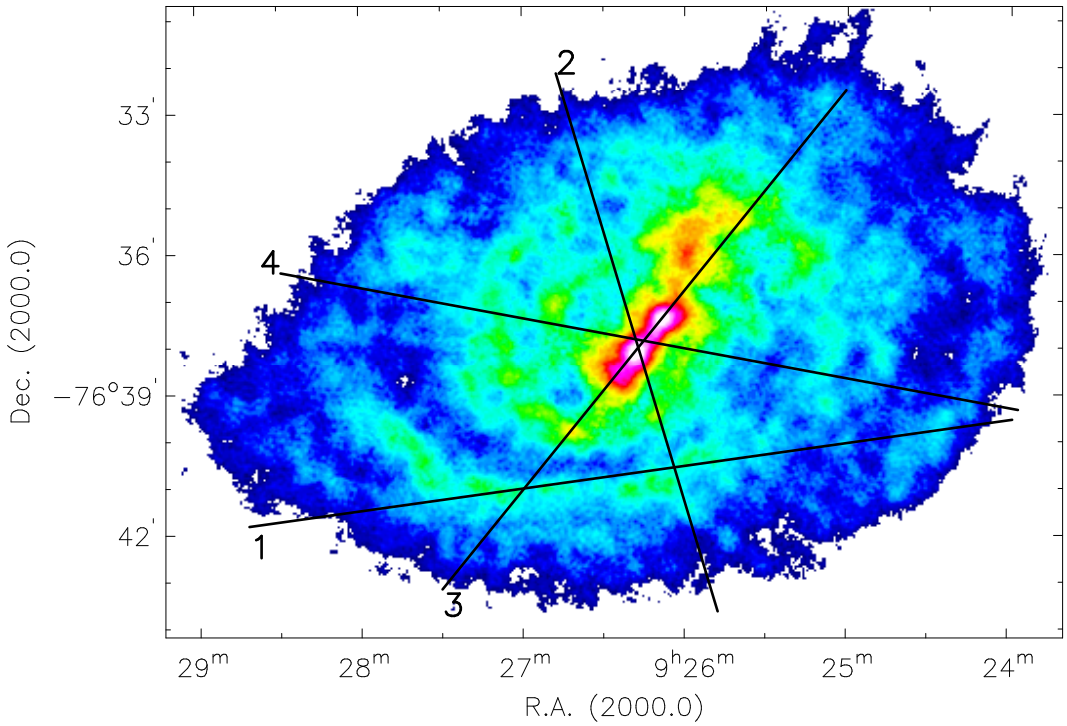

Figure 3.23: H I total intensity map with solid black lines representing the locations and orientations of the position-velocity slices (presented in Fig. 3.24) used to check the model cubes against the H I data cube.

near the centre of the galaxy? The second-order H I moment map presented in Sec. 2.4.5 exhibits a sharp increase from outer to inner disk, with second-order moments as high as $\sim$ 25 km s^{-1} near the centre of the galaxy. Is this sharp increase in the second-order moments of the H I line profiles an accurate representation of the H I velocity dispersions, or is it an artefact of the split line profiles near the centre of the galaxy? To check whether such an increase in velocity dispersion is consistent with the H I data, the second-order moment map radial profile was added as a velocity dispersion radial profile to model cubes CI and SI. The resulting model cubes are henceforth referred to as cubes CI+disp and SI+disp, and are presented in columns 3 and 4 of Fig. 3.24. Panels 10, 11, 12, 14, 15, 16 of Fig. 3.24 show that although these dispersion models are able to reproduce the large spreads in central velocities, they cannot match the double-peak structure of the H I line profiles. A highly dispersed central ISM therefore cannot explain the central gas kinematics of NGC 2915.

Since none of the purely circular models were able to match the H I kinematics of the inner disk, the final set of models included radial expansion velocities superimposed on the underlying

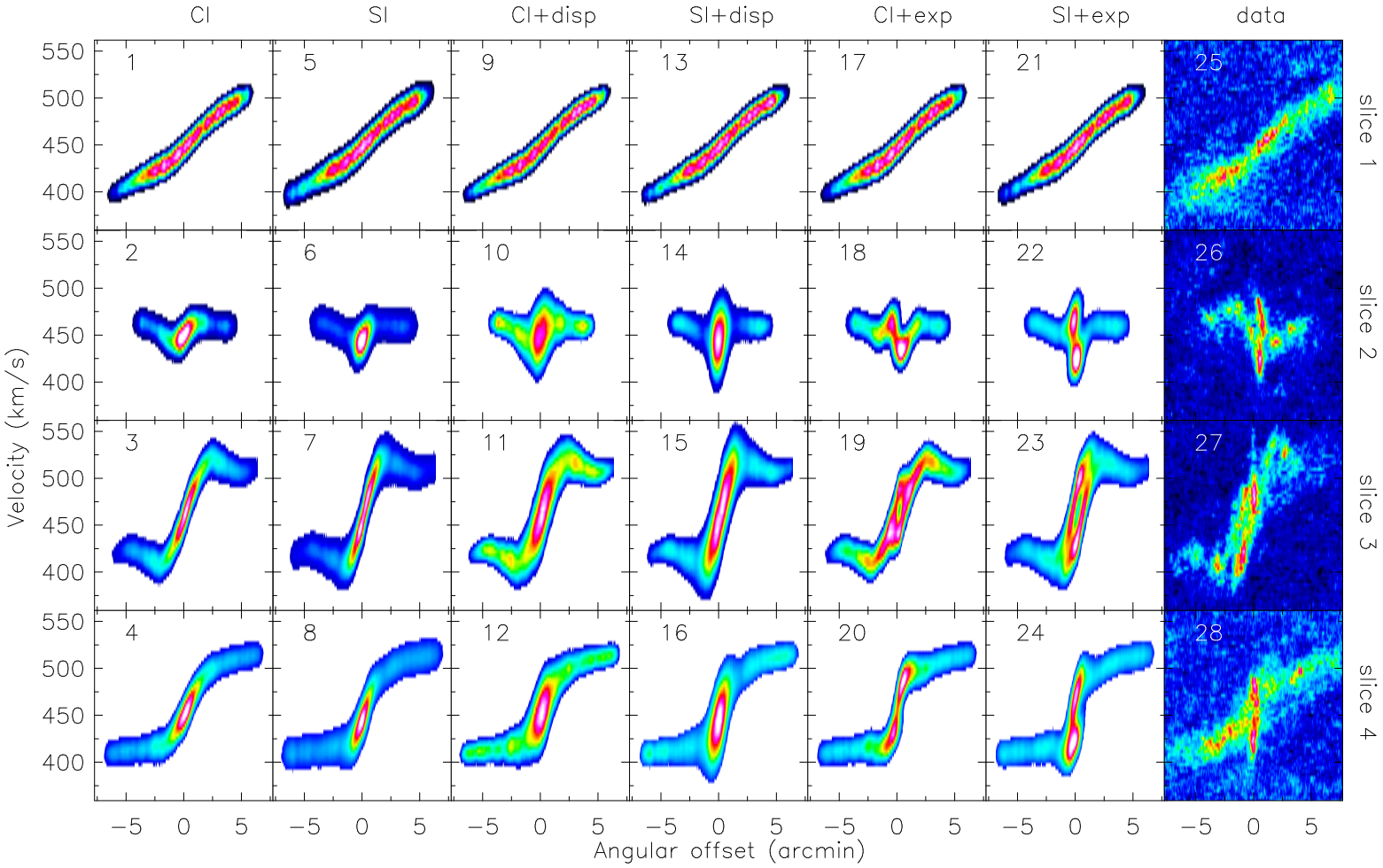

Figure 3.24: Position-velocity slices extracted from the model and H I data cubes. Each row represents a different position-velocity slice with the slice locations and orientations in the H I total intensity map shown in Fig. 3.23.

Comments on columns: Each of columns 1-6 (from left to right) represent a different model cube of a thin, rotating gas disk. Columns 1, 2: constant velocity dispersion of 10 km s^{-1} and no expansion velocities; columns 3, 4: high velocity dispersion towards the centre and no expansion velocities; columns 5, 6: constant velocity dispersion of 10 km s^{-1} and expansion velocities of $\sim$ 30 km s^{-1} near the centre. Column 7 shows the H I data cube position-velocity data.

circular kinematics. The results of Sec. 3.7.1 above show that, on average, H I line profiles are split by $\sim$ 60 km s^{-1} within the central 100″ of the galaxy. If this observed line splitting is interpreted as being due to an expanding gas component, the expansion speed is equal to half of the observed line splitting. Model cubes CI+exp and SI+exp were therefore constructed by adding radial expansion velocities (i.e. outflow) of V_{exp} = 30 km s^{-1} at all radii $R \leq 85''$ to model cubes CI and SI. These models are shown in columns 5 and 6 of Fig. 3.24. A distinct trend in the general structure of the model cube line profiles is noticeable when moving from column 1 to column 6 (left to right) in Fig. 3.24: columns 1 and 2 have single-component, relatively low-dispersion Gaussian-shaped line profiles. The remaining columns 3 - 6 have line profiles with higher second-order moments, yet columns 3 and 4 still only contain single-component line profiles. Most noticeable in columns 5 and 6 is the double-peaked nature of the inner-most line profiles, with the more specific nature of the splitting differing between columns 5 and 6. Various models incorporating radial inflows were also tested, yet were found to be inconsistent with the general data features.

The split line profiles seen in the model cubes (panels 18, 19, 20, 22, 23, 24) are mostly consistent with the double-peaked profiles seen in the data (panels 26, 27, 28). Clearly, however, it is cube SI+exp that best matches the data. The only significant difference between cubes CI+exp and SI+exp is the inclination of the inner disk, which was found to play a crucial role in determining the double-peaked nature of the central line profiles. Various inner disk inclinations in the range 70° - 80°, as suggested by the tilted ring models, were experimented with. All such inclinations were found to result in relatively poor matches to the observations in terms of split line profiles. Model SI+exp was finally constructed using a constant inner disk inclination of 85° out to a galactocentric radius of 140″. Figure 3.25 shows the inclination radial profile used for cube SI+exp (dash-dot curve) together with the profiles used for the purely circular models. Without this highly-inclined inner disk, the split line profiles at inner radii could not be matched. Radial velocities of order $V_{exp} \sim$ 30 km s^{-1}, together with a highly-inclined inner disk are therefore crucial in terms of the description of the central gas kinematics of NGC 2915.

Discussion

The distribution and kinematics of the H I near the centre of NGC 2915 are consistent with the simple physical scenario in which the young stellar core of the galaxy, with which the Hα emission is associated, expels the gas outwards from the centre of the disk. This process creates a central H I under-density and a radially expanding central gas component. Similar processes are observed in other nearby galaxies. As mentioned above, van Eymeren et al. (2009) detected prominent H I and Hα outflows in NGC 4816, with expansion velocities of $V_{exp} \sim$ 25 km s^{-1}

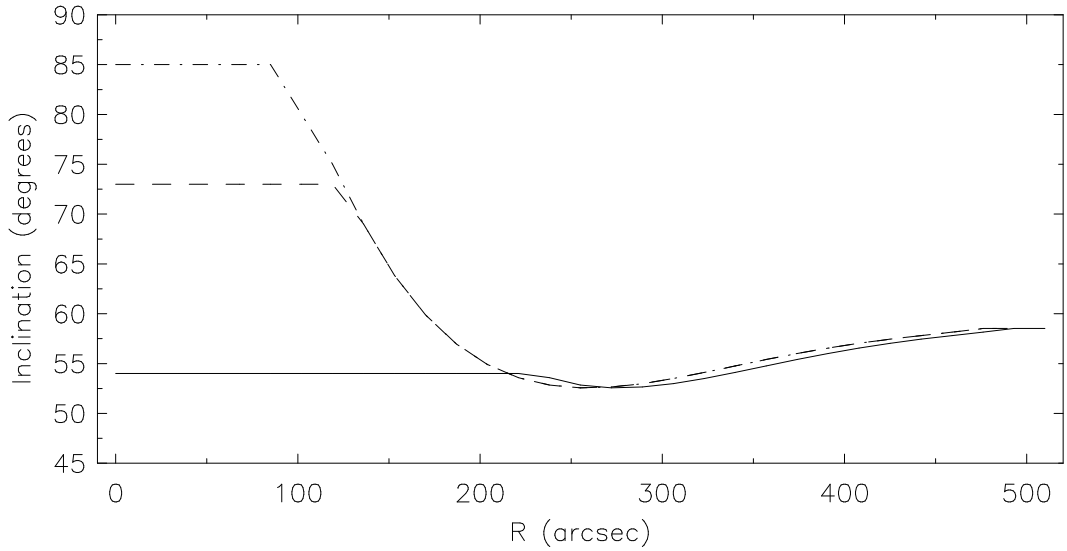

Figure 3.25: Inclination radial profiles used to generate model cubes. The solid and dash-dot curves represent the inclination radial profiles used for cubes CI+exp and SI+exp respectively. The inclination radial profile used to generate cube SI is shown as a dashed curve.

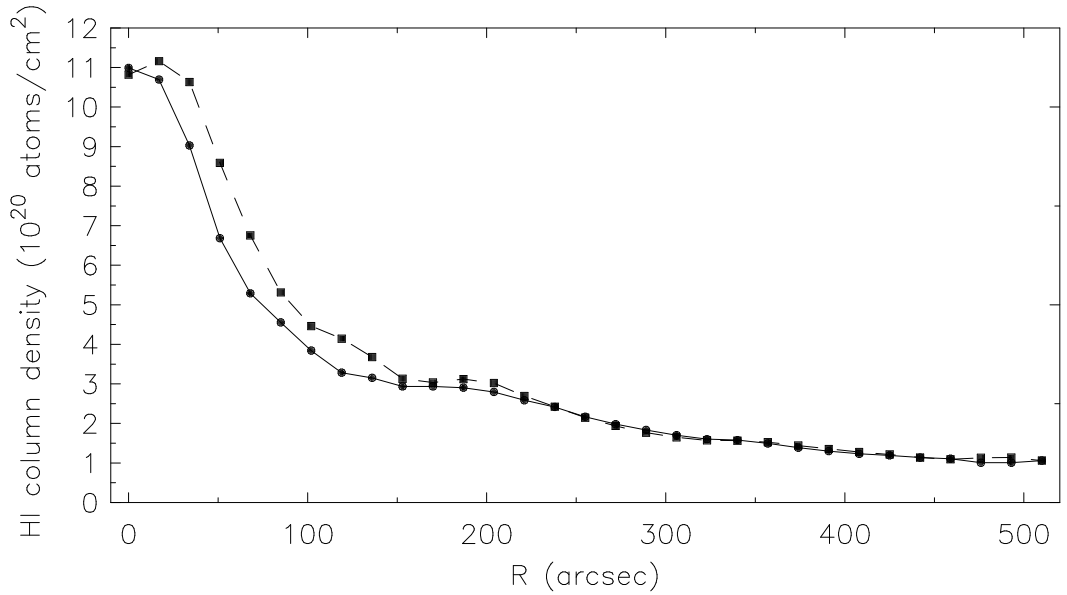

Figure 3.26: Inclination-corrected H I column density radial profiles used to construct the model cubes. All CI and SI cubes were generated using the profiles represented by the black-filled circles and squares respectively. Error bars have been omitted for the sake of clarity.

and $V_{exp} \sim 30$ km s^{-1} respectively. Such outflows can significantly effect the overall evolution of a galaxy. Star-bursts, with their associated gas expulsion processes, are indeed thought to be a possible evolutionary link between late- and early-type dwarfs. If a burst of star formation experienced by a gas-rich late-type dwarf is able to remove or at least redistribute a significant mass fraction of the ISM, star-formation could be quenched, resulting in the galaxy fading to become a red, gas-poor early-type dwarf. The redistribution of gas within a galaxy can also lead to episodic star formation activity, with the removal and subsequent replenishment of H I being associated with corresponding epochs of diminished and intensified star formation activity (e.g. Williams et al., 2010). Indeed, colour-magnitude diagrams of resolved stellar populations of nearby galaxies provide clear evidence of complex, episodic star formation histories (e.g. Monelli et al., 2003; Weisz et al., 2008).

Unclear is the reason why the inner portion of the H I disk of NGC 2915 should be so highly-inclined relative to the outer portion. It may be the case that the disk is severely warped. Numerical simulations of dissipative mergers carried out by Barnes (2002) have shown that extremely warped gas disks can result from the merging process. Barnes (2002) showed further that, even in the case of unequal mass mergers, extremely warped gas disk merger remnants can result. A warped gas structure can also develop in the case that gas with a slewed angular momentum accretes from the inter-galactic medium onto the inner portions of a galaxy's gas disk (Bournaud & Combes, 2003). The degree of the warping will depend on the ratio of the angular momentum of the in-falling gas to that of the disk, and is a function of the reorientation of the net angular momentum vector of the disk (Ostriker & Binney, 1989). Although direct evidence for the above-mentioned scenarios is lacking in the case of NGC 2915, they cannot be ruled out as possible causes of a highly-warped inner H I disk. A good example of a galaxy with an extremely warped disk is the "Spindle" galaxy (NGC 2685). Until recently, this system was generally regarded as being a two-ringed polar galaxy, consisting of two kinematically distinct disks aligned almost perpendicular to one another. Józsa et al. (2009) recently showed, however, that NGC 2685 forms a coherent, extremely warped disk which creates the appearance of two mutually inclined regions.

3.7.4 Fate of the expanding gas

Having established that the central H I kinematics of NGC 2915 are consistent with those of a radially-expanding gas component, the eventual fate of the expanding gas can be speculated on. Will the central gas eventually stop expanding and fall back towards the centre, thereby fuelling a subsequent burst of star formation, or will it escape into the inter-galactic medium?

Several authors have studied gas outflows in nearby dwarf galaxies (see Meurer et al., 1992;

Martin, 1996, for NGC 1705 and I Zw 18 respectively). In VVI Zw403, Papaderos et al. (1994) detected extended X-ray plumes which they interpreted as the outflow of hot gas. Mac Low & Ferrara (1999) modelled the effects of repeated supernova explosions from starbursts in dwarf galaxies on the ISM, taking into account the gravitational potential of their dark matter halos. They found that the mass ejection efficiency is very low in galaxies with a total mass $\gtrsim 10^7$ $M_\odot$. More specifically, they found that in galaxies more massive than $\sim 10^6$ $M_\odot$, the fraction of mass that is lost in a galactic blowout is as little as 10^{-6}. For reference, the total mass for NGC 2915 is $\sim 10^{10}$ $M_\odot$. Importantly, Mac Low & Ferrara (1999) showed that metal-enriched material from stellar winds and supernova ejecta is accelerated to velocities higher than the escape speed of the galaxy more easily than the gas, especially in the case of low-mass systems. This result, together with the fact that dwarf galaxies dominate the cosmic scenery in terms of number density (Springel et al., 2005; Sandage et al., 1985; Mateo, 1998), implies that dwarf galaxies play a crucial role in regulating the metallicity of the inter-galactic medium.

The gravitational potential of NGC 2915 is dominated by its dark matter halo. Treating the density profile of the dark matter halo as a pseudo iso-thermal sphere, the escape velocity of the system is given by

$$V_{esc}(R) = \sqrt{2V_c^2 \left(1 + \ln\left[\frac{R_{max}}{R}\right]\right)}, \tag{3.19}$$

where V_c is the asymptotic value of the circular rotation velocity at large radii, and R_{max} is the maximum radius of the pseudo-isothermal sphere. Based on the tilted ring model SI rotation curve, we adopt $V_c \sim 86$ km s^{-1} and $R_{max} \sim 8.7$ kpc. Using these values, an escape velocity radial profile was determined using Eqn. 3.19. For the sake of brevity, it is simply mentioned that the escape velocities at all radii are $\gtrsim 175$ km s^{-1}, much larger than the inferred expansion velocities of $V_{exp} \sim 30$ km s^{-1}. Furthermore, the dark matter halo of NGC 2915 is undoubtedly larger than the radial extent of the gas disk, implying that these escape velocities are lower limits. The expanding gas in the centre of NGC 2915 therefore stands very little chance of escaping into the inter-galactic medium, and is consistent with a central outflow rather than a galactic blow out or wind. Assuming an outflow time-scale of ~ 100 Myr, the average mass redistribution rate is ~ 0.021 $M_\odot$ yr^{-1}, roughly consistent with the estimated total star formation rate for the system, $SFR_{tot} \sim 0.028$ $M_\odot$ yr^{-1} (Section 3.7.2). Despite being unable to escape the gravitational potential of the galaxy, the redistributed gas will significantly affect the future star-forming properties of NGC 2915's stellar disk.

3.8 Chapter summary

The main focus of this chapter has been the H I dynamics of NGC 2915. A tilted ring model was fitted to the H I velocity field. The best-fitting model is one in which the H I disk is severely warped, with the inner and outer disks inclined at $i \sim 70$ - $75\ ^\circ$ and $i \sim 55^\circ$ respectively. This result is, however, made uncertain by the non-Gaussian line profiles near the centre of the galaxy. A model with an almost constant inclination of $i \sim 55^\circ$ for the entire H I disk was therefore also fitted. Both models yielded a rotation curve typical of a late-type spiral with $V(R) \propto R$ rotation out to $R \sim 150''$ and constant velocity thereafter. Rotation curves separately derived for the approaching and receding sides of the galaxy differ significantly within their steeply rising portions, providing evidence that NGC 2915 is a kinematically lopsided galaxy.

Mass modeling results show that the observed circular rotation curves cannot be accounted for by the stellar or gas disks of NGC 2915. Using the observed rotation curves as mass model inputs, the galaxy is found to be dark-matter-dominated at nearly all radii with the stellar disk unable to account for the $V(R) \propto R$ portion of the rotation curve. The best-fitting mass model is one in which the stellar disk does not contribute to the observed rotation curve and in which the inferred dark matter halo is parameterised as a pseudo-isothermal sphere. This model has a central core density of $\rho_0 = 0.17 \pm 0.03$ $M_\odot$ pc^{-3} and a core radius of $r_c = 0.9 \pm 0.1$ kpc. The non-circular gas motions at inner radii lead to uncertainties in the fitted dark matter halo parameters. These, together with the fact that neither DM halo parameterisation allows for an accurate match of the observed rotation curve at inner radii, do not allow a particular DM halo parameterisation to be confidently ruled out or confirmed. Further observations and modeling are required to more accurately determine the inner rotation curve of NGC 2915 and to therefore more confidently discriminate between various parameterisations of the DM halo. It is clear, however, that NGC 2915 has a very dense and compact dark matter core. At the last measured point on the rotation curve, this galaxy has a total mass to B-band light ratio of $M_{tot}/L_B \sim 140$ $M_\odot/L_\odot$, almost twice that of the upper limit placed by Meurer et al. (1996), thereby making it one of the most dark-matter-dominated galaxies known.

The results of an harmonic decomposition of the third-order Gauss-Hermite velocity field have been interpreted in the context of non-axisymmetric perturbations to the system's gravitational potential. The method allows the system's gravitational potential to be probed out to radii far beyond the edge of the stellar disk into the regions of the galaxy that are completely dark-matter-dominated. Evidence is found for an $m = 2$ term in the H I velocity field which can be linked to the spiral structure present within the H I disk. However, the $m = 2$ term is also indicative of a tri-axial dark matter halo. Using the s_1 and s_3 harmonics to estimate $\epsilon_{pot} \sin(2\varphi_2)$ yields an error-weighted mean value -0.41. This estimate of $\epsilon_{pot} \sin(2\varphi_2)$ is at least a factor

of 10 higher than corresponding estimates for other galaxies. While the results suggest the dark matter halo of NGC 2915 to be non-spherical, the intrinsic elongation cannot be unambiguously determined in the presence of the $m = 2$ spiral density wave perturbation. An oval distortion of the potential need not be incompatible with the observed H I spiral structure, it could indeed drive the formation of a bar as well as the spiral structure within the disk.

The possibility of elliptical streaming in a stationary bar-like potential also tarnishes the otherwise good evidence that is provided by the strong and weak s_1 and s_3 terms respectively for an axisymmetric radial outflow of the order of $5 - 17$ km s^{-1}. Such outflows, $\sim 6 - 20\%$ of the outer H I disk rotation velocity, do not provide intuitive insight into the formation history of the H I disk if it is thought of as having accumulated from the infall of pristine gas from the surrounding inter-galactic medium. It is possible, however, that some material is being re-distributed into the outer disk in order to conserve angular momentum as other material flows inwards along a bar. Such a scenario is consistent with our kinematic evidence for radial outflows. A clear understanding of the formation history of NGC 2915's extended H I disk is therefore still elusive. The limitation on the search for indirect evidence of radial flows set by the inherent non-axisymmetry of the galaxy gives rise to the need for deep H I observations of NGC 2915's outer disk. Such observations would allow for the direct detection of possible cold gas accretion processes.

Finally, the central H I dynamics of NGC 2915 have been modelled and shown to be consistent with those of a highly-inclined inner rotating disk. More specifically, radial expansion velocities of ~ 30 km s^{-1} are required for the models to consistently match the double-peaked and skewed H I line profiles observed near the very centre of the galaxy. The central H I energetics are shown to be consistent with the estimated energy output of the young stellar core of NGC 2915. This result lends itself to the scenario in which the galaxy's central gas reservoir is being depleted as the neutral gas is expelled outwards. Due to the galaxy's dominant dark matter component, however, the expanding central gas stands little chance of escaping into and enriching the surrounding inter-galactic medium.

Chapter 4

An HI study of NGC 1705

H I synthesis observations of NGC 1705 were carried out with the Australia Telescope Compact Array. These data serve as the highest resolution, most sensitive H I observations available for the galaxy. This chapter is dedicated to presenting the main NGC 1705 H I data products as well as the results of various detailed kinematic analyses. A brief introduction to NGC 1705 is followed by details of the data acquisition and reduction processes. Thereafter the various H I data products are presented together with detailed descriptions of the global profile, channel maps and moment maps. A rotation curve is determined for the galaxy and is used as mass-modelling input in order to determine the detailed distribution of mass within the dark matter halo.

4.1 Introduction to NGC 1705

4.1.1 Optical properties

The second galaxy that is dealt with in this thesis is NGC 1705. This dwarf galaxy is famous for hosting one of the most powerful starbursts (relative to its mass) in the local universe. It is generally referred to as a blue compact dwarf, yet its morphological classification in the 'Third Reference Catalogue of Bright Galaxies' (de Vaucouleurs et al., 1991) is type SA0-pec. Tosi et al. (2001), using the HST to resolve the brightest red giant stars in the galaxy, estimate the distance to be $D \sim 5.1$ Mpc. The celestial coordinates of NGC 1705 are $\alpha_{2000} = 04^{h}\ 54^{m}\ 13.50^{s}$, $\delta_{2000} = -53^{\circ}\ 21'\ 39.80''$ (Skrutskie et al., 2006). The system has a B-band absolute magnitude of $M_B = -15.6 \pm 0.2$ (Marlowe et al., 1999). A large aperture spectrum of the galaxy taken

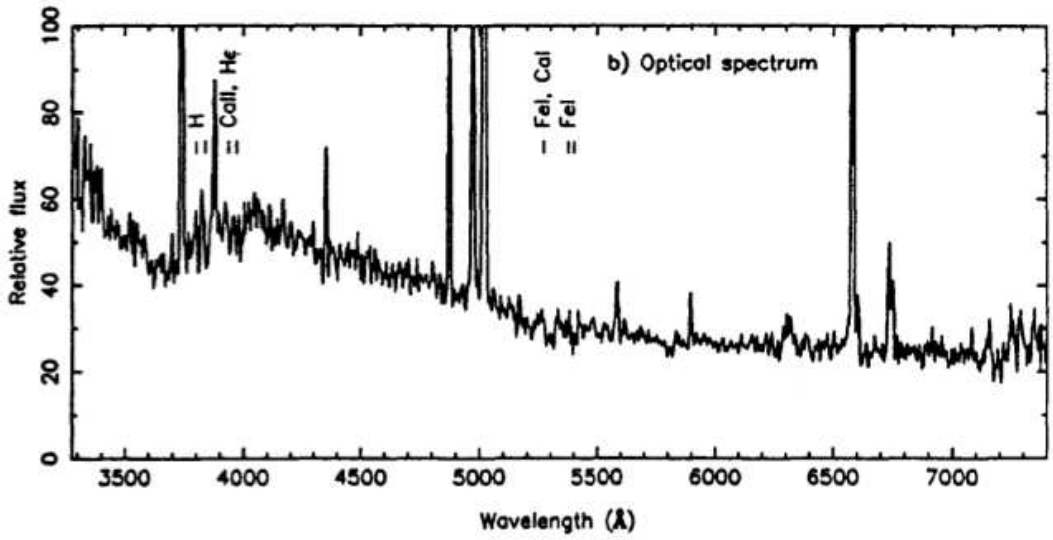

Figure 4.1: Optical large aperture spectrum of a portion of the high surface brightness stellar population of NGC 1705, taken from Meurer et al. (1992). Flux units are 10^{-14} erg cm^{-2} s^{-1}. Note the prominent emission lines, e.g. OII (3728 Å), Hβ (4862 Å), OIII (4960, 5008 Å), Hα (6564 Å) and SII (6718 Å).

from Meurer et al. (1992), highlighting its extreme star-bursting nature is shown in Fig. 4.1. A clear excess in continuum flux is noticeable at the blue end of the spectrum with several strong emission lines superimposed on the continuum. Meurer et al. (1992) identified two stellar populations in NGC 1705 which they refer to as the high and low surface brightness populations.

The galaxy's intense star formation activity is concentrated in the central high surface brightness population and is driven mainly by a powerful super star cluster, NGC 1705-1. This star cluster, first described by Sandage (1978) and later reported on in detail by Melnick et al. (1985), contributes almost half of the total ultra-violet luminosity of the galaxy (Meurer et al., 1998). NGC 1705-1 is one of the most luminous star clusters in the nearby universe. Assuming a distance of 6.2 Mpc, Meurer et al. (1995) used the HST Faint Object Camera to determine an absolute magnitude of $M_{220} = -16.6$[†] for NGC 1705-1. An HST image of the stellar core of NGC 1705 taken from the Hubble Heritage Gallery is shown in Fig. 4.2. In this image NGC 1705-1 is clearly discernible as a compact core near the centre of the galaxy. The central super star cluster is the main evolutionary driver of NGC 1705, powering a galactic-scale outflow that is stripping the galaxy of its inter-stellar medium. Meurer et al. (1998) estimated a large mass loss rate of $\sim 0.17 - 1.7$ M$_\odot$ yr^{-1} from the core of NGC 1705. A sustained outflow of this magnitude could

[†]Note that the HST Faint Object Camera filters are not the standard *UBVRI* filters. NGC 1705-1 is hence not more luminous than the entire galaxy.

Figure 4.2: HST multi-colour optical image of NGC 1705 taken from the Hubble Heritage Gallery. The super star cluster, made primarily of young blue stars, appears as a compact core near the centre of the image.

quench the star formation activity and will play a significant role in determining the evolutionary path of the galaxy.

NGC 1705 is not a young galaxy. Annibali et al. (2003) found evidence for star formation activity that commenced at least 5 Gyr ago. These authors also showed the star formation history of NGC 1705 to be very complex, confirming the existence of a recent burst of star formation between 10 and 15 Myr ago. Consistent with the HST observations of NGC 1705-1, Annibali et al. (2003) found the young and intermediate-aged stars to be concentrated near the very centre of the galaxy.

NGC 1705 is located in low-density environment. No interactions with nearby companion galaxies are seen in the ATCA H I data cubes that are presented in this thesis. A search of the NASA/IPAC Extragalactic data base yields no obvious nearby galaxy neighbours within 5° (445 kpc for a distance of $D = 5.1$ Mpc). It seems unlikely that a nearby external system can be the starburst trigger. Due to the intense star formation activity at its core, the central gas reservoir will be depleted on time-scales much smaller than the Hubble time.

4.1.2 HI and dark matter properties

Similar to NGC 2915, the optical core of NGC 1705 is embedded in a large H I disk, albeit not as extended as that of NGC 2915. Meurer et al. (1998) are the only group of investigators to have carried out synthesis observations of NGC 1705's H I disk. A contour plot of the total H I intensity measured by these authors is shown in Fig. 4.3. Meurer et al. (1998) propose that the H I feature extending from the centre of the galaxy in a north-westerly direction results from a galactic wind blowout that is powered by the central super star cluster. These authors claim that the gravitational potential of NGC 1705 is not deep enough to contain the outflow, and that the out flowing gas will escape into the inter-galactic medium. Meurer et al. (1998) generated radio continuum maps for NGC 1705. Coinciding with the position and orientation of the optical core of the galaxy is a strong continuum source of power $P_{1.4\ GHz} = 3.5 \times 10^{19}$ W Hz^{-1}. A grey-scale version of the 1.4 GHz radio continuum image from Meurer et al. (1998) is reproduced in Fig. 4.3. The position of NGC 1705-1 is marked in this radio continuum image with an open star.

The dynamics of NGC 1705's outer H I disk are regular enough to use as a tracer of the galactic potential. The dark matter properties of the galaxy were first modelled by Meurer et al. (1998). The galaxy was shown to be dark-matter-dominated at all radii with dark matter halo properties comparable to those of NGC 2915, the only other mass-modelled blue compact dwarf at the time.

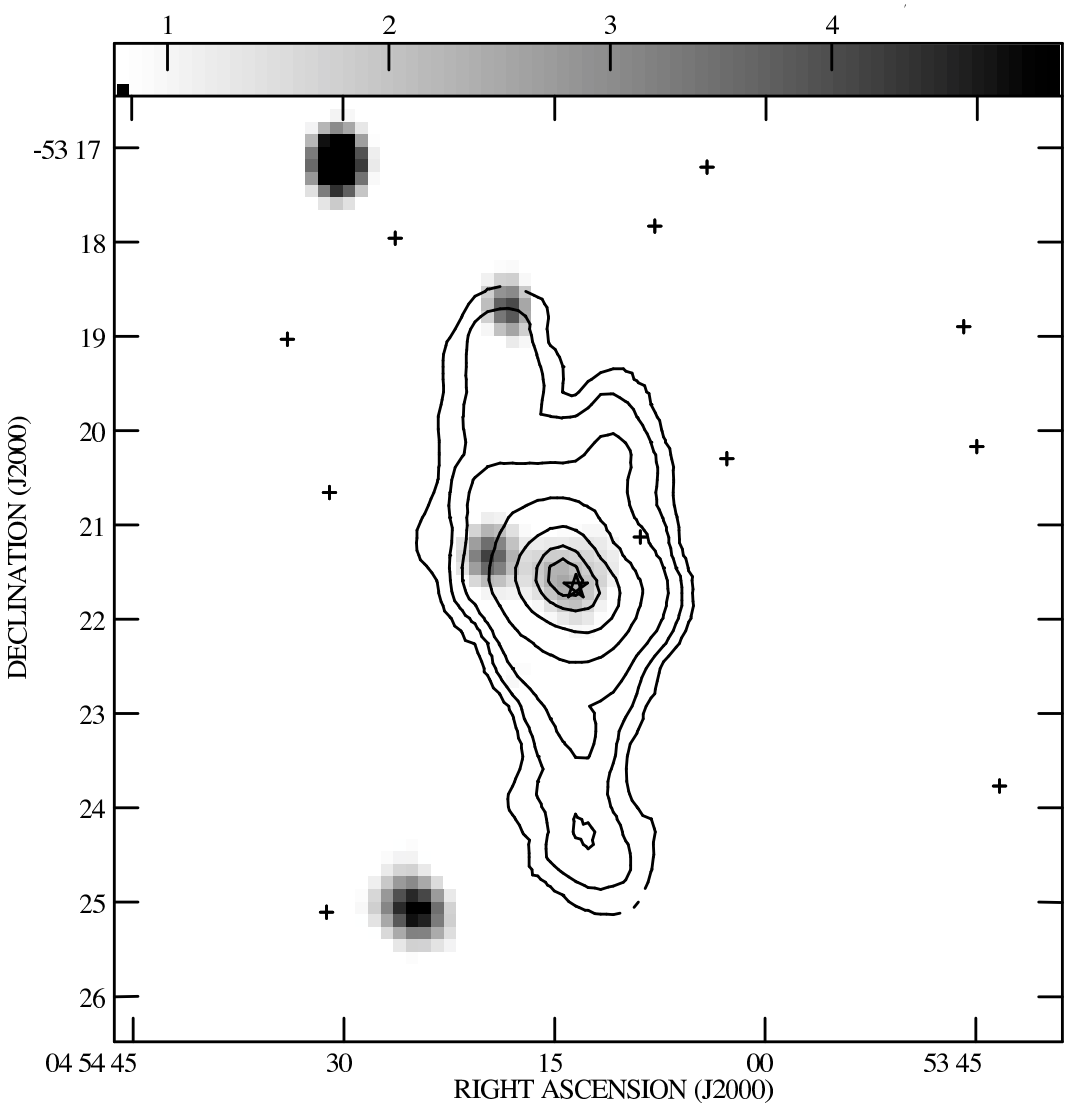

Figure 4.3: Greyscale 1.4 GHz radio continuum image of NGC 1705, taken from Meurer et al. (1998). The contours overlaid are those for the H I total intensity map. The continuum flux density in units of mJy beam^{-1} is specified by the bar at the top. Contour levels correspond to 2, 5, 10, 25, 50, 75 and 90 percent of the peak H I flux density of 2800 Jy beam^{-1} m s^{-1}. The crosses indicate the positions of field stars, and the position of NGC 1705-1 is indicated by a star. The three continuum sources furthest from the centre of the galaxy are background sources. Note that in this figure north is directly upwards, unlike Fig. 4.2.

4.2 HI aperture synthesis observations

NGC 1705 was observed between 22 November 2006 and 17 March 2007 with six different ATCA configurations using all six antennas (project number C1629). Table 4.1 lists all of the information specific to each of the observing runs. A single run consisted of a primary calibrator observation, regular secondary calibrator observations and source observations. Most runs were approximately 11 hours long. While a single run was carried out in each of the EW352, 750D, and 1.5B antenna configurations, four runs were carried out using the 6A configuration in order to boost high-resolution sensitivity to low surface brightness emission. No mosaicking was required and the telescope pointing centres were set to $\alpha_{2000} = 04^{h}\ 54^{m}\ 13.50^{s}$, δ_{2000} = -53° 21′ 39.80″, the optical centre of NGC 1705. The correlator was set to use 512 channels with a bandwidth of 8 MHz centered at 1418 MHz. The resulting velocity range is -126 km s^{-1} to 1561 km s^{-1} with an approximate channel spacing of 3.2 km s^{-1}. PKS B1934-630 and PKS B0407-658 were used as primary and secondary calibrators respectively for all runs. The typical calibrated flux densities of these sources (columns 7 and 9 of Table. 4.1) agree well with their average flux density values of 14.95 Jy beam^{-1} for PKS B1934-638 and 15.50 Jy beam^{-1} for PKS B0407-658, as stated on the ATCA website[1].

4.3 HI data reduction

Data cubes

Using the MIRIAD software package, the raw *uv* data for NGC 1705 were reduced in an identical manner to those of NGC 2915 in order to produce calibrated, deconvolved H I data cubes. A detailed description of the entire reduction process is not repeated here, and the reader is referred to Sec. 2.3 of Chapter 2 for specific details. As an example of the small phase-amplitude scatter in the primary calibrator *uv* data, the calibrated PKS B1934-638 data from the EW352 run have an r.m.s. scatter of $\sim$ 0.2 Jy beam^{-1} about the mean *uv* amplitude. The scatter about 0° of the *uv* phases is $\sim 1°$. Typical scaling factors were $\sim$ 0.94 when using the GPBOOT task to scale the secondary calibrator flux measurements based on the primary calibrator gain corrections.

The calibrated source data were continuum-subtracted by fitting a first order polynomial to the line-free channels which, for the observations of NGC 1705, were channels 50 – 150 and 350 – 460. Using the INVERT task, two naturally-weighted image cubes were produced from these continuum-subtracted data. In order to improve the detection of extended low-level emission,

[1] http://www.narrabri.atnf.csiro.au/

Table 4.1: Summary of NGC 1705 observing setups

1 Conf.	2 Date (yy-mm-dd)	3 Start (hh-mm-ss)	4 End (hh-mm-ss)	5 Dur. (hrs)	6 Amp. Cal	7 Flux (Jy)	8 Phase Cal.	9 Flux (Jy)
EW352	2006-10-22	11:18:27	22:59:16	11.68	1934-638	14.8 ± 0.41	0407-658	15.5 ± 0.21
750D	2007-03-17	05:24:35	12:51:46	7.59	1934-638	14.9 ± 0.35	0407-658	14.9 ± 0.19
1.5B	2006-11-24	07:42:00	18:57:17	11.25	1934-638	14.8 ± 0.13	0407-658	14.5 ± 0.30
1.5B	2006-11-25	07:27:17	18:57:15	11.50	1934-638	14.8 ± 0.12	0407-658	14.6 ± 0.28
6A	2007-02-13	02:11:55	14:11:42	12.00	1934-638	14.8 ± 0.42	0407-658	14.6 ± 0.38
6A	2007-02-14	02:08:38	12:34:42	10.43	1934-638	14.9 ± 0.30	0407-658	14.7 ± 0.31
6A	2007-02-17	01:29:35	11:05:57	9.61	1934-638	14.8 ± 0.33	0407-658	14.8 ± 0.45
6A	2007-02-18	01:26:25	13:59:01	12.54	1934-638	14.8 ± 0.40	0407-658	14.7 ± 0.42

Comments on columns: Column 1: ATCA configuration used; Column 2: start date of observation (UT); Column 3/4: start/end of observations (UT); Column 5: time on source; Column 6/7: name of amplitude calibrator and its flux density; Column 8/9: name of phase calibrator and its flux density.

a Gaussian taper of 15″ was applied to one of the visibility data sets using the INVERT task. Deconvolution of the resulting dirty images was carried out using a Steer CLEAN algorithm (Steer et al., 1984) as outlined in detail in Sec. 2.3.4 of Chapter 2. Each channel of the dirty image was CLEANed down to 2.5 times the typical r.m.s. of the flux in a line-free channel or for 50 000 iterations, whichever condition was met first in practice. After the deconvolution process, each of the CLEAN components was convolved with a Gaussian approximation of the synthesised beam. These Gaussians had full widths at half maximum of $16.7'' \times 14.5''$ and $33.2'' \times 28.6''$ for the two final H I data cubes, the larger beam corresponding to the Gaussian-tapered H I data cube. These two cubes are henceforth referred to as the high and low resolution H I data cubes. The spectral resolution of the cubes is $dV = 3.48$ km s^{-1} and $dV = 3.28$ km s^{-1} for the high- and low-resolution versions respectively with no Hanning smoothing having been applied to either cube. The small difference in spectral resolution of the two cubes is of no physical relevance. For each of the final H I data cubes, the noise in a line-free channel is Gaussian distributed. The high-resolution data have a standard deviation of 0.7 mJy beam^{-1} (Fig. 4.4, upper panel) while the low-resolution data have a standard deviation of $\sigma \sim 1.1$ mJy beam^{-1} (Fig. 4.4, lower

Table 4.2: Summary of NGC 1705 H I data cube properties

Quantity	High resolution value	Low resolution value	Units
image size	$200 \times 200 \times 61$	$300 \times 300 \times 61$	pixels
pixel size	$2.5 \times 2.5 \times 3.48$	$2.5 \times 2.5 \times 3.28$	arcsec×arcsec×km s^{-1}
beam	16.7×14.5	33.2×28.6	arcsec×arcsec
noise/pixel	0.7	1.1	mJy beam^{-1}

panel). The main properties of each data cube are summarised in Table 4.2.

Moment maps

GIPSY was used to smooth each of the H I data cubes down to a resolution of $40'' \times 40''$ and remove the noise from each channel. These smoothed, blotted cubes were applied as masks to their corresponding full-resolution cubes. From each of the masked H I data cubes an H I total intensity map, H I velocity field and a 2nd-order H I moment map was constructed from the zeroth, first and second-order moments of the H I line profiles. A dimensionless signal-to-noise map was then used to mask pixels in the outer regions of each map that had a corresponding signal to noise ratio in the range $2.75 < \mathrm{S/N} < 3.25$ (see Sec. 2.3.5 of Chapter 2 for a full description of the procedure as implemented for NGC 2915).

In addition to the intensity-weighted-mean H I velocity mentioned above, a second version of the H I velocity field was constructed by fitting third-order Gauss-Hermite polynomials to the line profiles of the high-resolution H I data cube. Three filters were used simultaneously when fitting the profiles: (1) profiles with fitted peak fluxes below 2.5σ were rejected; (2) profiles with a fitted line width less than the channel width were excluded; and (3) fitted profile peaks had to be within the velocity range of the data cube.

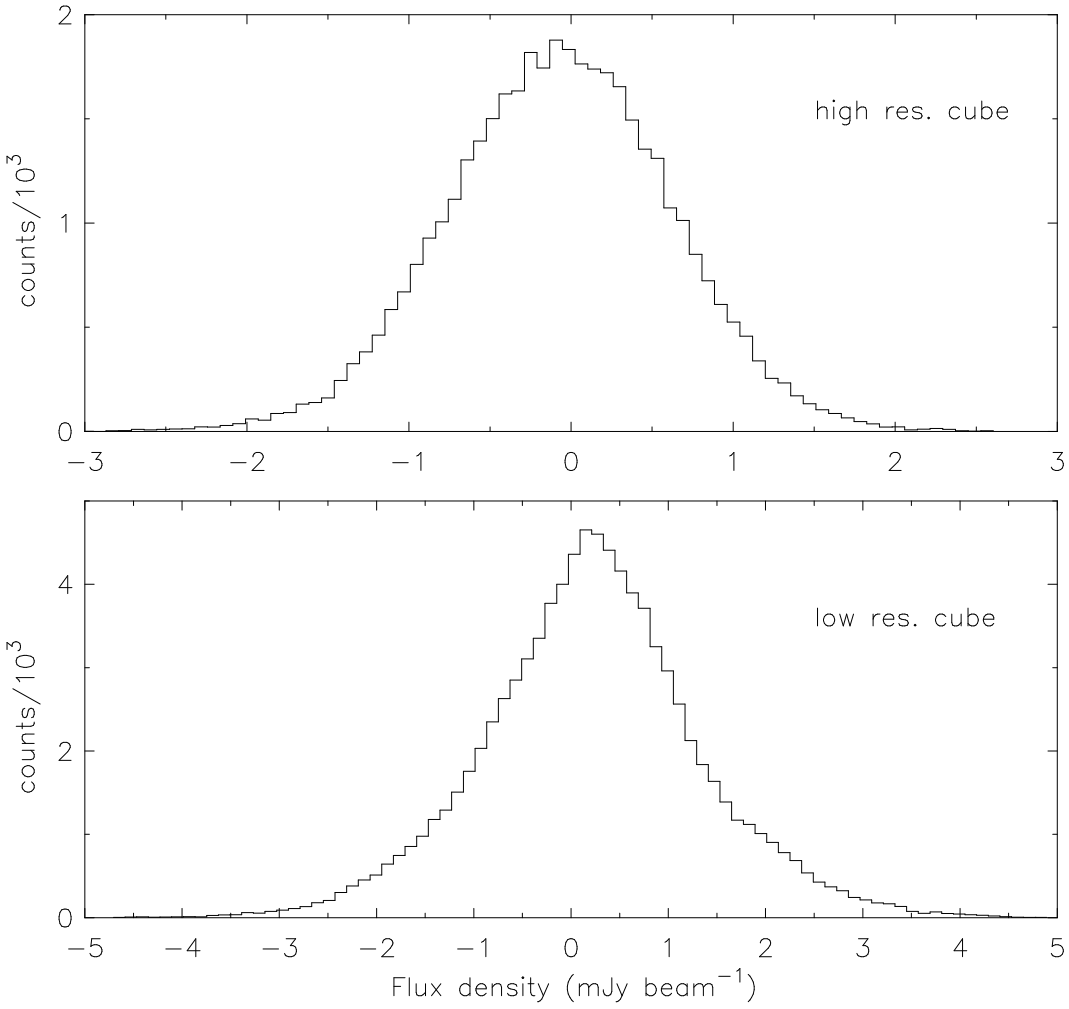

Figure 4.4: NGC 1705 flux density distributions for a single channel containing no galaxy emission. The Gaussian-distributed data have a mean of -3.4×10^{-5} mJy beam^{-1} and a standard deviation of 0.7 mJy beam^{-1} for the high-resolution cube. The low-resolution data have a mean of -0.02 mJy beam^{-1} and a standard deviation of $\sigma \sim 1.1$ mJy beam^{-1}.

4.4 HI data products

4.4.1 Channel maps

Grey-scale representations with contours overlaid of the high- and low-resolution H I channel maps are presented in Figs. 4.5 and 4.6 respectively. Although not plainly obvious, the emission does exhibit the pattern of a rotating disk, with the southern and the northern parts of the galaxy being blue- and red-shifted respectively. The high-resolution maps show small-scale H I concentrations separated by $\sim 30''$ near the centre of the H I disk, with fainter emission surrounding them. Clearly visible in the channel maps with heliocentric velocity 631.09 km s^{-1} $\lesssim$ V_{hel} $\lesssim$ 670.55 km s^{-1} is a drawn out H I feature approximately $\sim 100''$ in angular extent, emanating from the centrally dense portion of the galaxy in a north-westerly direction.

4.4.2 Global profile

Global H I profiles, generated by summing the H I emission in each velocity channel of the blotted H I data cubes, are presented in Fig. 4.7. The almost Gaussian-like shapes of the global profiles are in contrast to the double-horned global H I profile of NGC 2915. The H I intensity maps of Meurer et al. (1998) show the angular extent of NGC 1705's H I disk to be $\lesssim 10'$. The shortest baseline used for the H I observations was 31 m (as part of the EW352 antenna configuration), implying that the observations are less sensitive to H I structures larger than $\sim 23'$. The amount of H I missed in the global H I profiles is thus expected to be small. In Fig. 4.7 the global H I profiles are compared against the HIPASS global H I profile from Koribalski et al. (2004) for which the amount of missed flux should be very little. Our ATCA spectrum for NGC 1705 lies above the HIPASS spectrum due to the fact that all HIPASS-detected sources were treated as being unresolved, hence having some of the emission from their outskirts being incorrectly subtracted.

Profile widths for the high-resolution global H I profile were calculated as the differences between the high and low velocities of the galaxy at 20% and 50% of the peak flux density ($V_{high}^{20\%}$, $V_{low}^{20\%}$, $V_{high}^{50\%}$, $V_{low}^{50\%}$ respectively). The profile widths were not corrected for inclination. Two systemic velocity estimates were determined using the high-resolution global H I profile: the first from the midpoint of the two velocities at the 50% level in the global H I profile, and the second from the equation

$$V_{sys} = 0.25 \times (V_{high}^{20\%} + V_{low}^{20\%} + V_{high}^{50\%} + V_{low}^{50\%}). \quad (4.1)$$

Finally, for each global H I profile, the total H I mass was calculated as

$$M_{HI} = 2.36 \times 10^5 \times D^2 \times \int F dV, \quad (4.2)$$

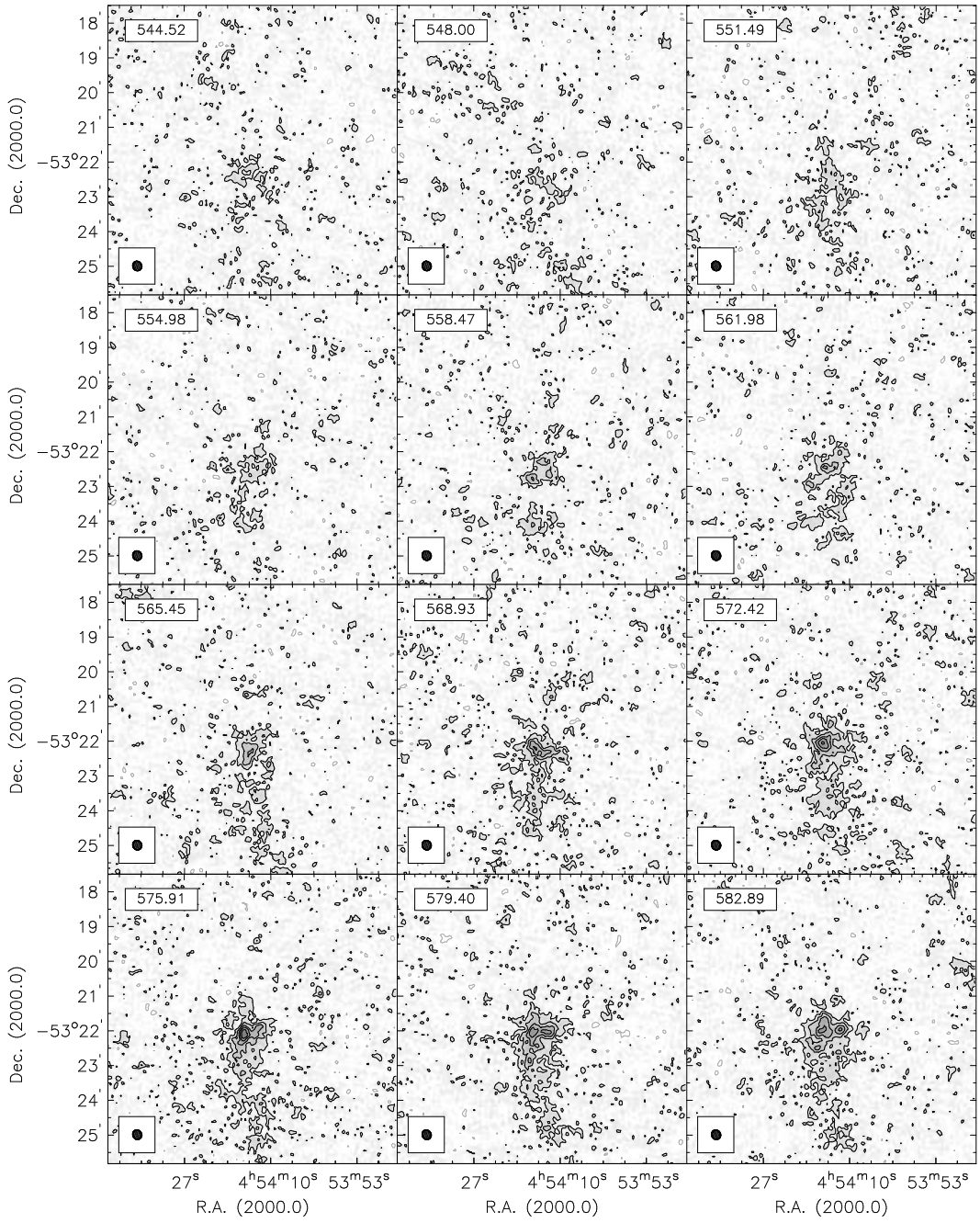

Figure 4.5: Channel maps of high-resolution NGC 1705 H I data cube. The heliocentric radial velocity (km s^{-1}) of each channel is shown in the upper left corner. The half-power-beam-width is shown in the bottom left corner. Grayscale range is from -0.7 mJy $beam^{-1}$ to 21.0 mJy $beam^{-1}$. Contour levels are -0.7 mJy $beam^{-1}$ (grey) and $1.4 - 21.0$ mJy $beam^{-1}$ in steps of 0.7 mJy $beam^{-1}$ (black). The r.m.s. noise in a channel is ~ 0.7 mJy $beam^{-1}$.

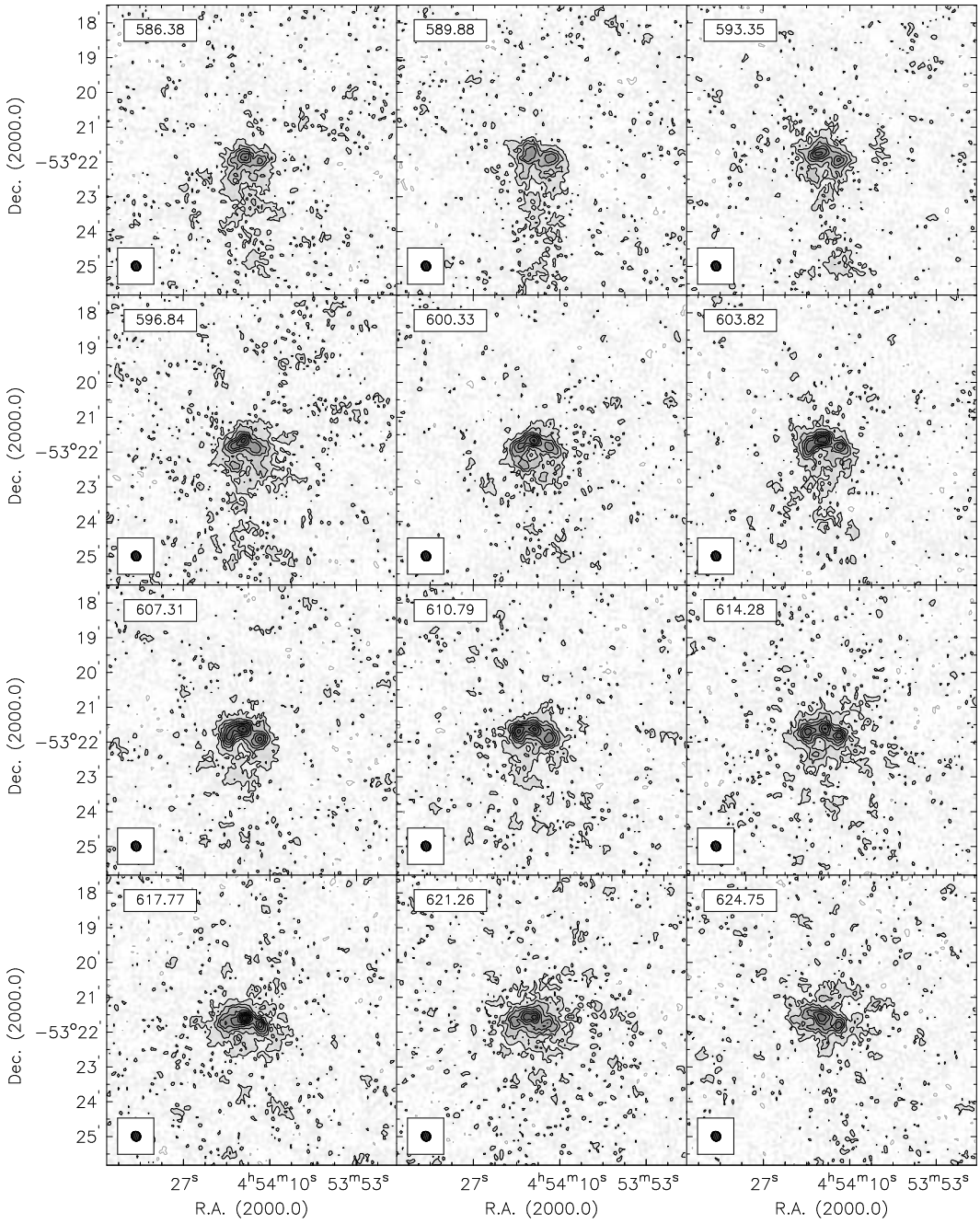

Figure 4.5: Continued.

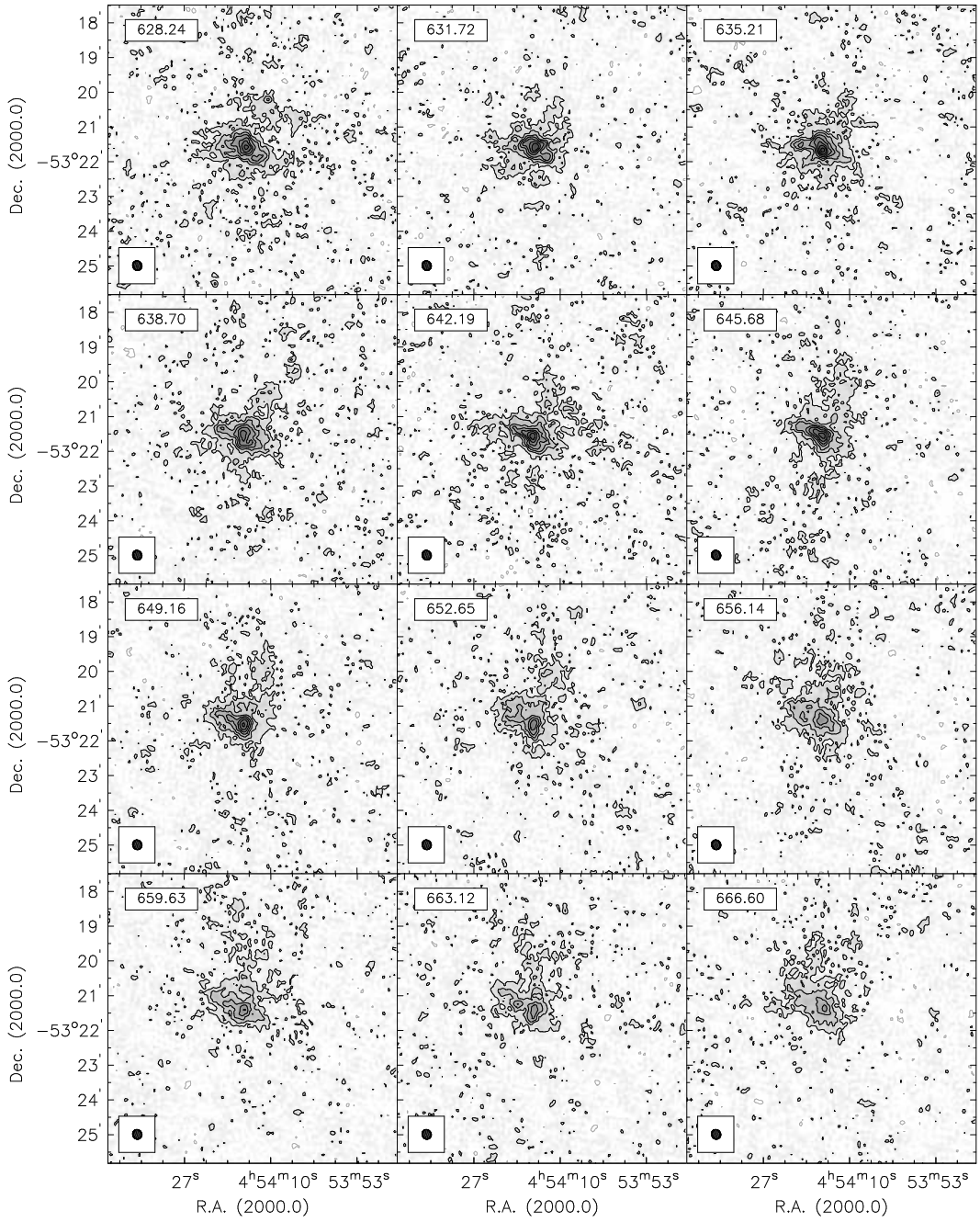

Figure 4.5: Continued.

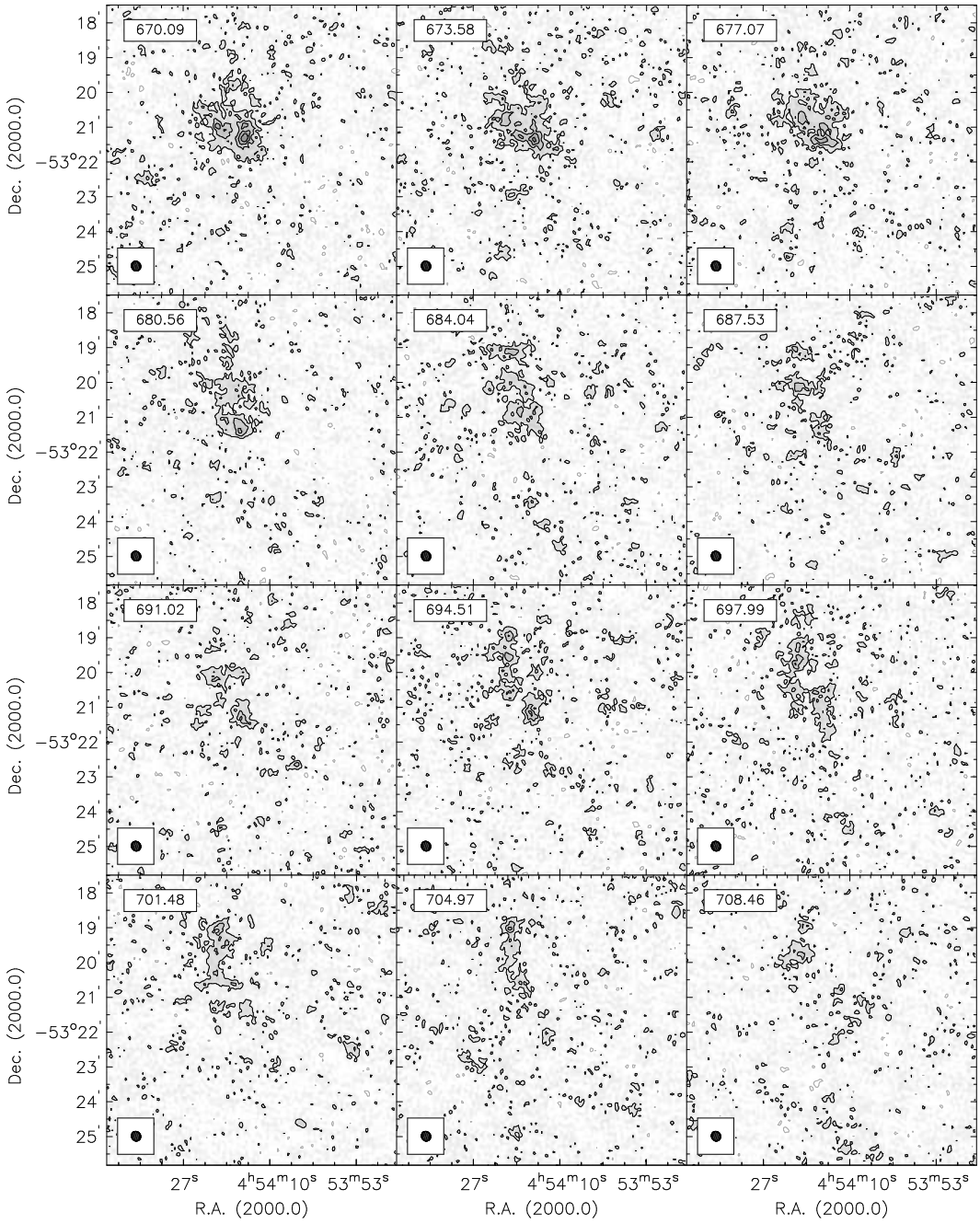

Figure 4.5: Continued.

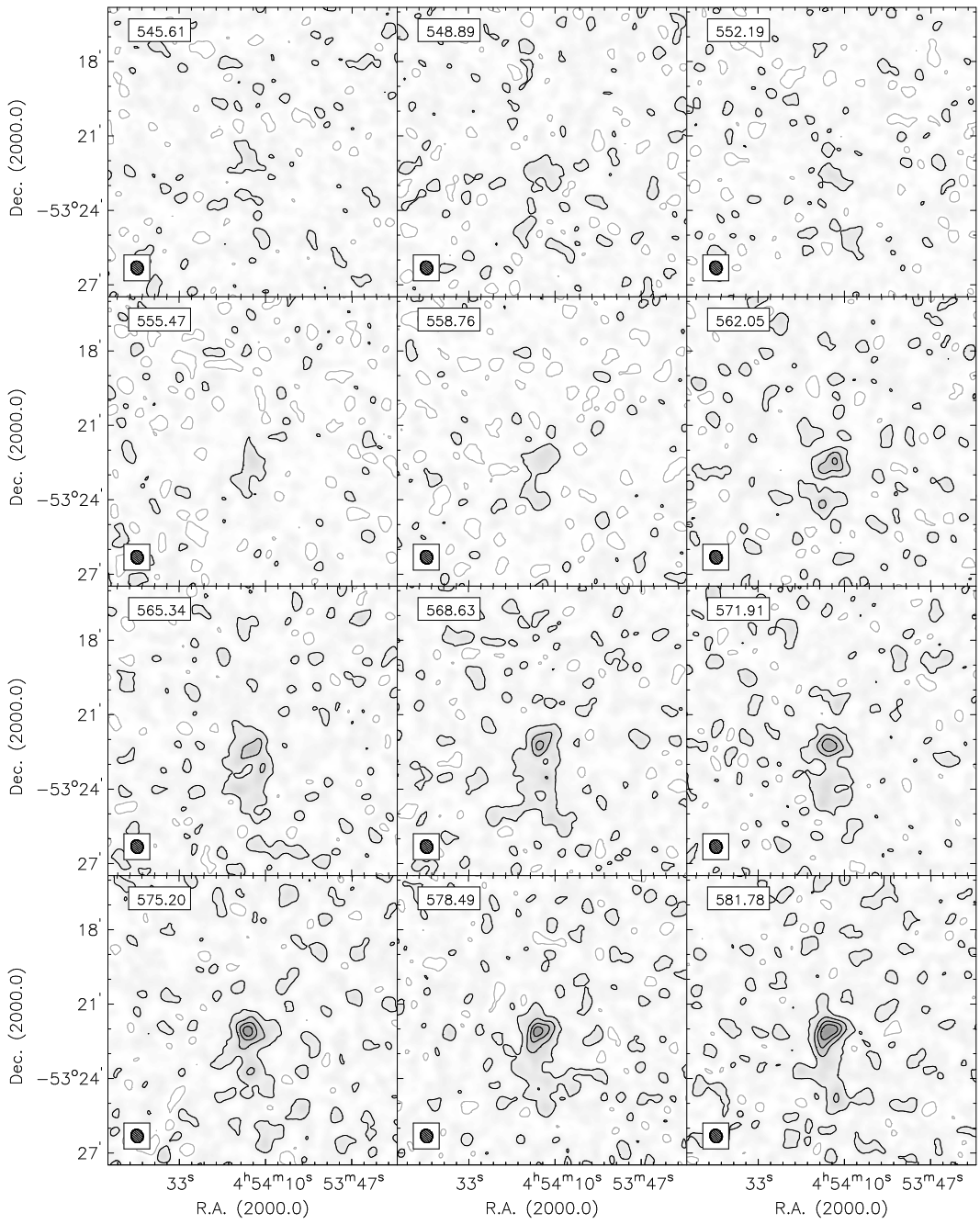

Figure 4.6: Channel maps of low-resolution NGC 1705 H I data cube. The heliocentric radial velocity (km s^{-1}) of each channel is shown in the upper left corner. The half-power-beam-width is show n in the bottom left corner. Grayscale range is from -1.1 mJy $beam^{-1}$ to 50.0 mJy $beam^{-1}$. Contour levels are -1.8 mJy $beam^{-1}$ (grey) and $1.8 - 35.0$ mJy $beam^{-1}$ in steps of 4.4 mJy $beam^{-1}$ (black). The r.m.s. noise in a channel is $\sim$ 1.1 mJy $beam^{-1}$.

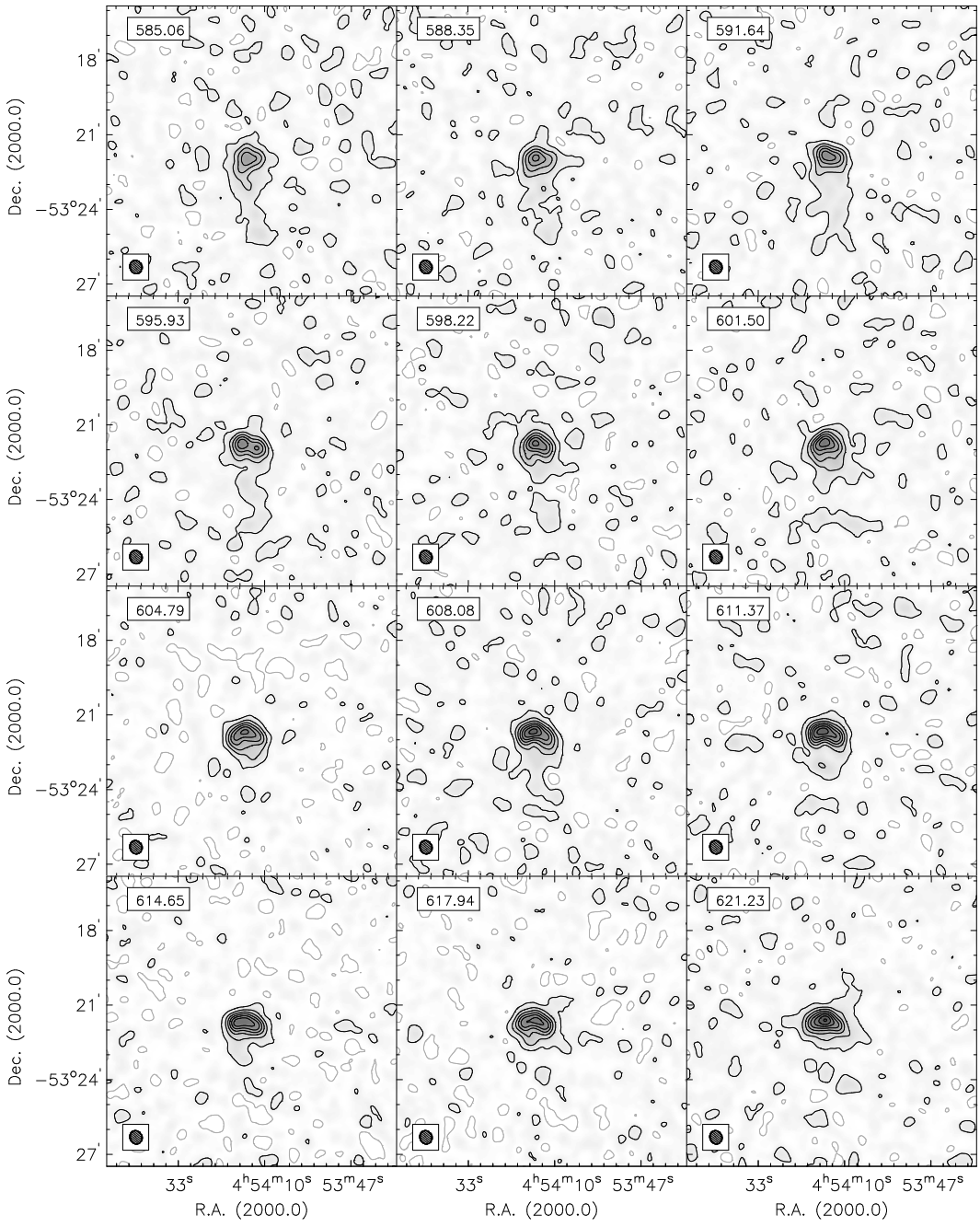

Figure 4.6: Continued.

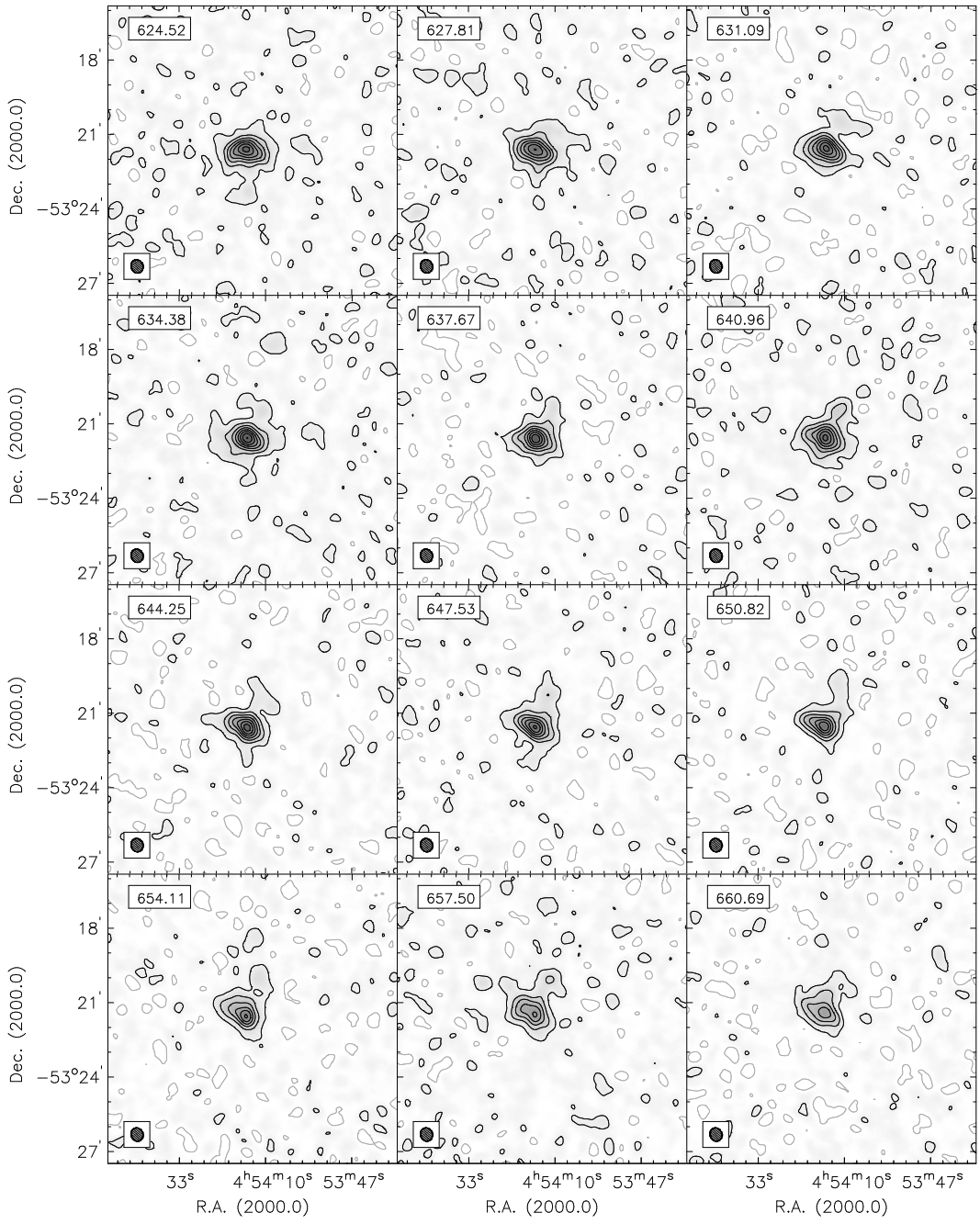

Figure 4.6: Continued.

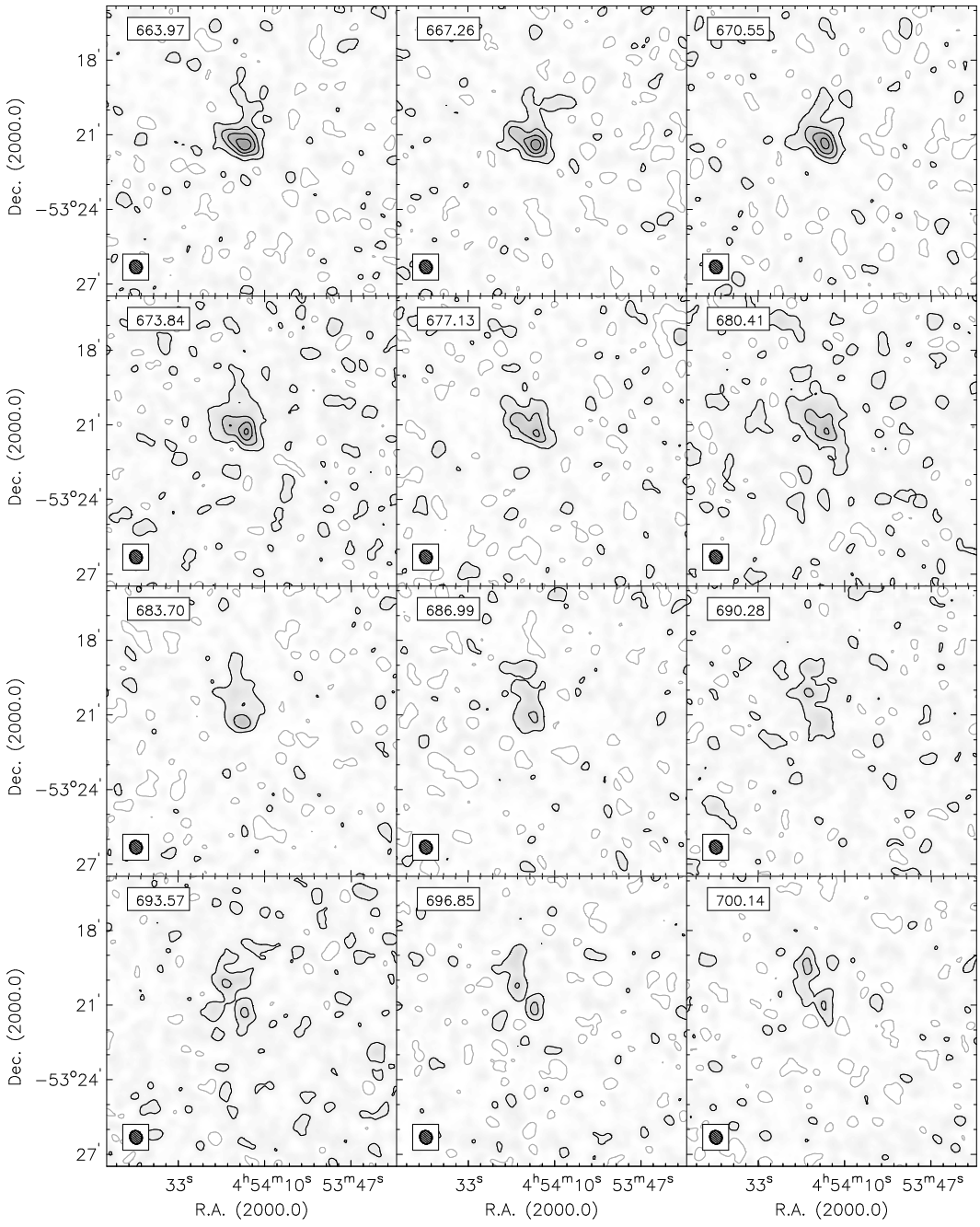

Figure 4.6: Continued.

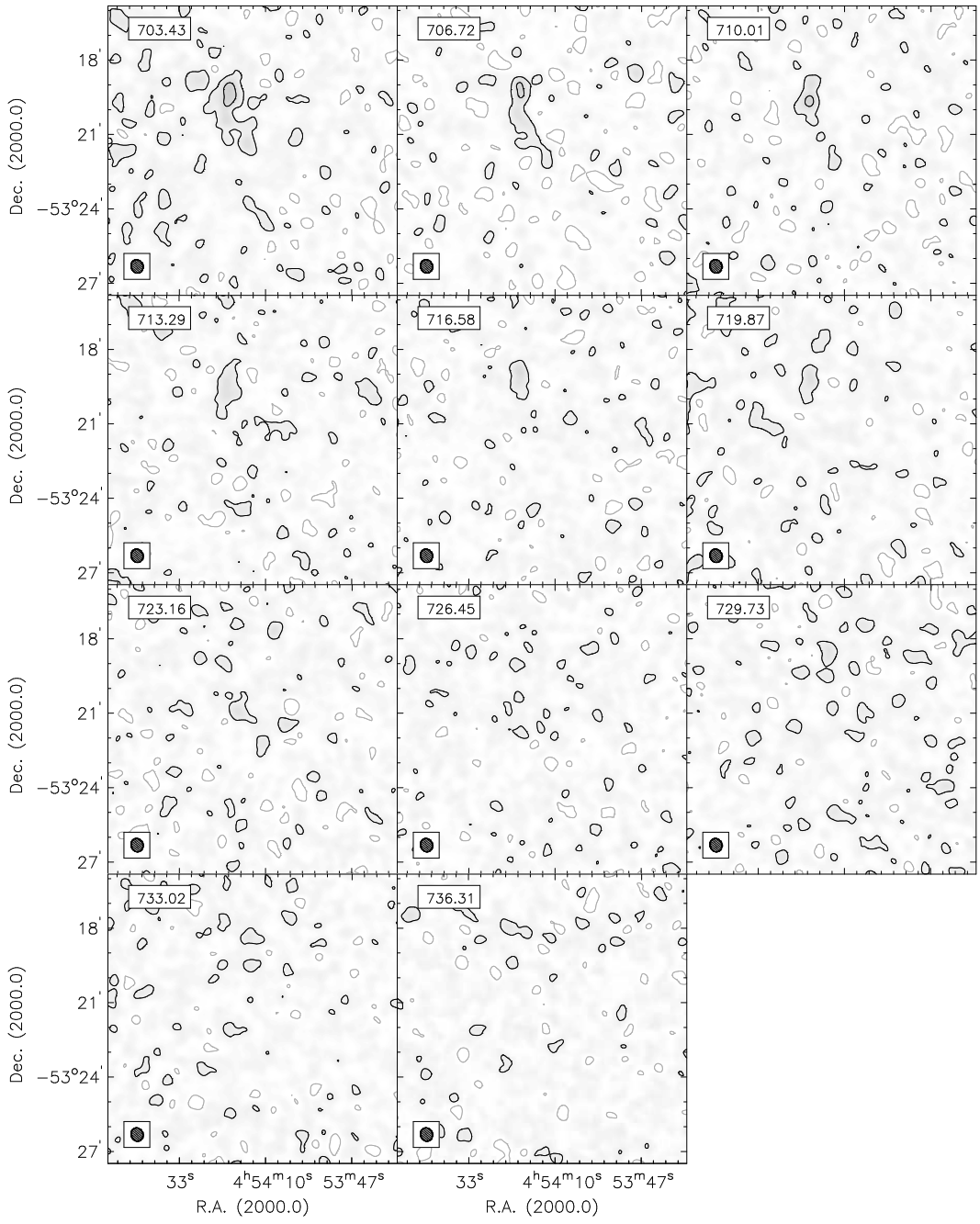

Figure 4.6: Continued.

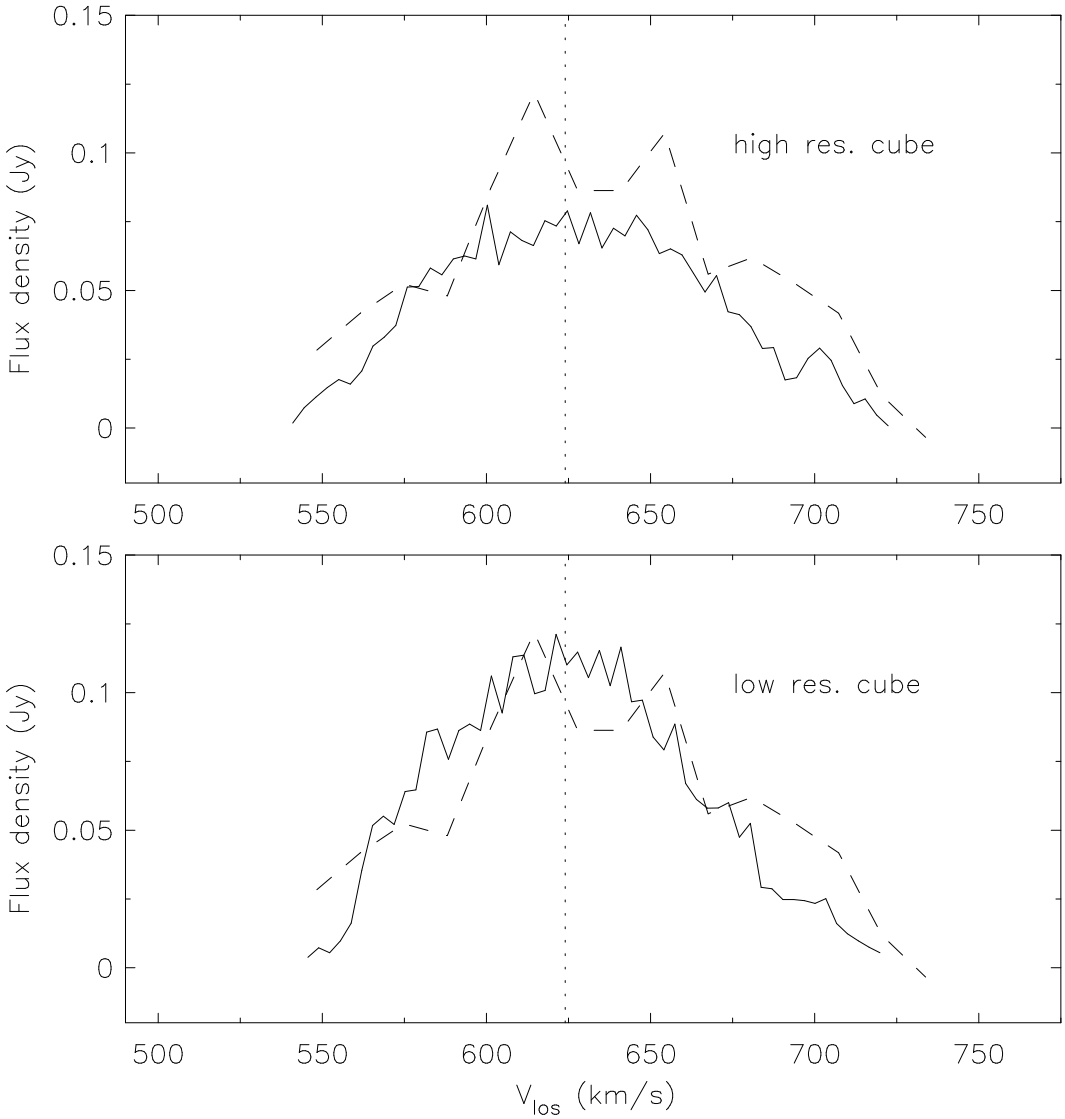

Figure 4.7: NGC 1705 global H I profiles extracted from the masked high- and low-resolution H I data cubes (solid curves) together with the HIPASS global H I profile (dashed curve). The dotted vertical line shows the systemic velocity as calculated using Eqn 4.1.

where D is the distance to the galaxy in units of Mpc and $\int F dV$ is the total H I line flux in units of Jy km s^{-1}. This determination of the total H I mass assumes that the H I is optically thin. Throughout this work a distance of $D = 5.1$ Mpc as determined by Tosi et al. (2001) is adopted.

Table 4.3 lists the determinations of the above mentioned quantities. The derived systemic velocities of $V_{sys} = 620$ km s^{-1} and $V_{sys} = 624$ km s^{-1} are similar to those of Meurer et al. (1998). They measured $V_{sys} = 628$ km s^{-1} and $V_{sys} = 620$ km s^{-1} from H I and optical data sets respectively. Using a distance of $D = 6.2$ Mpc, the total H I masses estimated by Meurer et al. (1998) were $M_{HI} = 1.19 \times 10^8$ M$_\odot$ and $M_{HI} = 1.53 \times 10^8$ M$_\odot$ for their uniformly- and naturally-weighted H I data cubes respectively. This distance of $D = 6.2$ Mpc was determined by Meurer et al. (1995) using the observed heliocentric velocity of NGC 1705. It is therefore expected to be a less reliable estimate of the true distance than that determined by Tosi et al. (2001) who used HST to resolve the brightest red giant stars in the galaxy. The H I masses from Meurer et al. (1998) reduce to $M_{HI} = 8.05 \times 10^7$ M$_\odot$ and $M_{HI} = 1.03 \times 10^8$ M$_\odot$ when placing the galaxy at a distance of $D = 5.1$ Mpc and are thus consistent with the new determinations presented in this work.

Table 4.3: Quantities derived from the global H I profiles of NGC 1705.

1	2	3	4	5	6
M_{HI}^{LR} (10^8 M$_\odot$)	M_{HI}^{HR} (10^8 M$_\odot$)	W_{50} (km s^{-1})	W_{20} (km s^{-1})	V_{sys}^{50} (km s^{-1})	$V_{sys}^{Eqn.1}$ (km s^{-1})
1.32 ± 0.28	1.07 ± 0.21	90.0 ± 6.3	138.0 ± 7.4	620.0 ± 6.3	624.0 ± 13.7

Comments on columns: Column 1/2: total H I mass for low-/high-resolution H I global profiles; Column 3/4: velocity width at 50%/20% of the peak flux; Column 5: systemic velocity from W_{50} midpoint; Column 6: systemic velocity from Eqn. 4.1. Results presented in columns 2-6 were all derived using the high-resolution global H I profile.

4.4.3 Total intensity map

The H I total intensity maps of NGC 1705, generated by determining the zeroth-order moments of the H I line profiles in the high- and low-resolution H I data cubes, are shown in Fig. 4.8

(left- and right-hand panels respectively). For comparative purposes the IRAC 3.6 μm image of the stellar disk is shown in Fig. 4.9. The photometric centre was determined by fitting ellipses to three 3.6 μm flux density annuli near the edge of the old stellar disk. The delimiting flux values for these three ellipses were 0.10, 0.12, 0.14 and 0.16 MJy ster^{-1} and are shown in Fig. 4.9. The average centre of the fitted ellipses is $\alpha_{2000} = 04^{h}\ 54^{m}\ 14.086 \pm 0.038^{s}$, $\delta_{2000} = -53^{\circ}\ 21'\ 39.05 \pm 0.53''$ and is adopted as the position of the photometric centre. For comparison, the 2MASS determination of the centre of the system is $\alpha_{2000} = 04^{h}\ 54^{m}\ 13.50^{s}$, $\delta_{2000} = -53^{\circ}\ 21'\ 39.80''$ (Skrutskie et al., 2006). To facilitate length-scale comparisons between IR and H I images, an ellipse with a semi-major axis length of $a = 47''$, the B-band R_{25} radius as determined by Meurer et al. (1992); inclination $i = 45^{\circ}$ and a position angle $PA = 45^{\circ\dagger}$ is added in all the maps presented in this section.

No distinct spiral structure is visible in the H I total intensity maps of NGC 1705. The high-resolution map shows the H I emission to be concentrated near the optical centre of the galaxy. The H I mass within the B-band R_{25} radius is $\sim 5.1 \times 10^{7}$ M$_{\odot}$. The new H I data clearly resolve this central H I concentration into three over-densities with a combined mass of $\sim 3 \times 10^{7}$ M$_{\odot}$. The east-most and west-most concentrations have their peaks are separated by $\sim 35''$ (0.8 kpc). These H I peaks straddle the extremely luminous super star cluster, NGC 1705-1, discussed in Sec. 4.1. The central position of NGC 1705-1 is indicated in Fig. 4.8 with a green-filled star. As is the case for NGC 2915, the region between the H I concentrations seen near the centre of NGC 1705 could be filled with molecular gas (e.g. Galametz et al., 2009). In Sec. 5.3.5 of Chapter 5, the measured total star formation rate surface densities of NGC 1705 are used to infer the mass distribution of a possible molecular gas component at its centre. A total molecular gas mass of $M_{H2} = 7.4^{+4.3}_{-7.0} \times 10^{7}$ M$_{\odot}$ is estimated for NGC 1705. A radial profile of the inferred molecular gas component is shown in Sec. 4.6.1.

The H I total intensity maps reveal a drawn-out H I feature emanating from the centre of the galaxy in a north-westerly direction. This feature is most clearly seen in the low-resolution H I channel maps. If measured from the photometric centre to its approximate edge (cyan line in the right-hand panel of Fig. 4.8), this feature has an angular extent of $\sim 130''$ (3.3 kpc). Meurer et al. (1998) treat it as evidence for a galactic wind blow out. They propose the H I spur, as they call it, to be a result of the ambient ISM that has been swept up by an expanding, over-pressurised bubble of thermalised supernovae remnants associated with the starburst. What we're seeing, they say, is the ISM that has been accelerated into the halo. Meurer et al. (1992) show the H$_{\alpha}$ morphology of NGC 1705 to consist of multiple arcs and loops extending out to the Holmberg radius ($R_{Ho} = 2.1$ kpc). The orientation of the optical outflow they identify is consistent with the position angle of the H I spur, suggesting that the spur results from a galactic

†As measured eastwards (anti-clockwise) from north.

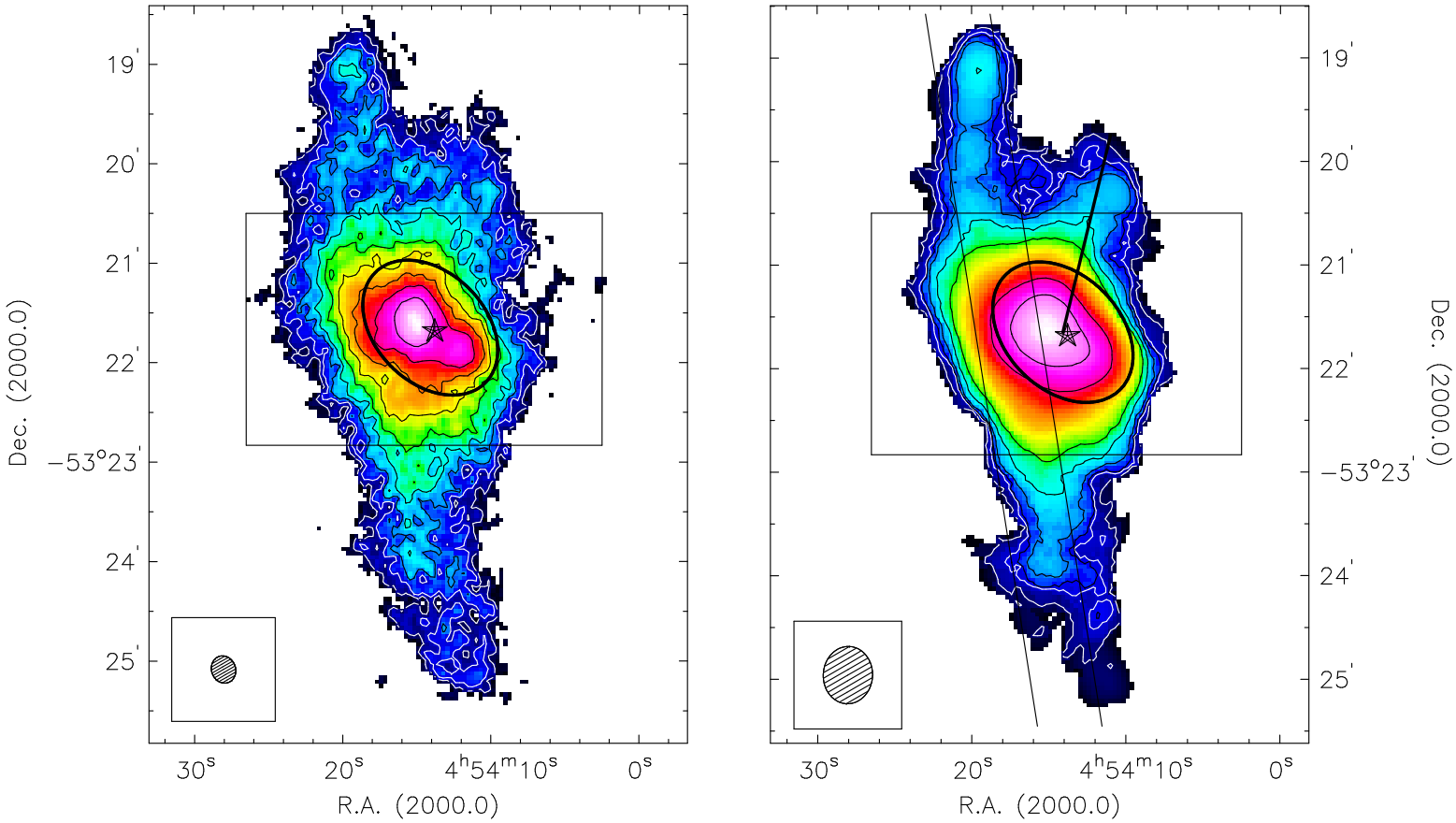

Figure 4.8: NGC 1705 H I total-intensity maps extracted from the high-resolution (left-hand panel) and low-resolution (right-hand panel) H I data cubes. The colour scale is logarithmic. Contour levels in the left-hand panel are at 7.5, 11.2, 17.0, 25.1, 37.2, 55.0, 83.2, 123.0, 186.2 mJy beam^{-1} km s^{-1}. Contour levels in the right-hand panel are at 15.5, 24.0, 36.3, 56.2, 85.1, 131.8, 209.0, 309.0, 578.6 mJy beam^{-1} km s^{-1}. The black ellipse in each panel has a semi-major axis length of 47″ and represents the B-band R_{25} radius. The black box in each panel delimits the IRAC 3.6 μm image shown in Fig. 4.9. The two thin solid lines in the right-hand panel delimit the integrated position-velocity slice shown in Fig. 4.14. The black-filled star in each panel marks the central position of the super star cluster, NGC 1705-1. The thick black line in the right-hand panel depicts the approximate length of the extended H I feature. The hatched circles in the lower corners of each panel represent the half power beam width of the synthesised beam.

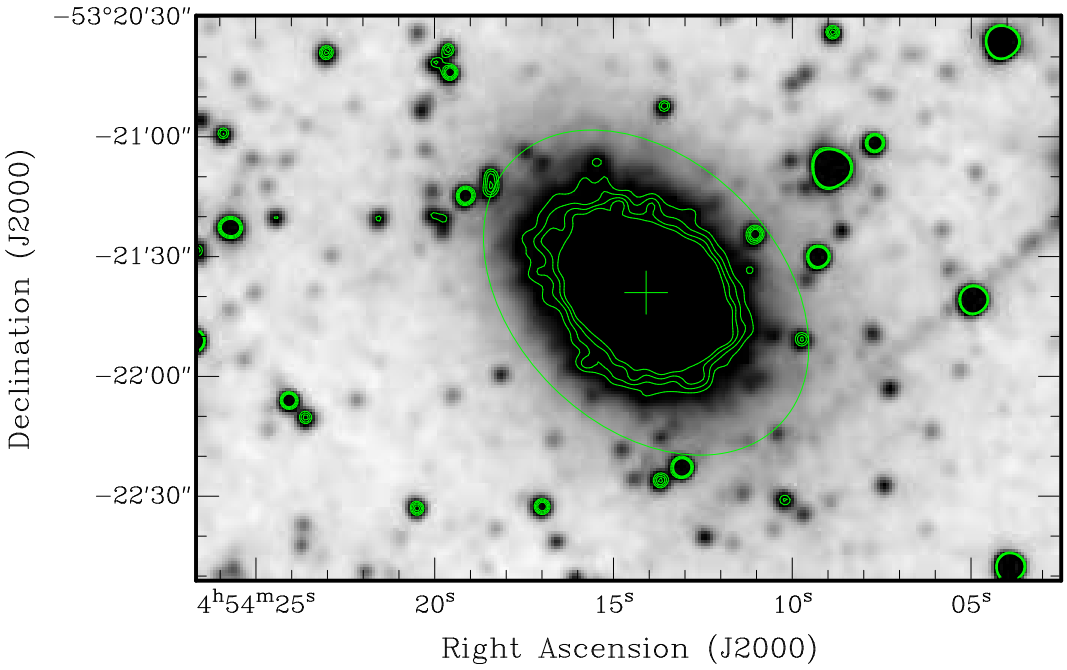

Figure 4.9: Grey scale image of the 3.6 μm IRAC *Spitzer* image of NGC 1705. The flux contour levels are 0.10, 0.12, 0.14, 0.16 MJy ster^{-1} and represent the three flux annuli used to estimate the position of the photometric centre (green cross). The green ellipse is the same as the red ellipse shown in Fig. 4.8 and represents the *B*-band R_{25} radius of 47″.

wind blowout. The one-sided nature of the spur is predicted by models of galactic winds (e.g. Mac Low & Ferrara, 1999) in which the energy source is displaced off the disk plane.

Assuming a plausible time-scale range of $\sim 10 - 100$ Myr, Meurer et al. (1998) estimate a mass outflow rate of $\sim 0.17 - 1.7$ M$_\odot$ yr^{-1}, roughly equal or larger by an order of magnitude than the total star formation rate of 0.13 M$_\odot$ yr^{-1} derived from the H$_\alpha$ flux by Meurer et al. (1992). A sustained mass outflow rate of this magnitude while significantly impact the star-forming properties of the stellar disk, and will presumably quench the current starburst.

4.4.4 Velocity field

The high- and low-resolution intensity-weighted-mean H I velocity fields as well as the third-order Gauss-Hermite velocity field constructed from the high-resolution H I data cube are shown in Fig. 4.10. The high number of blank pixels in the Gauss-Hermite velocity field is attributed to the large fraction of H I line profiles that were rejected by the fitting filters (Sec. 4.3). A

striking feature of Fig. 4.10 is the relatively high degree of regularity in the orientations of the iso-velocity contours of the inner disk. Furthermore, the iso-velocity contours are surprisingly regular and smooth close to the stellar core. This is true for both the Gauss-Hermite and the intensity-weighted-mean versions of the H I velocity field. The extended H I feature seen in the low-resolution H I total intensity map (marked by a cyan line in the right-hand panel of Fig. 4.8) exhibits typical line-of-sight velocities that are fairly consistent with those of the nearby inner portion of the H I disk. The velocity fields as well as the H I channel maps for NGC 1705 suggest that the two central concentrations seen in the H I total intensity map are not significantly separated in velocity. Both of the H I concentrations are present in channels with 600 km s^{-1} $\lesssim V_{los} \lesssim$ 640 km s^{-1}, with the peak flux of each concentration occurring close to the systemic velocity at $V_{los} \sim$ 620 km s^{-1}.

4.4.5 Second-order moment map

The high- and low-resolution second-order moment maps are presented in Fig. 4.11. A very sharp rise in the second-order moments is observed from the outer to the inner H I disk, with typical central second-order moments of the order of $\sigma_{gas} \sim$ 30 km s^{-1} near the galaxy centre. Figure 4.12 shows the radial profile of the second-order moments. This profile was constructed by dividing the high-resolution map into concentric rings of width 16″ and inclination 60°. The outer disk second-order moments of $\sim$ 15 km s^{-1} are similar to the outer disk velocity dispersion measured in other galaxies (e.g.: $\sim$ 11 km s^{-1}, Leroy et al., 2008). It is interesting to note that the elongation in the second-order moment map contours near the centre of the galaxy are in a direction that is aligned with neither the H I major axis, nor the optical major axis, nor the axis towards the H I plume.

4.5 HI dynamics

4.5.1 Tilted ring model

A tilted ring model was fitted to the high-resolution intensity-weighted-mean H I velocity field (i.e. middle panel of Fig. 4.10). Similar to the procedure outlined in Sec. 3.1.1 of Chapter 3, various combinations of fixed and free parameters were used to determine the radial dependence of the systemic velocity, position angle, inclination and the position of the kinematic centre (V_{sys}, PA, i and X_c, Y_c). The variations with radius exhibited relatively little scatter with no significant changes in the fitted parameters when moving from the outer to the inner disk.

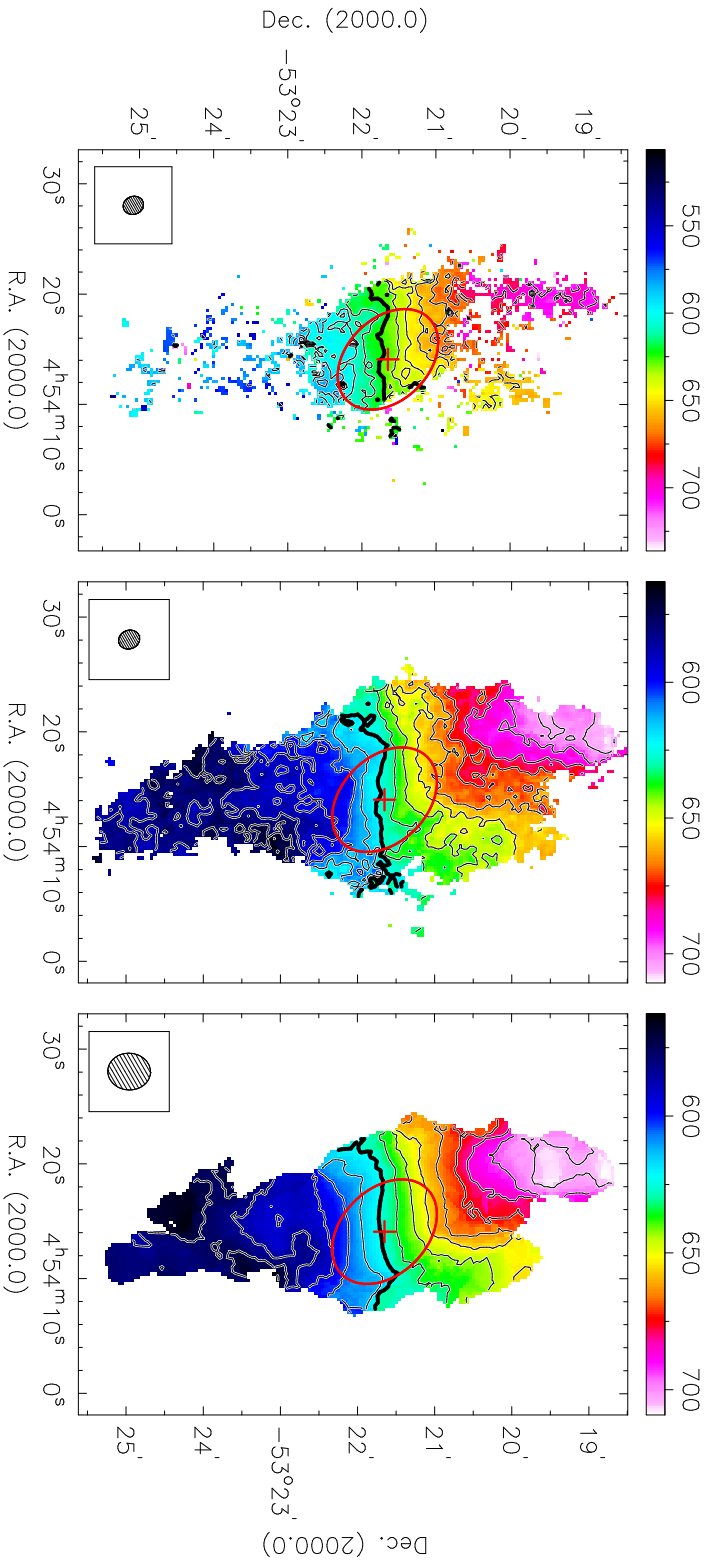

Figure 4.10: High-resolution (middle panel) and low-resolution (right-hand panel) intensity-weighted-mean H I velocity fields and the third-order Gauss-Hermite velocity field (left-hand panel) of NGC 1705. The colour scale of each map is specified by the colour bar at the top of the panel. In all panels, contours are separated by 10 km s^{-1} with the thick contour marking the systemic velocity at 624 km s^{-1}. The red ellipses are the same as the black ellipses shown in Fig. 4.8. The red crosses mark the position of the photometric centre. The hatched circles in the lower corner of each panel represents the half power beam width of the synthesised beam.

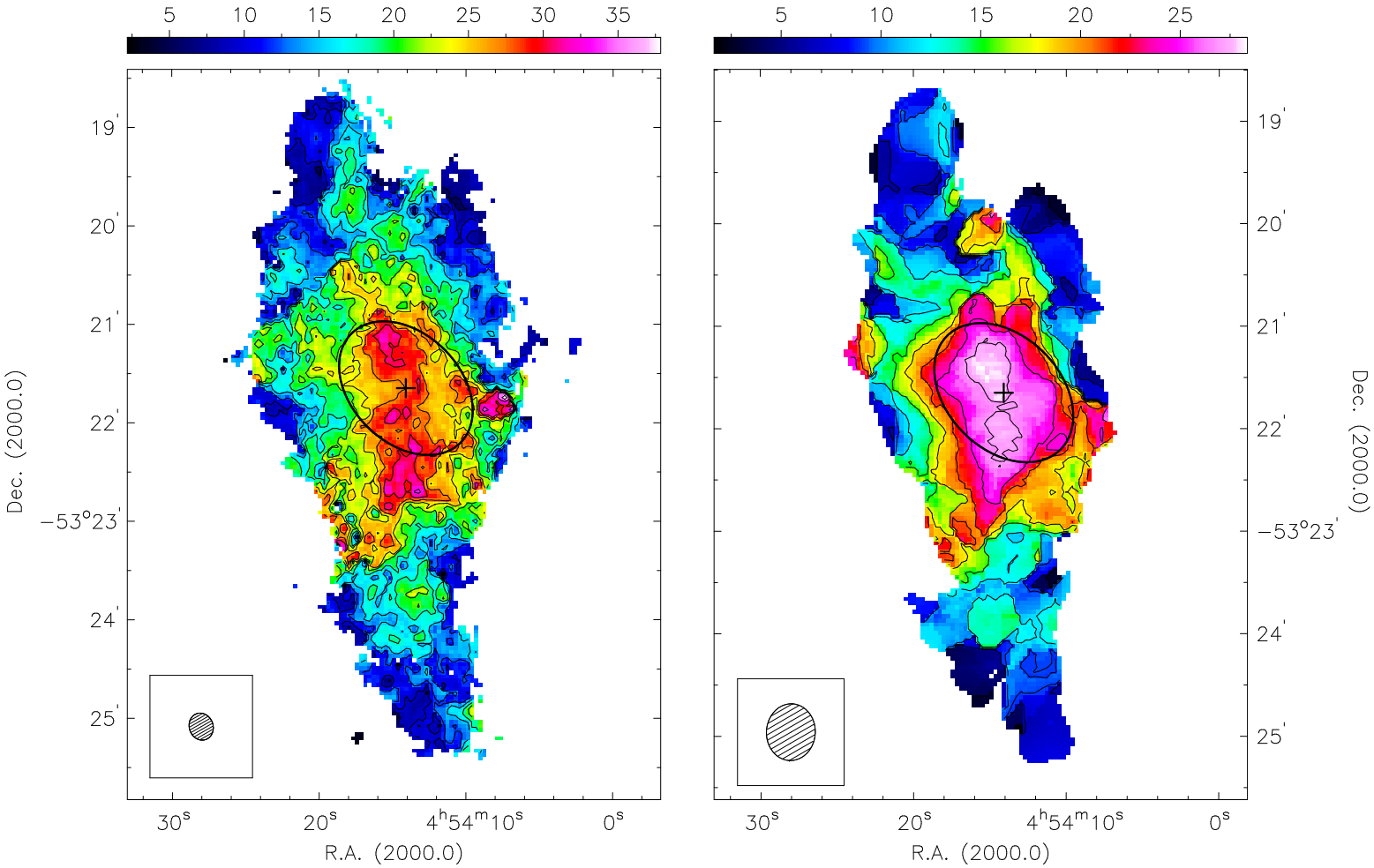

Figure 4.11: High-resolution (left-hand panel) and low-resolution (right-hand panel) 2nd-order H I moment maps of NGC 1705. The colour scale of each map is specified by the colour bar at the top of the panel. Contour levels run from 3 - 48km s^{-1} in steps of 3 km s^{-1}. The hatched circles in the lower left corner of each panel represent the half power beam width of the synthesised beam. The black ellipses and crosses are the same as those presented in Fig. 4.8.

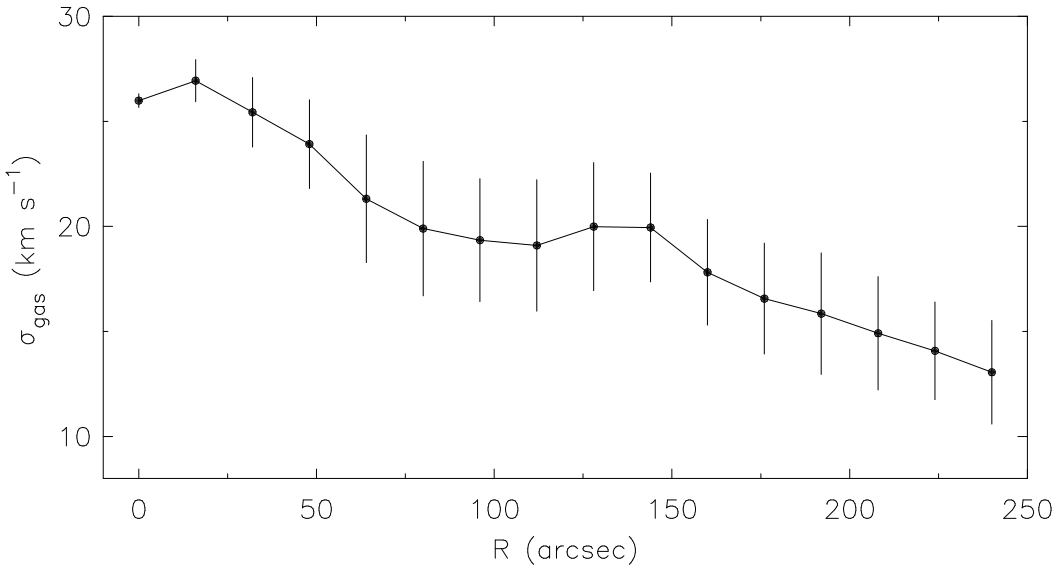

Figure 4.12: Second-order H I moment radial profile of NGC 1705. Error bars represent the r.m.s. spread of the second-order moments in each azimuthally-averaged ring of width 16″ and inclination 60°.

Various combinations of free and fixed parameter sets were also used to check the stability of the fitted parameter values.

For the derivation of the final rotation curve, the V_{sys}, i, X_c and Y_c parameters were all fixed to be constant with radius while the PA radial profile was parameterised as a fourth-order polynomial. These fixed versions of the radial profiles are shown as solid curves in panels A, B, C, D and E of Fig. 4.13. The filled circles in these panels represent the parameter values just before they were fixed. To derive the final rotation curve, only V_{rot} was allowed to vary. The final fitted tilted ring model is shown in Fig. 4.13.

The model predicts the H I disk of the galaxy to be rotating as $V(R) \propto R$, a solid-body type of rotation often associated with low-mass dwarfs. The r.m.s. circular velocity uncertainties are ~ 3.26 km s^{-1} on average for $R \leq 105''$, and ~ 4.13 km s^{-1} for the entire radial range. The preferred average inclination of the H I disk is $i \sim 80°$. This is close to the determination of $i \sim 78°$ which was estimated by Meurer et al. (1998) from the shape of the outer H I isophotes (excluding the extended H I feature). These authors point out that if the true inclination is lower in the centre of the disk as implied by optical isophotes, then the central V_{rot} estimates may be higher by a factor $\lesssim 1.5$.

To compare the fitted tilted ring model to the H I data cube, the fixed radial parameter

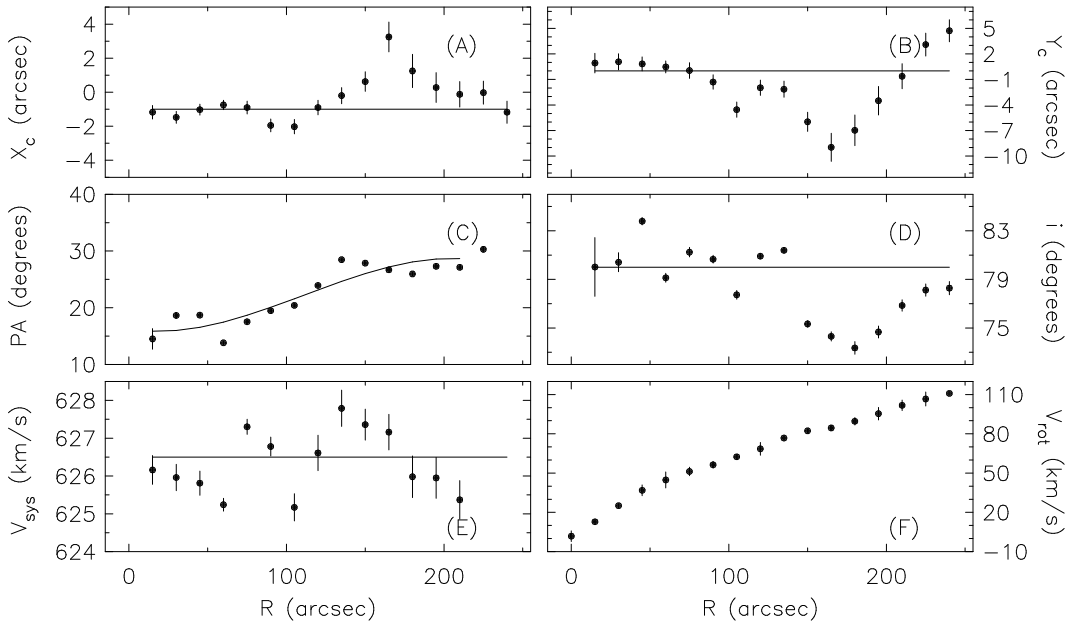

Figure 4.13: Radial variations of tilted ring parameters fitted to the high-resolution intensity-weighted-mean H I velocity field of NGC 1705. Panels are A: central X positions, B: central Y positions, C: position angles, D: inclinations, E: systemic velocities, and F: circular rotation velocities. Filled circles show the radial variations just before the parameter profiles were smoothed and fixed in order to derive the final rotation curve. Error bars represent the formal least-squares errors. The smoothed profiles used to construct the final tilted ring model are shown as solid curves. Panel F shows the final rotation curve. Error bars represent the absolute difference in rotation velocities derived separately for the approaching and receding halves of the galaxy.

profiles (i.e. solid curves in Fig. 4.13) were used to project the fitted rotation curve onto a position-velocity slice extracted from the low-resolution H I data cube. A "standard" position-velocity slice with a thickness of a single RA-DEC pixel in the H I data cube (2.5″ in the case of NGC 1705) is inadequate for this purpose because of the relatively low signal-to-noise levels associated with the outer H I disk. To boost the signal, an integrated 35″-thick position velocity slice was created by summing 14 adjacent single-pixel position-velocity slices. These slices have a common position angle of $PA = 11°$and were taken parallel to the outer H I disk of the galaxy at large enough distances from the centre to be unaffected by any possibly anomalous kinematics associated with the galaxy's star-bursting core. The solid black lines in the right-hand panel of Fig. 4.8 represent the edges of the integrated position-velocity slice. The final 35″-thick integrated position-velocity slice is shown in the top panel of Fig. 4.14 with the tilted ring model line-of-sight velocities overlaid. For comparative purposes, the 2.5″-thick position-velocity slice

positioned exactly in the middle of the two red lines (i.e. the seventh out of the 14 2.5″-thick position velocity slices) is shown in the bottom panel of Fig. 4.14. The rotation curve of the fitted tilted ring model is able to match the general $V(R) \propto R$ trend of the the observed line-of-sight velocities fairly well, but it does not accurately match the line profile peaks. Line-of-sight velocities are generally under-estimated for $50'' \lesssim R \lesssim 75''$, and over-estimated for $R \gtrsim 75''$.

An interesting feature of the integrated position-velocity slice is the asymmetric H I line profiles at angular offsets of $-100''$ to $-200''$. These profiles are clearly skewed towards the systemic velocity, and are lagging in velocity relative to the main disk. This emission is analogous to that of the "H I beard" seen in the NGC 2915 data cube. It could therefore also be the case that this lagging emission is caused by gas that is accreting from the nearby inter-galactic medium onto the outer H I disk of NGC 1705.

4.5.2 Rotation curve

To derive an alternative rotation curve for NGC 1705, the H I line profiles of the integrated position-velocity slice were parameterised. Each line profile was fitted with: (1) a single-component Gaussian, (2) a single-component third-order Gauss-Hermite polynomial and (3) a double-component Gaussian. Using the GIPSY task XGAUFIT as before (Sec. 4.3), three filters were used simultaneously when fitting the profiles. The results are shown in Fig. 4.15.

The single-Gaussian parameterisations seem to best characterise the line-of-sight velocities and were used to extract the rotation curve as described below. Each profile's angular offset was taken as the radial offset from the dynamical centre of the galaxy, a permitted treatment in this case since the integrated position-velocity slice lies along the kinematic major axis of the H I disk. A systemic velocity of $V_{sys} = 626.5$ km s^{-1} was subtracted from each of the fitted line-of-sight velocities to yield $V_{rot} \sin i$. This value of the systemic velocity, as opposed to those of $V_{sys} = 624.5$ km s^{-1} and $V_{sys} = 620$ km s^{-1} determined using the global H I profile in Sec. 4.4.2, allows for the smallest discrepancies between the derived circular velocities of the approaching and receding sides of the galaxy, indicating that it corresponds closely to the dynamical centre of the system. For all further analyses, $V_{sys} = 626.5$ km s^{-1} is adopted as the preferred systemic velocity estimate. The column-by-column $V_{rot} \sin i$ measurements were averaged in bins of width 17.5″. Some of the fitted velocities were clearly adversely affected by the asymmetric shapes of some H I profiles, and were hence inaccurate estimates of the line-of-sight velocities. For these cases, the line-of-sight velocities were estimated by eye to ensure a a more reliable fit to the data. A comparison between the fitted and estimated velocities is shown in Fig. 4.17. The final set of line-of-sight velocities is shown in Fig. 4.16. The adjustments were largest (~ 25 km s^{-1}) for $100'' \lesssim R \lesssim 150''$. Most of the estimated line-of-sight velocities differed by $\lesssim 10$ km s^{-1}

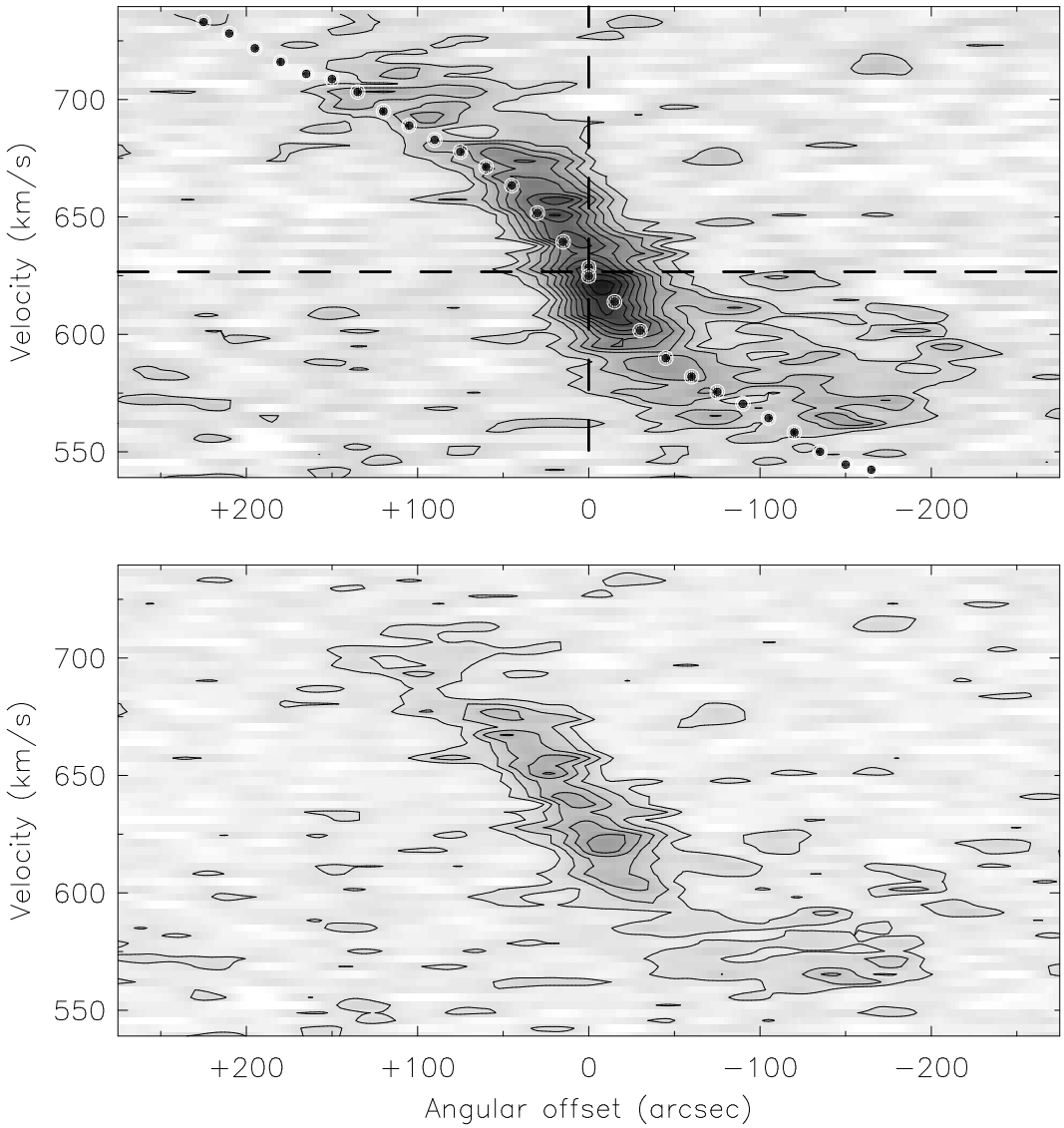

Figure 4.14: **Top panel:** 35″-thick integrated position-velocity slice extracted from the low-resolution H I data cube of NGC 1705. The edges of the integrated slice are shown as solid red lines in the right-hand panel of Fig. 4.8. Overlaid on the slice is the rotation curve of the fitted tilted ring model, projected using the smoothed radial parameter profiles shown as solid curves in Fig. 4.13. The dashed horizontal line marks the systemic velocity at 626.5 km s^{-1}. Contour levels start at 18 mJy beam^{-1} and are spaced by 25 mJy beam^{-1}. **Bottom panel:** One of the constituent 2.5″-thick position-velocity slices used to generated the integrated slice. The velocity resolution is $dV = 3.28$ km s^{-1}. Contour levels start at 1.6 mJy beam^{-1} and are spaced by 2 mJy beam^{-1}.

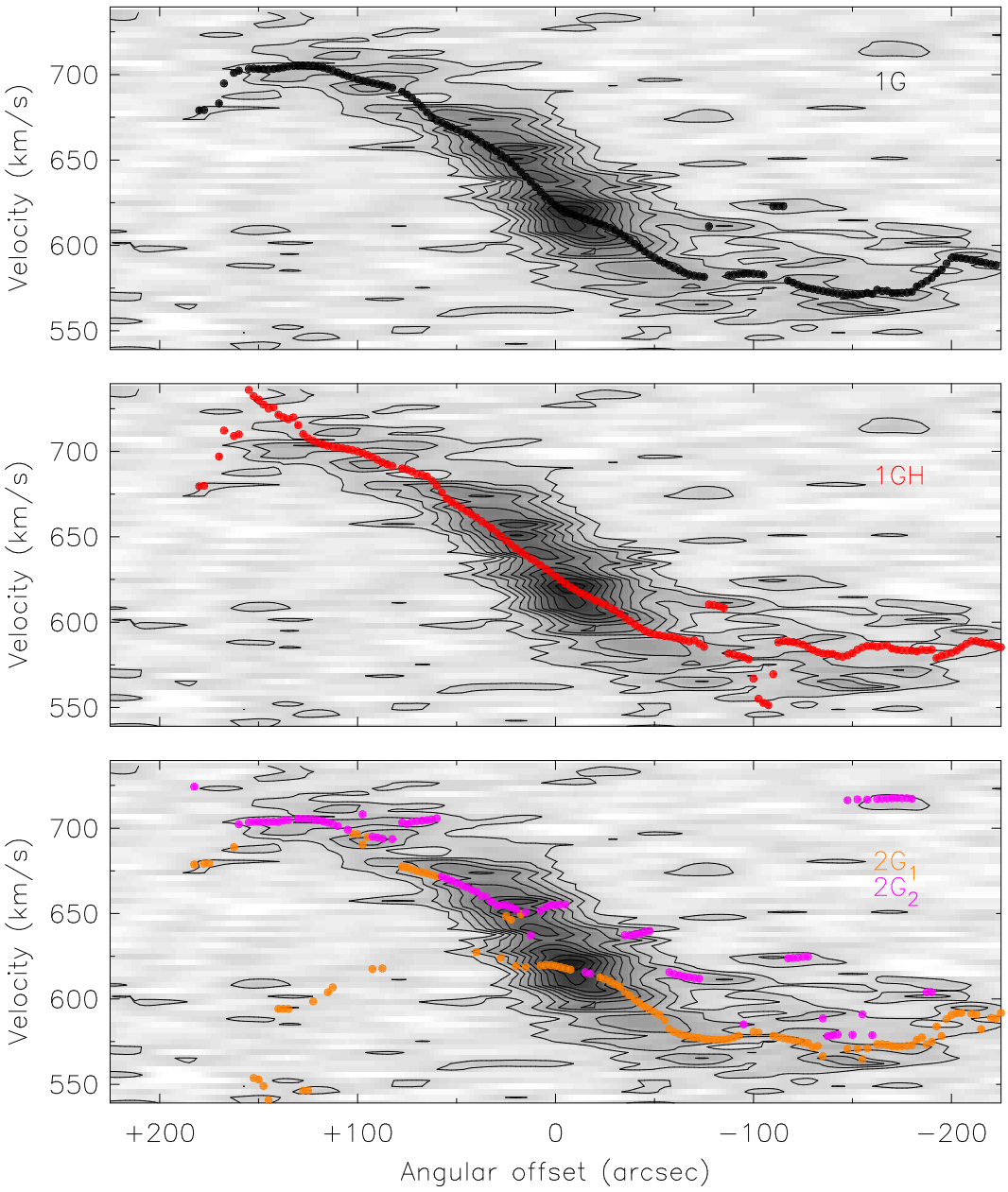

Figure 4.15: 35″-thick integrated position-velocity slice extracted from the low-resolution H I data cube of NGC 1705. Overlaid on the slice are the peaks of single-component Gaussians (**top panel**), third-order Gauss-Hermite polynomials (**middle panel**) and double-component Gaussians (**lower panel**) fitted to each of the H I line profiles. At a given angular offset in the bottom panel, the orange and purple filled circles represent the two fitted peaks of the double-component Gaussian. Details concerning the properties of the integrated position-velocity slice are provided in the caption of Fig. 4.14.

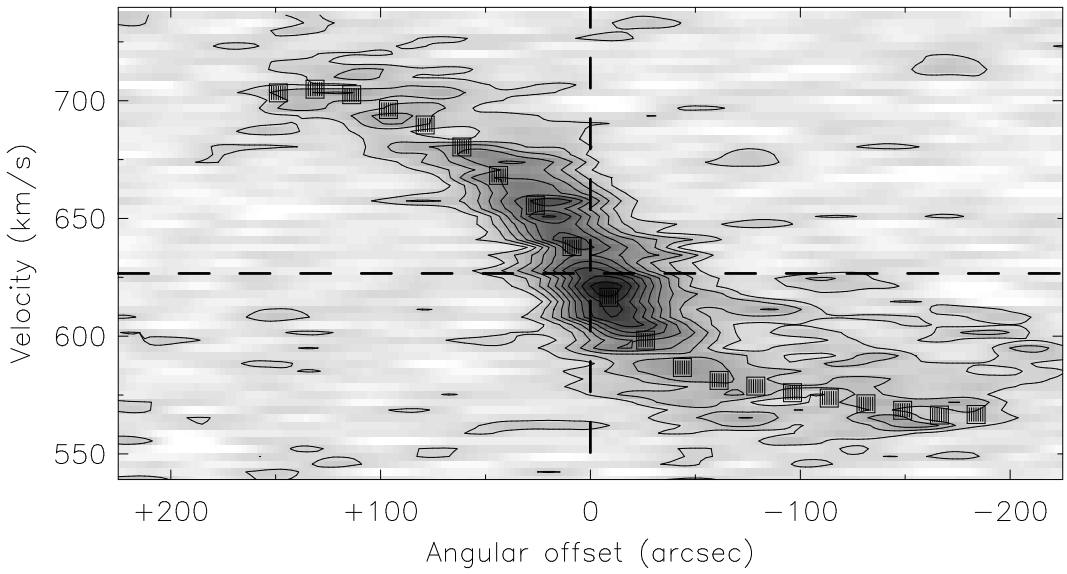

Figure 4.16: 35″-thick integrated position-velocity slice extracted from the low-resolution H I data cube of NGC 1705. Overlaid on the slice are the beam-averaged peaks of the single-component Gaussians fitted to each of the H I line profiles. Details concerning the properties of the integrated position-velocity slice are provided in the caption of Fig. 4.14.

to the corresponding fitted velocities. Assuming an inclination of $i = 80°$, the circular velocity estimates were recovered. This final rotation curve is given in Table 4.4. The absolute differences between the rotation curves derived separately for the approaching and receding halves of the galaxy were used as the corresponding uncertainty estimates for the averaged rotation curve (right-most column of Table 4.4). We do not apply asymmetric drift corrections to our derived NGC 1705 rotation velocities. While it is plausible that turbulent pressure within the ISM could be providing the H I with some dynamical support, an asymmetric drift correction would be largely uncertain and ambiguous due to the edge-on orientation of the inner disk as well as the strong case for optical outflow from the optical data of Meurer et al. (1998).

For comparison, the final rotation curve is plotted together with the tilted ring model rotation curve in Fig. 4.18 (red-filled squares and green-filled circles respectively). Also shown is the rotation curve derived by Meurer et al. (1998) (blue-filled triangles). Our best estimate of rotation curve is very similar to that of Meurer et al. (1998) with the exception that it does not extend as far as theirs. Beyond the last measured point of our rotation curve ($R = 148''$), the V_{rot} estimates of Meurer et al. (1998) start to decline out to a radius of $R \sim 200''$. Although such a decline is consistent with some of the iso-velocity contours in the low-resolution intensity-weighted-mean H I velocity field that are closed on the receding half of the galaxy

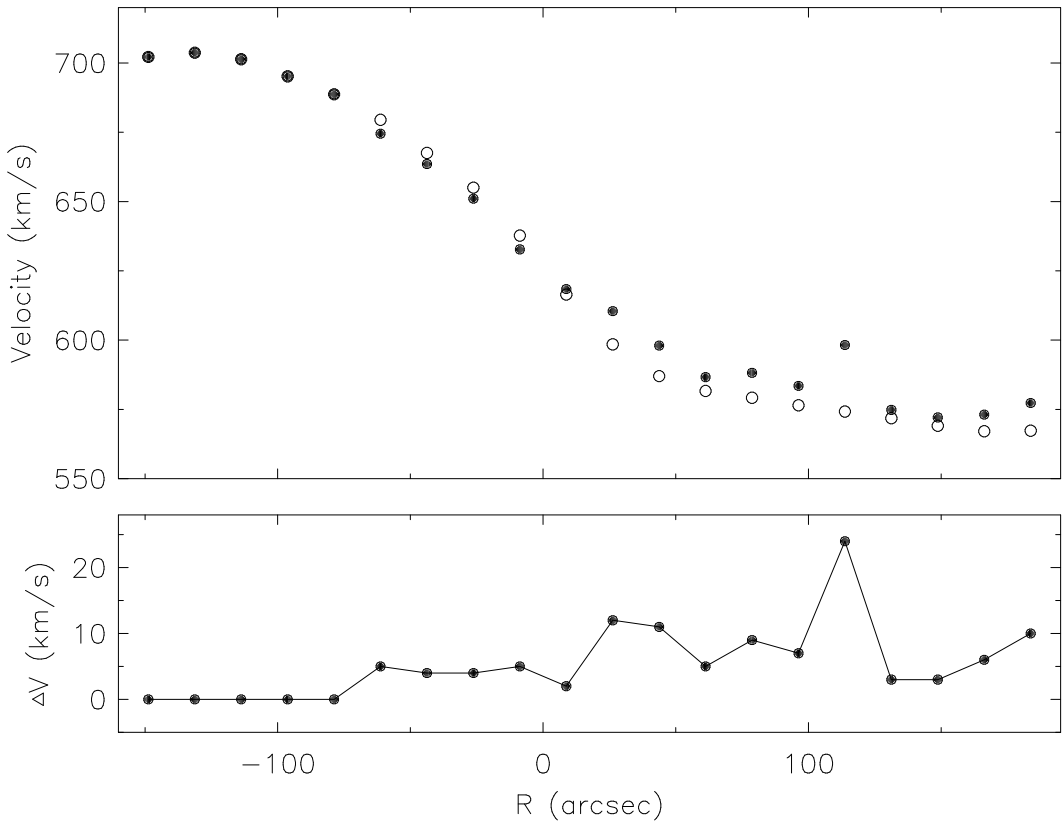

Figure 4.17: **Top panel:** Comparison between estimated line-of-sight velocities from single-Gaussian fits to H I line profiles (filled circles) and the line-of-sight velocities that were adjusted by eye to better fit the data (open circles). **Bottom panel:** Absolute residual of the corresponding line-of-sight velocities shown in the top panel.

(Fig. 4.10, right-hand panel), it is inconsistent with the integrated position-velocity slice. Thus, for mass-modeling purposes, only our derivation of the rotation curve (i.e. the red-filled squares in Fig. 4.18) is used.

4.6 Mass modeling

In this section a mass model is constructed for NGC 1705. The aim is to accurately characterise the dark matter halo by using our determination of the rotation curve together with the superior *Spitzer* infrared imaging of NGC 1705.

The rotation curves of the individual mass components of a galaxy, when summed in quadra-

Table 4.4: Adopted rotation curve of NGC 1705.

1	2	3
R ($''$)	V_{rot} (km s^{-1})	δV_{rot} (km s^{-1})
8.75	10.89	1.17
26.25	28.92	0.52
43.75	41.17	1.60
61.25	50.02	8.32
78.75	55.98	15.23
96.25	60.69	19.08
113.75	64.99	23.10
131.25	67.42	23.03
148.75	68.04	18.68

Comments on columns: Column 1: galactocentric radius; Column 2: adopted circular velocity; Column 3: uncertainty in adopted circular velocity.

ture, yield the square of the total rotation curve, V_{tot}. For stellar, gaseous and dark matter components

$$V_{tot}^2 = \alpha_{gas} V_{gas}^2 + \Upsilon_* V_*^2 + V_{DM}^2, \tag{4.3}$$

where V_{gas}, V_*, and V_{DM} are the contributions to the total rotation curve of the gas, the stars and the DM respectively. To match this total rotation curve to the observed rotation curve, estimates of the gas scaling factor, α_{gas}, and the stellar mass-to-light, Υ_*, ratio are required.

4.6.1 Gas and stellar distributions

The observed H I distribution is used to calculate the contribution of the gas rotation curve, V_{gas}, to the total rotation curve. Meurer et al. (1998) provide a parameterisation of the face-on H I column densities of NGC 1705 (Σ_{HI}, in units of atoms cm^{-2}) as a function of galactocentric radius (R, in units of arcsec):

$$\log_{10} \Sigma_{HI} = 19.86 - 0.00169R + 1.46 \exp(-[R/50.2]^2/2). \tag{4.4}$$

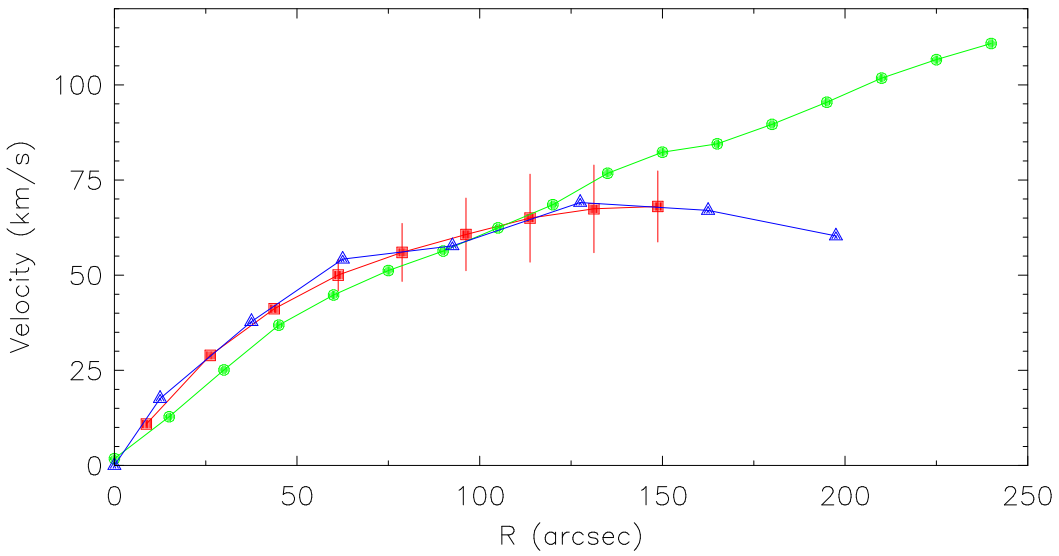

Figure 4.18: Various determinations of the rotation curve of NGC 1705 including that from the tilted ring model fitted to the H I velocity field (**green filled circles**), that presented in Fig. 4.16 above (**red filled squares**) and that of Meurer et al. (1998) (**blue filled triangles**). Error bars represent the absolute differences between the rotation curves of the approaching and receding halves of the galaxy.

This parameterisation adopts a linear decline with a Gaussian core for the intrinsic $\log_{10} \Sigma_{HI}$ profile. The parameerisation *assumes that the observed column densities represent the integrated flux of an edge-on disk*, and corrections have been applied to account for the changing fraction of the disk that a line of sight will sample as it moves from the centre to the edge of the disk. These face-on, parameterised H I column densities, converted to units of $M_\odot$ pc^{-2}, are shown in Fig. 4.19. Meurer et al. (1998) point out that the functional form of this parameterisation is not supposed to provide insight into the physics of the H I mass distribution. Rather, it merely fits their data fairly well. This parameterisation of the face-on H I surface densities was used as ROTMOD input. Assuming an infinitesimally thin H I disk, the component of the full rotation curve due to the mass of H I was calculated. To account for the presence of helium and other metals in the ISM, this rotation curve was scaled by $\alpha_{gas} = 1.37$ to yield V_{gas}.

A measure of the stellar mass distribution is required to generate the stellar rotation curve. The observed flux densities from the *Spitzer* IRAC 3.6 μm image (Fig. 4.9) were divided into rings of width $\Delta R = 16''$, inclination $i = 45°$ and position angle $PA = 45°$. These orientation parameters match those of the ellipses fitted to the 3.6 μm flux density annuli as described in Sec. 4.8. The median flux density for each ring was calculated. The resulting inclination-

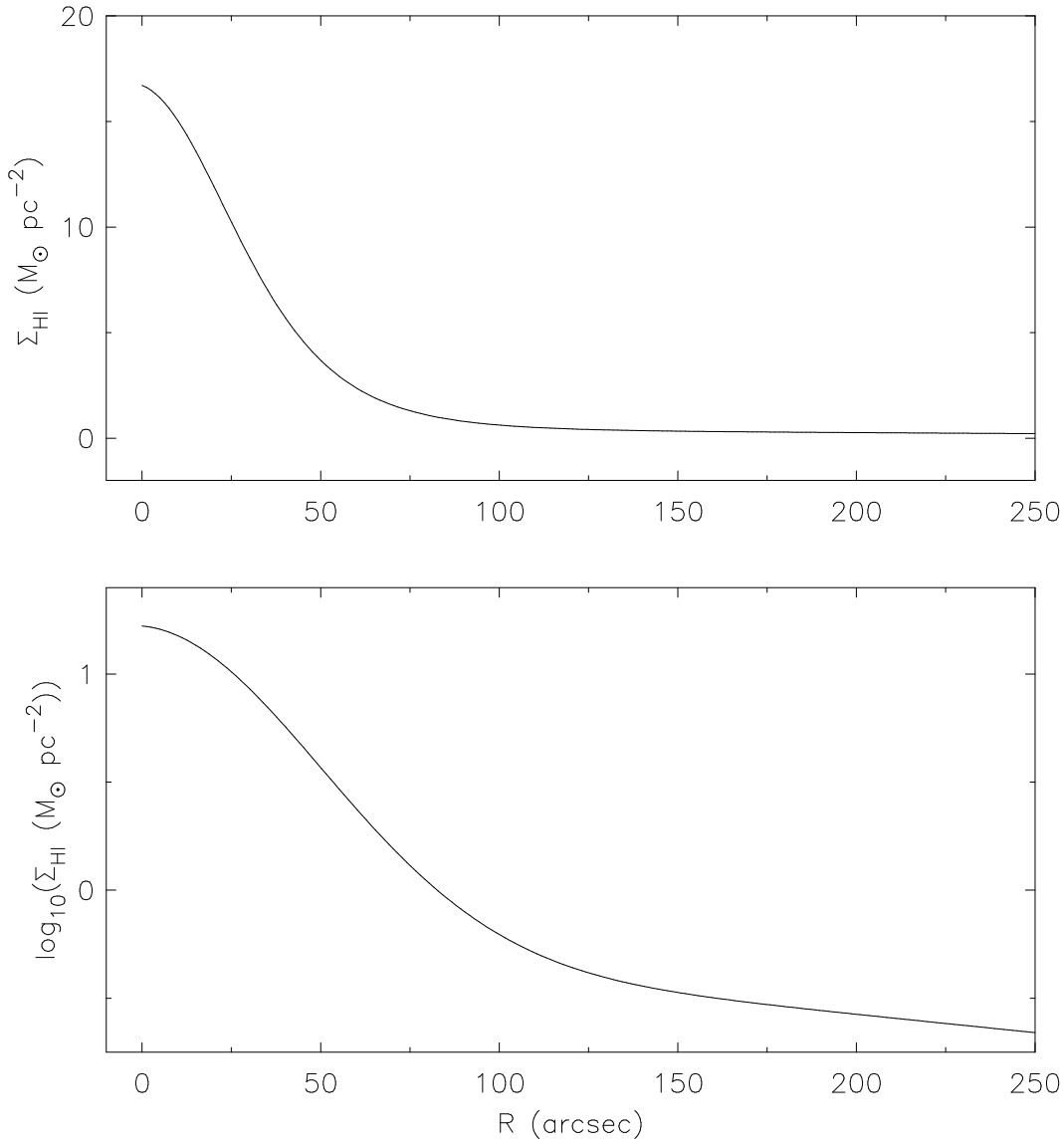

Figure 4.19: Linear **(top panel)** and logarithmic **(bottom panel)** versions of the face-on H I column density radial profile for NGC 1705 as parameterised by Meurer et al. (1998).

corrected stellar surface density radial profile was converted from units of MJy ster^{-1} to units of $M_\odot$ pc^{-2} using the prescription of Oh et al. (2008) (described later in Sec. 5.3.4 of Chapter 5). Figure 4.20 shows the logarithmic stellar surface density profile. The profile was fitted with a first-order polynomial, shown as a solid curve in Fig. 4.20. This parameterisation of the stellar surface density profile was converted into a stellar rotation curve assuming a sech^2 vertical distribution (van der Kruit, 1981) and a scale height $z_0 = 0.12$ kpc, one fifth of our parameterised scale length of the old stellar disk.

It may be the case that NGC 1705 contains a molecular gas components near its centre, the associated gravitational potential of which could significantly contribute to the observed rotational properties of the galaxy. In Sec. 5.3.5 of Chapter 5, the measured total star formation rate surface densities of NGC 1705 are used to determine the distribution of a possible H_2 component. The total molecular gas mass is estimated to be $M_{H2} = 7.4^{+4.3}_{-7.0} \times 10^7$ $M_\odot$. The azimuthally-averaged distribution of the H_2 surface densities is shown in Fig. 4.21 which shows that most of the H_2 is contained within the central $\sim 100''$ of the galaxy. From our rotation curve derived in Sec. 4.5.2, a total (dynamical) mass of $\sim 1.3 \times 10^8$ $M_\odot$ is contained within $26.3''$ of the centre of the galaxy (i.e. the second point on our derived rotation curve). Since this amount of total mass, which is more than the inferred H_2 mass, is contained well within the radial extent of the H_2 component, we do not expect the associated H_2 potential to significantly contribute to the overall potential. We therefore do not include an H_2 rotation curve in our mass models.

An estimate of the stellar mass-to-light ratio is required. Dynamically estimating the stellar mass-to-light ratio from the rotation curve alone is problematic, since it is possible that a range of ratios will allow for equally well-fitted mass models (e.g. van Albada et al., 1985; Swaters, 1999). To estimate a 3.6 μm stellar mass-to-light ratio ($\Upsilon_*^{3.6}$) for NGC 1705, the same approach as that for NGC 2915 in Sec. 3.2.1 of Chapter 3 was adopted. A K-band stellar mass-to-light ratio (Υ_*^K) was first estimated using the relationship $\log_{10}\left(\Upsilon_*^K\right) = b^K \times (B-V) + a^k$, presented by Bell & de Jong (2001). The constants a^K and b^K for varying colours and metallicities of $Z = 0.008$ and $Z = 0.02$ are provided in their Table 4. Storchi-Bergmann et al. (1994) showed the youngest objects in NGC 1705 to have a metallicity of $Z \sim 0.004$. Tosi et al. (2001), using HST WFPC2 photometry of the resolved stellar population of NGC 1705, demonstrated that the vast majority of resolved stars are more metal rich than $Z = 0.0004$, yet more metal poor than $Z = 0.008$. The a^K and b^K values from Table 4 of Bell & de Jong (2001) corresponding to $Z = 0.008$ were therefore adopted to derive the K-band stellar mass-to-light ratio, i.e. $a^K = -0.59$ and $b^K = 0.60$. Together with $B - V = 0.33 \pm 0.008$ (de Vaucouleurs et al., 1991; Schlegel et al., 1998), $\Upsilon_*^K \sim 0.41$ is yielded by the Bell & de Jong (2001) relation. Using the relation from Oh et al. (2008) that links the $K-$ and 3.6 μm – band stellar mass-to-light ratios (Sec. 3.2.1

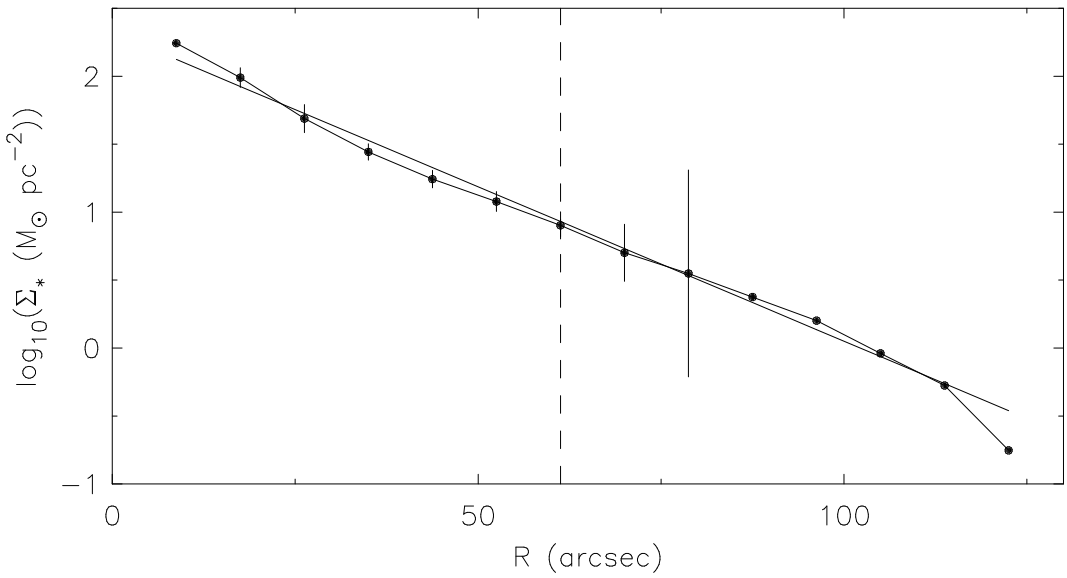

Figure 4.20: Stellar surface density radial profile for NGC 1705. The black filled circles represent the median flux densities in a thin ring of thickness $\Delta R = 16''$ in the *Spitzer* IRAC 3.6 μm image. Error bars represent the r.m.s. spread of the flux densities in a ring. The solid curve in represents the first-order polynomial fit to the logarithmic profile, while the dashed line is drawn at $R = 60''$.

of Chapter 3), $\Upsilon_*^{3.6} \sim 0.32$ was derived for NGC 1705. This estimate is almost identical to the corresponding estimate of $\Upsilon_*^{3.6} \sim 0.30$ determined for NGC 2915.

The GIPSY task ROTMAS was used to mass model NGC 1705, using the observed rotation curve together with the H I and stellar rotation curves as input. The dark matter halo was parameterised as a pseudo-isothermal sphere and an NFW halo. A discussion of the properties of these two DM halo parameterisations is provided in Sec. 3.2.2 of Chapter 3. Four mass models were generated for each DM halo parameterisation. These included: (1) maximum disk models, (2) minimum disk models, (3) models in which the stellar mass-to-light ratio was fixed to $\Upsilon_*^{3.6} = 0.32$, and (4) models in which $\Upsilon_*^{3.6}$ was allowed to freely vary. For the maximum and minimum disk cases, the stellar mass-to-light ratio was fixed at $\Upsilon_*^{3.6} = 0.72$ and $\Upsilon_*^{3.6} = 0.0$ respectively.

4.6.2 Fitting procedure

The mass-modelling results are presented in Table. 4.5. In the case of NGC 1705, well-fitted mass models could be obtained when the DM halo was modelled as a pseudo-isothermal sphere.

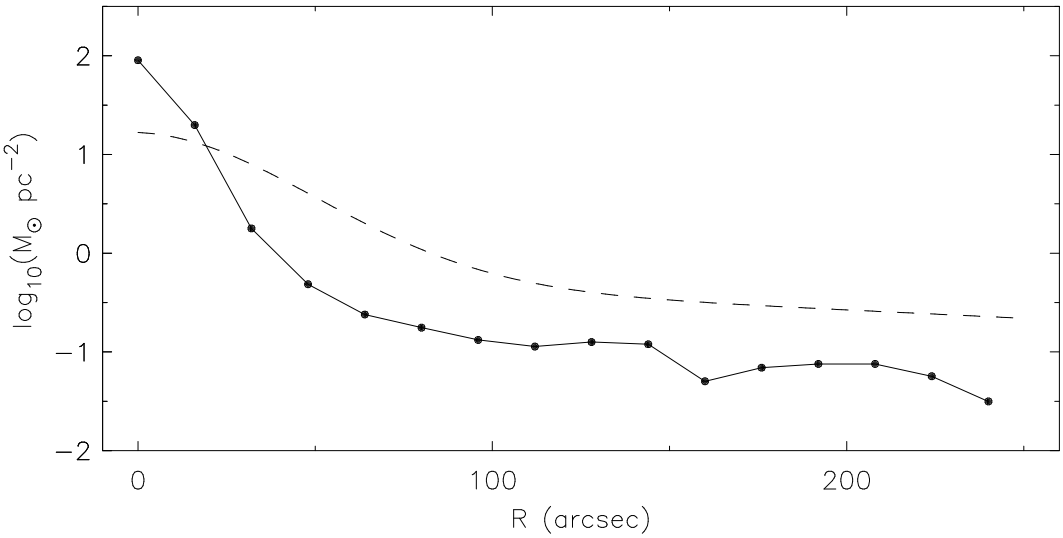

Figure 4.21: H_2 surface density radial profile (filled circles) derived from the star formation rate surface density map in Sec. 5.3.5 of Chapter 5. For comparison, the H I surface density profile from Meurer et al. (1998) is also shown (dashed line). Both sets of surface densities are inclination-corrected to their face-on values.

However, no meaningful NFW DM halo parameterisation could be found that allowed for a well-fitted mass model. Simultaneously fitting two or more model parameters yielded unphysical results for the NFW cases, as well as the maximum disk case for the pseudo-isothermal sphere DM halo parameterisation. To circumvent this problem, an iterative approach was adopted in which the model parameters were fitted one at a time. As an example, for the NFW case in which Υ_*, c and V_{200} were fitted (α_{gas} was fixed to 1.37 for all mass models), a typical fitting method was:

1. Fix c and V_{200} to values typical of dwarf systems and fit Υ_*.

2. Fix Υ_* to its best-fitting value, keep c fixed and fit V_{200}.

3. Keep Υ_* and V_{200} fixed to their best-fitting values and fit c.

For this example, the value of c fitted in step 3 would be used as the final DM halo parameter estimate. Steps 1-2 would then be repeated in order to estimate Υ_*, say, and then step 1 repeated to finally estimate V_{200}. Deriving mass model parameters in this manner is clearly not

ideal since the final set of fitted parameters will depend on (1) the initial parameter estimates used in step 1, (2) the combinations of fixed and free parameters used in the remaining steps, and (3) the order in which the parameters are methodologically fixed.

To check the stability of the fitted parameters, the above-mentioned procedure was carried out several times in order to generate each mass model. Various sets of initial estimates were used as well as varied fix-free parameter combinations. The order in which the various parameters were fitted was also varied. Uncertainty estimates could not be obtained for some of the final parameter estimates due to these parameters being fixed when generating the final mass model. These parameters therefore do not have an associated uncertainty given in Table 4.5. Thus, in conclusion, for the NFW cases as well as the maximum disk pseudo-isothermal sphere case, the final parameters presented in Table 4.5 should be fairly well-converged, yet these mass models should only be used as an indication of the distribution of DM in NGC 1705.

4.6.3 Results and discussion

The resulting parameters for each mass model are listed in Table 4.5 while Fig. 4.22 shows the relative contributions to the observed rotation curve from the gaseous and stellar disks as well as the DM halo for each mass model. With the exception of the maximum disk case, all pseudo-isothermal sphere mass models are very well-fitted, allowing for excellent agreement between the observed and total rotation curves. In contrast, the NFW mass models are relatively poorly fit. For this reason, and because of the fairly non-standard manner in which their final parameters were estimated, the NFW models are not discussed further.

The best-fitting mass model for NGC 1705 is one in which the DM halo is parameterised as a pseudo-isothermal sphere with a core density of $\rho_0 = 0.091 \pm 0.001$ $M_\odot$ pc^{-3} and a core radius of $r_c = 1.2 \pm 0.1$ kpc. This occurs for the minimum disk case in which the stellar rotation curve does not contribute to the total rotation curve. An almost equally well-fitted mass model is obtained for the case in which $\Upsilon_* = 0.04$ is determined dynamically. For this model $\rho_0 = 0.082 \pm 0.009$ $M_\odot$ pc^{-3} and $r_c = 1.3 \pm 0.1$ kpc. The determination of $\Upsilon_* \sim 0.32$ for the stellar mass-to-light ratio, generated using the relations from Bell & de Jong (2001) and Oh et al. (2008), is a factor of eight larger than the corresponding dynamical estimate. The dynamical estimate of Υ_* matches closely the forced value of $\Upsilon_* = 0.0$ for best-fitting minimum-disk mass model. Consistent with the findings of de Blok & McGaugh (1997b), this result demonstrates that the rotation curve cannot reliably constrain the relative contribution of the stellar component. The pseudo-isothermal sphere mass modeling results are similar to those of Meurer et al. (1998). These authors estimated a core density of $\rho_o \sim 0.1$ $M_\odot$ pc^{-3}, very close to our best-fitting $\rho_0 = 0.091 \pm 0.001$ $M_\odot$ pc^{-3} estimate. Their fitted core radii,

Table 4.5: Mass modeling results for NGC 1705

		1	2	3	4	5	6	7	8
	DM halo	ISO_{fixed}	ISO_{max}	ISO_{min}	ISO_{free}	NFW_{fixed}	NFW_{max}	NFW_{min}	NFW_{free}
1	χ^2_{red}	0.28	23.61	0.01	0.02	39.80	53.44	48.80	5.21
2	r.m.s. (km s^{-1})	1.17	2.73	0.84	0.51	1.47	2.63	2.23	10.4
3	Υ_* ($M_\odot/L_\odot$)	0.32	0.72	0.0	0.04	0.32	0.72	0.0	0.03
4	ρ_0 (10^{-3} $M_\odot$ pc^{-3})	37.6 ± 2.2	57.9	91.1 ± 1.1	82.6 ± 9.6	...	...	...	...
5	r_c (kpc)	3.7 ± 1.8	1.4 ± 0.1	1.2 ± 0.1	1.3 ± 0.1	...	...	...	...
6	V_{200} (km s^{-1})	...	...	...	...	64.7	72.6 ± 10.4	50.9 ± 3.8	42.3 ± 4.2
7	c	...	...	...	...	9.3 ± 0.9	68	14.9	9.9
	At last measured pt:								
8	M_{tot} (10^8 $M_\odot$)	42.6	32.1	32.2	33.2	29.1	29.1	29.0	15.9
9	M_{HI}/M_{tot} (10^{-3})	40.3	53.5	53.4	51.7	59.2	59.2	59.4	108.1
10	M_{DM}/M_{tot} (10^{-2})	88.4	72.1	94.7	93.5	83.0	69.1	94.1	87.5
11	M_{DM}/M_{lum}	3.9	1.4	17.7	8.1	2.5	1.3	15.8	4.2
12	M_{tot}/L_B ($M_\odot/L_\odot$)	39.6	29.8	29.9	30.9	27.1	27.1	26.9	14.8

Comments on rows: Row 1: Reduced χ^2 goodness-of-fit statistic; Row 2: r.m.s. of the difference between the observed and total rotation curves; Row 3: stellar mass-to-light ratio; Row 4: central density for pseudo-isothermal sphere; Row 5: core radius for pseudo-isothermal sphere, Row 6: circular rotation speed at virial radius for NFW halo; Row 7: concentration parameter for NFW halo; Row 8: dynamical mass; Row 9: H I to total mass ratio; Row 10: Dark to total mass ratio; Row 11: Dark to luminous mass ratio; Row 12: Total mass to B-band light ratio.

Comments on columns: For each model, columns 1 and 5 show the mass modelling results for the case in which Υ_* is fixed to the predetermined value of 0.32. Columns 2 and 6 show the results for the maximum disk case while columns 3 and 7 are for the minimum disk case. Columns 4 and 8 show the results of models for which Υ_* was determined dynamically.

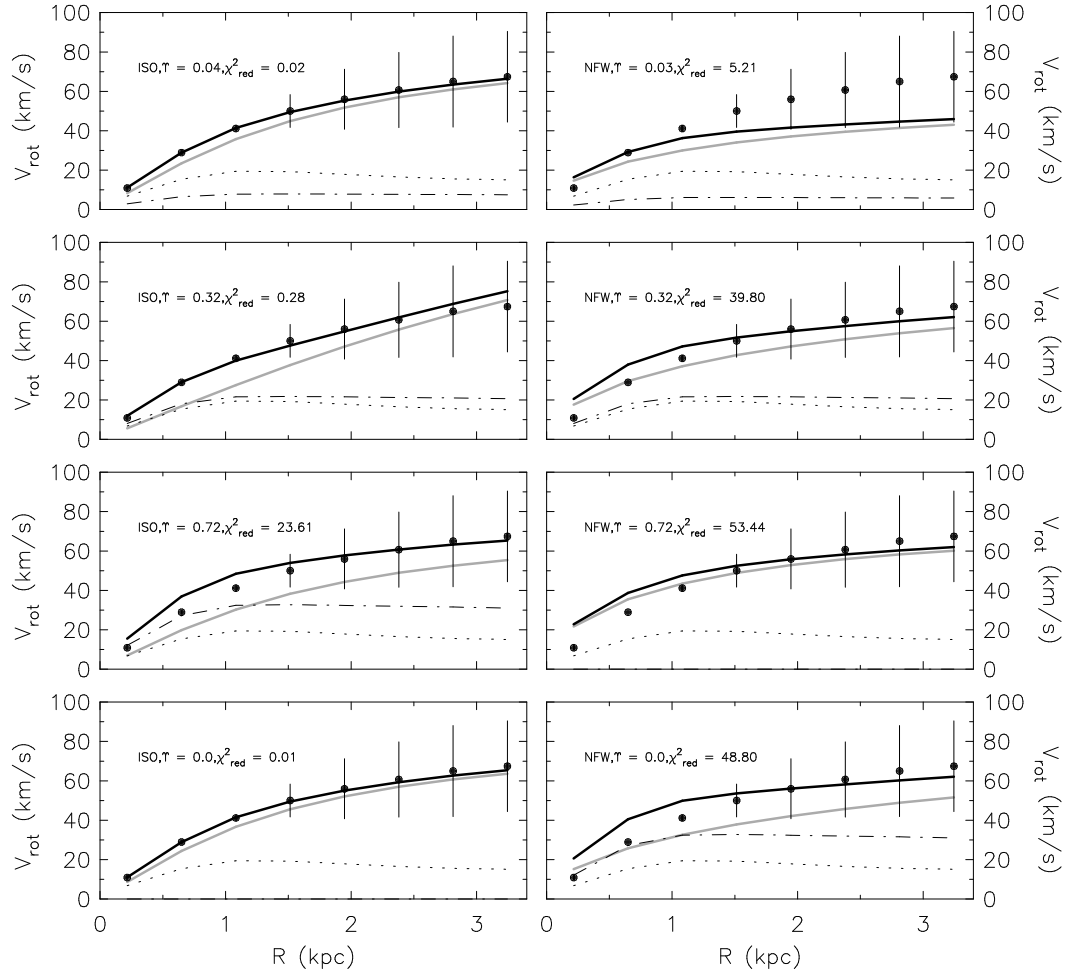

Figure 4.22: NGC 1705 mass models. The panels on the left show the fits using the pseudo-isothermal sphere while the panels on the right show the fits using an NFW halo. The top row shows the fits when Υ_* is determined dynamically. The second row shows the fits when the stellar rotation curve is scaled by our predetermined value of $\Upsilon_* = 0.32$. The third and fourth rows show the fits for the maximum and minimum disk cases respectively. In all panels the black filled circles represent the observed rotation curve while the error bars represent the absolute difference in the rotation curves derived separately for the receding and approaching halves of the galaxy. The black dot-dash curve shows the rotation curve of the stars. The black dotted curve shows the rotation curve of the gaseous disk. The solid grey curve shows the resulting rotation curve of the DM halo. Finally, the solid black curve represents the total rotation curve resulting from the best-fitting model. In each panel the reduced χ^2 goodness-of-fit statistic is presented.

however, range from $r_c = 0.74 - 1.2$ kpc, approximately a half to a third of the lengths of those presented in Table 4.5 which range from $r_c = 1.2 - 3.7$ kpc. The results of this work therefore show the dark matter core of NGC 1705 to be less compact than previously thought. Some authors suggest that the core densities of dark matter halos should be correlated with surface brightness. Meurer et al. (1998) argue that dark matter halos can regulate star formation by setting the critical density for self-gravitation of the ISM within the baryonic disk. They suggest that blue compact dwarfs such as NGC 1705 are expected to have stellar disk surface brightnesses ~ 2.5 mag arcsec^{-2} brighter than dwarf irregulars, as is typically observed.

It is clear that NGC 1705 is a very dark-matter-dominated galaxy. For the minimum disk case as well as the case in which Υ_* was determined dynamically, this statement holds at all radii. For the remaining cases the statement holds for radii beyond $R \sim 1.25$ kpc. Mass ratios as well as total mass to B-band light ratios are presented for each model in Table 4.5. For the pseudo-isothermal sphere mass models, the DM constitutes $\sim 87\%$ of the dynamical mass on average, corresponding to a dark mass of $M_{DM} \sim 3.1 \times 10^9$ M$_\odot$. This dark mass is much larger than the H I and stellar masses of $M_{HI} \sim 1.1 \times 10^8$ M$_\odot$ and $M_* \sim 8.0 \times 10^8$ M$_\odot$ respectively. This large dark mass component leads to a correspondingly large mean value of the total mass to B-band light ratio of $M_{tot}/L_B \sim 32.6$ M$_\odot$/L$_\odot$.

Compared to the THINGS sample of mass-modelled galaxies from de Blok et al. (2008), the inferred DM properties of NGC 1705 are relatively extreme. Figure 4.23 shows the fitted core densities and radii of the NGC 1705 pseudo-isothermal sphere mass models together with those of the THINGS sample. With the exception of the $\Upsilon_*^{3.6} = 0.32$ case, our fitted core densities are higher and the fitted core radii smaller than those of most of the THINGS galaxies. Thus NGC 1705 has a dark matter halo that is very dense and compact relative to other late-type systems. The only other galaxies that are as dark-matter-dominated as NGC 1705 are the early-type dSph galaxies which have typical core densities of ~ 0.5 M$_\odot$ pc^{-3} (Gilmore et al., 2007). Our estimated core density for NGC 1705 is hence not as extreme as its comparison to the THINGS late-type galaxies suggests it to be. In order to more directly compare the sort of mass modeling results that we have derived for NGC 1705 to the results of cosmological simulations, rotation curves from high-quality simulations would need to be fitted with stellar, gaseous and dark matter components. This would allow the results of cosmological simulations to be compared in the same parameter space to the mass models generated using observed rotation curves (e.g. Governato et al., 2010).

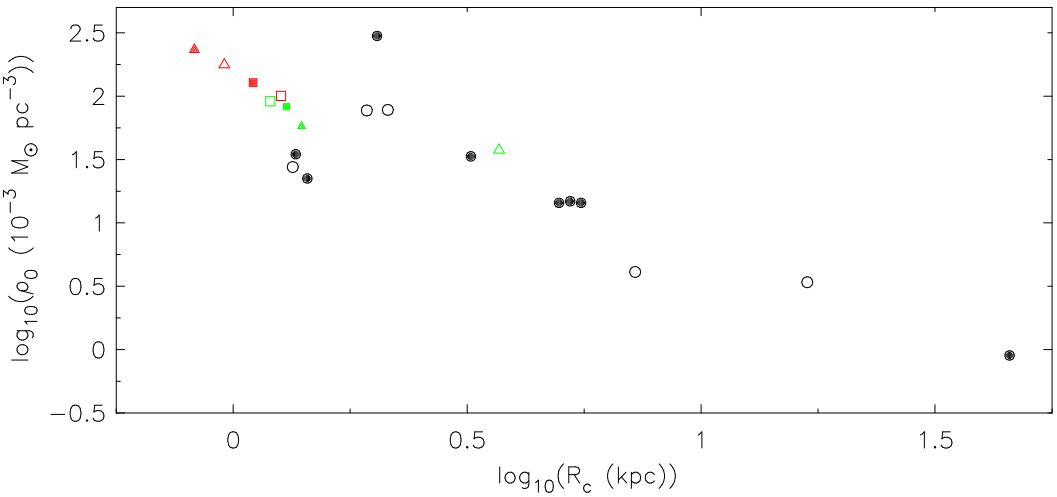

Figure 4.23: Mass modeling results for the cases in which the DM halo of NGC 1705 is modelled as a pseudo-isothermal sphere, compared to the mass modeling results of the THINGS sample of de Blok et al. (2008). Green filled and open squares represent, respectively, the case in which Υ_* varied freely and the minimum disk case. Green filled and open triangles represent, respectively, the maximum disk case and the case in which Υ_* was fixed to the pre-determined value of $\Upsilon_* = 0.32$. The mass modeling results from the THINGS sample of de Blok et al. (2008) are shown as open circles for dwarf galaxies and filled circles for all other galaxies. For comparison, the NGC 2915 mass modeling results from Fig. 3.12 are reproduced as red symbols

4.7 Chapter summary

New deep, sensitive H I synthesis observations of NGC 1705 have been obtained and used to investigate the H I properties of the system. Our high-resolution H I observations are able to clearly resolve the inner H I distribution into two over-densities which straddle the extremely luminous central super star cluster. As shown by Meurer et al. (1998), this star cluster is the main energy source powering a galactic outflow. The low resolution channel maps make clear the presence of a drawn-out H I feature, emanating from the centre of the galaxy and spanning $\sim$ 2.5 kpc. The H I velocity field of NGC 1705 shows the the extended H I feature not to be kinematically separated from the main disk of the galaxy.

A tilted ring model fitted to the H I velocity field yields a rotation curve that is inconsistent with the observations of the outer H I disk. An approach was therefore adopted in which the H I line profiles of an integrated position-velocity slice were parameterised in order to estimate their peak-associated velocities. The resulting rotation curve varies roughly as $V(R) \propto R$ all the way

out to the last measured point, typical of dwarf systems.

As for the previous chapter, the main results of this section pertain to the mass models generated for NGC 1705 which allow for a characterisation of the distribution of its dark matter content. The galaxy is dark-matter-dominated at all radii with a pseudo-isothermal sphere parameterisation of its dark matter halo allowing for mass models that accurately match the observations. The best-fitting mass model has a core density of $\rho_0 \sim 0.091 \pm 0.001$ $M_\odot$ pc^{-3} and a core radius of $r_c \sim 1.2 \pm 0.1$ kpc. The stellar disk does not contribute to the observed rotation curve in this mass model. At the last measured point on the rotation curve, a total mass to B-band light ratio of $M_{tot}/L_B \sim 32$ $M_\odot/L_B$ is estimated. No reliable, well-fitted NFW mass model could be obtained for NGC 1705. Although its dark matter properties are not as extreme as those inferred for NGC 2915, the galaxy's dark matter core is nevertheless very dense and compact in comparison to other late-type systems.

Chapter 5

Star formation in NGC 2915 and NGC 1705

5.1 Introduction

Galaxies are gravitationally bound systems of stars, gas and dark matter. The interaction and subsequent evolution of these components results in a change of the observable properties of the galaxy as a whole. A comprehensive understanding of the quantitative relationship between star formation (SF) activity and the properties of the inter-stellar medium (ISM) is therefore required to better constrain galaxy evolution models. Current observing facilities allow for high-quality multi-wavelength observations of comparable resolution and sensitivity to be carried out for nearby galaxies. These observations are used to test our theories of SF and its links with the ISM. Dwarf galaxies are particularly interesting in this regard because they are much simpler systems than larger spiral galaxies. They allow for unique examinations of SF processes together with their dependencies and effects on the ISM.

This chapter is dedicated to the quantitative study of the links between the observed SF activity and ISM properties in NGC 2915 and NGC 1705. The chapter is split into three broad sections. The first part presents the GALEX far ultra-violet (FUV) and *Spitzer* 24 μm data sets that are used to trace the SF activity in each galaxy. The second portion investigates star formation recipes - empirical relations between the SF activity and other observable quantities such as galactocentric radius, H I surface density and stellar surface density. The purpose of these comparisons is to understand which properties of each galaxy regulate efficient star formation

activity. Finally, the last part of the chapter deals with the investigation of star formation models that combine various properties of the ISM in an attempt to describe which parts of each galaxy should be actively producing stars. Both the success and failure of these models offer insight into the complex interplay between the various ISM properties that ultimately control the SF activity. Before entering into the discussions, an introduction to each of the SF recipes and models is presented in a separate, dedicated sub-section. The simplest SF models are presented first, followed by progressively more complex models.

NGC 2915 and NGC 1705 are not typical star-forming dwarfs. The former contains an extended H I disk with well-defined spiral structure, yet seemingly no ongoing star formation activity in its outer parts. The small stellar core is located at the very centre of the large H I disk where the observed H I surface densities are highest. NGC 1705 is a star-bursting galaxy. It too has its star-forming core at the centre of an extended H I disk, yet the integrated star formation rate is much higher than typical dwarfs. NGC 2915 and NGC 1705 have both been shown to be very dark-matter-dominated, containing dark matter cores that are denser and more compact than other typical late-type systems. The observed star formation activity and its links to the various mass components in each of these unusual systems needs to be understood. It shall be instructive to interpret the NGC 2915 and NGC 1705 findings in the context of the SF characteristics of other late-type systems. Wherever possible, the results presented in this chapter are compared to the results of Leroy et al. (2008) and Bigiel et al. (2008) who carried out similar analyses for samples of 23 and 19 THINGS galaxies respectively.

5.2 Tracing the star formation activity

A suitable tracer of the SF activity is required to carry out an analysis that is aimed at understanding the star-forming characteristics of a galaxy. One of the most widely used tracers of high-mass star formation is the Hα emission line arising from the recombination of ionised hydrogen. This traces a galaxy's SF over the relatively short lifetimes (a few million years) of the most massive stars. In recent years, GALEX observations of nearby galaxies have allowed the ultra-violet (UV) flux, originating from the photospheres of high-mass O- and B- type stars to be used as diagnostic for SF. As Lee et al. (2009) point out, a galaxy's UV flux probes a fuller mass spectrum of massive stars, and "thus measures star formation averaged over a longer $\sim 10^8$ yr time-scale".

Several authors (e.g. Salim et al. 2007 and references therein) have compared Hα and UV SFRs for nearby galaxies. The general consensus is that UV SFRs tend to be slightly lower than Hα SFRs. The discrepancy is attributed to the effects of internal dust extinction which

lowers the observed UV flux. When UV emission from high-mass stars is absorbed by dust, it is re-emitted at infrared wavelengths. Combining a measure of a star-forming galaxy's infrared emission with a measure of its UV emission should therefore yield a measure of the total SFR that is consistent with the rate inferred from Hα spectroscopic imaging. Calzetti et al. (2007), for a sample of 33 nearby galaxies observed with the the *Spitzer* MIPS instrument at 24 μm, showed that using the 24 μm emission to account for the dust extinction allows for an accurate determination of the total number of ionising photons in an HII region.

Both NGC 2915 and NGC 1705 have been observed with the GALEX satellite (Martin et al., 2005) as part of the GALEX Nearby Galaxy Survey (Gil de Paz et al., 2007) and with the *Spitzer* satellite as part of the *Spitzer* Nearby Galaxies Survey (SINGS, Kennicutt et al., 2003). The GALEX far ultra-violet and *Spitzer* 24 μm imaging of each galaxy is combined to estimate its total star formation rate. The remainder of this section is dedicated to presenting the GALEX and *Spitzer* images for each galaxy as well as describing the method used to generate the corresponding estimates of the total SFR.

5.2.1 GALEX far ultra-violet imaging

The GALEX far ultra-violet (FUV) band, centered at 1450 Å, covers the wavelength range 1350–1750 Å. The angular resolution for the FUV band is $\sim 4.5''$. The FUV imaging provides a direct measure of the average photospheric emission from young O- and B-type stars over time-scales of 10–100 Myr. The FUV image of each galaxy is combined with the 24 μm image to trace the total SFR. To facilitate a direct comparison of the FUV, 24 μm and the H I images of each galaxy, all images were placed on the same astrometric grid with the same spatial resolution. The FUV image of each galaxy was smoothed, using a Gaussian convolution function, to a resolution equal to the full-width-at-half maximum of the synthesised beam of the H I observations ($17'' \times 18.2''$ and $16.6'' \times 14.4''$ for NGC 2915 and NGC 1705 respectively). Next, these images were re-gridded to place them on the same $2.5'' \times 2.5''$astrometric grid as the H I line data. The smoothed, re-gridded FUV images of NGC 2915 and NGC 1705 are shown in Fig. 5.1 and Fig. 5.2 respectively.

The FUV data were photometrically calibrated and corrected for attenuation due to dust in the Galaxy. The Schlegel et al. (1998) dust extinction maps were used to estimate $E(B-V) \sim 0.^{\rm m}275$ and $E(B-V) \sim 0.^{\rm m}008$ for NGC 2915 and NGC 1705 respectively. These $B-V$ extinction measures were converted to FUV extinction magnitudes of $A_{FUV} = 8.24 \times E(B-V) = 2.^{\rm m}26$ and $A_{FUV} = 8.24 \times E(B-V) = 0.^{\rm m}06$ (Wyder et al., 2007). Neither the FUV nor 24 μm images of either galaxy suffer from significant star crowding effects. No foreground star subtraction was necessary.

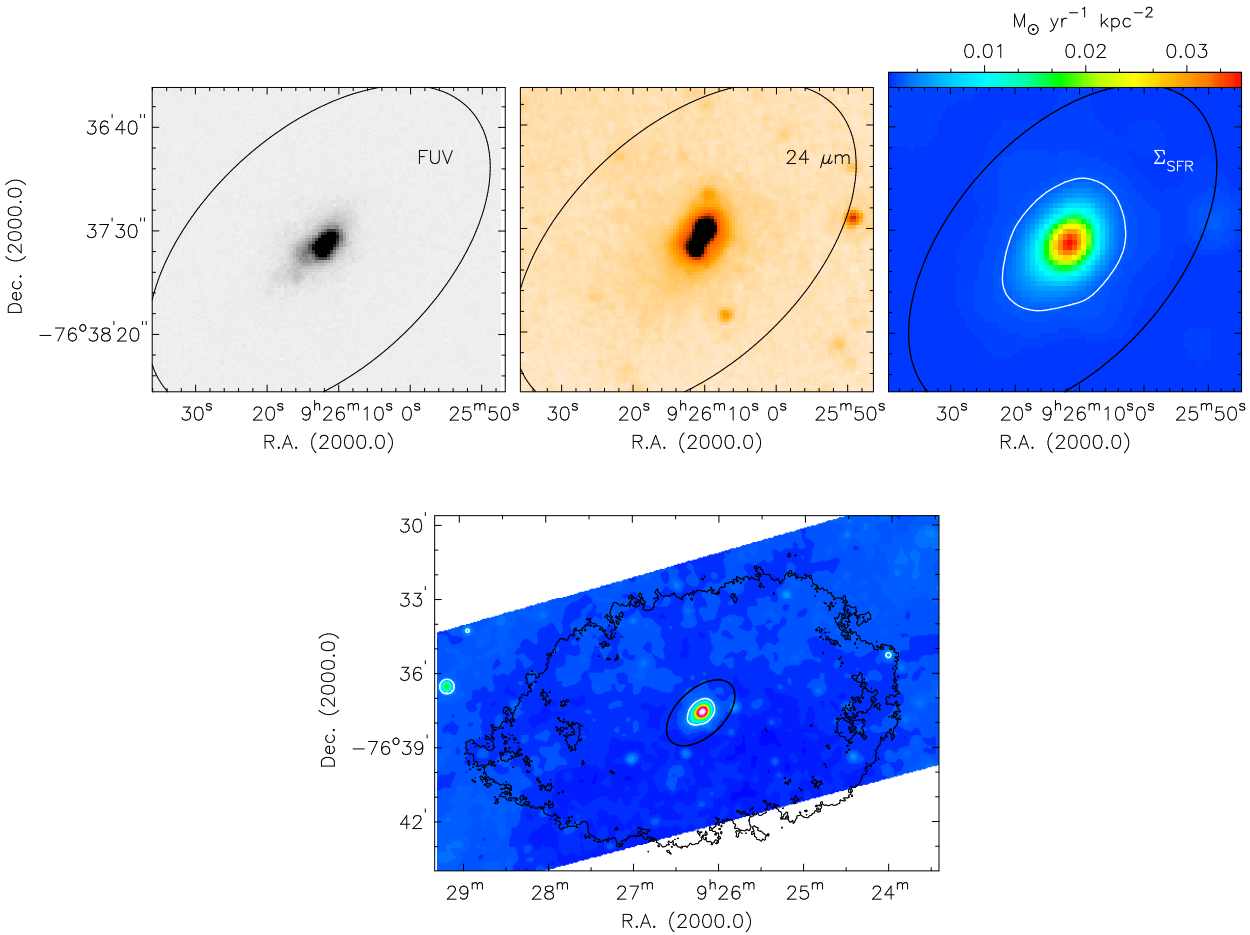

Figure 5.1: FUV, 24 μm and total star formation rate surface density maps for NGC 2915. **Top left:** GALEX FUV image of stellar core. **Top middle:** *Spitzer* 24 μm image of stellar core. The FUV and 24 μm images have been smoothed and re-gridded. **Top right:** Star formation rate surface density map for the stellar core, constructed by combining the smoothed, re-gridded, calibrated FUV and 24 μm images according to Eqn. 5.1. **Bottom panel:** The full star formation rate surface density map. The single black contour, representing the edge of H I disk, is at a flux density of 1.6 mJy beam^{-1} km s^{-1}. The white contour, at a level of 0.0018 M$_\odot$ yr^{-1} kpc^{-2}, is arbitrarily chosen to coincide with the approximate edge of the star-forming core of NGC 2915.

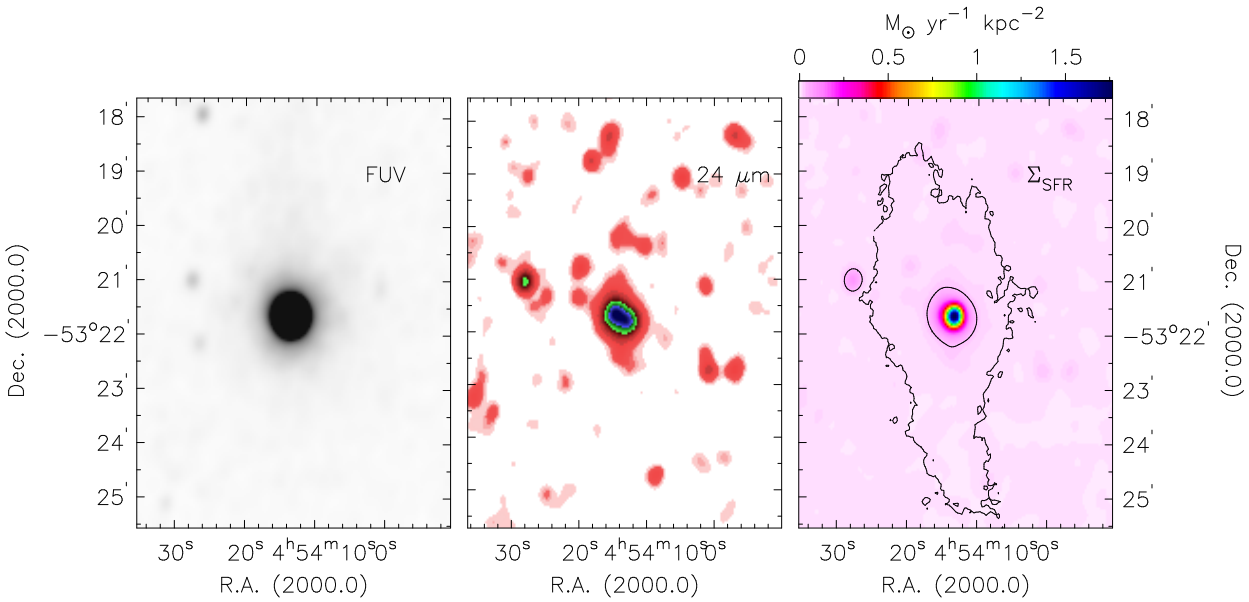

Figure 5.2: FUV, 24 μm and total star formation rate surface density maps for NGC 1705. **Left:** GALEX FUV image of stellar core. **Middle:** *Spitzer* 24 μm image of stellar core. The FUV and 24 μm images have been smoothed and re-gridded. **Right:** Star formation rate surface density map, constructed by combining the smoothed, re-gridded, calibrated FUV and 24μm images according to Eqn. 5.1. The outer black contour represents the approximate edge of the H I disk and is at an H I surface density level of 0.5 $M_\odot$ pc^{-2}. The inner black contour is arbitrarily chosen to coincide with the approximate edge of the star-forming core of NGC 1705 and is at a level of 0.1 $M_\odot$ yr^{-1} kpc^{-2}.

5.2.2 *Spitzer* 24 μm imaging

The MIPS instrument onboard the *Spitzer* satellite has a pointed field-of-view of $5.4' \times 5.4'$ in the 24 μm band with a resolution of $\sim 6''$ and high signal-to-noise ratios. As with the GALEX FUV images of each galaxy, the 24 μm images were similarly smoothed and re-gridded to make them directly comparable to the H I data. Bigiel et al. (2008) allude to the fact that the MIPS point-spread-function at 24 μm is severely non-Gaussian, yet presents no significant problems when the data are smoothed to resolutions of $\sim 20''$. Again, no foreground star subtraction was performed for either galaxy. The smoothed, re-gridded 24 μm images of NGC 2915 and NGC 1705 are shown in Fig. 5.1 and Fig. 5.2 respectively.

The above-applied correction for dust attenuation compensates for the amount of FUV emission obscured by dust in our own Galaxy. It does not, however, account for internal extinction due to dust *within* the target galaxies. Without correcting for this, the FUV image alone gives an underestimate of the total SFR (Lagache et al., 2005). As Kennicutt (1998) points out, this extinction serves as one of the largest sources of systematic error in SFR measurements. The *integrated* infrared emission of a galaxy is needed to measure the total dust-obscured SFR. However, specific infrared passbands can be used instead (Kennicutt et al., 2009). Calzetti et al. (2007) calibrated the *Spitzer* 24 μm band as a high-mass SFR tracer. As an example of its application, Bendo et al. (2007) chose MIPS 24 μm imaging of 65 SINGS galaxies as their preferred tracer of the dust-obscured SFR. For this thesis, the *Spitzer* 24 μm imaging of each galaxy is utilised as the tracer of the dust-obscured high-mass SFR.

It is interesting to note that the 24 μm image of NGC 1705 (Fig. 5.2, middle panel) shows low-level 24 μm emission that is elongated in a North-South direction. This is similar to the elongation of the second-order moments seen in Fig. 4.11 , and has a similar spatial extent to that of the plume-like H I feature seen in the H I total intensity maps (Fig. 4.8).

5.2.3 The total star formation rate

We use the GALEX FUV and *Spitzer* 24 μm imaging to trace the directly observable and dust-obscured SFRs of each galaxy. The prescription of Leroy et al. (2008) is used to linearly combine these images to yield our preferred diagnostic of the total SFR, the total SFR surface density, Σ_{SFR}, in units of $M_\odot$ yr^{-1} kpc^{-2}:

$$\frac{\Sigma_{SFR}}{M_\odot \text{ yr}^{-1} \text{ kpc}^{-2}} = 3.2 \times 10^{-3} \frac{I_{24}}{\text{MJy ster}^{-1}} + 8.1 \times 10^{-2} \frac{I_{FUV}}{\text{MJy ster}^{-1}}, \qquad (5.1)$$

where I_{24} and I_{FUV} are the 24 μm and FUV surface brightness respectively. Very importantly, Leroy et al. (2008) show that this choice of coefficients yields Σ_{SFR} values that are consistent

with the Hα-24 μm calibration of Calzetti et al. (2007) and that, when the 24 μm emission is ignored, the FUV Σ_{SFR} estimates reduce to those of Salim et al. (2007). The calibration of Σ_{SFR} uses the IMF from Calzetti et al. (2007), which is a Kroupa-type two-component IMF that extends to 120 $M_{\odot}$. Some authors (e.g. Meurer et al., 2009) argue that the IMF is not universal, and that the slope of the upper end varies systematically. A non-universal IMF implies that the SFR measured in a galaxy is highly sensitive to the tracer used in the measurement. However, in this work we assume a standard two-component Kroupa IMF.

The Σ_{SFR} maps for NGC 2915 and NGC 1705 are shown in Fig. 5.1 and Fig. 5.2 respectively. A discussion of the estimated total SFRs is presented in the subsequent sections of this chapter. In Fig. 5.3, the radial profiles of the SFR surface densities derived from the individual FUV and 24 μm images as well as the total SFR surface density map are presented for NGC 2915 and NGC 1705 (top and bottom panels of respectively). These radial profiles show that the effects of dust extinction on the FUV radiation are relatively unimportant for these two galaxies. All SFR surface density radial profiles were inclination-corrected (by 55° and 45° for NGC 2915 and NGC 1705 respectively), and hence represent the face-on estimates. Some of the SFR surface densities derived from the smoothed, re-gridded 24 μm maps drop below zero, leading to slightly lower total SFR surface densities than the FUV SFR surface densities. Although the negative SFR surface densities from the 24 μm map are non-physical, we do not correct for them since their effect on the total SFR surface densities is negligible. The uncertainty in each of the azimuthally-averaged total SFR surface densities is estimated as the r.m.s. spread of Σ_{SFR} with a 17″-wide ring. The r.m.s. spread is expected to over-estimate the uncertainty near the centre of the galaxies where the Σ_{SFR} estimates are high. This is because much of the variation in Σ_{SFR} probably comes from real structure within the galaxies. At the faint end of the profile, the uncertainty is expected to be slightly under-estimated due to the fact that we have not included the systematic error associated with the sky level. Figure 5.3 shows that the highest star formation rates do indeed occur within the stellar disk of each galaxy. The observed SFRs within NGC 2915 drop off sharply with radius, reaching zero with $R \sim 0.5R_{25} = 49''$. A more gradual decline is observed for NGC 1705, with the total SFR continuing to drop beyond the R_{25} radius.

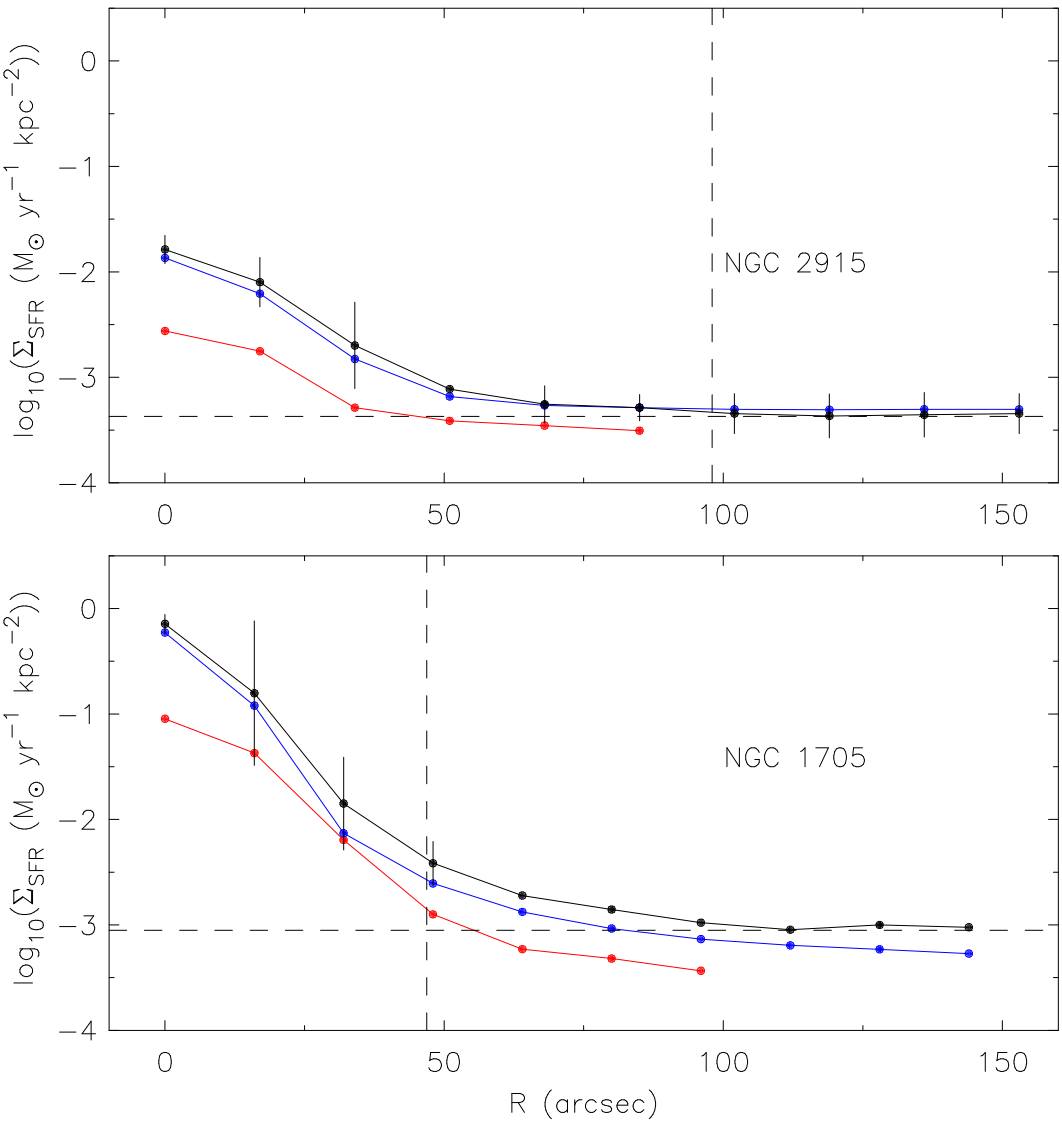

Figure 5.3: Radial profiles of the star formation rate surface densities measured from the smoothed, re-gridded MIPS 24 μm **(solid red curves)** and FUV maps **(solid blue curves)** and their linear combination (according to Eqn. 5.1), the total star formation rate surface density **(solid black curves)** for NGC 2915 and NGC 1705. The dashed horizontal lines represent the star formation rate surface density backgrounds of $10^{-3.37}$ and $10^{-3.05}$ $M_\odot$ yr^{-1} kpc^{-2} for NGC 2915 and NGC 1705, respectively. The dashed vertical lines represent the R-band R_{25} radius of each galaxy. Note that some of the azimuthally-averaged 24 μm surface densities drop below zero, they are therefore not included in these logarithmic plots. The negative values cause the total SFR to drop slightly below the FUV SFR at some outer radii. Error bars represent the r.m.s. spread of Σ_{SFR} within an azimuthally-averaged ring. For the sake of clarity, error bars are not shown for the FUV and 24 μm profiles.

5.3 Star formation recipes

5.3.1 Introduction

Empirical relations between the SFR and other galaxy properties provide insight into how efficiently galaxies convert their ISM into stars. A quantitative understanding of the relationship between the SFR and the properties of the ISM in nearby galaxies is not yet well-understood, yet is essential for understanding galaxy evolution. Sections 5.3.2–5.3.4 are dedicated to measuring the SFR and star formation efficiency as a function of galactocentric radius, H I surface density and stellar surface density in NGC 2915 and NGC 1705. The complementary, high-quality multi-wavelength FUV, 24 μm and H I data allow comparisons of the SFR with the above-mentioned galaxy properties on a pixel-by-pixel basis in order to accurately search for empirical relations. Until recently, such analyses have been limited by the lack of a combination of multi-wavelength data sets of comparable quality.

Wherever possible, the results for the inner parts of NGC 2915 and NGC 1705 ($R \lesssim 1.2{-}2R_{25}$) are compared to the results of Leroy et al. (2008). They carried out similar analyses for a sample of 23 THINGS galaxies, 11 of which were dwarfs. In these comparisons, galactocentric radius is expressed in terms of the R-band R_{25} radius of each galaxy. Leroy et al. (2008) use the star formation efficiency (SFE) rather than the SFR surface density as their preferred SF tracer. The two quantities are related to one another via the gas surface density, Σ_{gas}. The SFE is defined by Leroy et al. 2008 as being the SFR surface density per unit gas surface density along a line of sight, i.e. $SFE = \Sigma_{SFR}/\Sigma_{gas}$. The definition of the SFE is the inverse of the gas depletion time, the time for ongoing SF to deplete the current gas supply. The SFR *and* SFE results for each SF recipe are presented for NGC 2915 and NGC 1705.

No published CO data exist for NGC 2915 and NGC 1705. It's the CO that is used to trace the molecular hydrogen content which cannot be observed directly. For this reason, the gas surface densities, usually treated as the sum of the atomic and molecular hydrogen surface densities, are necessarily approximated by the H I surface densities throughout this chapter, i.e. $\Sigma_{gas} \approx \Sigma_{HI}$ is assumed. Indeed, NGC 1705 is known to show no signs of CO content to very sensitive levels (Greve et al., 1996; Hoopes et al., 2004)

5.3.2 Galactocentric radius

To begin with, the relationship between the SF activity and galactocentric radius is investigated. Plots of Σ_{SFR} versus R and SFE versus R for each galaxy are shown in Fig. 5.4 and Fig. 5.5

respectively. For comparative purposes the plot of SFE versus R from Leroy et al. (2008) for 11 dwarf galaxies in their THINGS sample is shown in Fig. 5.6.

The most striking feature of Fig. 5.4 is the general trend of an exponentially decreasing SFR surface density when moving radially outwards from the centre of each galaxy. For NGC 2915 the trend is seen out to $\sim 0.6R_{25}$, albeit with a large scatter of ~ 1 dex. Beyond $R \sim 0.6R_{25}$ the SFR surface density remains approximately constant at the level of the background noise (i.e. no star formation). NGC 1705 exhibits a similar exponential trend all the way out to $R \sim 2R_{25}$ with considerably less scatter. At $R \sim 2R_{25}$ the SFR surface densities reach the background noise level.

To better place these radial trends in the context of other dwarf systems, we consider the radial variation of each galaxy's SFE as opposed to its SFR surface density. These results (Fig. 5.5) are directly comparable with those of Leroy et al. (2008) (Fig. 5.6). Included as a solid red line in each panel of Fig. 5.5 is the relation between SFE and R determined by Leroy et al. (2008) for their sample of 11 dwarf galaxies. The scatter about this regression is ~ 0.4 dex (a factor of ~ 2.5).

Both NGC 2915 and NGC 1705 have SFEs that decrease exponentially as a function of galactocentric radius. The measured SFEs for the star-bursting NGC 1705 are a factor $\gtrsim 100$ higher than the SFEs found by Leroy et al. (2008). The average SFR for the inner $R \leq 1.2R_{25}$ region of NGC 1705 is measured to be SFR ~ 24 $M_{\odot}$ yr^{-1}. This system is therefore converting its gas into stars much more efficiently than other dwarf galaxies at its centre. Gas depletion times range from $\sim 10^7$ yr at its centre to $\sim 10^8$ yr at $R \sim R_{25}$. The central gas reservoir of NGC 1705 should thus be depleted on time-scales much shorter than the Hubble time, an event that will eventually quench the galaxy's SF. The situation is not as extreme for NGC 2915. It's average SFR for the inner $R \leq 1.2R_{25}$ region is SFR ~ 0.3 $M_{\odot}$ yr^{-1}, almost two orders of magnitude lower than NGC 1705. In the context of the Leroy et al. (2008) results, it is clear that SFE in NGC 2915 drops off more rapidly with radius than it does in other dwarf galaxies.

5.3.3 HI surface density

What is the underlying cause of the radially decreasing SFEs observed in NGC 2915 and NGC 1705? Is the efficiency of the SF regulatory process itself decreasing with radius, thereby resulting in a corresponding observed decrease in SFE? To begin answering this question, trends in SFE with H I surface density within each galaxy are explored. The results are interpreted in the context of the Kennicutt-Schmidt law (Kennicutt, 1998). The results are also compared to the results of Leroy et al. (2008).

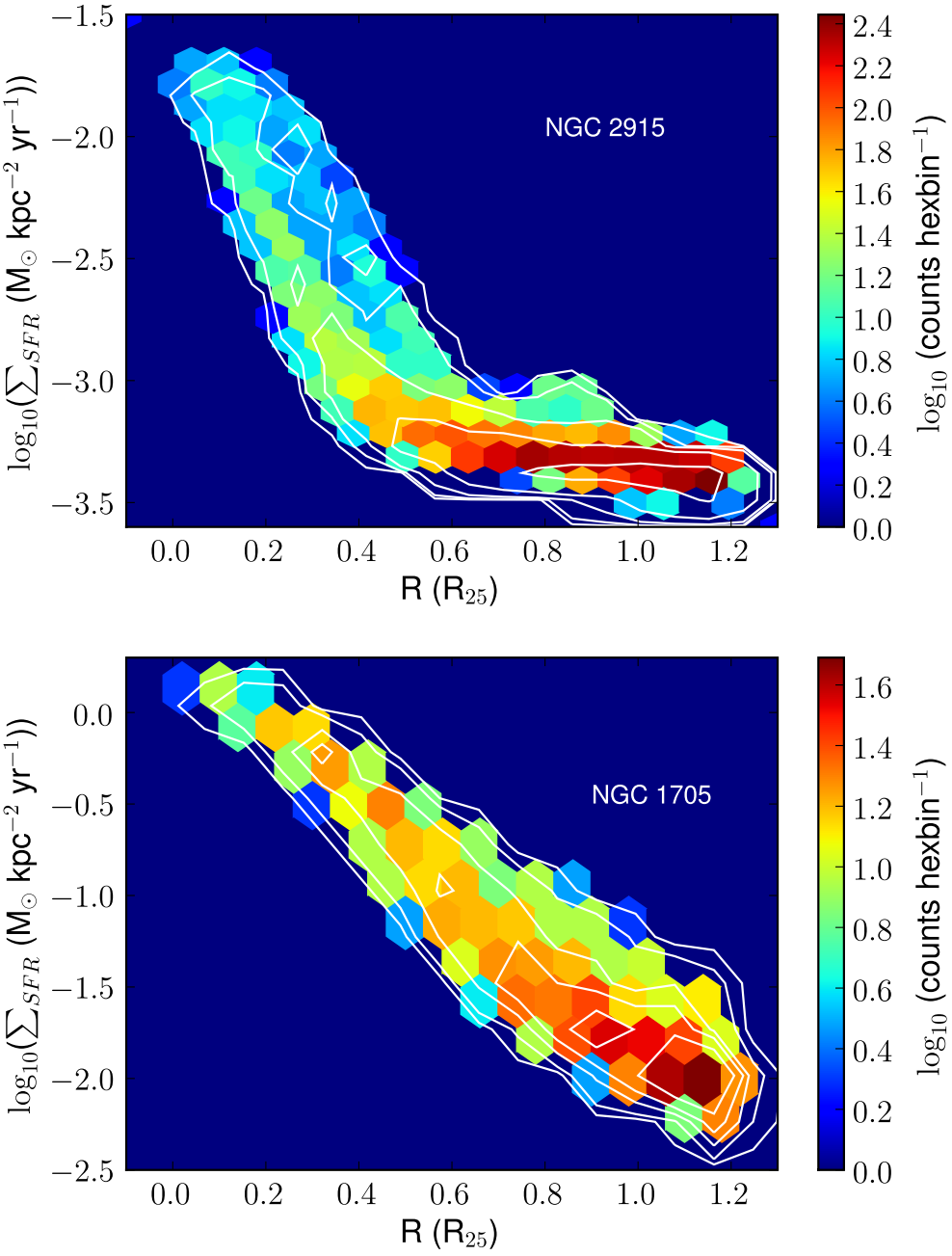

Figure 5.4: Total star formation rate surface density as a function of galactocentric in NGC 2915 and NGC 1705. The plot region is sub-divided into hexagonal bins. The colour bar indicates the logarithm of the number of points within each hexagonal bin. The white contours are at levels of $\log_{10}$(0.3, 0.8, 1.3, 1.8, 2.3) for the upper panel, and $\log_{10}$(0.3, 0.7, 1.1, 1.3, 1.5) for the lower panel.

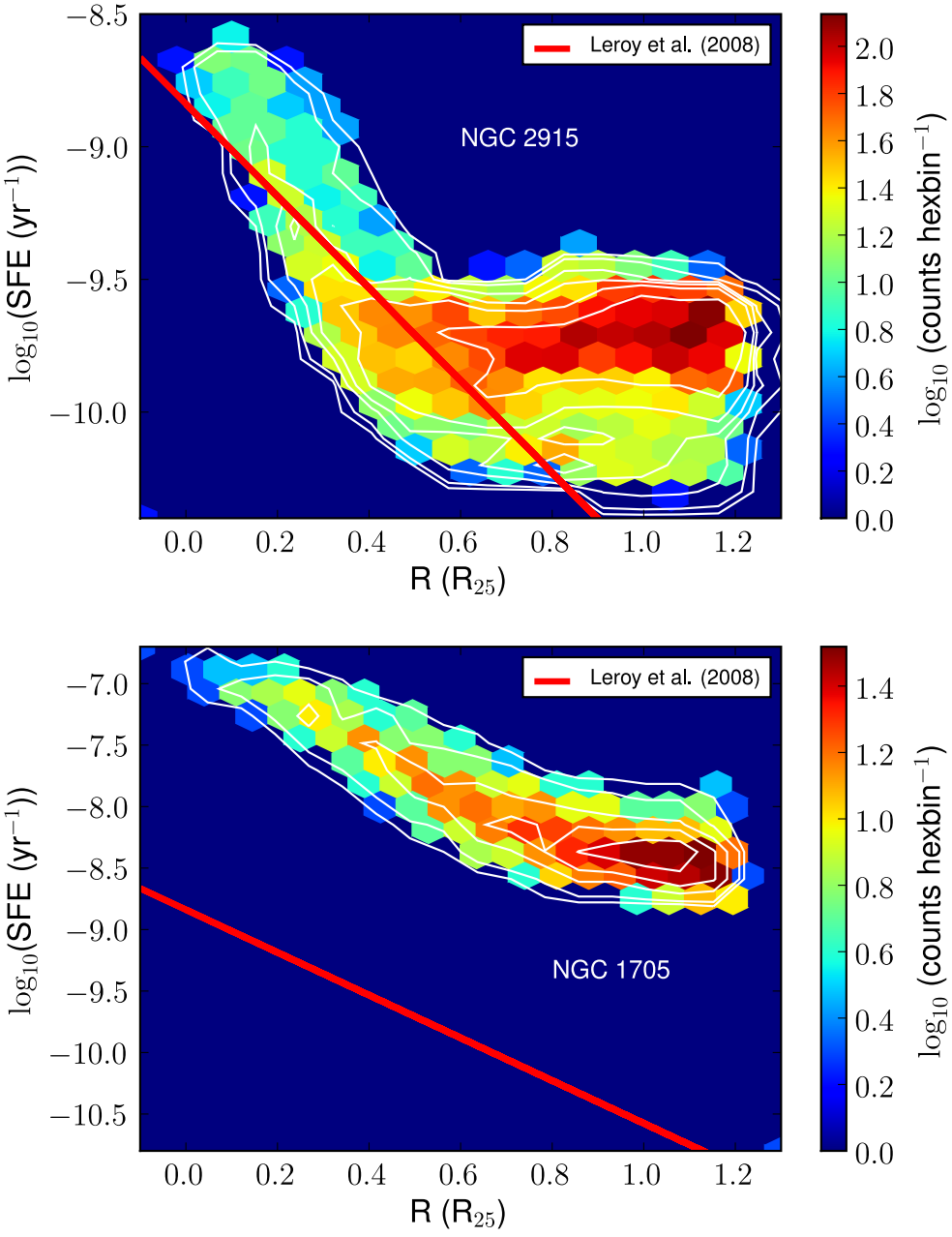

Figure 5.5: Star formation efficiency as a function of galactocentric radius in NGC 2915 and NGC 1705. The plot region is sub-divided into hexagonal bins. The colour bar indicates the logarithm of the number of points within each hexagonal bin. The white contours are at levels of $\log_{10}$(0.3, 0.7, 1.1, 1.3, 1.5,1.8) for the upper panel, and $\log_{10}$(0.3, 0.7, 1.1, 1.3, 1.5) for the lower panel. The solid red line represents the relation between SFE and R measured by Leroy et al. (2008) using their sample of 11 THINGS dwarf galaxies (i.e. the dashed line in Fig. 5.6).

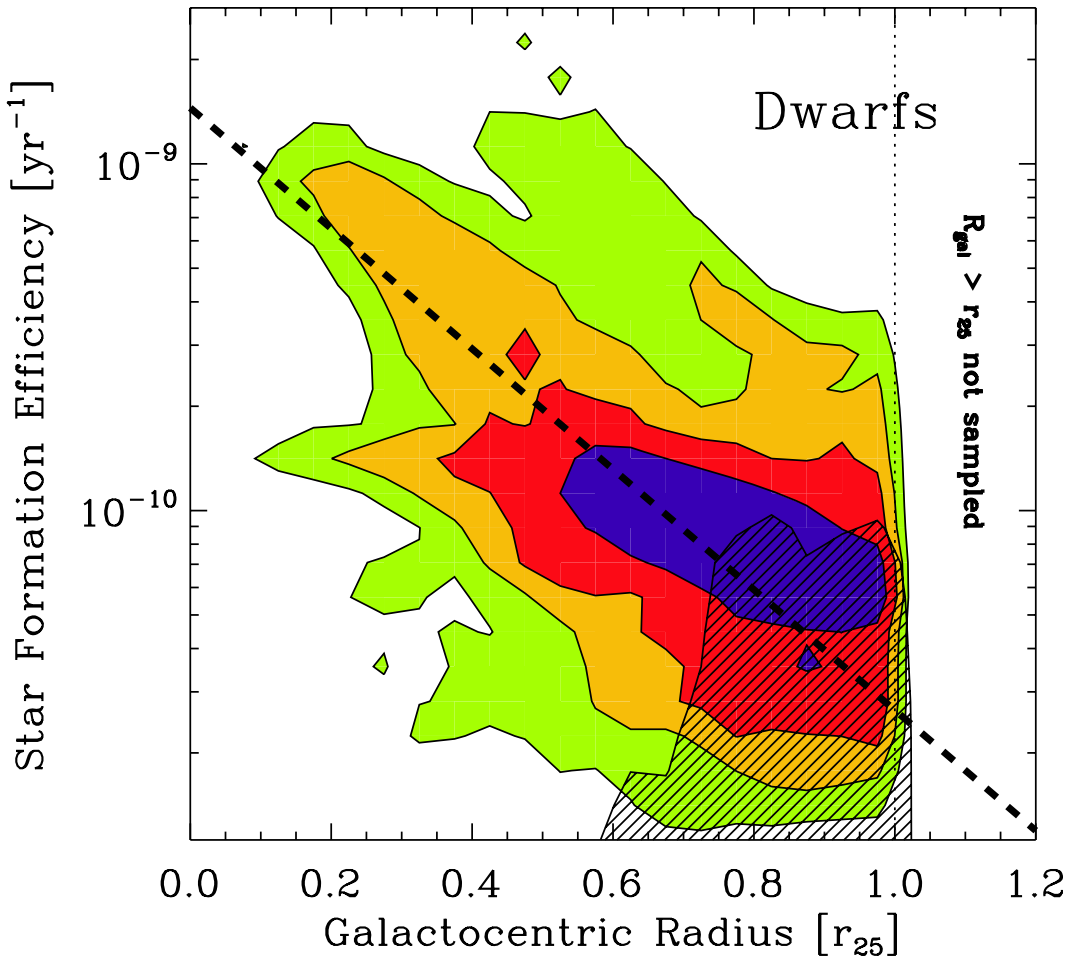

Figure 5.6: Star formation efficiency as a function of galactocentric radius for the THINGS sample of dwarf galaxies, taken from Leroy et al. (2008). The figure shows data from 11 dwarf galaxies for individual lines of sight. Equal weight is given to each galaxy and contours include 90%, 75%, 50% and 25% of the data. The hatched region indicates where the THINGS survey is incomplete. The thick dashed line shows the relation of SFE to galactocentric radius (their Eqn. 23).

Introduction

A galaxy's gas reservoir serves as its main source of fuel for star formation. Observed SF activity is therefore expected to correlate with the spatial distribution of the gas. Schmidt (1959) was the first to relate the SFR of the Galaxy to the density of its interstellar gas via a power law. He suggested that the SFR volume density and gas volume density, ρ_{SFR} and ρ_{gas} respectively, are related according to

$$\rho_{SFR} \propto \rho_{gas}^{n}, \tag{5.2}$$

with $n \sim 2$. Kennicutt (1989) reassessed the dependence of the massive star formation rate on the density and dynamics of inter-stellar gas. For a sample of 15 galaxies, a Schmidt-type power law was found to represent the two observables. The relationship was further assessed by Kennicutt (1998) who measured the distribution of Hα emission in a sample of 97 nearby galaxies, including spirals, luminous infrared galaxies and star-bursting galaxies. By averaging the observable quantities over the entire disk of each galaxy, he found the calibrated, directly observable form of the Schmidt law (expressed in terms of surface densities) to be

$$\Sigma_{SFR} = (2.5 \pm 0.7) \times 10^{-4} \Sigma_{gas}^{1.4 \pm 0.15}, \tag{5.3}$$

where Σ_{SFR} and Σ_{gas} are the SFR and gas surface densities in units of $M_{\odot}$ yr^{-1} kpc^{-2} and $M_{\odot}$ pc^{-2} respectively. This relation is commonly referred to as the Kennicutt-Schmidt law. Kennicutt (1998) points out that the scatter in the relationship must be real, reflecting a real variation in the mean Kennicutt-Schmidt law. This law therefore provides a convenient means of specifying the overall SF properties of a gas disk. Present day high-resolution observations of the neutral and molecular gas in nearby galaxies allow for better constraints on the correlations between these properties and the observed star formation activity of a galaxy.

Face-on HI surface densities

To allow for a pixel-by-pixel comparison of the SF activity and the H I surface densities of each galaxy, the observed H I surface densities have to be inclination-corrected to bring them in line with the true face-on surface densities. Based on the shapes of the outer total H I flux contours, an inclination of 55° was estimated for the H I disk of NGC 2915. All observed NGC 2915 H I surface densities were scaled by a constant factor of cos(55°) to obtain the corresponding face-on surface density estimates.

As mentioned in Sec. 4.8 of Chapter 4, Meurer et al. (1998) provide a parameterisation of the approximate face-on H I column densities of NGC 1705: $\log_{10} \Sigma_{HI} = 19.86 - 0.00169R + 1.46 \exp(-[R/50.2]^2/2)$. The directly-observed H I column densities of NGC 1705 will be higher

than the parameterised values due the H I disk of the galaxy being highly inclined. A constant inclination of 78° for the H I disk of NGC 1705 was assumed by Meurer et al. (1998). Using this inclination, the inclination-corrected radial profile of the observed NGC 1705 surface densities is shown as black-filled squares in Fig. 5.7. For comparison the radial profile of the face-on surface densities from Meurer et al. (1998) is shown as a blue curve. The two profiles are clearly inconsistent with one another for $R \lesssim 60''$, suggesting that an inclination correction factor of cos(78°) cannot be used for the observed HI surface densities. Also shown in Fig. 5.7 as red-filled circles is the inclination-corrected radial profile generated by assuming an H I disk inclination of 60°. This radial profile traces very closely the profile of Meurer et al. (1998). For this reason, all observed H I surface densities for NGC 1705 are scaled by a factor of cos(60°) throughout this chapter, for all SF recipes and models that require a measure of Σ_{HI}

NGC 2915 and NGC 1705 results and discussion

Plots of Σ_{SFR} and SFE versus Σ_{HI} are shown in Fig. 5.8 and Fig. 5.9 for each galaxy. For comparative purposes the plot of SFE versus Σ_{HI} from Leroy et al. (2008) for all 11 of the dwarf galaxies in their THINGS sample is reproduced in Fig. 5.10.

NGC 2915 exhibits no significant correlation between Σ_{SFR} and Σ_{HI}. For any given H I surface density in the range $10^{0.6} - 10^{1}$ $\log_{10} \Sigma_{HI}$ ($\sim 4 - 10$ $M_{\odot}$ pc^{-2}), the corresponding SFR surface densities vary by a factor of ~ 10. The H I surface densities therefore do not seem to efficiently predict the SF activity in NGC 2915, and they cannot account for the observed radial declines in Σ_{SFR} and SFE in Fig. 5.8 and Fig. 5.9. Our results can be compared to those of Bigiel et al. (2008) who carried out a sub-kpc resolution investigation of the links between Σ_{SFR} and Σ_{gas} for a sample of seven spiral and 11 late-type/dwarf THINGS galaxies. These authors investigated how the SF law differs between the the H_2-dominated centres of spirals, their H I-dominated outer disks and the H I-dominated dwarf systems. One of their main results is that a Schmidt-type power law does not successfully relate the observed SFR to the total gas surface density, with most galaxies showing little or no correlation between the two observable properties. They do, however, find that a molecular Kennicutt-Schmidt-type law ($\Sigma_{gas} = \Sigma_{H_2}$) with index $N = 1.0 \pm 0.2$ is able to relate the SFRs and H_2 surface densities in their sample. This H_2 Schmidt law becomes a total gas Schmidt law within the stellar disks of spirals where the H_2 usually dominates the ISM. Without any information of the H_2 content of NGC 2915, it can only be speculated that a similar molecular Kennicutt-Schmidt law might hold true for the galaxy.

The SFR surface density in NGC 1705 shows more of an exponential correlation with the observed H I surface densities, suggesting that Σ_{HI} plays a more significant role in regulating the

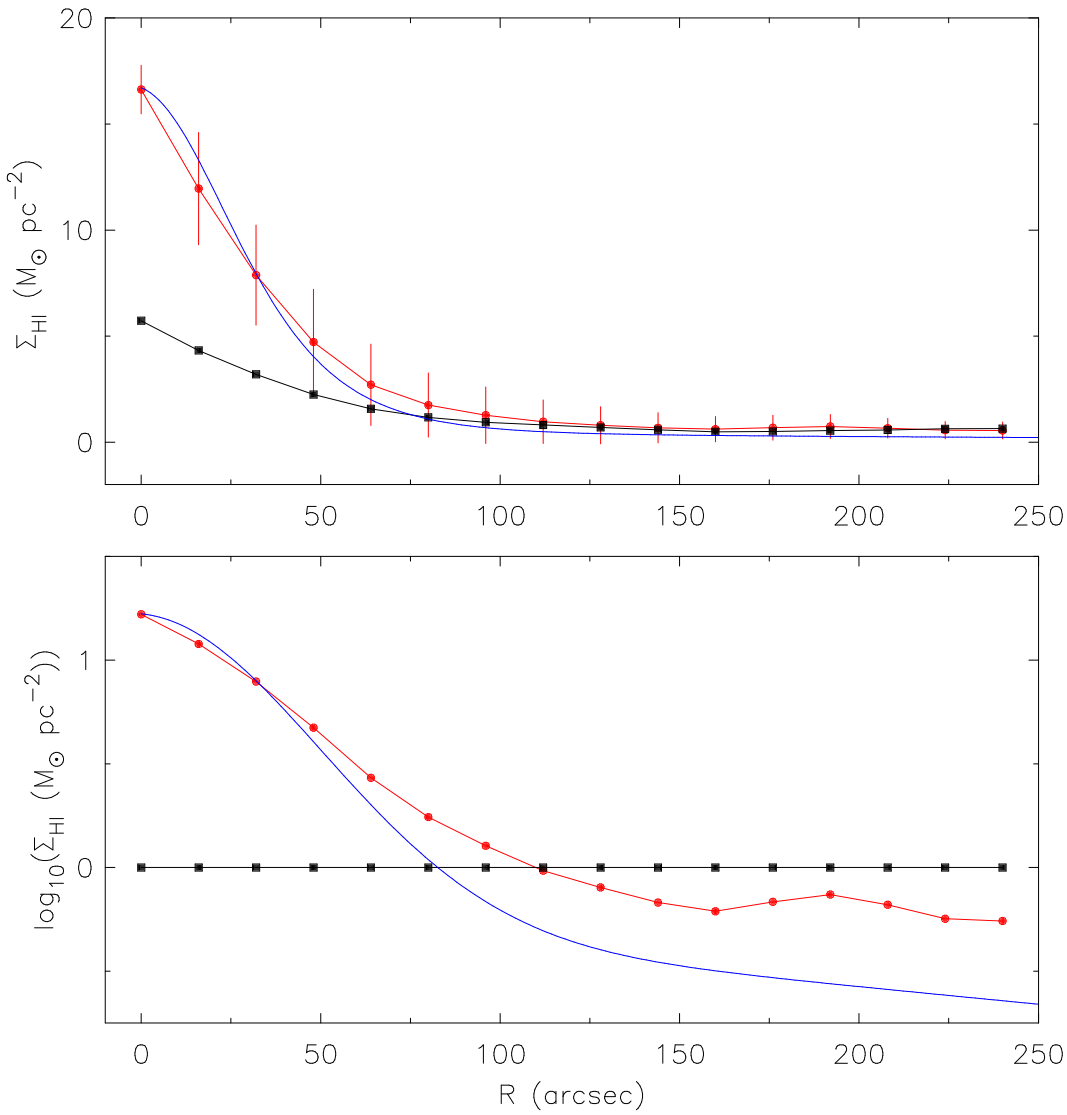

Figure 5.7: Comparisons between face-on H I surface densities from Meurer et al. (1998) (blue curve) and inclination-corrected H I surface density radial profiles for NGC 1705. The profiles represented by the red-filled circles and black-filled squares were generated assuming inclinations of 60° and 78° of the H I disk. The error bars in the top panel represent the r.m.s. spread of the observed H I surface densities in a ring of thickness 16″. For the sake of clarity, no error bars are shown for the 78° profile. The top and bottom panels use linear and logarithmic ordinates respectively.

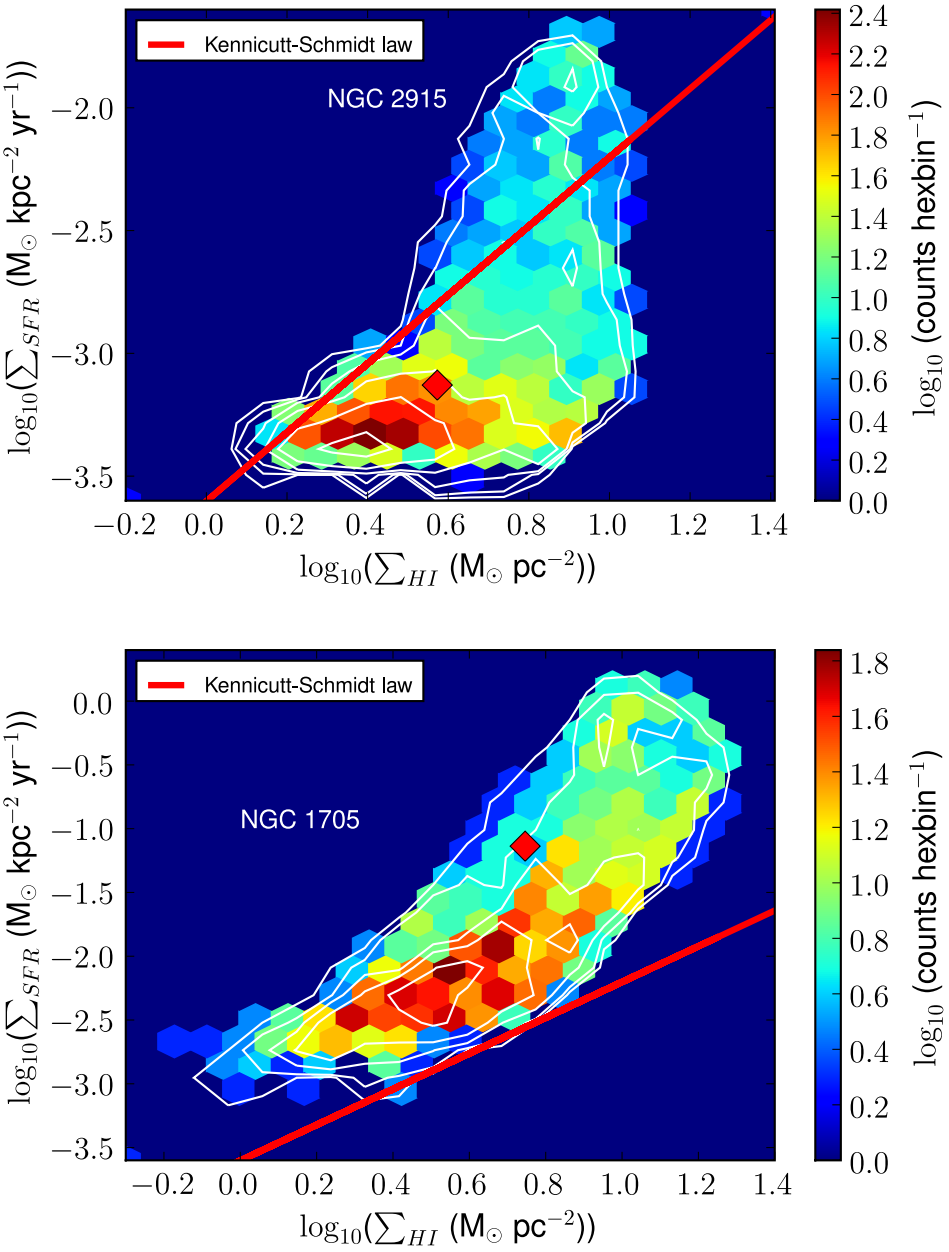

Figure 5.8: Total star formation rate surface density as a function of H I surface density for the inner $R \leq 1.2R_{25}$ portions of NGC 2915 and NGC 1705. The plot region is sub-divided into hexagonal bins. The white contours are at levels of $\log_{10}$(0.3, 0.7, 1.1, 1.3, 1.5,1.9, 2.3) for the upper panel, and $\log_{10}$(0.3, 0.7, 1.1, 1.4, 1.7, 2.0) for the lower panel. The colour bar indicates the logarithm of the number of points within each hexagonal bin. The solid red line represents the Kennicutt-Schmidt law. The solid red diamond marker represents the disk-averaged Σ_{SFR} and Σ_{HI} values.

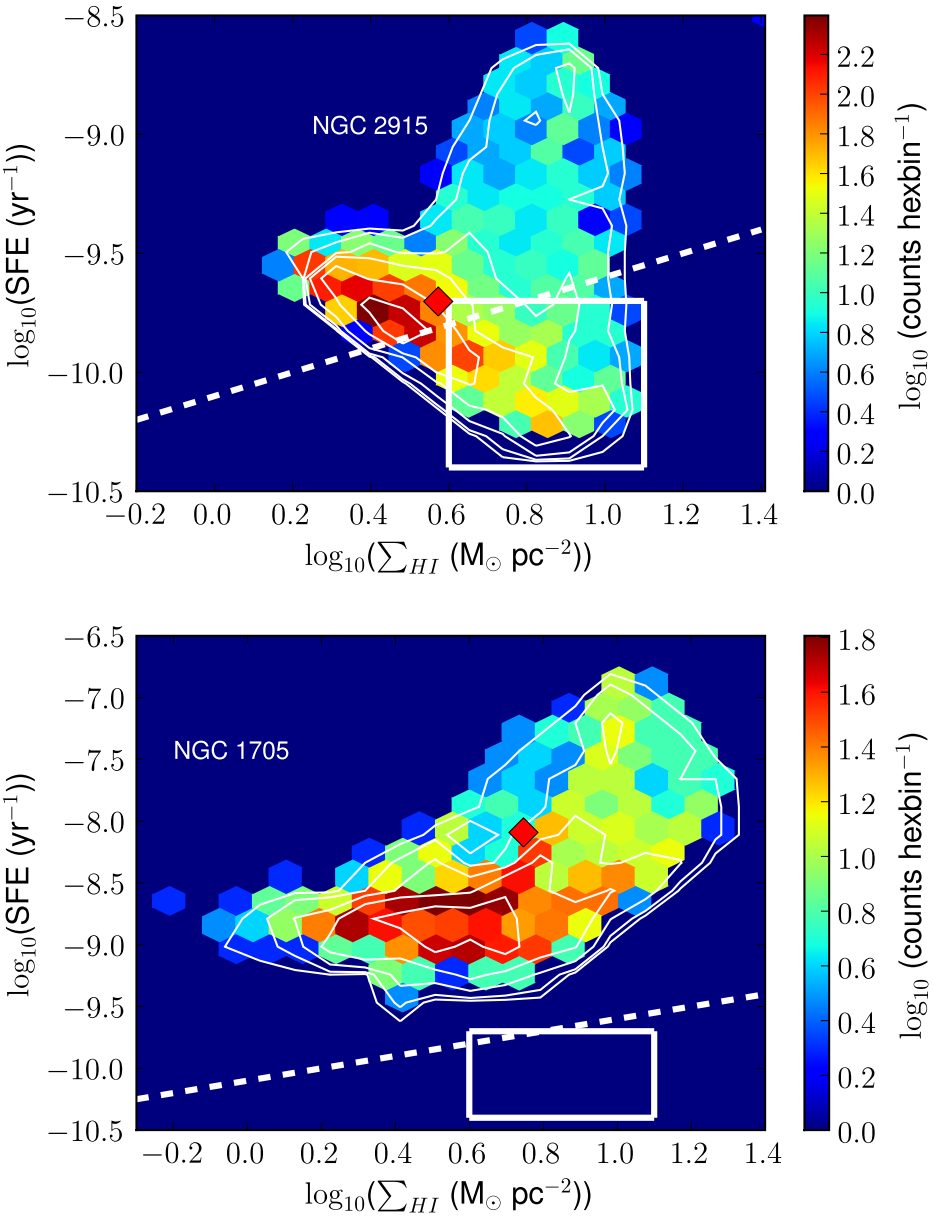

Figure 5.9: Star formation efficiency as a function of H I surface density for the inner $R \leq 1.2R_{25}$ portions of NGC 2915 and NGC 1705. The plot region is sub-divided into hexagonal bins. The colour bar indicates the logarithm of the number of points within each hexagonal bin. The white contours are at levels of $\log_{10}$(0.3, 0.7, 1.1, 1.3, 1.5,1.9, 2.3) for the upper panel, and $\log_{10}$(0.3, 0.7, 1.1, 1.4, 1.7, 2.0) for the lower panel. The solid red diamond marker represents the disk-averaged SFE and Σ_{HI} values. The dashed white line shows the SFE proportional to the free-fall time in a fixed scale height disk (i.e. the black dashed line in Fig. 5.10). The white box in each panel encloses the same region as the black box shown in Fig. 5.10.

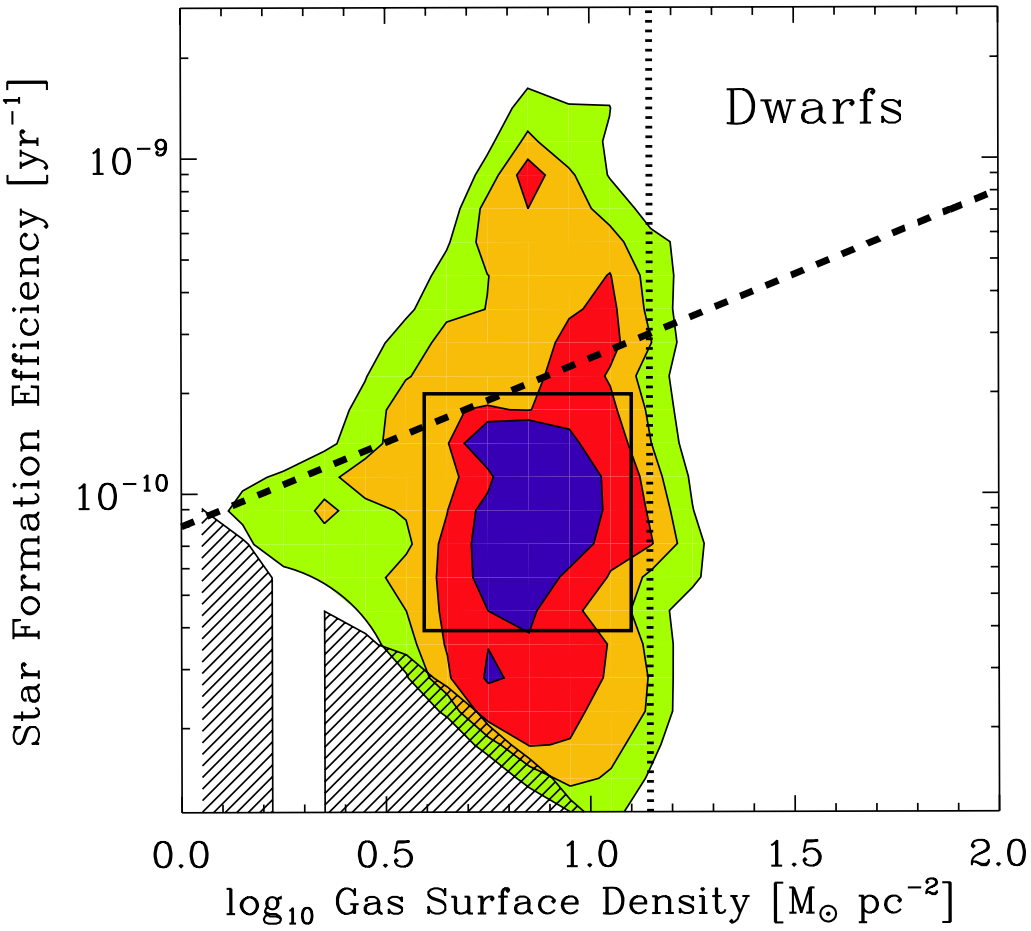

Figure 5.10: Star formation efficiency as a function of H I surface density for the THINGS sample of dwarf galaxies, taken from Leroy et al. (2008). The figure shows data from 11 dwarf galaxies for individual lines of sight. Equal weight is given to each galaxy and contours include 90%, 75%, 50% and 25% of the data. The hatched region indicates where the THINGS survey is incomplete. The thick dashed line shows the SFE proportional to the free-fall time in a fixed scale height disk. The vertical dotted line represents the surface density in their sample of spirals at which the H I-to-H_2 transition occurs. The black box encloses the same region as the white boxes shown in Fig. 5.9.

galaxy's SF activity than it does in the case of NGC 2915. The rate of exponential increase with increasing H I surface density is in fact similar, yet steeper, to that predicted by the Kennicutt-Schmidt law, albeit with a lot of scatter, for $0.4 \lesssim \log_{10} \Sigma_{HI} \lesssim 1.0$. The steeper trend could perhaps be attributed to the absence of H_2 in our gas surface densities.

Changing from SFR surface densities to SFEs, the relation between SFE and Σ_{HI} is displayed for each galaxy in Fig. 5.9. These results are directly comparable to those of Leroy et al. (2008), shown in Fig. 5.10. To facilitate comparisons between Figs. 5.9 and 5.10, a rectangular box enclosing a densely-filled portion of the plot region of Fig. 5.10 is provided. This rectangular box is then reproduced in Fig. 5.9 to give a sense of the relative placement of the NGC 2915 and NGC 1705 results. This practice is implemented throughout this chapter.

Leroy et al. (2008) demonstrate that for an H I disk of fixed scale height in which stars form with a characteristic time-scale equal to the free-fall time in the gas disk, the SFE versus Σ_{gas} analogy of the Kennicutt-Schmidt law is SFE $= 2.5 \times 10^{-4}$ ${\Sigma_{gas}}^{0.5}$. This relation is included in Fig. 5.10 as a dashed black line. The results for NGC 2915 are consistent with the finding of Leroy et al. (2008) that the link between SFE and Σ_{HI} is not well-described by a SFE $\propto \Sigma_{HI}^{0.5}$ law. NGC 2915, like the dwarf galaxies studied by Leroy et al. (2008), is forming stars less efficiently than expected. The lack of a correlation between SFE and Σ_{HI} is indicative of the fact that while the H I surface densities may play a part in regulating a galaxy's SF activity, they clearly are not solely responsible. The general trend of the NGC 1705 results are slightly more consistent with the expected SFE $\propto \Sigma_{HI}^{0.5}$ behaviour, albeit with a lot of scatter in SFE for a given Σ_{HI}. By nature of its star-burst activity, this galaxy is converting its gas into stars far more efficiently than other dwarf systems. Again, this suggests that the central gas reservoir of the galaxy will be depleted on time-scales much less than the Hubble time. NGC 1705 therefore offers use the opportunity to study star formation activity in an extreme starburst environment, an environment in which the SFEs is much higher than those typically studied by Leroy et al. (2008) using their THINGS galaxies.

Both galaxies exhibit a definite H I surface density saturation level at $\Sigma_{HI} \sim 11-16$ $M_\odot$ pc^{-2}. This is consistent with the result of Bigiel et al. (2008) who observed a sharp saturation level of H I surface densities at $\Sigma_{HI} \sim 9$ $M_\odot$ pc^{-2} in both their spiral and dwarf galaxy samples. In the case of spirals, they observe the gas in excess of this limit to be molecular. The sharp Σ_{HI} cut-off observed in NGC 2915 and NGC 1705 may therefore be indicative of an undetected molecular gas component near the centre of each galaxy.

5.3.4 Stellar surface density

The previous section showed that the distribution of H I in NGC 2915 and NGC 1705 is not tightly correlated with the observed SF activity. The observed H I distribution therefore does not lend itself to an explanation of the observed radial decline in SFE and Σ_{SFR} with galactocentric radius (Sec. 5.3.2). The final SF recipe that is considered is the link between SF activity and stellar surface density.

The *Spitzer* 3.6 μm imaging of each galaxy was used to estimate its stellar surface densities. These data were converted from units of MJy ster^{-1} to units of mag arcsec^{-2} using the prescription of Oh et al. (2008):

$$\mu_{3.6\mu m} = -2.5 \times \log_{10}\left[\frac{S_{3.6\mu m} \times 2.35 \times 10^{-5}}{ZP_{3.6\mu m}}\right], \tag{5.4}$$

where $\mu_{3.6\mu m}$ is the 3.6 μm flux in units of MJy ster^{-1}, $S_{3.6\mu m}$ is the surface brightness in units of mag arcsec^{-2} and $ZP_{3.6\mu m} = 280.9$ is the IRAC zero magnitude flux density measured in Jy (Reach et al., 2005). To convert to surface brightness units of $M_\odot$ pc^{-2}, a constant stellar mass-to-light ratio of $M/L = 0.3\ M_\odot/L_\odot$ was used. This mass-to-light ratio is consistent with those that were estimated from the mass models.

Figures 5.11 and 5.12 show the Σ_{SFR} and SFE versus Σ_* results for each galaxy. A relatively tight correlation between Σ_{SFR} and Σ_* exists for both NGC 2915 and NGC 1705. These correlations are consistent with the tight Σ_{SFR}–R correlations if one realises that the galactocentric radii are measured in units of R_{25} which itself is a property of the stellar distribution. Considering only SFR rate surface densities above the background (e.g. $\Sigma_{SFR} \gtrsim 10^{-3}$ $M_\odot$ kpc^{-2} yr^{-1} for NGC 2915), the observed Σ_{SFR}–Σ_* correlations suggest that together with the gas surface density, the stellar surface density plays a significant role in controlling the star formation activity in each galaxy. This could be due to the extra self-gravity that the stellar potential adds to the ISM which yields it more susceptible to gravitational collapse and hence SF activity. This possibility is investigated further in Sec. 5.4.5. Changing from Σ_{SFR} to SFE, Fig. 5.12 can be used to directly compare the results for NGC 2915 and NGC 1705 to those of Leroy et al. (2008) shown in Fig. 5.13. These authors find a linear relation between SFE and Σ_* analogous to the trends we observe for NGC 2915 and NGC 1705. It has already been shown in the previous sections that the SFEs of NGC 2915 are broadly similar to those of other dwarf galaxies, although it is clear from Fig. 5.11 (upper panel) that the linear relationship between SFE and Σ_* is not as steep as the one for other galaxies. The SFE-Σ_* relationship for NGC 1705 (Fig. 5.11, lower panel) is consistent with that of other late-type galaxies, yet the SFEs of this star-bursting system are generally significantly higher.

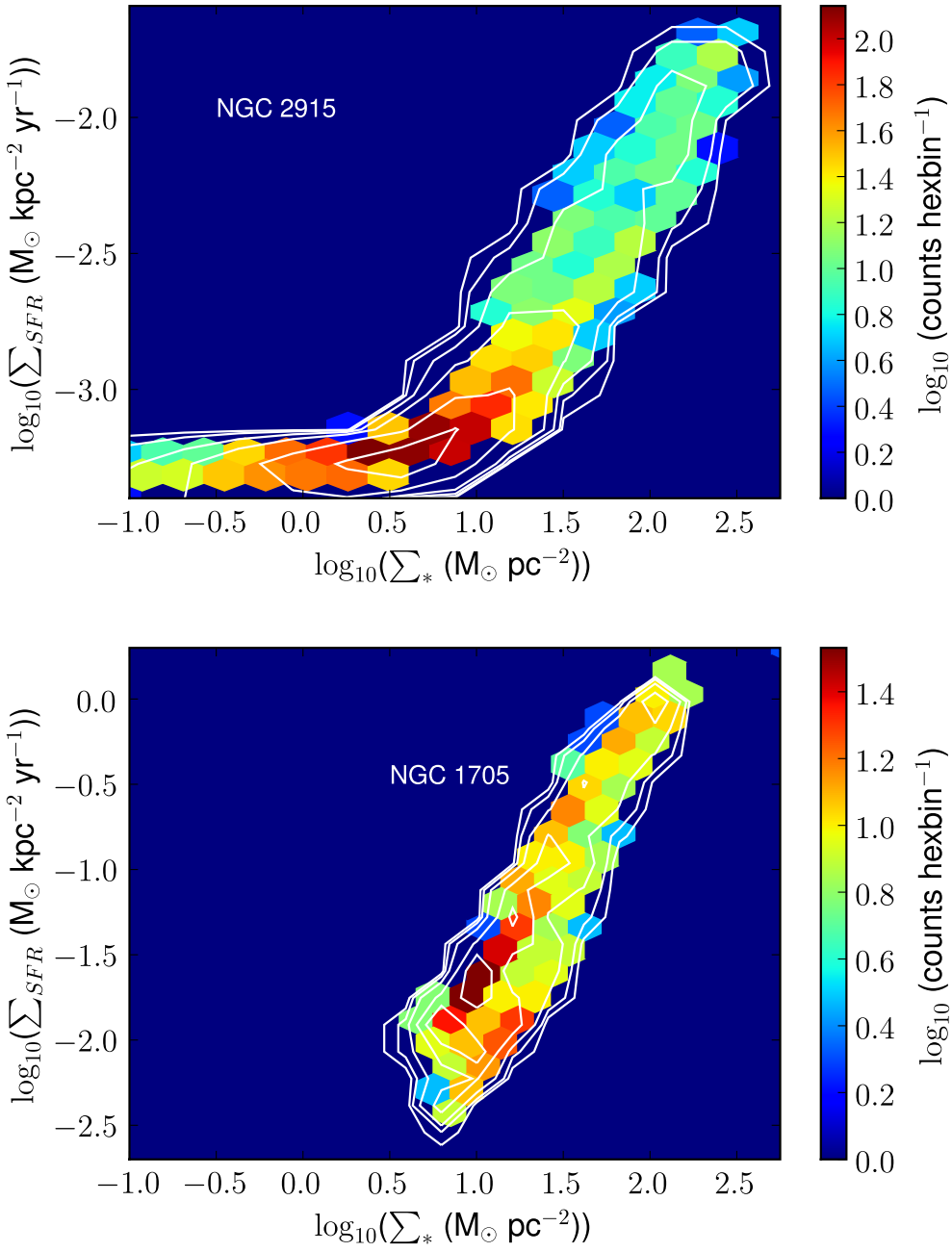

Figure 5.11: Total star formation rate surface density as a function of stellar surface density for the inner $R \leq 1.2R_{25}$ portions of NGC 2915 and NGC 1705. The plot region is sub-divided into hexagonal bins. The colour bar indicates the logarithm of the number of points within each hexagonal bin. The white contours are at levels of $\log_{10}$(0.3, 0.7, 1.1, 1.4, 1.8, 2.2) for the upper panel, and $\log_{10}$(0.2, 0.5, 0.8, 1.1, 1.3) for the lower panel.

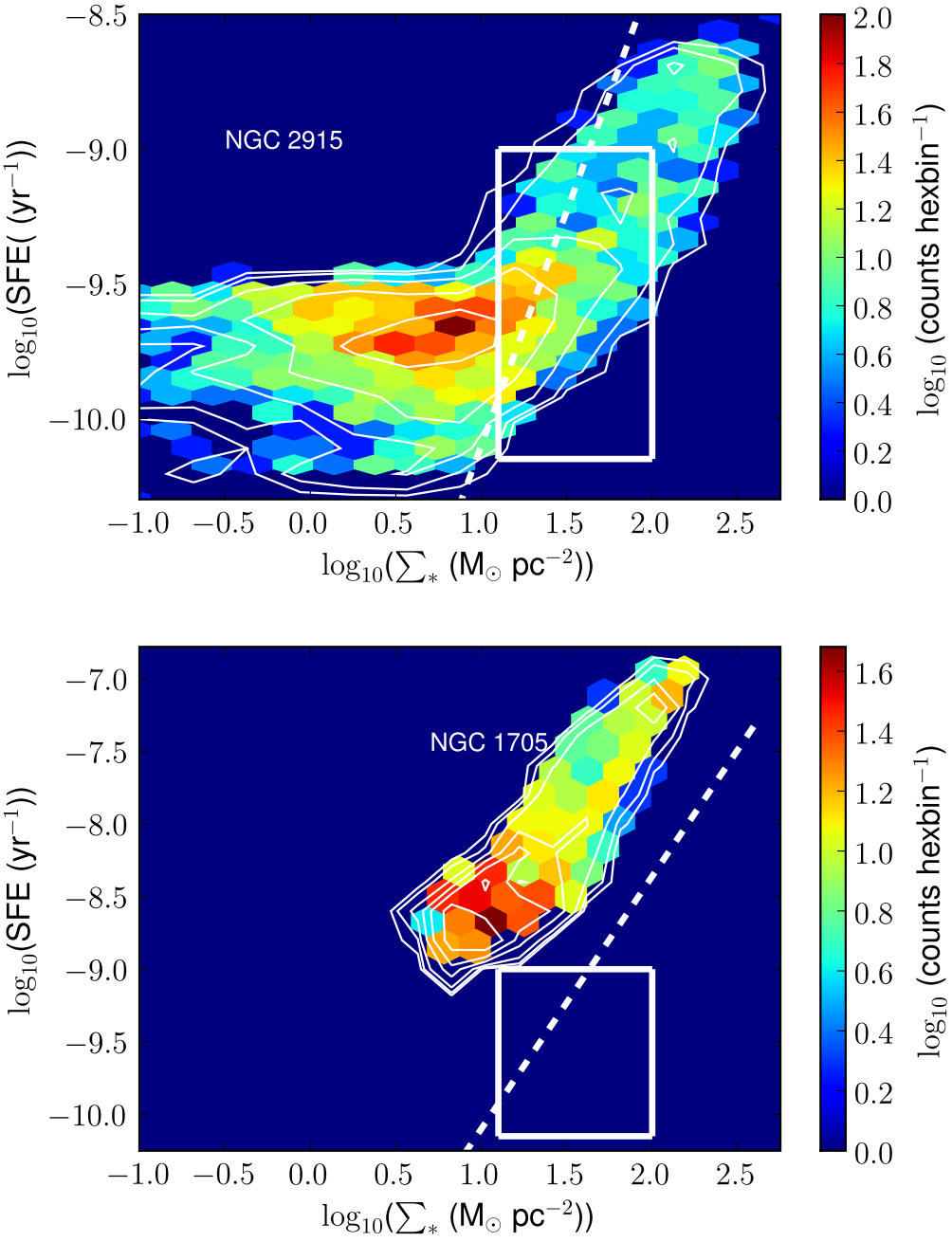

Figure 5.12: Star formation efficiency as a function of stellar surface density for the inner $R \leq 1.2R_{25}$ portions of NGC 2915 and NGC 1705. The plot region is sub-divided into hexagonal bins. The colour bar indicates the logarithm of the number of points within each hexagonal bin. The white contours are at levels of $\log_{10}$(0.3, 0.7, 1.1, 1.4, 1.8, 2.2) for the upper panel, and $\log_{10}$(0.2, 0.5, 0.8, 1.1, 1.3, 1.5) for the lower panel. The thick dashed line shows the linear relationship between SFE and Σ_* expected for the mean stellar assembly time and Σ_{gas} of the sample (i.e. the thick dashed line in Fig. 5.13) The white box in each panel encloses the same region as the black box shown in Fig. 5.13.

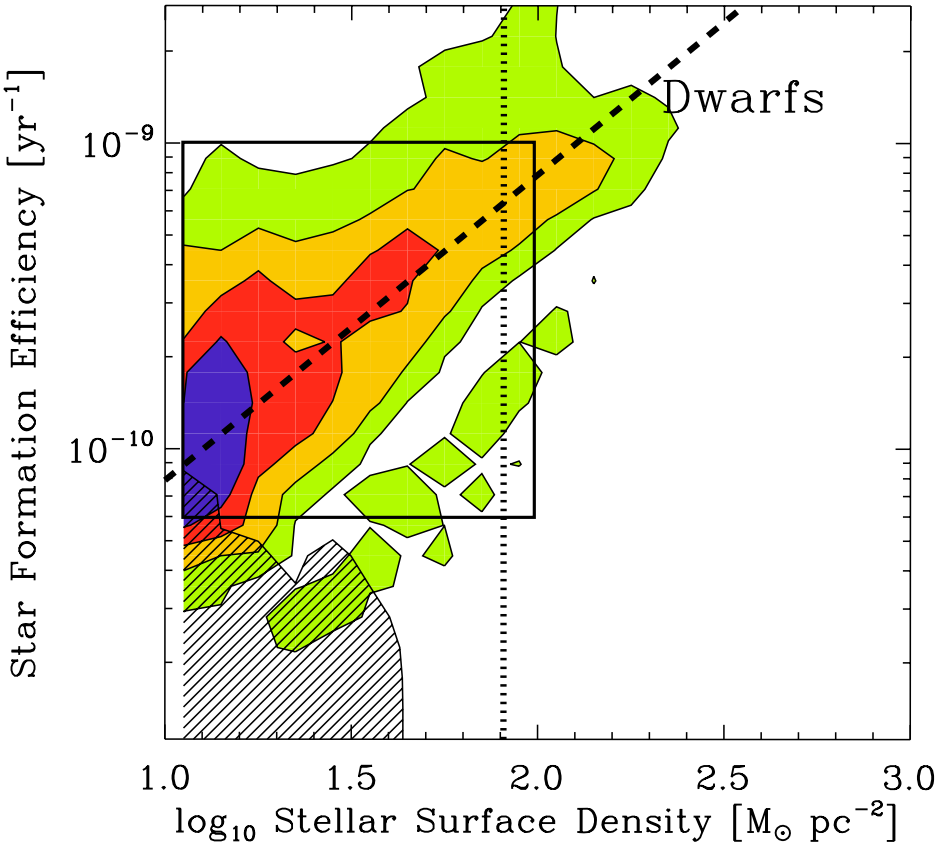

Figure 5.13: Star formation efficiency as a function of stellar surface density for the THINGS sample of dwarf galaxies, taken from Leroy et al. (2008). The figure shows data from 11 dwarf galaxies for individual lines of sight. Equal weight is given to each galaxy and contours include 90%, 75%, 50% and 25% of the data. The hatched region indicates where the THINGS survey is incomplete. The thick dashed line shows the linear relationship between SFE and Σ_* expected for the mean stellar assembly time and Σ_{gas} of the sample. The vertical dotted line shows Σ_* where the ISM is equal parts of H I and H_2 in spiral galaxies, $\Sigma_* = 81 \pm 25$ M$_\odot$ pc^{-2}. The black box encloses the same region as the white boxes shown in Fig. 5.12.

5.3.5 Molecular hydrogen surface density map

Bigiel et al. (2008) showed that a Schmidt-type power law with index $N = 1.0 \pm 2$ relates Σ_{SFR} to the molecular gas surface density (Σ_{H_2}) across a sample of spiral galaxies, implying that H_2 forms stars at a constant efficiency. This relation allows an estimate of the molecular content of a system to be obtained from its Σ_{SFR} estimates. Using the total star formation rate surface density maps of NGC 2915 and NGC 1705, respective total molecular gas masses of $M_{H2} = 5.7^{+3.4}_{-2.1} \times 10^7$ $M_\odot$ and $M_{H2} = 7.4^{+4.3}_{-7.0} \times 10^7$ $M_\odot$ are inferred. The Σ_{H_2} radial profiles derived from the Σ_{SFR} radial profiles are presented in Fig. 5.14.

5.3.6 Summary

In an attempt to better understand how efficiently NGC 2915 and NGC 1705 are converting their ISM into stars, the SF activity has been measured as a function of galactocentric radius (R), H I surface density (Σ_{HI}) and stellar surface density (Σ_*) on length scales of $\sim 50-60$ pc. Both the star formation rate surface density (Σ_{SFR}) and the star formation efficiency (SFE $= \Sigma_{SFR}/\Sigma_{HI}$) have been used to trace the SF activity in each galaxy.

The bursting nature of NGC 1705's SF activity is made evident by its measured SFR surface densities which are a factor of ~ 100 larger than typical SFR surface densities observed for the THINGS dwarfs. This system is very efficiently converting its ISM into stars, with gas depletion times ranging from only $\sim 10^7$ yr at its centre to $\sim 10^8$ yr at $R = R_{25}$. NGC 1705 exhibits SFEs that decrease exponentially with increasing galactocentric radius at a rate similar to other dwarf galaxies. The SFEs observed for the small stellar core of NGC 2915, however, drop at a faster exponential rate.

The distribution of H I in NGC 2915 does not appear to be responsible for the observed radial decline in SFE. No significant correlation is observed between Σ_{SFR} or SFE and Σ_{HI}. This result is consistent with that of Bigiel et al. (2008) and Leroy et al. (2008) who find no clear link between the SF activity and Σ_{HI} in their respective samples of dwarf galaxies. The SF activity in NGC 1705 seems to be approximately exponentially related to Σ_{HI}, suggesting that Σ_{HI} could play some role in regulating the galaxy's SF activity.

Finally, a clear relationship is observed between the SF activity and the stellar surface density of each system. Although the relation is expected (i.e. SF activity scales with the number of stars), it does provide some insight into the effects of the stellar potential, in addition to the gaseous potential, on the gravitational instability of the ISM. The trend is again similar to that found by Leroy et al. (2008) for their sample of dwarf galaxies.

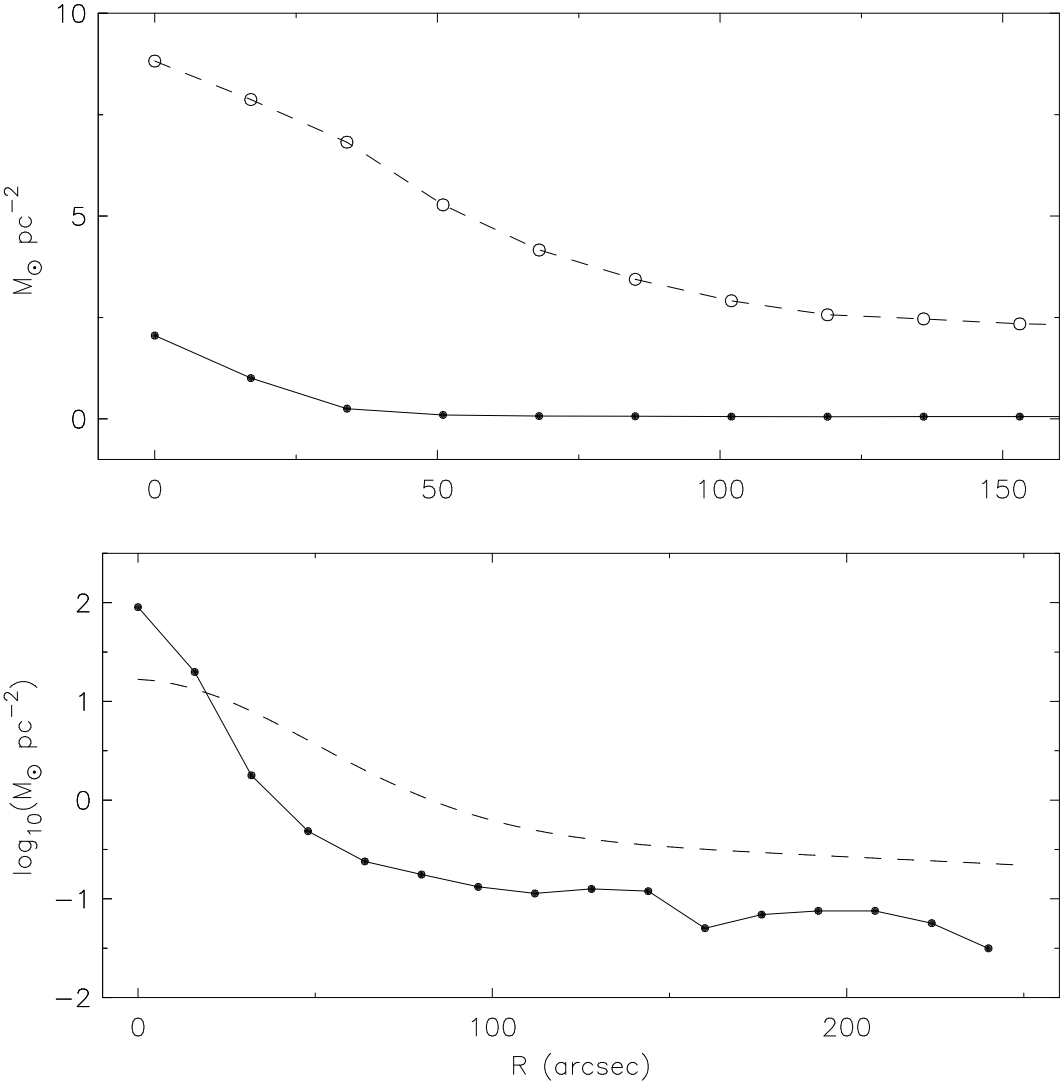

Figure 5.14: H I (open circles) and H_2 (filled circles) surface density profiles for NGC 2915 and NGC 1705 (top and bottom panels respectively). All surface densities have been inclination-corrected to their face-on values. Note that ordinate of the lower panel uses a logarithmic scaling of the surface densities.

In conclusion, the star formation recipes investigated in this chapter provide no definitive insight into the properties that regulate the SF activity in either NGC 2915 and NGC 1705. They suggest rather that, apart from the high star formation rates observed for NGC 1705, the galaxies are broadly similar to other dwarf and late-type systems.

To gain further insight into the processes that regulate the SF activity, various SF models are investigated in the remainder of this chapter. These models take into account the combined effects of various star formation regulatory properties of the ISM and attempt to link them to the observed star formation.

5.4 Star formation models

5.4.1 Introduction

The star formation recipes improve our understanding how efficiently the ISM forms stars. They do not, however, tell us *which* regions of a galaxy should be forming stars. The various properties of the ISM that regulate a galaxy's star formation activity do not act independently of one another. For example, while self-gravity drives gas perturbations to collapse under mutual gravity, the centrifugal forces associated with the rotational motions of the gas perturbations will impede the structure growth by counteracting the inward gravitational force. Similarly, rotational shear will tear apart adjacent gas clouds before they have the chance to coalesce to form a single, larger, denser body of gas. The remainder of this chapter is dedicated to the investigation of star formation models applied to NGC 2915 and NGC 1705. Both the ability and inability of these models to accurately describe the locations of the star-forming regions in each galaxy will contribute to a further understanding of the complex interplay between the various ISM properties that regulate the SF activity and the SF activity itself.

The results of these analyses are compared to those of Leroy et al. (2008) who carried out similar analyses for their sample of THINGS galaxies. This is done so that the results can be interpreted in the context of other typical star-forming dwarf galaxies. When comparing our results for NGC 2915 and NGC 1705 to those of Leroy et al. (2008), only the innermost parts of the galaxies ($R \lesssim 1.2R_{25}$) are considered. Each SF model/threshold is presented separately, with the order of presentation of the various models chosen to facilitate the progression from simple to more complex models.

5.4.2 Rotation curve and ISM phases

Before presenting the various star formation models, this section introduces some of the input parameters and functions that are required for the models and that are used throughout the remainder of this chapter.

Rotation curve parameterisation

Some model parameters are functions of the rotation curve. To simplify the determination of these parameters, the rotation curve of each galaxy is parameterised using the function

$$V(r) = V_{flat}[1 - \exp(-r/l_{flat})], \tag{5.5}$$

where V_{flat} and l_{flat} approximate the asymptotic velocity of the outer rotation curve and the length-scale over which it approaches this constant velocity respectively. This parameterisation is easily analytically differentiable. For NGC 2915, the rotation curve derived from tilted ring model SI as fitted to its H I velocity (Sec. 3.1) field is used. The best-fitting parameters are $V_{flat} = 83.9$ km s^{-1} and $l_{flat} = 74.8''$. The rotation curve derived for NGC 1705 by fitting the H I line profiles of the integrated position-velocity slice (Sec. 4.5.2) is best parameterised with $V_{flat} = 72.8$ km s^{-1} and $l_{flat} = 52.9''$. These observed rotation curves together with their respective parameterisations are shown in Fig 5.15.

Broad and narrow components of the neutral inter-stellar medium

The star formation thresholds investigated in this chapter require an estimate of the gas velocity dispersion. Kennicutt (1983), Kennicutt (1989) and Martin & Kennicutt (2001) used a constant gas velocity dispersion of $\sigma_{gas} = 6$ km s^{-1} in their respective gas stability analyses, a value that is commonly implemented as the conventional velocity dispersion estimate for the gas. Several authors have, however, emphasised a cold gas phase as a specific requirement for star formation. Elmegreen & Parravano (1994) predicted that the H I in the outer parts of galaxies should have most of their mass at temperatures of several thousands of Kelvin, thereby leaving very little mass in a dense form suitable for star formation. Schaye (2004) showed that the transition from the warm to the cold gas phase triggers gravitational instability over a wide range of scales. For the case of NGC 6822, de Blok & Walter (2006) studied the H I line profiles of the galaxy to identify separate warm and cold gas phases with velocity dispersions of ~ 8.2 km s^{-1} and ~ 4.4 km s^{-1} respectively. They showed that the velocity dispersion of the cool component when used with a Toomre Q criterion gives an optimal description of ongoing star formation in NGC 6822, superior to that using the more conventional dispersion value of 6 km s^{-1}.

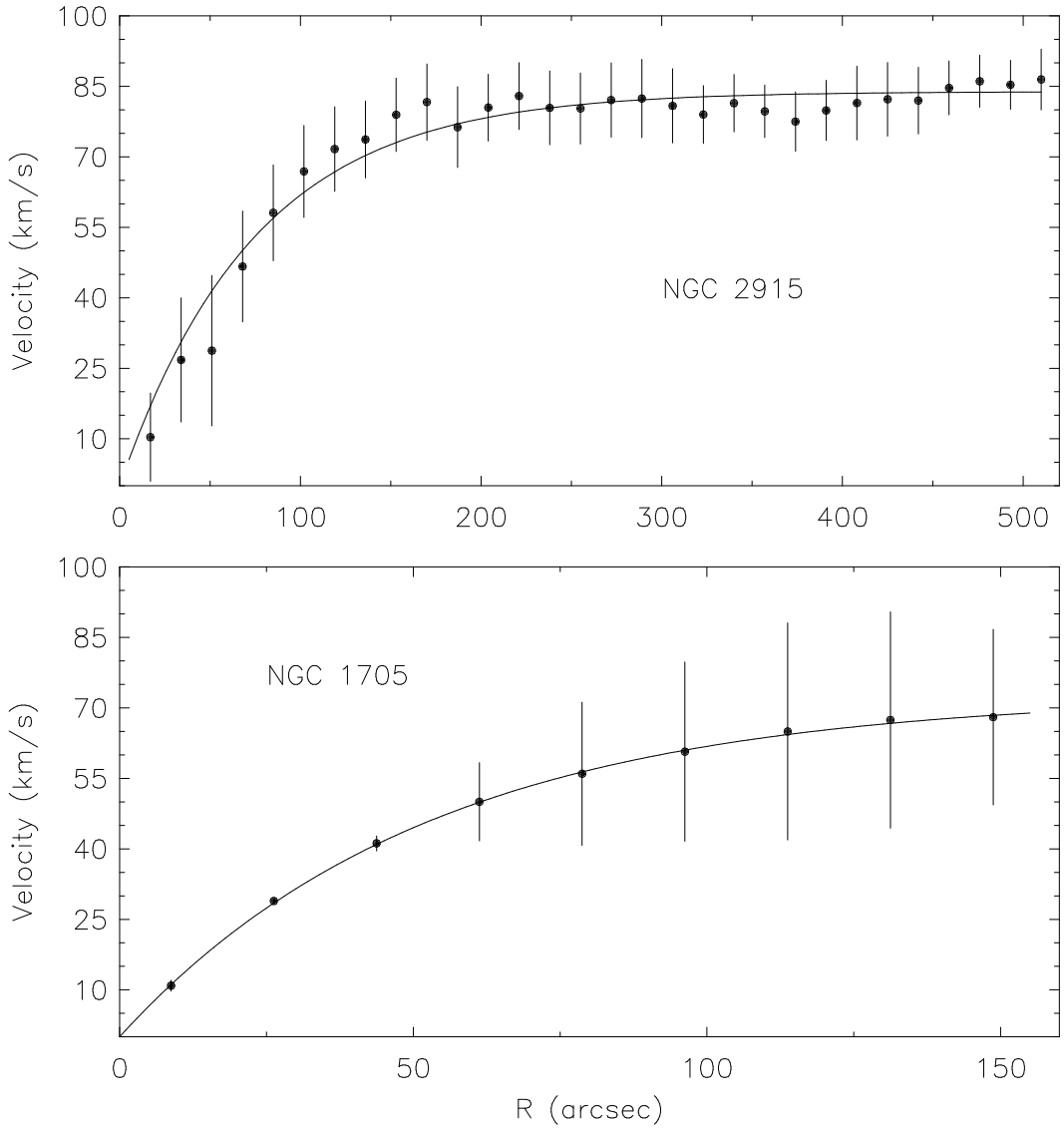

Figure 5.15: Observed rotation curves of NGC 2915 and NGC 1705 **(black-filled circles)** and their parameterisations **(solid black curves)**. Error bars in the top panel represent the r.m.s. velocity of each ring in tilted ring model SI. Error bars in the bottom panel represent the absolute difference in rotation velocity derived separately for each side of the galaxy.

In this work, a negligible metal content of each galaxy's ISM is assumed. The total gas surface densities, Σ_{gas}, are approximated as the H I gas surface densities, Σ_{HI}, derived directly from the H I total intensity maps. An investigation of the H I line profiles analogous to that of de Blok & Walter (2006) was carried out for this galaxy. The full H I data cube was Hanning-smoothed and re-gridded from a pixel size of $2.5'' \times 2.5''$ to a pixel size of $17.5'' \times 17.5''$. The full width at half maximum of the synthesised beam of our H I observations is $17'' \times 18.2''$. Re-gridding the H I data cube ensured that adjacent pixels contained independent H I line profiles. Using the GIPSY task XGAUFIT, single- and double-component Gaussians were fitted to all profiles. Only fitted profiles with a fitted peak amplitude larger than three times the r.m.s. noise of a line-free channel were kept, the rest were blanked. Figure 5.16 shows the fitted Gaussians for an example profile from the re-gridded H I data cube.

Figure 5.17 shows the distributions of the dispersions of the fitted single Gaussians as well as the dispersions of the narrow and broad components of the fitted double Gaussians. The dispersions of the fitted single Gaussians are approximately Gaussian distributed with an estimated mean of $< \sigma_{gas} >= 10.7$ km s^{-1} (black dashed line in Fig. 5.17). As de Blok & Walter (2006) mention, the distribution of these dispersions is close to the distribution of the 2nd-order moments of the H I line profiles. In Sec. 3.7.1 it was shown that a large fraction of the NGC 2915 H I line profiles are significantly asymmetric. Despite these inherent asymmetries, it is clear from Fig. 5.17 that the dispersions of the broad and narrow components of the fitted double Gaussians are approximately Gaussian distributed about mean values of $< \sigma_{gas} >= 8.8$ km s^{-1} and $< \sigma_{gas} >= 4.9$ km s^{-1}, respectively (red and blue dashed lines in Fig. 5.17). It is due to these intrinsic profile asymmetries that the fitted dispersions of the single-component Gaussians are typically slightly higher than those of the narrow or broad components of the double Gaussians.

Important to our star formation threshold analyses is an estimate of the cold phase H I velocity dispersion. The distribution of the fitted narrow-component dispersions exhibits a clear peak at a dispersion of $\sigma_{gas} \sim 4.9$ km s^{-1}. This value is very close to the mean dispersion of $< \sigma_{gas} >= 4.4$ km s^{-1} determined by de Blok & Walter (2006) for the cold gas phase of the neutral ISM of NGC 6822. For our star formation threshold analyses we use $\sigma_{gas} = 4.9$ km s^{-1} as the cold gas phase velocity dispersion of NGC 2915. We also carry out the various star formation analyses using $\sigma_{gas} = 8.8$ km s^{-1}, the gas velocity dispersion associated with the broad component of the neutral ISM. A procedure analogous to that mentioned above was carried out for NGC 1705 in order to estimate the narrow and broad component H I dispersions. However, the procedure proved unsuitable due to the small angular size of NGC 1705's H I disk. The re-gridded H I data cube contained very few pixels within the region of the H I disk, yielding poor statistics of the fitted Gaussians. Meaningful estimates of the typical dispersions could not be obtained. The estimates obtained for NGC 2915 were therefore also used for NGC 1705.

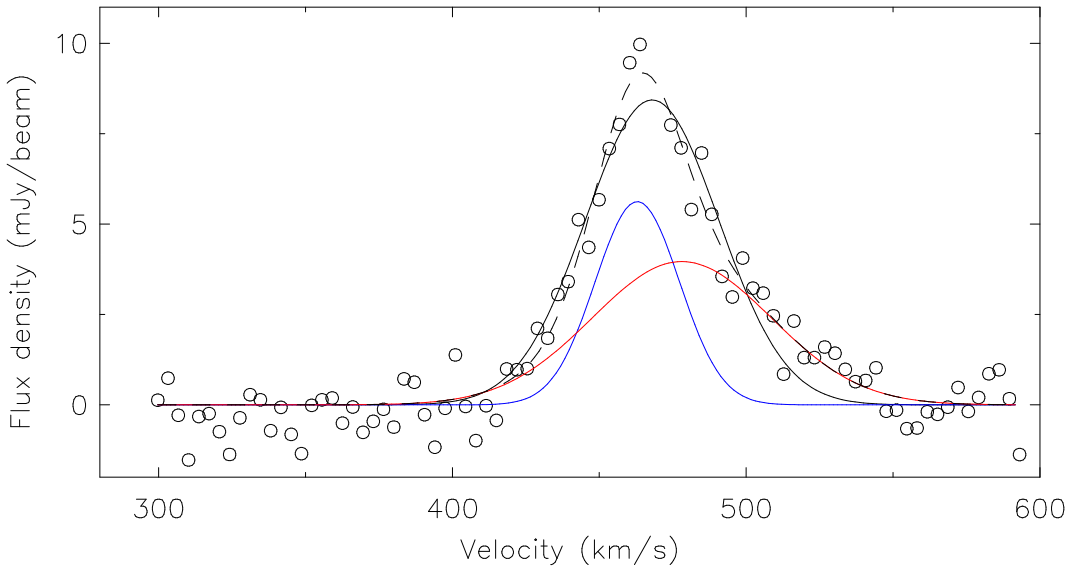

Figure 5.16: Example of a non-Gaussian line profile from the re-gridded H I data cube. Circles represent that data, the solid black curve represents a single-component Gaussian fit, and the dashed black line represents a double-component Gaussian fit. The individual components of the double-component Gaussian are shown as blue and red curves. The broad component has a dispersion of 30.5 km s^{-1}, and the narrow component a dispersion of 14.4 km s^{-1}. The dispersion of the single-component Gaussian is 22.7 km s^{-1}.

With measures of the H I distribution (H I total intensity map), the global kinematics (parameterisation of the observed rotation curve) and the pressure of the ISM (warm and cold phase H I velocity dispersions) of each galaxy, the various star formation models can now be investigated.

5.4.3 Thermo-gravitational instability

Introduction

Schaye (2004) studied global star formation thresholds in the outer parts of galaxies by investigating the influence of dark matter halos on the stability of disk galaxies. He argues that the transition of the ISM from the warm ($T \sim 10^4$ K) to the cold ($T \sim 10^2$ K) phase results in the onset of star formation over a wide range of scales within a galaxy's gas disk. Specifically, he shows that a decrease in thermal velocity dispersion associated with the phase transition triggers the gravitational instability and that the transition occurs at a surface density that agrees well with empirically derived surface density thresholds for star formation (e.g. $\sim 10^{21}$ atoms cm^{-2},

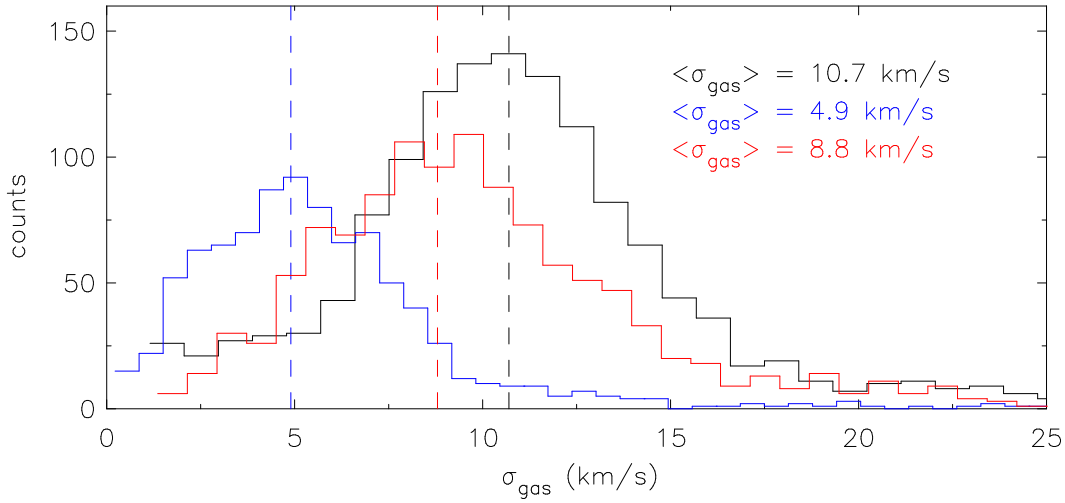

Figure 5.17: Histograms of the dispersions derived from the one component Gaussian fits (solid black curve) for NGC 2915 and from the two-component fits with, with the warm and cold components shown as the red and blue solid curves respectively. The mean velocity dispersions for the Gaussian portions of the distributions (i.e. excluding the high dispersion tails) are shown in the figure and are represented by dashed lines.

Skillman, 1987). For his range of models, Schaye (2004) found the description of the variation of the critical gas surface density to be

$$\log\left(\frac{\Sigma_{c,Sch}}{1\ M_{\odot}\ \mathrm{pc}^{-2}}\right) \approx 0.8 + 0.3\log f - 0.3\log\left(\frac{Z}{0.1\ Z_{\odot}}\right) + 0.2\log\left(\frac{I}{10^{6}\ \mathrm{cm}^{-2}\ \mathrm{s}^{-1}}\right), \quad (5.6)$$

where $\Sigma_{c,Sch}$ is the critical gas surface density, Z the metallicity, I the flux of the ionising radiation and $f \equiv f_g/f_{th}$, with f_g the mass fraction in gas and f_{th} the fraction of the pressure that is thermal. Note that this expression *does not* contain any gas kinematics terms.

Using this thermo-gravitational instability criterion, Schaye (2004) predicted the star formation threshold density to fall in the range $\Sigma_c \approx 3 - 10\ \mathrm{M}_{\odot}\ \mathrm{pc}^{-2}$. An important result of his investigation is that "the phase transition triggers gravitational instability even in the presence of relatively strong turbulence". This, Schaye emphasises, allows his model to successfully identify the star-forming regions of a gaseous disk while other instability criteria, taking into account the dynamics of the gas, might fail. Furthermore, he finds that the transition to the cold phase of the neutral ISM coincides with a large increase in the fraction of molecular hydrogen (H_2). This, he argues, occurs because the increased H_2 formation rate must compensate for the drop in pressure associated with the cold phase transition.

de Blok & Walter (2006) investigated the SF threshold in NGC 6822 on sub-kiloparsec length-

scales. They found that a constant H I column density of $N_{HI} = 10^{20.75}$ cm^{-2} ($\sim$ 4.5 M$_\odot$ pc^{-2}) serves as a star formation threshold that accurately traces the observed high-mass star formation within the galaxy.

NGC 2915 and NGC 1705 results and discussion

Equation 5.6 was used to determine the H I surface density for NGC 2915 and NGC 1705 at which the gravitational instability, resulting from the transition of the thermal velocity dispersion of the gas to a cold phase, occurs. Schaye (2004) motivated $f = 1$, $Z = 0.1\ Z_\odot$ and $I = 10^6$ cm^{-2} s^{-1} as his choices for the fiducial values of these parameters. By investigating how the results of his model change when different parameter values are used, he concluded that "the star formation threshold turns out to be insensitive to small (an order of magnitude or less) variations in these parameter values". In lieu of accurate estimates of Z and I for NGC 2915 and NGC 1705, the above-mentioned fiducial parameter values from Schaye (2004) are adopted. This choice of parameter values results in a critical surface density of $\Sigma_{c,Sch} = 6.3$ M$_\odot$ pc^{-2}.

Figures 5.18 and 5.19 show the inner parts of the H I surface density maps of NGC 2915 and NGC 1705 respectively, with various H I surface density contours overlaid. Also displayed is the edge of the star-forming disk of each galaxy, represented as an ellipse. These figures demonstrate that no single H I surface density traces the edge of the star-forming core of either galaxy. For NGC 2915, the south-eastern edge of the star-forming core intercepts all H I surface densities in the range $4 - 10$ M$_\odot$ pc^{-2}. These observations are consistent with the results of Young et al. (2003) who, by analysing the H I line profiles of five nearby dwarf galaxies, found no apparent relation between the cold phase fraction of the ISM and the Hα luminosity spanning more than three orders of magnitude in L$_{H\alpha}$. The situation for NGC 2915 and NGC 1705 is akin to that of UGCA 292 for which Young et al. (2003) found a relatively small incidence of a cold neutral medium but a relatively large star formation rate. For the case of NGC 6822, de Blok & Walter (2006) suggest that their results emphasise that the SF threshold in that galaxy does not depend on global kinematics but is a purely local phenomenon. This is clearly not the case for NGC 2915 and NGC 1705. In the sections that follow we investigate SF models that incorporate the effects of gas kinematics on SF activity.

The SFE as a function of $\log_{10}(\Sigma_{c,Sch}/\Sigma_{HI})$ in NGC 2915 and NGC 1705 is presented in Fig. 5.20. Leroy et al. (2008) found that a cold H I phase is expected over most of the disk in dwarf galaxies (see Fig. 5.21 for their results). They labelled the Schaye (2004) threshold as being "of limited utility for predicting the SFE *within* a star-forming disk". These authors go on to point out, however, that Schaye (2004) was primarily interested in predicting the *edges* of star forming disks. The situations for NGC 2915 and NGC 1705 seem to be similar to those for the

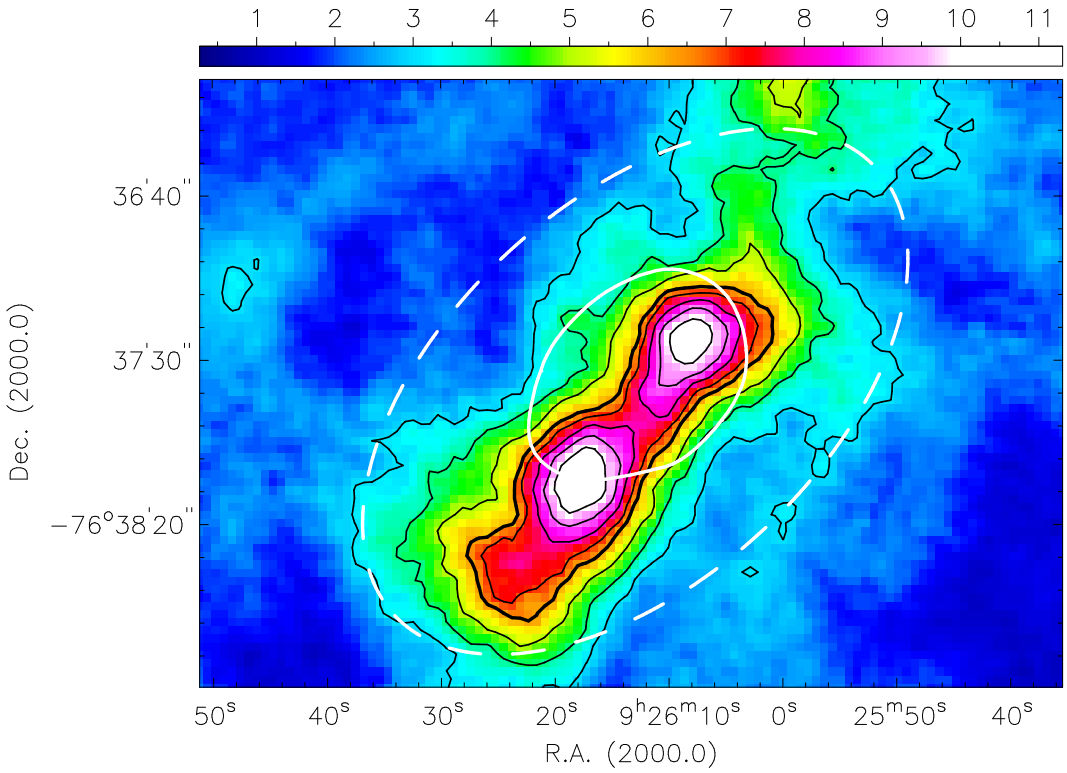

Figure 5.18: Colour image of the inner part of the H I surface density map of NGC 2915 with contours of constant surface density overlaid. The intensity scale is specified in units of $M_\odot$ pc^{-2} by the colour bar at the top of the panel. The solid black contours are at levels of Σ_{HI} = 3, 4, 5, 6.3, 7, 8, 9, 10 $M_\odot$ pc^{-2} with the Σ_{HI} = 6.3 $M_\odot$ pc^{-2} contour appearing thicker than the others. The solid white contour represents the edge of the star-forming core and is at a level of Σ_{SFR} = 0.0018 $M_\odot$ yr^{-1} kpc^{-2}. The white dashed ellipse represents the R–band R_{25} radius of NGC 2915 at $R = 98''$.

sample of Leroy et al. (2008) in the sense the Schaye (2004) criterion does clearly discriminate between high and low SFE parts if the disk. Regions that are expected to be super-critical are generally associated with lower SFEs. Thus, for these two galaxies, although a cold gas phase may be a necessary condition for gravitational instability of their neutral ISM, it alone is insufficient to ensure that star formation occurs.

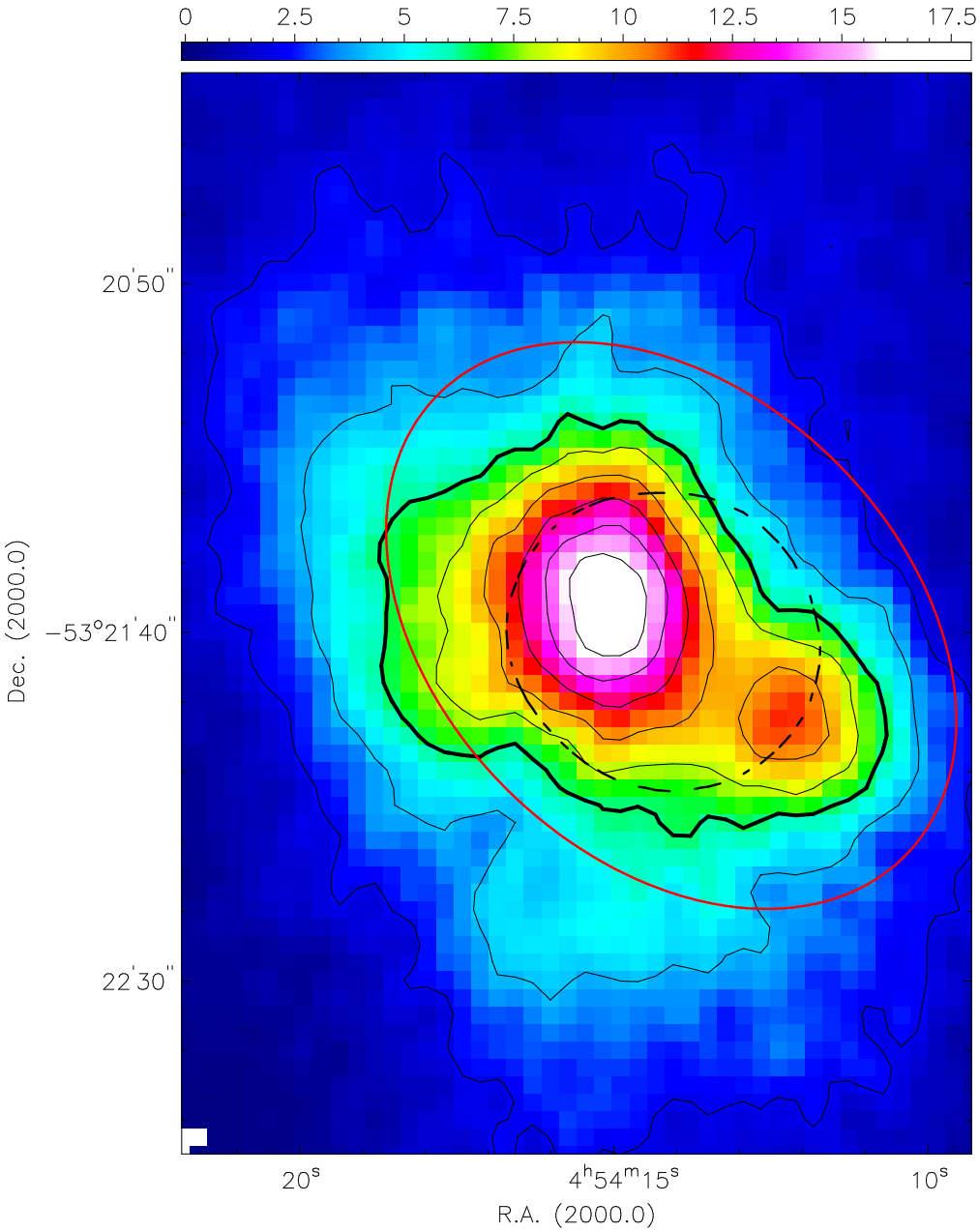

Figure 5.19: Colour image of the inner part of the H I surface density map of NGC 1705 with contours of constant surface density overlaid. The intensity scale is specified in units of $M_\odot$ pc^{-2} by the colour bar at the top of the panel. The solid black contours are at levels of Σ_{HI} = 2, 4, 6.3, 8, 10, 12, 14, 16, 18 $M_\odot$ pc^{-2} with the Σ_{HI} = 6.3 $M_\odot$ pc^{-2} contour appearing thicker than the others. The black dashed contour represents the edge of the star-forming core and is at a level of Σ_{SFR} = 0.1 $M_\odot$ yr^{-1} kpc^{-2}. The solid red ellipse represents the B–band R_{25} radius of NGC 1705 at $R = 46.9''$.

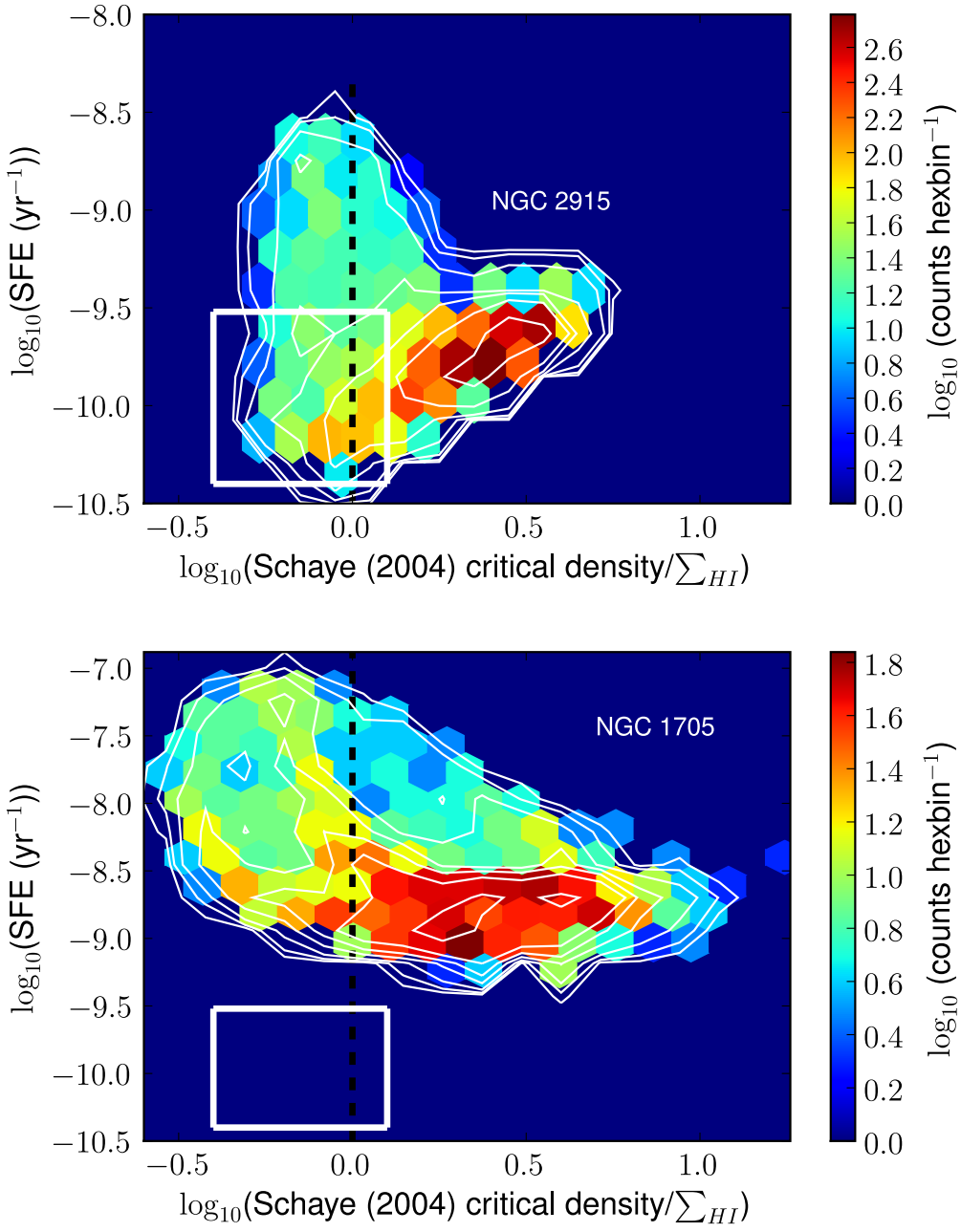

Figure 5.20: Star formation efficiency as a function of $\Sigma_{c,Sch}/\Sigma_{HI}$ for the inner $R \leq 1.2R_{25}$ parts of NGC 2915 and NGC 1705. The plot region is sub-divided into hexagonal bins. The colour bar indicates the logarithm of the number of points within each hexagonal bin. The white contours are at levels of $\log_{10}$(0.2, 0.6, 1.0, 1.4, 1.8, 2.2, 2.6) for the upper panel, and $\log_{10}$(0.2, 0.5, 0.8, 1.1, 1.3, 1.5, 1.8) for the lower panel. The subsets of parameter space leftward and rightward of the black dashed line represent the regions where Schaye (2004) estimates that a cold phase can and cannot form respectively. The white box in each panel encloses the same region as the black box shown in Fig. 5.21.

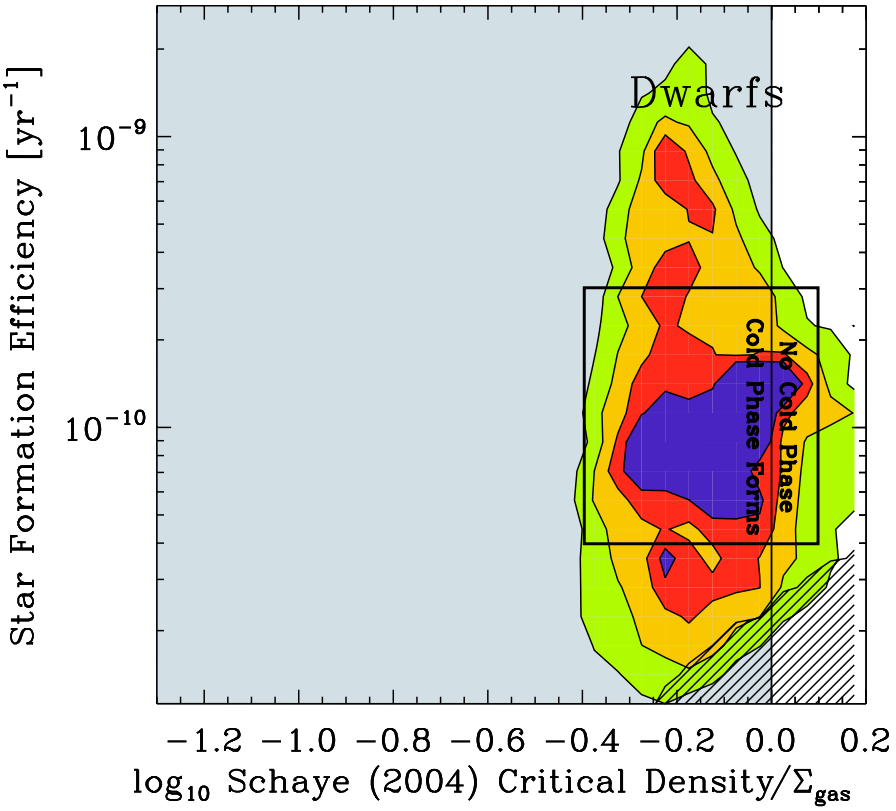

Figure 5.21: Star formation efficiency as a function of $\Sigma_{c,Sch}/\Sigma_{HI}$ for the THINGS sample of dwarf galaxies, taken from Leroy et al. (2008). The figure shows data from 11 dwarf galaxies for individual lines of sight. Equal weight is given to each galaxy and contours include 90%, 75%, 50% and 25% of the data. The hatched region indicates where the THINGS survey is incomplete. The grey area indicates where Schaye (2004) estimates that a cold phase can form. The black box encloses the same region as the white boxes shown in Fig. 5.20.

5.4.4 Single-fluid Toomre criterion

In the previous section it was demonstrated that SF activity in NGC 2915 and NGC 1705 is not a purely local phenomenon and that it must depend at least in part on global kinematics. In this section the Toomre instability criterion for a thin rotating disk is investigated. Besides a measure of the local gas density, this criterion also incorporates measures of the local gas pressure and kinematics. It should therefore provide insight into the way in which these properties of the ISM work together to possibly regulate the SF activity in each system.

Introduction

Safronov (1960) was the first to show that perturbations in a thin, rotating gaseous disk can become unstable to gravitational collapse due to the effects of the disk's self-gravity. Building on the work of Safronov (1960), Toomre (1964) showed that a stellar disk that is fairly smooth or uniform, and that is rotating in approximate equilibrium between its self-gravitational and centrifugal forces, cannot be entirely stable against the tendency to gravitationally collapse. This, he says, is the case unless the random motions within the disk are sufficiently large. Today, the Toomre criterion is most commonly used to quantify the gravitational growth of perturbations within a thin, rotating gaseous disk. According to this criterion, the disk should be unstable to axisymmetric disturbances in regions where the Toomre parameter,

$$Q_{gas} \equiv \frac{\sigma_{gas}\kappa}{\pi G \Sigma_{gas}}, \tag{5.7}$$

is less than unity. The self-gravity, pressure and kinematics of the gas disk are represented by Σ_{gas}, σ_{gas} and κ respectively. G is the gravitational constant. The epicyclic frequency, κ, is a measure of the Coriolis or centrifugal forces stemming from the rotation of the perturbations. Following Kennicutt (1989), κ is estimated as,

$$\kappa(R) = 1.41\frac{V}{R}\sqrt{1 + \frac{R}{V}\frac{dV}{dR}} \tag{5.8}$$

where V is the rotation velocity, derived directly from the rotation curve, at a radius R. In the Toomre criterion, the combination of random motions and centrifugal accelerations from epicyclic eddies are what supports the ISM against collapse due to self-gravity. Indeed, it makes sense that a galaxy's kinematics should play a role in regulating its SF activity. In the case of a centrifugal type force associated with a rotating perturbation in the gas distribution, one can imagine it acting as a restoring force against the self-gravity of the perturbation, thereby hindering the process of gravitational collapse. The Toomre criterion therefore describes the abilities of perturbations to rotate around their centre of gravity and thus their stability against gravitational collapse.

Kennicutt (1989), using a sample of 15 spiral galaxies, was the first to observationally test the Toomre criterion on galactic length-scales. More recently, Martin & Kennicutt (2001) applied the prescription of Toomre (1964) to a sample of 32 star-forming spiral galaxies and compared the radial distributions of Q_{gas} with the distributions of the observed star-forming regions. Assuming a constant gas velocity dispersion $\sigma_{gas} \sim 6$ km s^{-1}, they found a median value of $Q_{gas} = 1.5$ at the edges of most star forming disks. Using this empirical calibration, the Toomre criterion as expressed in Eqn. 5.7 becomes

$$Q \equiv \frac{\alpha_Q \sigma_{gas} \kappa}{\pi G \Sigma_{gas}}, \tag{5.9}$$

with $\alpha_Q = 0.69$. This calibrated version of the Toomre stability criterion is used throughout this chapter.

NGC 2915 and NGC 1705 results and discussion

The Toomre Q_{gas} parameter was calculated for every resolution element in the H I surface density map of each galaxy. Based on the results of Sec. 5.4.2, Q_{gas} maps were generated using: (1) $\sigma_{gas} = 8.8$ km s^{-1}, and (2) $\sigma_{gas} = 4.9$ km s^{-1}. Using a radially-varying velocity dispersion profile based on the H I second-order moments would be difficult in the cases of NGC 2915 and NGC 1705 due to the fact that the H I is not in virial equilibrium near their centers. Using velocity dispersions of ~ 25 km s^{-1} for the central regions of NGC 2915's H I disk will, for example, lead to Q_{gas} parameter estimates that are ~ 5 times higher than the estimates that are based on $\sigma_{gas} = 4.9$ km s^{-1}. In assuming a constant H I velocity dispersion, we have emulated the approaches adopted by Kennicutt (1989, 1998); Martin & Kennicutt (2001); Leroy et al. (2008). The epicyclic frequency, κ, was determined using Eqn. 5.8. The parameterisation of the observed rotation curve of each galaxy was used to analytically determine $\frac{dV}{dR}$. An azimuthally averaged approximation of the epicyclic frequency was then used for each of the resolution elements at a particular galactocentric radius. The Q_{gas} maps shown in this section can therefore be thought of as the H I map modulated by a radial function that is largely determined by the rotation curve. More sophisticated maps can be produced by allowing the H I velocity dispersion to vary radially, but in this work we assume a constant velocity dispersion.

The results for NGC 2915 and NGC 1705 are shown in Figs. 5.22 and 5.23 respectively. Most striking is that, using the above-mentioned inputs, the Toomre criterion predicts the H I disk of both galaxies to be sub-critical, that is, $Q_{gas} > 1$ for every resolution element in the H I total intensity map. According to this stability criterion, the gas in NGC 2915 and NGC 1705 is stable everywhere against large-scale gravitational collapse. This result is inconsistent with the star forming cores that are observed at the centres of the galaxies. The lower panels of Fig. 5.22 show that the logarithmic Q_{gas} distribution for NGC 2915 is approximately Gaussian, peaking at

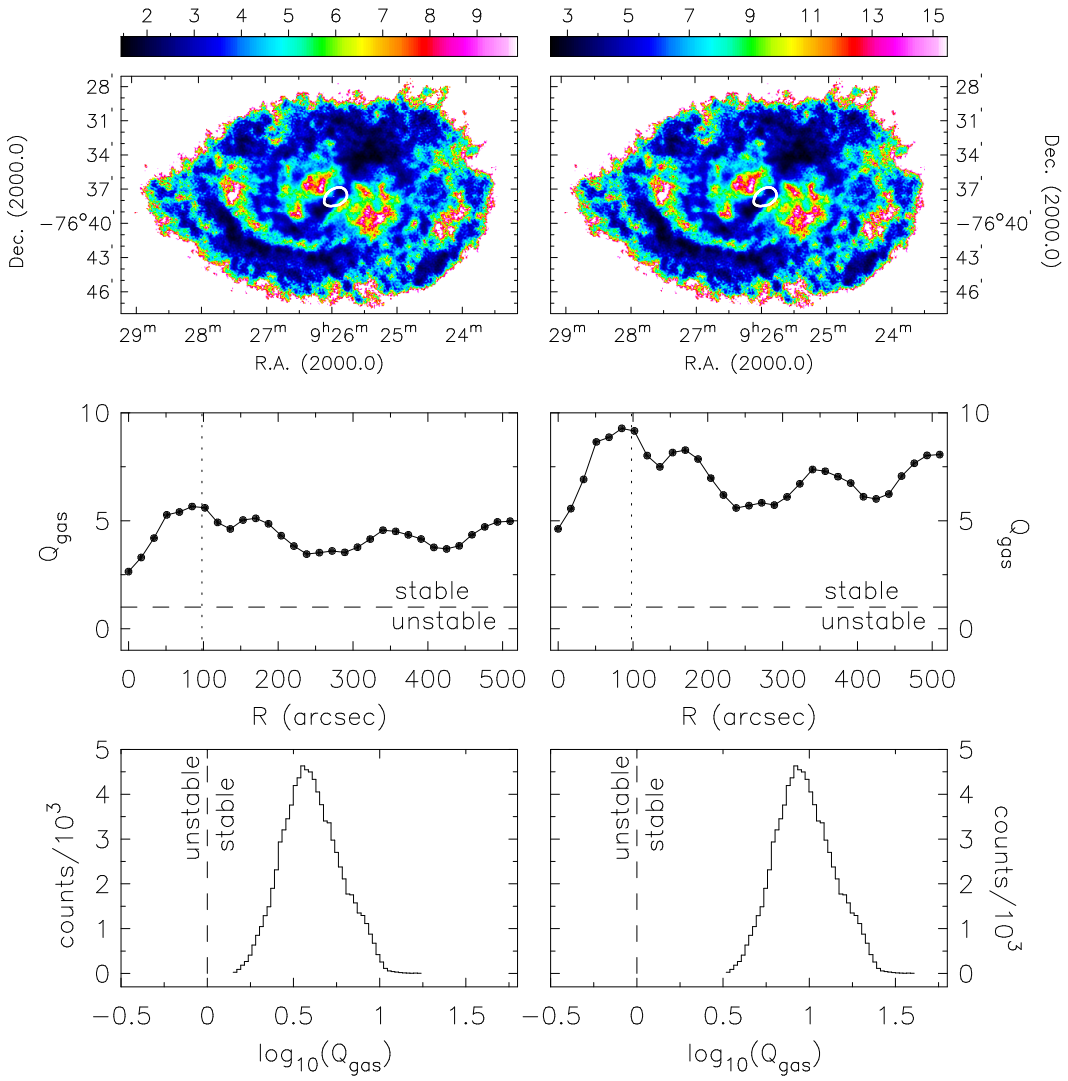

Figure 5.22: NGC 2915 Toomre Q_{gas} instability maps. All figures in the left- and right-hand columns correspond to a constant gas velocity dispersion of 4.9 km s^{-1} and 8.8 km s^{-1} respectively. **Top row:** Q_{gas} maps for the H I disk of NGC 2915. **Middle row:** Radial profiles of Q_{gas} maps. **Bottom row:** Distribution of Q_{gas} parameters. The colour bars above the upper panels specify the Q_{gas} intensity scale for the Q_{gas} maps. The gas is expected to be unstable to gravitational collapse in regions where the Toomre parameter is less than unity. The single white contour in the upper panels, at a level of $\Sigma_{SFR} = 0.0018$ M$_\odot$ yr^{-1} kpc^{-2}, approximates the edge of the star-forming core of NGC 2915. The dotted vertical lines shown in the middle panels represent the R-band R_{25} radius at 98″. The large steps up in Q_{gas} values near the edges of the H I disks are due to low signal-to-noise ratios and are therefore physically insignificant.

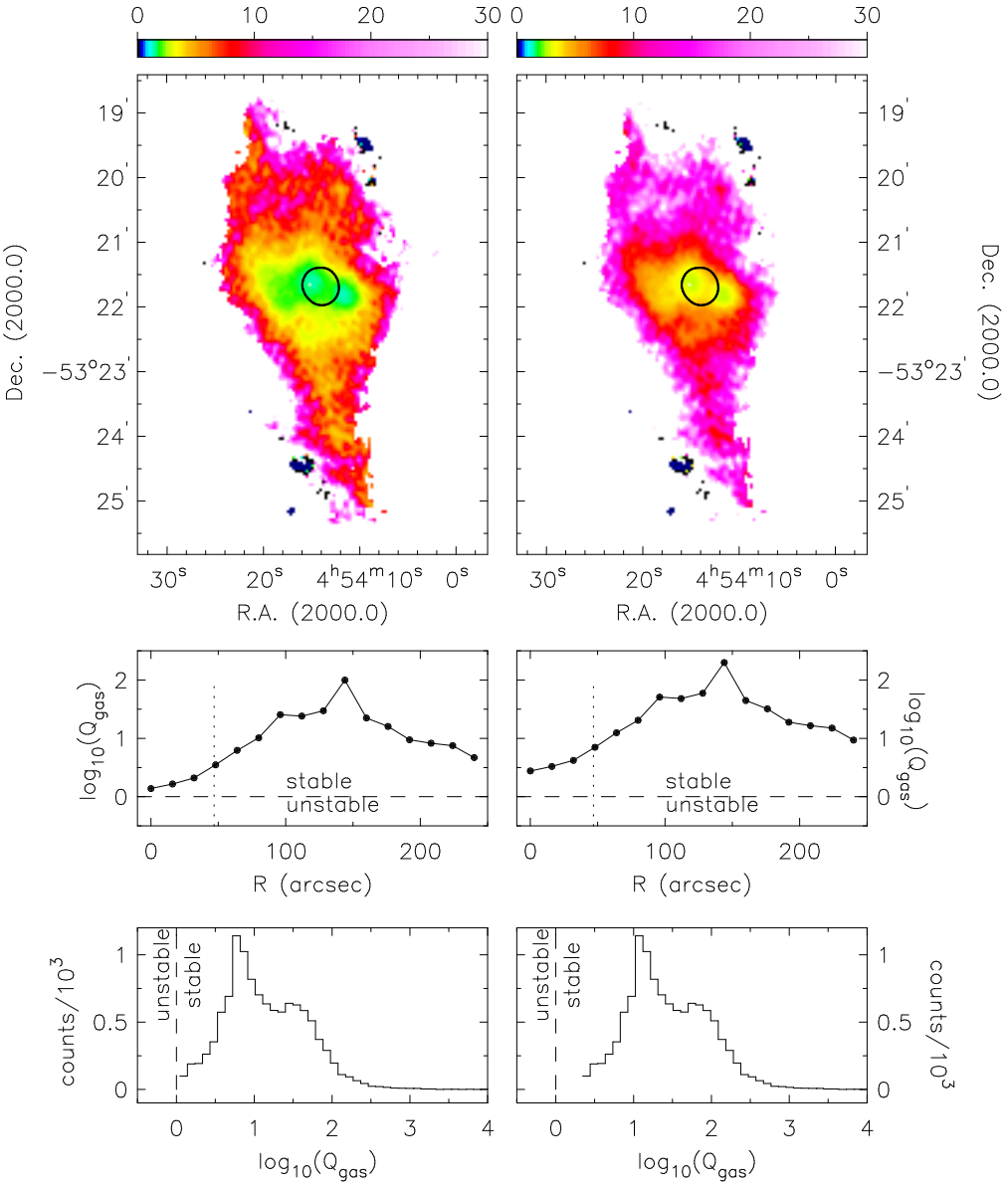

Figure 5.23: NGC 1705 Toomre Q_{gas} instability maps. All figures in the left- and right-hand columns correspond to a constant gas velocity dispersion of 4.9 km s^{-1} and 8.8 km s^{-1} respectively. **Top row:** Q_{gas} maps for the H I disk of NGC 1705. **Middle row:** Radial profiles of Q_{gas} maps. **Bottom row:** Distribution of Q_{gas} parameters. The colour bars above the upper panels specify the Q_{gas} intensity scale for the Q_{gas} maps. The gas is expected to be unstable to gravitational collapse in regions where the Toomre parameter is less than unity. The single white contour in the upper panels, at a level of $\Sigma_{SFR} = 0.1$ M$_\odot$ yr^{-1} kpc^{-2}, approximates the edge of the star-forming core of NGC 1705. The dotted vertical lines shown in the middle panels represent the B-band R_{25} radius at 46.9″.

$\log Q_{gas} \approx 0.55$ and $\log Q_{gas} \approx 0.92$ for the cold and warm cases respectively, far-removed from $Q_{gas} = 1$ required for gravitational instability.

Despite there being no $Q_{gas} \leq 1$ in the presence of clear SF activity at the centre of NGC 2915, the Q_{gas} maps do exhibit the sort of structure that one might hope for if they were to correctly predict the locations of star-forming regions. Radial profiles created for each of the NGC 2915 Q_{gas} maps show that the lowest Q_{gas} values do indeed occur at the centre of the galaxy. A clear drop in the Q_{gas} radial profile occurs at $R \sim R_{25}$ (dotted lines in middle panels of Fig. 5.22), the edge of the stellar disk. Furthermore, low Q_{gas} values are observed along the H I spiral arms, and higher values in-between the spiral arms. This structure of the Q_{gas} map is consistent with the notion of star formation occurring along spiral arms where the gas is compressed by spiral density waves passing through the disk.

The situation is similar for NGC 1705 whose logarithmic Q_{gas} distribution is double-peaked with $Q_{gas} > 1$ throughout the H I disk. This galaxy's intense SF activity is not well-described by the Q_{gas} criterion. The very large $Q_{gas} \sim 10^{1.5} \sim 30$ estimates for the outer H I disk (for the cold phase H I) are consistent with the results of Meurer et al. (1998). Again, despite $Q_{gas} > 1$ throughout the H I disk, the lowest Q_{gas} values do indeed occur near the galaxy's central star-forming core (R_{25} is again marked by a dotted vertical line in the middle panels of Fig. 5.23).

Comparison to other star-forming dwarfs

How do the results of NGC 2915 and NGC 1705 compare to those of other star-forming dwarfs? Figure 5.24 shows the star formation efficiency as a function of Q_{gas} for NGC 2915 and NGC 1705. The corresponding figure for the THINGS dwarf galaxies sample of Leroy et al. (2008) is shown in Fig. 5.34. These authors found almost no area of the inner disk to be formally unstable to gravitational collapse. Rather, they found that $Q_{gas} \sim 4$ is typical for the region $R \lesssim 0.8 R_{25}$ and that $Q_{gas} \gtrsim 10$ is common for larger radii. In this sense, the results for NGC 2915 and NGC 1705 are consistent with the sample of Leroy et al. (2008). The authors find no clear evidence of a Q_{gas} threshold that can unambiguously distinguish between star-forming regions of high and low efficiency. Leroy et al. (2008) did, however, use $\sigma_{gas} = 11$ km s^{-1} as their preferred measure of the kinetic support of the ISM. They go on to point out that under various assumptions regarding the H_2 content and the thermal pressure of the galaxies, the median value of Q_{gas} in the outer disks of dwarfs agrees quite well with the threshold value of Q_{gas} determined by Kennicutt (1989) and Martin & Kennicutt (2001). Our results for NGC 2915 and NGC 1705 as well as those of Leroy et al. (2008) are also similar to those of Hunter et al. (1998) who, for their sample of dwarf galaxies, found Q_{gas} to be systematically higher by a factor of ~ 2 than

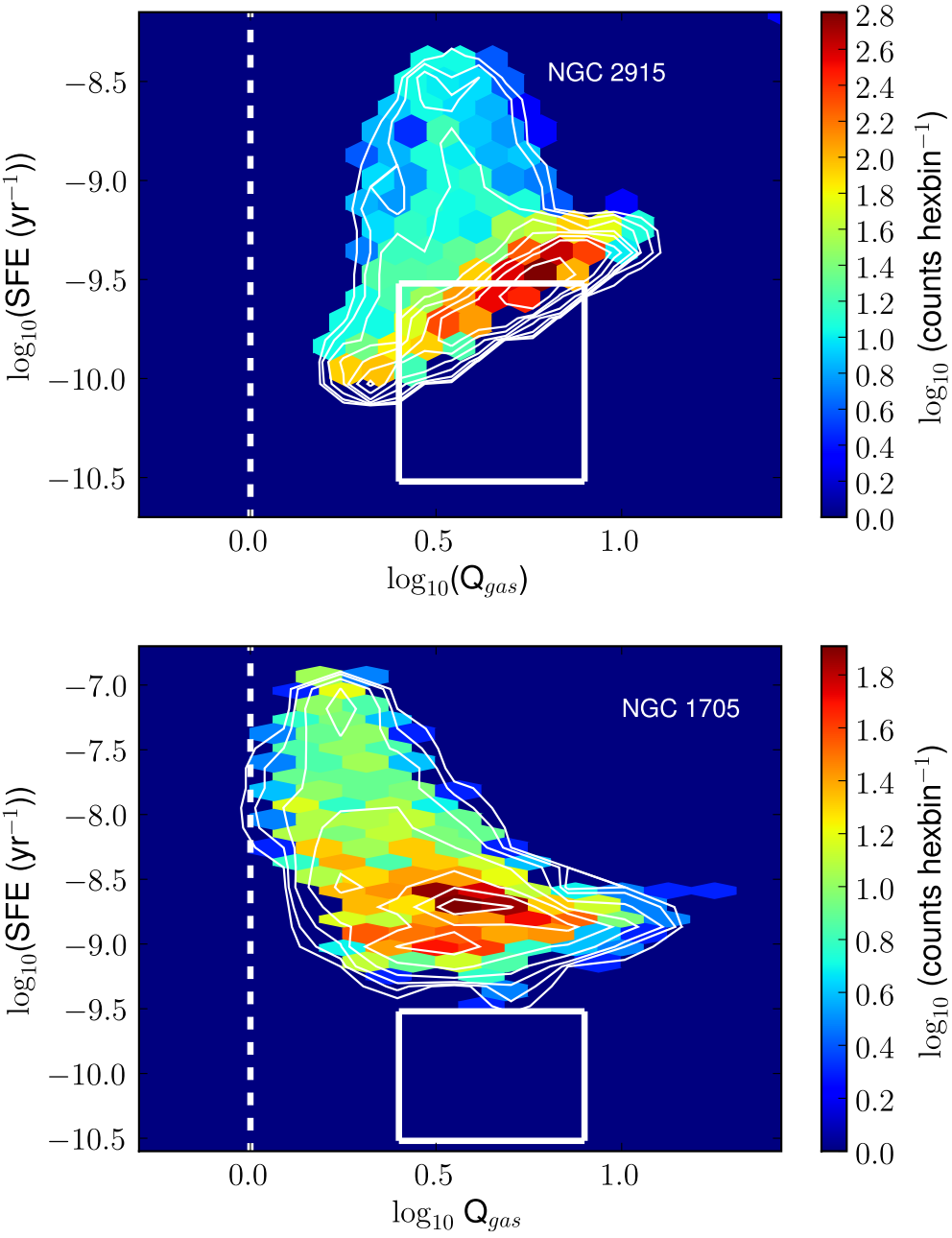

Figure 5.24: Star formation efficiency as a function of Q_{gas} for the inner $R \leq 1.2R_{25}$ parts of NGC 2915 and NGC 1705. A constant $\sigma_{gas} = 4.9$ km s^{-1} was assumed for both plots. The colour bar indicates the logarithm of the number of points within each hexagonal bin. The white contours are at levels of $\log_{10}$(0.3, 0.6, 0.9, 1.2, 1.5, 1.8, 2.1, 2.4) for the upper panel, and $\log_{10}$(0.3, 0.6, 0.9, 1.2, 1.5, 1.8, 2.0, 2.4) for the lower panel. The subsets of parameter space leftward and rightward of the white dashed line represent the regions where gravitational instability of the ISM is and is not expected respectively. The white box in each panel encloses the same region as the black box shown in Fig. 5.34.

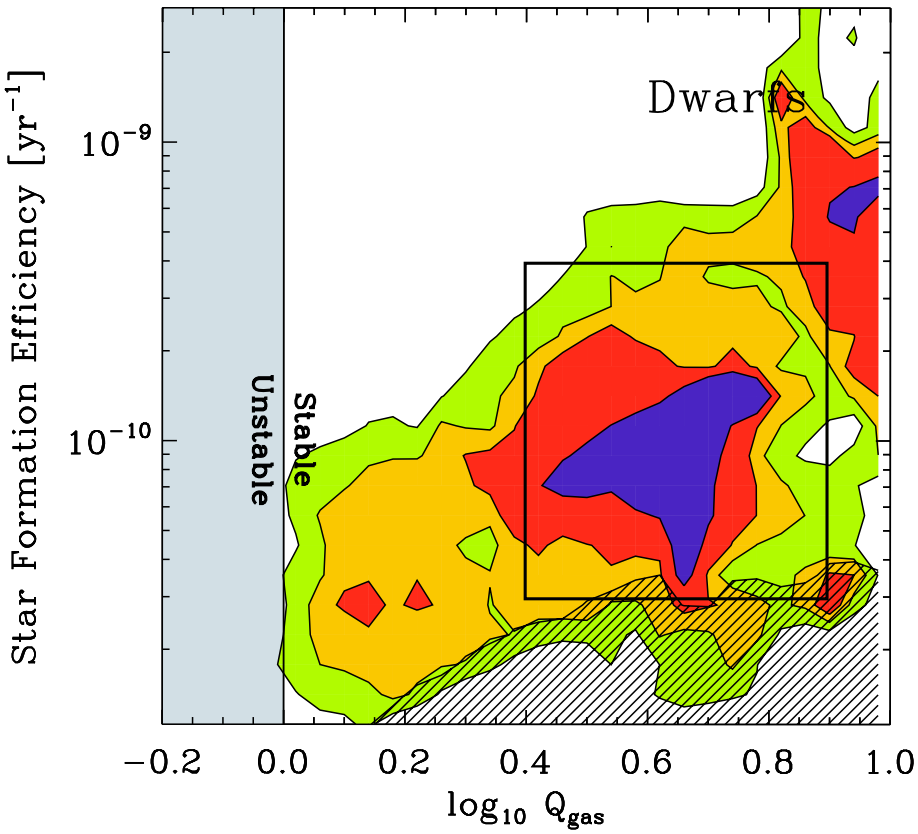

Figure 5.25: Star formation efficiency as a function of Q_{gas} for the THINGS sample of dwarf galaxies, taken from Leroy et al. (2008). The figure shows data from 11 dwarf galaxies for individual lines of sight. Equal weight is given to each galaxy and contours include 90%, 75%, 50% and 25% of the data. The hatched region indicates where the THINGS survey is incomplete. The grey area shows where instability of the ISM is expected. The black box encloses the same region as the white boxes shown in Fig. 5.24.

the value of determined by Kennicutt (1998).

5.4.5 Star+gas two-fluid Toomre criterion

Introduction

The Toomre criterion of the previous section was a single-fluid model. It incorporates only the gravitational potential of the gaseous disk. An additional fluid-like mass component distributed within the gas disk can significantly affect the instability of the gas, essentially increasing the self-gravity of small perturbations. Two-fluid instability models are important for systems in which the stellar and gas masses are comparable. It was shown in Sec. 5.3.4 that the SF activity in NGC 2915 and NGC 1705 is tightly correlated with their stellar surface densities. This section deals with an investigation of a two-fluid instability model in which the gravitational potential of the gas *and* the stars is considered simultaneously.

First, the relative distributions of the gaseous and stellar components within each galaxy is considered. In Sec. 2.4.2 the H I mass of NGC 2915 was found to be $M_{HI} \sim 5.4 \times 10^8$ M$_\odot$. The *Spitzer* 3.6 μm imaging probes the bulk of the stellar mass in the form of the red stellar population. The total stellar mass of NGC 2915 is estimated to be $M_* \sim 1.2 \times 10^9$ M$_\odot$. The stellar mass is therefore about twice the gas mass. Moreover, the distribution and *concentration* of the stellar mass differs significantly to the gas mass. This is evident from surface density profiles for the H I and the old stars shown in Fig. 5.26. All gas surface densities out to a radius of $R \sim 510''$, are of the order of a few M$_\odot$ pc^{-2}. The stellar surface densities are of the order of a hundred M$_\odot$ pc^{-2} for $R \lesssim 75''$, and approximately zero thereafter. The stellar mass is much more centrally concentrated than the gas mass. The situation is almost identical in the case of NGC 1705. This suggests that SF activity within the central disk of each galaxy should be better described by a two-fluid instability model as opposed to a single fluid model.

Wang & Silk (1994) produced a gravitational instability model which included the stellar contribution to the instability. They derived an effective Toomre Q parameter, Q_{eff}, such that $Q_{eff} = Q/\alpha_{eff}$, with

$$\alpha_{eff} = \left(1 + \frac{\Sigma_* \sigma_{gas}}{\Sigma_{gas} \sigma_*}\right)^{-1}, \tag{5.10}$$

where Σ_* and σ_* are the stellar surface density and velocity dispersion respectively. The equation implies that when the stellar surface density is very low or the stellar velocity dispersion very high, $\alpha_{eff} \approx 1$, and Q_{eff} reduces to the standard Toomre criterion (i.e. $Q_{eff} \approx Q_{gas}$).

Rafikov (2001) determined the dispersion relation for axisymmetric density waves propagating through a thin, rotating disk composed of gas and several stellar components. He showed that,

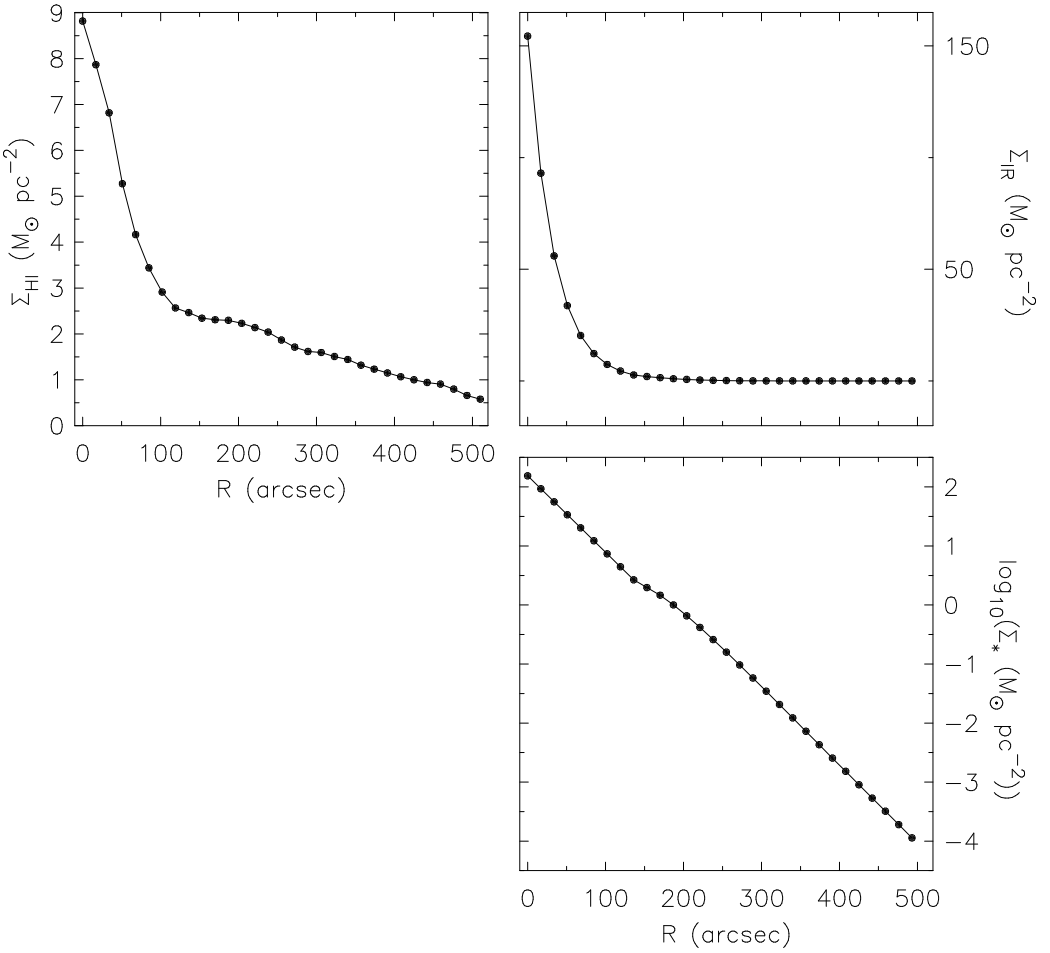

Figure 5.26: Mass surface density radial profiles for NGC 2915. **Top left panel:** HI surface density radial profile. **Top right panel:** Stellar surface density radial profile. **Bottom right panel:** Logarithmic stellar surface density radial profile. All surface densities have been inclination-corrected.

in the case of two components, one stellar and one gaseous, the instability condition is

$$\frac{1}{Q_{gas,*}} \equiv \frac{2}{Q_*}\frac{q}{1+q^2} + \frac{2}{Q_{gas}}R\frac{q}{1+q^2R^2} > 1. \tag{5.11}$$

In this equation, $Q_* \equiv \kappa\sigma_{*,r}/\pi G\Sigma_*$, $q \equiv k\sigma_{*,r}/\kappa$, with k the wave number of the instability. $R \equiv \sigma_{gas}/\sigma_{*,r}$. $\sigma_{*,r}$ is the *radial* velocity dispersion of the stars in the plane of the stellar disk. This is the two-fluid star formation model investigated in this section.

Methodology

The gravitational effects of the stellar mass component of each galaxy are determined using the *Spitzer* 3.6 μm image. The stellar light distributions of NGC 2915 and NGC 1705 are fairly smooth. The 3.6 μm isophotes of each galaxy share a common centre, orientation and ellipticity. For reference, the *Spitzer* 3.6 μm image of NGC 2915's stellar disk, with contours of constant surface brightness, is shown in Fig. 5.27. A corresponding image for NGC 1705 is shown in Fig. 4.8 of Chapter 4. An approach is adopted in which the 3.6 μm surface density for each resolution element in the instability map is approximated as the azimuthally-averaged value corresponding to its radius. This was done using the stellar surface density radial profiles for NGC 2915 and NGC 1705 which were presented in Sec. 3.2 of Chapter 3 and Sec. 4.6 of Chapter 4 respectively. The profiles were parameterised using a scaled exponential function:

$$\log_{10}\left(\frac{\Sigma_*}{M_\odot\ pc^{-2}}\right) = (-0.012 \pm 0.0001)\frac{R}{arcsec} + (2.208 \pm 0.030) \tag{5.12}$$

for NGC 2915, and

$$\log_{10}\left(\frac{\Sigma_*}{M_\odot\ pc^{-2}}\right) = (-0.015 \pm 0.0001)\frac{R}{arcsec} + (2.374 \pm 0.0171) \tag{5.13}$$

for NGC 1705.

The two-fluid stability criterion of Rafikov (2001) requires an estimate of the radial component of a galaxy's stellar velocity dispersion, $\sigma_{*,r}$. The prescription of Leroy et al. (2008) was followed to determine $\sigma_{*,r}$ as a function of galactocentric radius. They made four assumptions in order to determine the radial stellar velocity dispersion:

1. The scale height of an exponential stellar disk is constant with galactocentric radius. This is a typical observation for edge-on galaxies (Kregel et al., 2002).

2. A flattening ratio of $l_*/h_* = 7.3 \pm 2.2$, where l_* and h_* are the disk scale length and scale height respectively. This is the average volume-corrected flattening of the disk light for the sample of 34 edge-on spiral galaxies of de Grijs (1998) as determined by Kregel et al. (2002). The stellar disk scale lengths of NGC 2915 and NGC 1705 were determined to be $l_* \sim 0.6$ kpc and $l_* \sim 0.14$ kpc respectively, leading to $h_* \sim 0.08$ kpc and $h_* \sim 0.02$ kpc.

3. The stellar disk is isothermal in the z-direction. Under the assumption of hydrostatic equilibrium, this leads to $h_* = 1/2\sqrt{\sigma_{*,z}^2/2\pi G\rho_*}$ (van der Kruit & Searle, 1981), where ρ_* is the mid-plane stellar volume density. Using $\Sigma_* = 4\rho_* h_*$ and eliminating ρ_* then yields $\sigma_{*,z} = \sqrt{2\pi G\Sigma_* h_*}$ (van der Kruit, 1988), leading to

$$\sigma_{*,z} = \sqrt{\frac{2\pi G l_* \Sigma_*}{7.3}}. \tag{5.14}$$

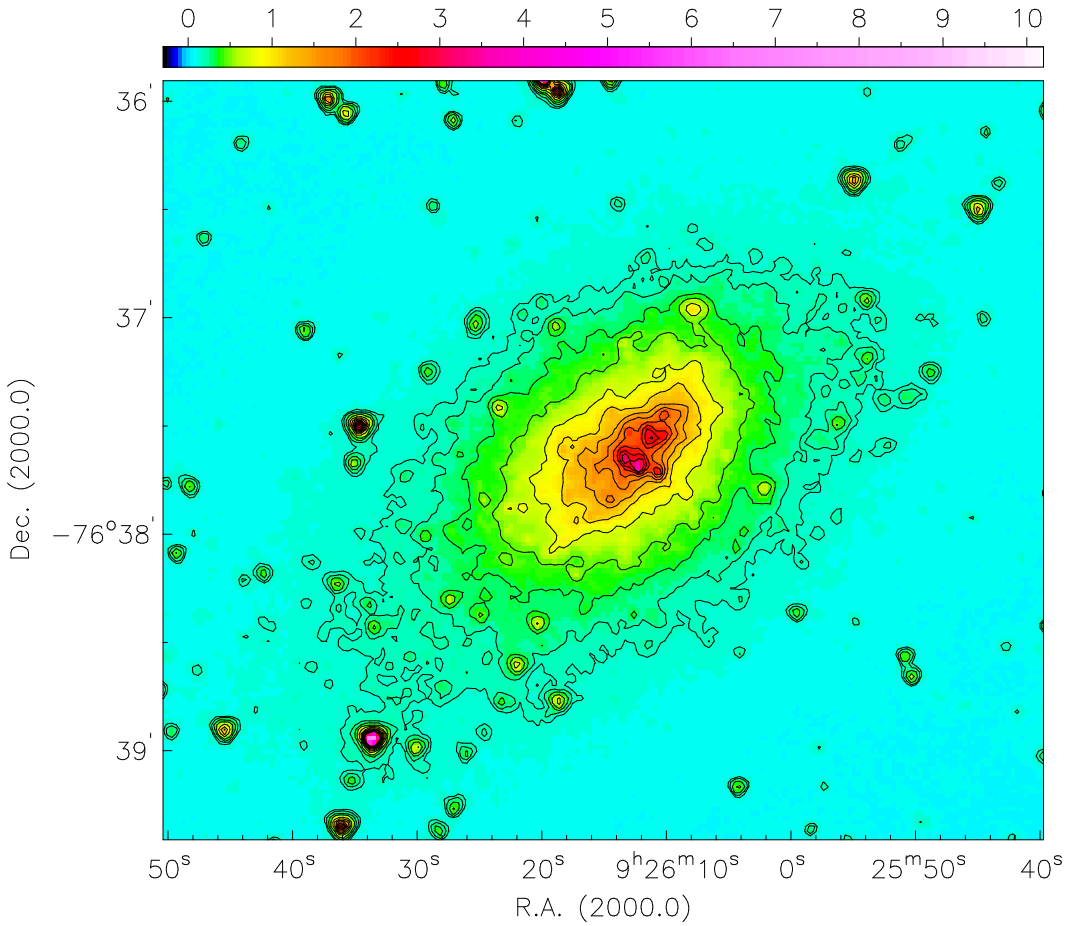

Figure 5.27: 3.6μm IRAC *Spitzer* image of NGC 2915 with isophote contours overlaid. The intensity scale is specified in units of MJy ster^{-1} by the colour bar. Contour levels are at 0.1, 0.15, 0.25, 0.4, 0.7, 1.0, 1.3, 1.6, 1.9, 2.2, 2.5, 2.8, 3.1 MJy ster^{-1}.

4. A fixed ratio of $\sigma_{*,z}/\sigma_{*,r} = 0.6$ to relate the vertical and radial stellar velocity dispersions. This assumption is based on limited available evidence for late-type systems (Shapiro et al., 2003).

The first-order polynomial parameterisation of each galaxy's logarithmic stellar surface density radial profile was used together with the h_* approximation (step 3 above) to yield $\sigma_{*,r}$ as a function of galactocentric radius. Figure 5.28 displays these $\sigma_{*,r}$ radial profiles. At inner radii they are similar to the constant $\sigma_{*,r} = 25$ km s^{-1} estimate used by Rafikov (2001) for the implementation and testing of his two-fluid stability criterion. The radial stellar velocity dispersion monotonically approaches zero beyond the stellar disk.

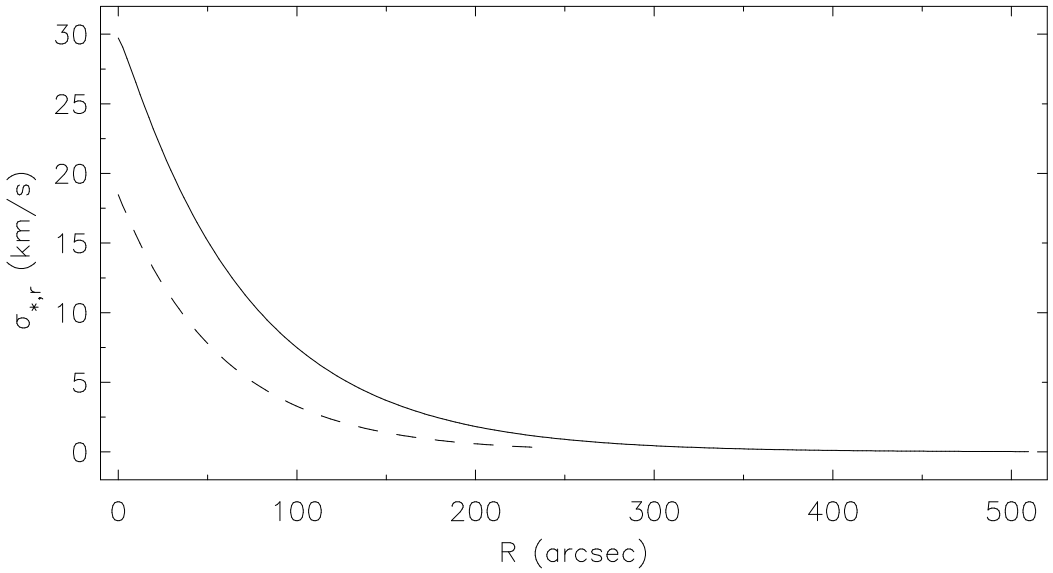

Figure 5.28: Radial profiles of the stellar velocity dispersion parallel to the plane of the stellar disk for NGC 2915 and NGC 1705 (solid and dashed curves respectively), from parameterising the stellar surface density radial profiles.

So far, the prescriptions used to estimate Σ_* and $\sigma_{*,r}$ have been presented. These parameters together with the epicyclic frequency radial profile of each galaxy allow Q_* in Eqn. 5.11 to be determined. The other parameters in Eqn. 5.11 that need to be considered are q and R. The q parameter is a function of $k = 2\pi/\lambda$, the wavenumber of the instability. Specifying k determines q. According to Rosolowsky & Blitz (2005), 80% of the Milky Way's molecular gas is contained within giant molecular clouds ranging in size from $\sim$ 2 pc to $\sim$ 100 pc. Since we have no a priori knowledge of the linear size of a typical giant molecular cloud in NGC 2915 or NGC 1705, a set of perturbation wavenumbers was selected that spans this length scale range. Perturbation length scales of λ = 0.005, 0.1, 0.2, 0.3, 0.5, 0.8 kpc were considered, each resulting in a separate instability map. These perturbation length scales correspond to wavenumbers of k = 40, 20, 10, 6, 4, and 2.5 times π. In the context of the instability maps, they span the linear extent of a single resolution element, as well as the entire gaseous disk. Finally, $R = \sigma_{gas}/\sigma_{*,r}$ was specified by assuming $\sigma_{gas} = 4.9$ km s^{-1} for all two-fluid instability maps and using the radial $\sigma_{*,r}$ profiles shown in Fig. 5.28.

NGC 2915 and NGC 1705 results and discussion

The results of the $1/Q_{gas,*}$ two-fluid instability analyses for NGC 2915 and NGC 1705 are presented in figures 5.29 to 5.32. Figures 5.29 and 5.30 contain the full instability maps for the above wave numbers for NGC 2915 and NGC 1705 respectively. Figure 5.31 shows the radial profiles of these maps, while Fig. 5.32 shows the distributions of the $1/Q_{gas,*}$ resolution elements that constitute each map.

The NGC 2915 results are considered first. Even with the gravitational potential of the stellar disk included, the galaxy is sub-critical with $1/Q_{gas,*} < 1$ throughout its H I disk for all implemented wave numbers. This two fluid instability criterion, like the single fluid instability considered in the previous section, formally fails to predict the observed SF activity at the centre of NGC 2915. The extra self-gravity of the ISM induced by the stellar potential is still not enough to counteract the large epicyclic frequencies at inner radii. Despite this formal failure for the central part of the galaxy, the instability maps again produce the sort of structure that one might expect for a late-type galaxy. Beyond the radial extent of the stellar core, the two-fluid $1/Q_{gas,*}$ maps resemble the single-fluid Q_{gas} maps. This result is expected since the stellar potential is negligible in the outer gaseous disk of the galaxy.

The situation is only slightly better for the NGC 1705 instability maps which, for some of the implemented wave numbers, have $1/Q_{gas,*} > 1$. The $Q_{gas,*} = 1$ level is shown as a single black contour in the instability maps shown in Fig. 5.30. The best instability model is that for a wave number of $k = 10\pi$, which corresponds to a perturbation length-scale of $\lambda = 200$ pc. This model predicts the very central regions of NGC 1705's H I disk to be unstable. In the context of a two-fluid Toomre criterion, the gravitational potential of NGC 1705's stellar disk seems to add enough self-gravity to the ISM to yield the central disk unstable.

The top panel of Fig. 5.31 shows the radial profiles of the various NGC 2915 $1/Q_{gas,*}$ maps presented in Fig. 5.29. The radial profiles demonstrate clearly that the two-fluid instability parameters never exceed unity for all considered wavenumbers. Including the gravitational influence of the stellar disk does, however, leave NGC 2915's inner gaseous disk only marginally stable against gravitational collapse for wavenumbers $k \sim 4\ \pi$, corresponding to perturbation length-scales of ~ 0.5 kpc. This result is fairly consistent with those of Leroy et al. (2008). The authors found no clear evidence of a single-fluid Toomre Q_{gas} criterion that could unambiguously distinguish between high and low star formation efficiency regions, yet when using Eqn. 5.11 to include the effects of stellar gravity, found some regions became gravitationally unstable. Including the stellar gravity led to large portions of the gaseous disks in their sample being only marginally stable against large-scale gravitational collapse. The radial profiles of NGC 1705's instability maps (Fig. 5.31) show that large perturbation length-scales of $\lambda \sim 0.8$ kpc make the

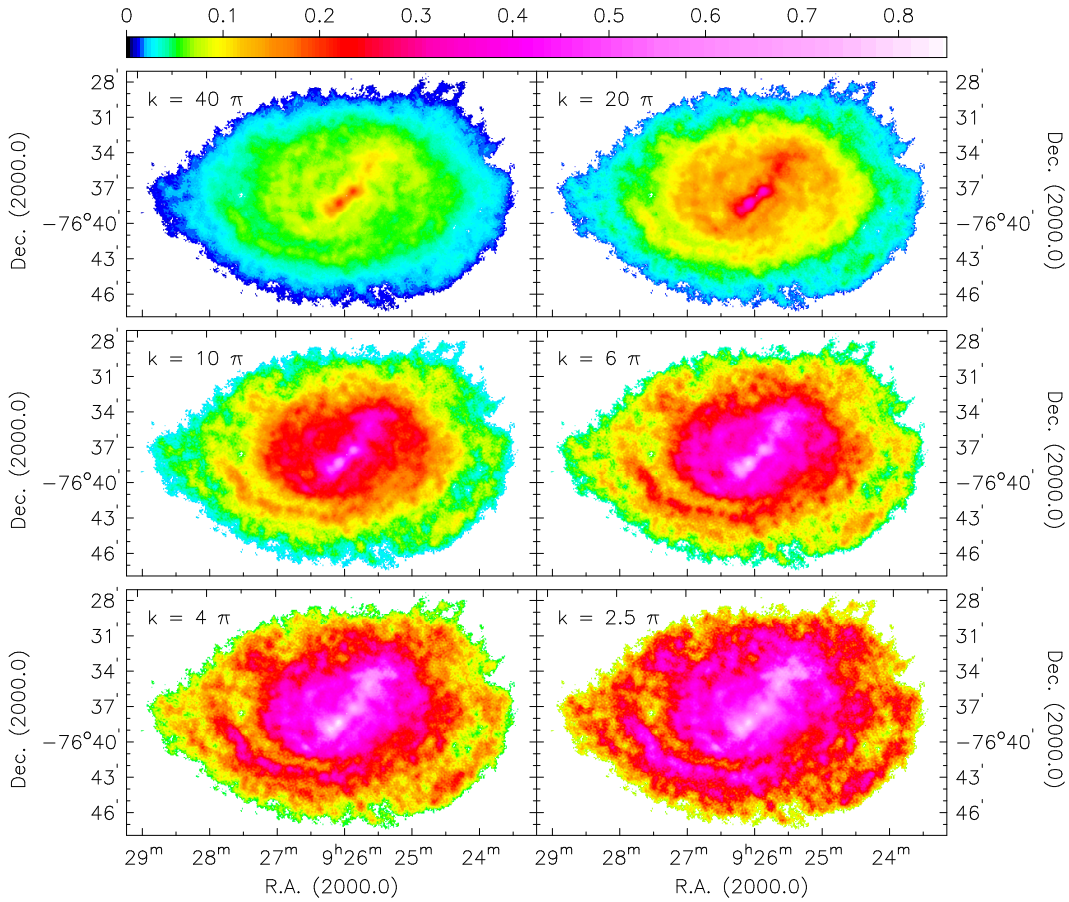

Figure 5.29: NGC 2915 colour images of stars+gas two-fluid instability maps for various perturbation length scales. The common logarithmic intensity scale is specified by the colour bar at the top of the figure and represents the two-fluid instability parameter, $1/Q_{gas,*}$. The perturbation wavenumber, $k = 2\pi/\lambda$, for each instability map is shown in the top left corner of the panel. Wavenumbers of $k = 40$, 20, 10, 6, 4, 2.5 times π correspond to wavelengths of $\lambda = 0.005$, 0.1, 0.2, 0.3, 0.5, 0.8 kpc respectively. The gaseous disk is expected to be unstable to large-scale gravitational collapse in regions where $1/Q_{gas,*} > 1$. For all of the above-presented wavenumbers, the instability criterion predicts a sub-critical gaseous disk for NGC 2915. An H I velocity dispersion of $\sigma_{gas} = 4.9$ km s^{-1} was assumed for all maps.

Figure 5.30: NGC 1705 colour images of stars+gas two-fluid instability maps for various perturbation length scales. The intensity scale of each map is specified by the colour bar at the top of the panel and represents the two-fluid instability parameter, $1/Q_{gas,*}$. The perturbation wavenumber, $k = 2\pi/\lambda$, for each instability map is shown in the top left corner of the panel. Wave-numbers of k = 40, 20, 10, 6, 4, 2.5 times π correspond to wavelengths of λ = 0.005, 0.1, 0.2, 0.3, 0.5, 0.8 kpc respectively. The gaseous disk is expected to be unstable to large-scale gravitational collapse in regions where $1/Q_{gas,*} > 1$. The single black contour shown in the middle and bottom panels is at a level of $1/Q_{gas,*} = 1$ and encloses the region of the galaxy in which gravitational instability is formally expected. An H I velocity dispersion of $\sigma_{gas} = 4.9$ km s^{-1} was assumed for all maps.

entire H I disk of of the galaxy unstable against gravitational collapse. This demonstrates the inappropriateness of the perturbation size. Perturbations with wavenumber $k \sim 10\pi$ yield only the inner disk unstable while the degree of instability is roughly constant over the outer H I disk.

Lastly, the distributions of $1/Q_{gas,*}$ parameters for each instability map are shown in Fig. 5.32. One distinct trend is noticeable for both galaxies: $1/Q_{gas,*}$ parameters corresponding to higher wavenumbers are generally shifted or skewed towards lower values. This trend is consistent with the general decrease in $1/Q_{gas,*}$ with increasing wavenumber as seen in the radial profiles of the maps. For NGC 2915, a second trend is observed. A smaller range in $1/Q_{gas,*}$ parameters is associated with instability maps corresponding to larger wavenumbers. Each of the $1/Q_{gas,*}$ distributions for NGC 1705 exhibit very distinct, narrow peaks. As Leroy et al. (2008) point out, a small spread in $1/Q_{gas,*}$ values is consistent with a self-regulating star formation scenario in which the gravitational potential associated with newly formed stars will seed further gravitational collapse of the ISM. Such a scenario is consistent with the tight correlation between star formation rate surface density and stellar surface density observed in Sec. 5.3.4.

Finally, it should be mentioned that several sources of uncertainty affect the results of these two-fluid instability analyses. The main source is the lack of direct measurements of the stellar velocity dispersions. The observed stellar surface density radial profile of each galaxy has been used to infer a stellar velocity dispersion profile. This approach *assumes* that $\sigma_* \propto \Sigma_*^{0.5}$ (Leroy et al., 2008). This assumption may well affect the results of the star/gas two-fluid stability analyses.

Comparison to other dwarfs

How do the results of our star+gas two-fluid instability analysis compare with corresponding results for other galaxies? The SFE of each galaxy as a function of $1/Q_{gas,*}$ is shown in Fig. 5.33. For comparison, the corresponding results from Leroy et al. (2008) are shown in Fig. 5.34. The main finding of Leroy et al. (2008) was that including the stars does not render large, extended portions of the disk unstable. This claim is consistent with the NGC 2915 results for which the entire H I disk is formally stable against gravitational collapse for all implemented wavenumbers. The NGC 1705 results are better aligned with the Leroy et al. (2008) findings. This galaxy has a significant fraction of its inner disk being formally unstable. These results should be compared to the corresponding results for the simple Toomre case in which only the gaseous potential was considered and for which no formal gravitational instability was predicted for either galaxy (i.e. $Q_{gas} > 1$ throughout the disk).

The other main finding by Leroy et al. (2008) was that the $1/Q_{gas,*}$ parameters exhibit a

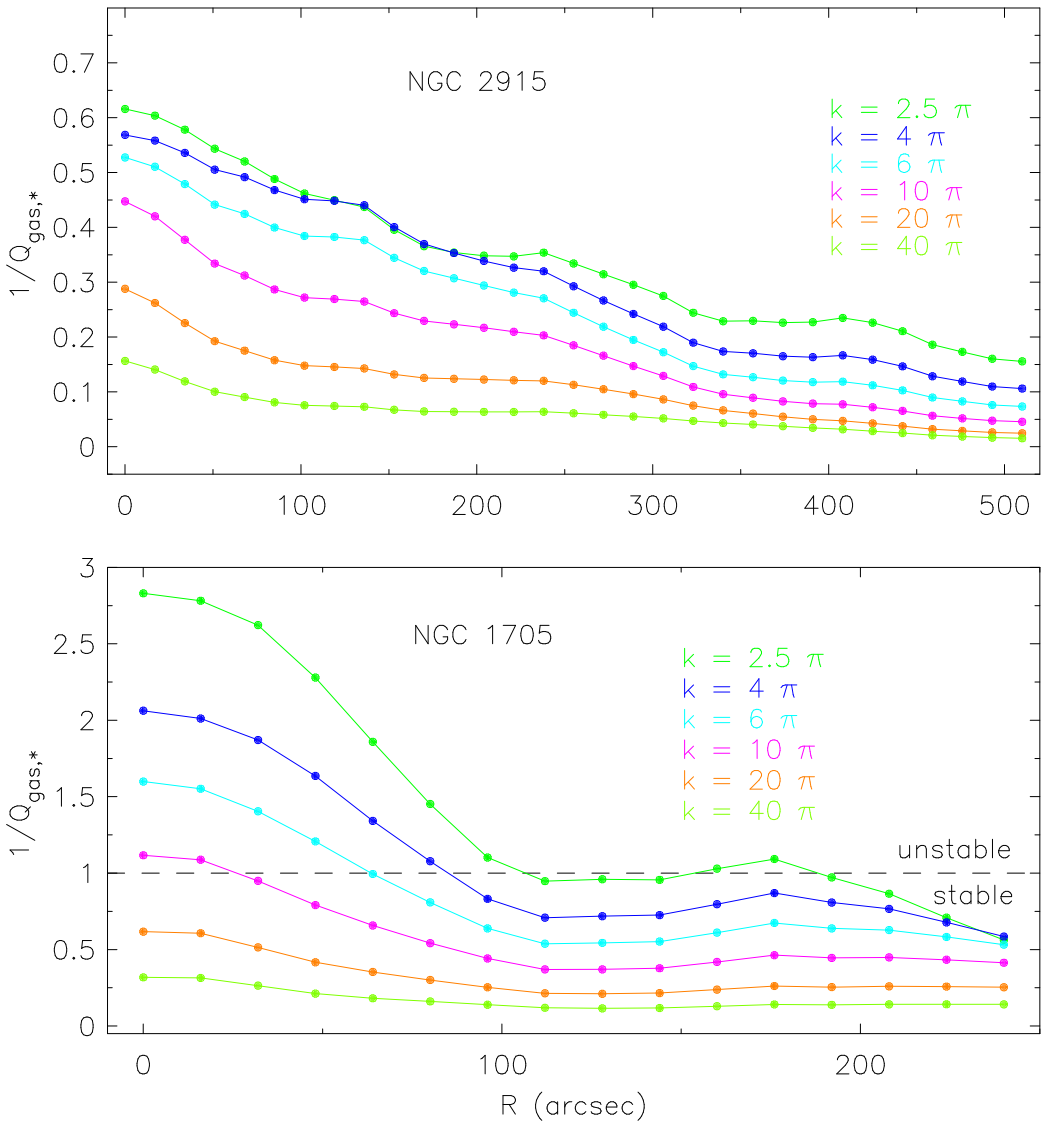

Figure 5.31: Radial profiles of NGC 2915 and NGC 1705 stars+gas two-fluid instability maps for various perturbation length scales. The perturbation wavenumber, $k = 2\pi/\lambda$, for each instability map is shown in the top right corner of the panel. Wave-numbers of k = 40, 20, 10, 6, 4, 2.5 times π correspond to wavelengths of λ = 0.005, 0.1, 0.2, 0.3, 0.5, 0.8 kpc respectively. The gaseous disk is expected to be unstable to large-scale gravitational collapse in regions where $1/Q_{gas,*} > 1$. For all of the above-presented wavenumbers, the instability criterion predicts a sub-critical gaseous disk for NGC 2915. An H I velocity dispersion of σ_{gas} = 4.9 km s^{-1} was assumed for all maps.

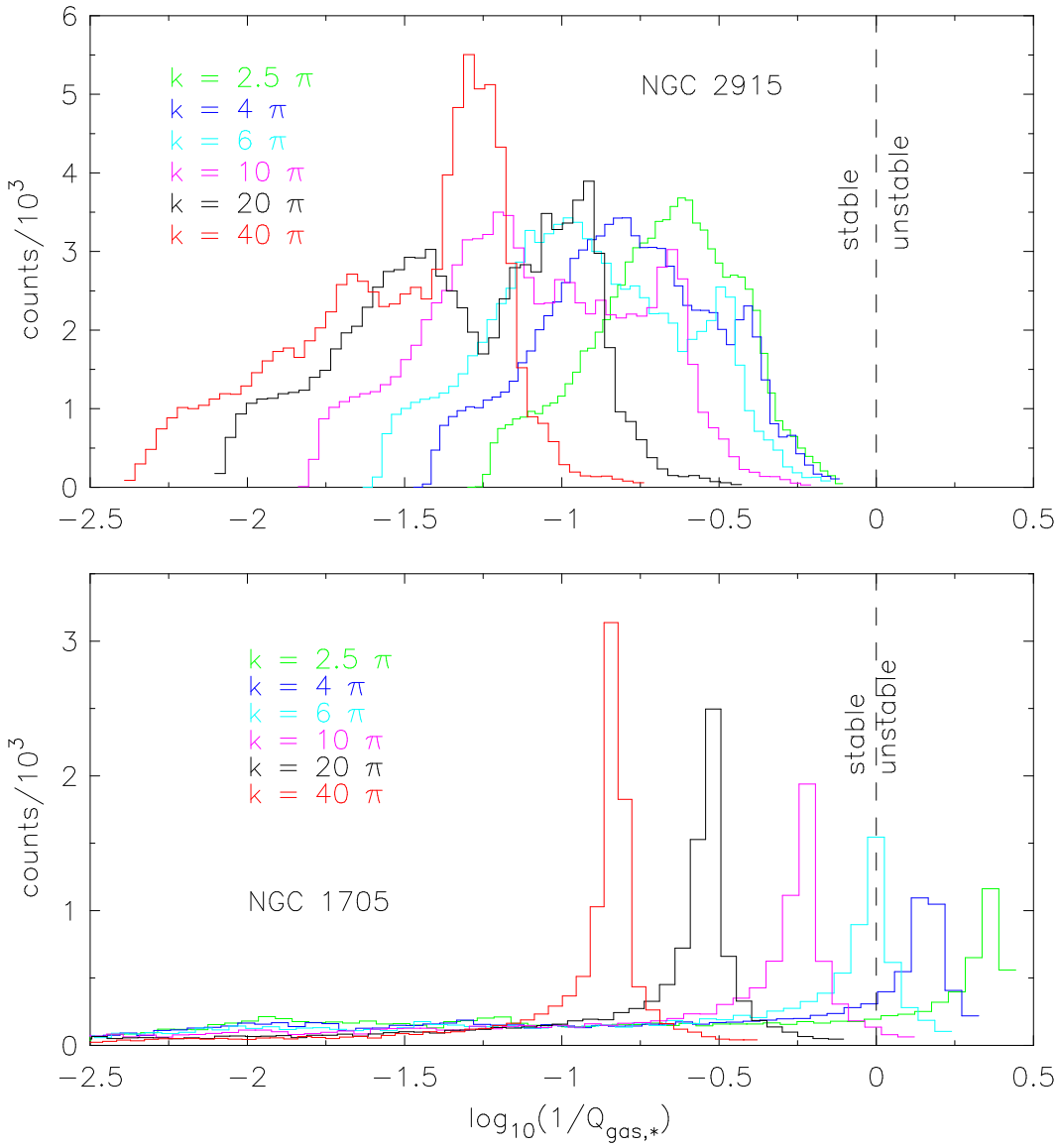

Figure 5.32: Distributions of NGC 2915 and NGC 1705 stars+gas two-fluid instability $1/Q_{gas,*}$ parameters for various perturbation length scales. The perturbation wavenumber, $k = 2\pi/\lambda$, for each distribution is shown in the top left corner of the panel. Wave-numbers of k = 40, 20, 10, 6, 4, 2.5 times π correspond to wavelengths of λ = 0.005, 0.1, 0.2, 0.3, 0.5, 0.8 kpc respectively. The gaseous disk is expected to be unstable to large-scale gravitational collapse in regions where $\log_{10}(1/Q_{gas,*}) > 0$. An H I velocity dispersion of $\sigma_{gas} = 4.9$ km s^{-1} was assumed for all maps.

narrower range of values than the Q_{gas} parameters. This is clearly the case for NGC 1705 for which $\log_{10} 1/Q_{gas,*}$ spans a range of ~ 0.3. Leroy et al. (2008) suggest that a narrow range

of $1/Q_{gas,*}$ values means that $1/Q_{gas,*}$ offers little leverage to predict the locations of efficient star-formation. NGC 1705 seems to contradict this statement by having its inner star-forming core closely traced by the $Q_{gas,*} = 1$ contour for $k = 10\pi$.

5.4.6 Dark matter+gas two-fluid Toomre criterion

Introduction

The results of the previous section demonstrate the important role that a galaxy's stellar gravitational potential, in addition to its gaseous potential, can play in regulating the systems SF activity. This section attempts to answer the question of whether the DM can play a similar role. NGC 2915 and NGC 1705 both have stellar cores of fairly significant mass ($\sim 10^8$ $M_\odot$), but they also contain a lot of dark matter. NGC 2915 contains about 1.4×10^{10} $M_\odot$ of dark mass within 510″ of its centre (Sec. 3.2.4). The dark matter (DM) density distribution was shown to be strongly concentrated, with a core radius of $r_c \sim 0.9$ kpc for the case in which the DM halo is treated as a pseudo-isothermal sphere. The situation is similar for NGC 1705. This galaxy contains $\sim 3.1 \times 10^9$ $M_\odot$ of DM within $\sim 240''$ from its centre (Sec. 4.6), considerably more than its H I and stellar masses of $M_{HI} \sim 1.1 \times 10^8$ $M_\odot$ and $M_* \sim 8 \times 10^8$ $M_\odot$ respectively. This system also has a dense DM core, with a core radius of ~ 1.3 kpc. Since these galaxies contain large amounts of DM where the active SF is observed, it is feasible that the portion of each galaxy's DM halo that is co-located with its H I disk plays a crucial role in terms of regulating the SF activity.

For NGC 2915, Bureau et al. (1999) proposed the self-gravitational effects of a large disk dark matter component as a possible explanation for its observed H I spiral structure. Masset & Bureau (2003) used hydrodynamical simulations to further explore this proposed mechanism, comparing the results to the observations using customised column density constraints. They found that when the observed H I density is scaled up by a factor of 10, the disk develops a spiral structure that closely resembles the observed one. They conclude that this result suggests that the disk of NGC 2915 contains a large dark mass component that is closely linked to the observable neutral ISM. They show furthermore that the proposed scaling does not result in wide-spread star formation in the outer H I disk, consistent with observations. This section investigates the possibility that the portion of each galaxy's DM halo that is co-located with its thick gaseous disk is supplementing the self-gravity of the gas, thereby inducing the gravitational collapse of the ISM.

Based on the estimates of $\sim 5.5 \times 10^8$ $M_\odot$ and $\sim 6.7 \times 10^7$ $M_\odot$ for the total H I mass of NGC 2915 and NGC 1705 respectively, boosting the observed H I surface densities by a factor

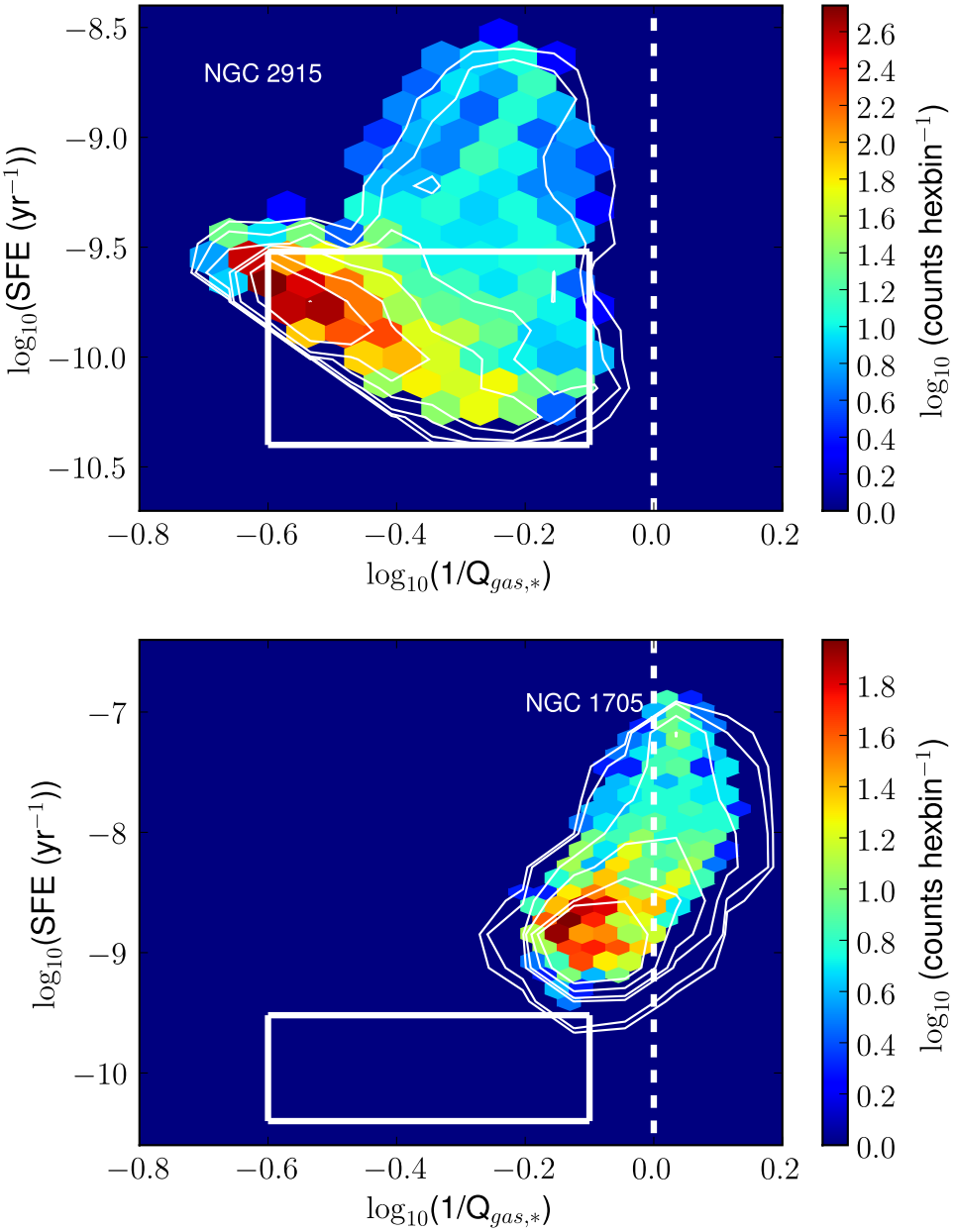

Figure 5.33: Star formation efficiency as a function of $1/Q_{gas,*}$ for the inner $R \leq 1.2R_{25}$ parts of NGC 2915 and NGC 1705. Both corresponding instability maps were generated assuming a perturbation wavenumber of $k = 10\pi$. The colour bar indicates the logarithm of the number of points within each hexagonal bin. The white contours are at levels of $\log_{10}(0.4, 0.8, 1.2, 1.6, 2.0, 2.4, 2.8)$ for the upper panel, and $\log_{10}(0.3, 0.6, 0.9, 1.2, 1.5, 1.8, 2.0)$ for the lower panel. The subsets of parameter space rightward and leftward of the white dashed line represent the regions where gravitational instability of the ISM is and is not expected respectively. An H I velocity dispersion of $\sigma_{gas} = 4.9$ km s^{-1} was assumed for both instability maps. The white box in each panel encloses the same region as the black box shown in Fig. 5.34.

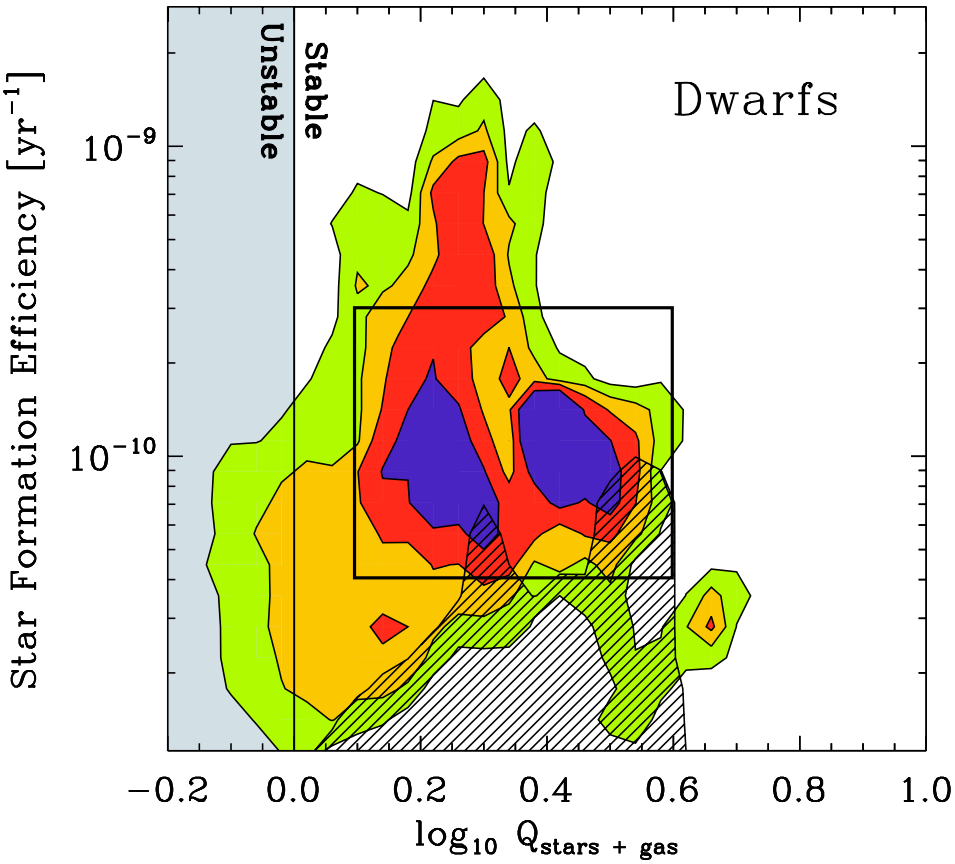

Figure 5.34: Star formation efficiency as a function of $1/Q_{gas,*}$ for the THINGS sample of dwarf galaxies, taken from Leroy et al. (2008). The figure shows data from 11 dwarf galaxies for individual lines of sight. Equal weight is given to each galaxy and contours include 90%, 75%, 50% and 25% of the data. The hatched region indicates where the THINGS survey is incomplete. The grey area shows where instability of the ISM is expected. The black box encloses the same region as the white boxes shown in Fig. 5.33.

of 10 as Masset & Bureau (2003) did for NGC 2915, requires $\sim 50 \times 10^8$ $M_\odot$ and 6×10^8 $M_\odot$ of dark mass distributed within the H I disks of the respective galaxies. This means that 30% and 20% of the total DM in NGC 2915 and NGC 1705 respectively needs to be distributed within their H I disks. Upon first consideration it may seem unlikely to have this relatively large fraction of the dark mass coinciding with the gaseous disk, yet both NGC 2915 and NGC 1705 have thick gaseous disks. In Sec.3.7.3 the H I disk scale height of NGC 2915 was shown to be $h_{gas} \sim 413$ pc. Using the exact same approach with $R_{max} = 148.75''$ and $V_{max} = 68$ km s^{-1} for NGC 1705, an H I scale height of $h_{gas} \sim 242$ pc is estimated. These thick H I disks imply that a significant fraction of the halo dark matter will reside within each of them.

Methodology

In the previous chapters, the rotation curve of each galaxy was used to determine a DM density profile, $\rho_{DM}(r)$. This provides a measure of the average DM volume density in units of $M_\odot$ pc^{-3}. The dynamics of both galaxies were best explained using a pseudo-isothermal sphere parameterisation of their DM halos, $\rho_{DM}(r) = \rho_0/[1 + (r/r_c)^2]$. Assuming the DM to have the same kinematics as the gas, the DM surface density (Σ_{DM}, in units of $M_\odot$ pc^{-2}) along a particular line of sight is modelled as the DM volume density at the corresponding galactocentric radius (given by the DM density profile in units of $M_\odot$ pc^{-3}) integrated over the thickness of the H I disk:

$$\Sigma_{DM}(r) = \int_{-h_{gas}}^{h_{gas}} \rho_{DM}(r) dh \tag{5.15}$$

$$= \int_{-h_{gas}}^{h_{gas}} \frac{\rho_0}{1 + (r/r_c)^2} dh, \tag{5.16}$$

$$= \frac{2\ h_{gas}\ \rho_0}{1 + (r/r_c)^2}. \tag{5.17}$$

Adopting particular ρ_0 and r_c pseudo-isothermal sphere parameters for each galaxy leads to a DM surface density profile. This Σ_{DM} profile is used to approximate the disk DM surface density for each line of sight as the azimuthally-averaged surface density at the corresponding galactocentric radius. This leads to a radially-symmetric correction factor that can be used to add the self-gravity of the DM to the neutral ISM. The DM surface density profile for each galaxy, based on its best-fitting pseudo-isothermal sphere parameters, is shown as a solid curve in Fig. 5.35. Also shown in this figure as dashed curves are alternative versions these profiles, generated by scaling each profile by a factor of 0.3.

Hunter et al. (1998) state that disk dark matter "effectively acts like stars in a two-fluid instability, giving extra self-gravity to small perturbations in the gas". A simple Toomre Q_{gas}

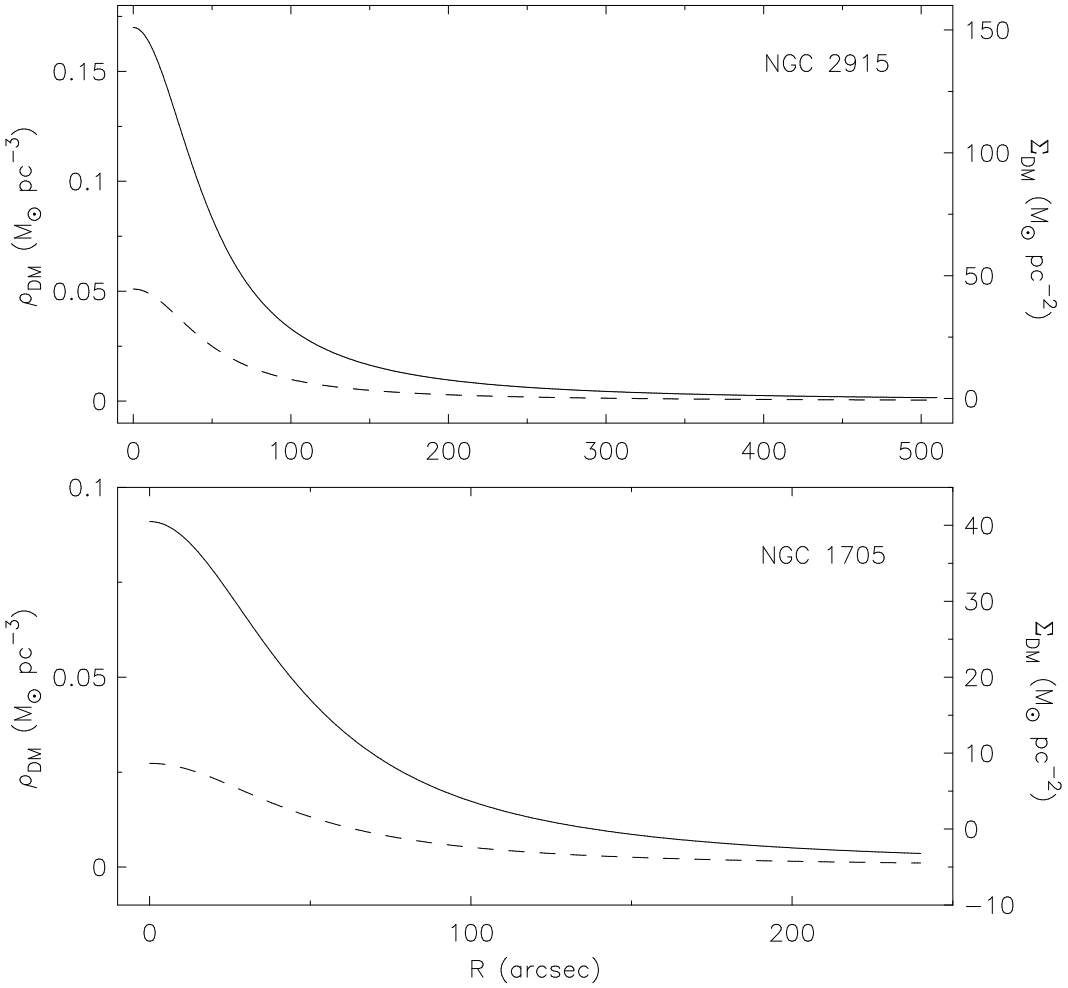

Figure 5.35: NGC 2915 and NGC 1705 dark matter volume/surface density profiles, as specified by Eqn. 5.17, used to construct the various two-fluid instability maps. The solid curves represent the DM profiles for the best-fitting pseudo-isothermal sphere parameters. For NGC 2915 and NGC 1705 these best-fitting parameters are $\rho_0 = 0.17$ $M_\odot$ pc^{-3}, $r_c = 0.9$ kpc and $\rho_0 = 0.091$ $M_\odot$ pc^{-3}, $r_c = 1.2$ kpc respectively. The dashed curves represent the best-fitting profiles scaled by a factor of 0.3.

criterion was therefore tested in which the observed H I surface density, Σ_{HI}, for each resolution element within the H I disk of each galaxy was boosted by an amount equal to the corresponding inferred DM surface density, Σ_{DM}. The condition for gravitational instability then is

$$Q_{gas,DM} \equiv \frac{\alpha_Q \sigma_{gas} \kappa}{\pi G(\Sigma_{gas} + \Sigma_{DM})} < 1. \quad (5.18)$$

NGC 2915 and NGC 1705 results and discussion

Two $Q_{gas,DM}$ instability maps were generated for each galaxy: (1) using the ρ_0 and r_c parameters for the best-fitting mass model, and (2) using the best-fitting profiles scaled by a factor of 0.3. Such a study was not carried out by Leroy et al. (2008), hence a comparison cannot be made to the THINGS galaxies.

The results for NGC 2915 and NGC 1705 are presented in Figs. 5.36 and 5.37. These figures include the full instability maps as well as radial profiles for two different DM halo parameterisations. All of the maps were generated assuming $\sigma_{gas} = 4.9$ km s^{-1}. The top-left panels of the figures demonstrate that a large part of the inner H I disk of each galaxy is formally unstable to gravitational collapse when the best-fitting ρ_0 and r_c parameters are used to estimate the DM surface densities, i.e. when all of the DM that is expected to reside within the H I disk is treated as contributing to the self-gravity of the neutral ISM. The unstable regions (yellow contour in $Q_{gas,DM}$ maps) are much larger than the observed sizes of the star-forming cores of NGC 2915 and NGC 1705 (white contour in $Q_{gas,DM}$ maps). The radial profiles of these $Q_{gas,DM}$ maps (black filled circles in the lower panels of Fig. 5.36 and Fig. 5.37) demonstrate that in addition to the inner disks being unstable, the outer H I disks are also only marginally stable with $Q_{gas,DM} \lesssim 2$ for nearly all radii in each galaxy. This mismatch between the formally unstable and the star-forming regions within each galaxy suggests it to be unlikely the case that *all* of the DM co-located with the disk is in fact contributing to the self-gravity of the ISM.

Of course, not *all* of the dark mass co-located with the H I disk need boost the H I self-gravity. Alternate versions of the $Q_{gas,DM}$ maps for which only 30% of the expected disk dark matter boosts the H I self-gravity were generated. To construct these maps, the best-fitting DM volume/surface density profiles were scaled by a factor of 0.3. These instability maps are shown in the top right-hand panels of Fig. 5.36 and Fig. 5.37, and demonstrate how the unstable region of each galaxy's H I disk decreases in size as the fraction of its disk DM that contributes to the H I self-gravity is lowered. Furthermore, the edges of the unstable parts better coincide with the edges the star-forming cores. For example, the edge of NGC 2915's star-forming core as marked by the white contour in the top right-hand panel of Fig. 5.36 is accurately traced by the $Q_{gas,DM} = 1$ contour of the $Q_{gas,DM}$ map (yellow contour). Similarly, the entire unstable region

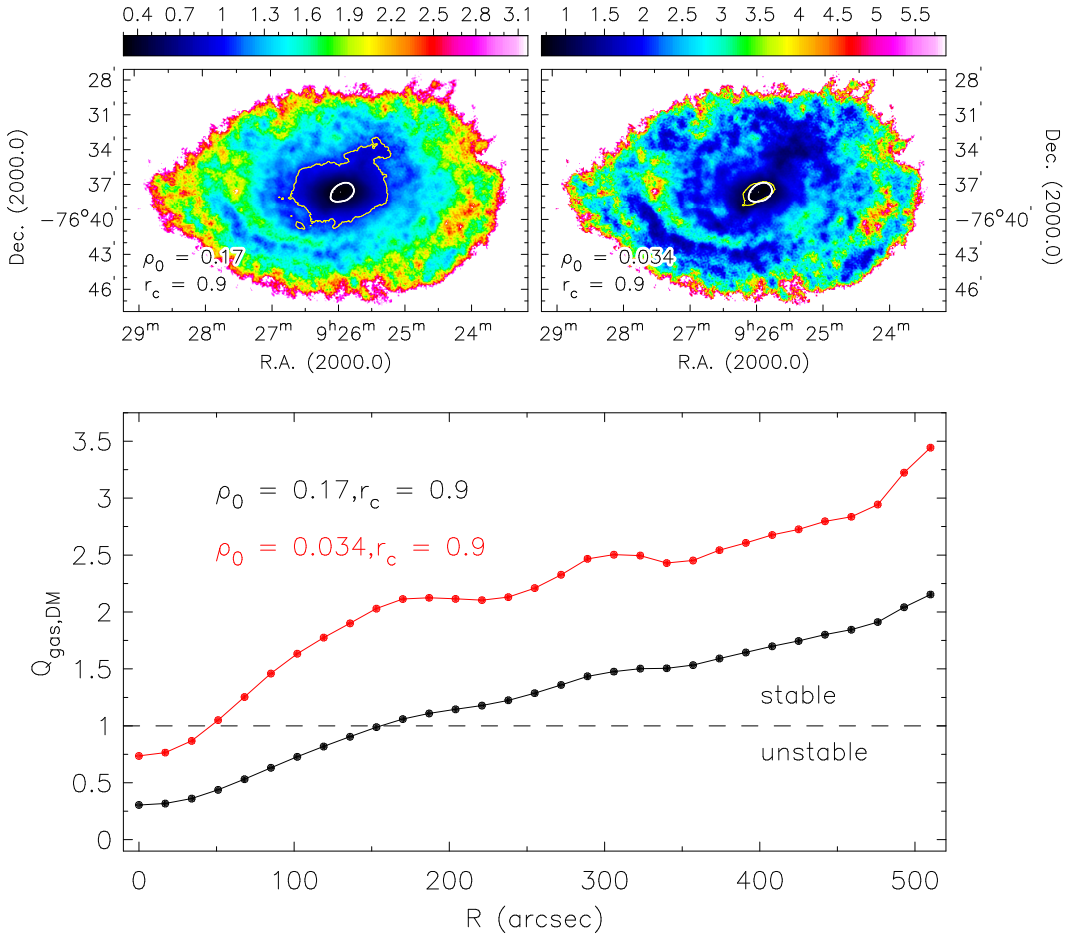

Figure 5.36: **Top panels:** NGC 2915 gas+DM two-fluid instability maps for various pseudo-isothermal sphere DM halo parameterisations. The colour bar above each panel specifies the intensity scale of each map. The pseudo-isothermal parameters used to generate each map are specified in the lower left corner of each panel. ρ_0 and r_c are in units of $M_\odot$ pc^{-3} and kpc respectively. In each panel the edge of the star-forming core is outlined by an arbitrarily selected solid white $\Sigma_{SFR} = 0.0018$ $M_\odot$ pc^{-2} contour while the gravitationally unstable portion of the gas disk is outlined by a solid yellow $Q_{gas+DM} = 1$ contour. **Bottom panel:** Radial profiles of the instability maps.

of NGC 1705's H I disk is contained within its star-forming core.

Crucial to the above-demonstrated success of this two-fluid instability model is the radial distribution of the dark matter surface densities used to boost the observed H I surface densities. Using each galaxy's pseudo-isothermal sphere parameterisation to estimate the amount of DM co-

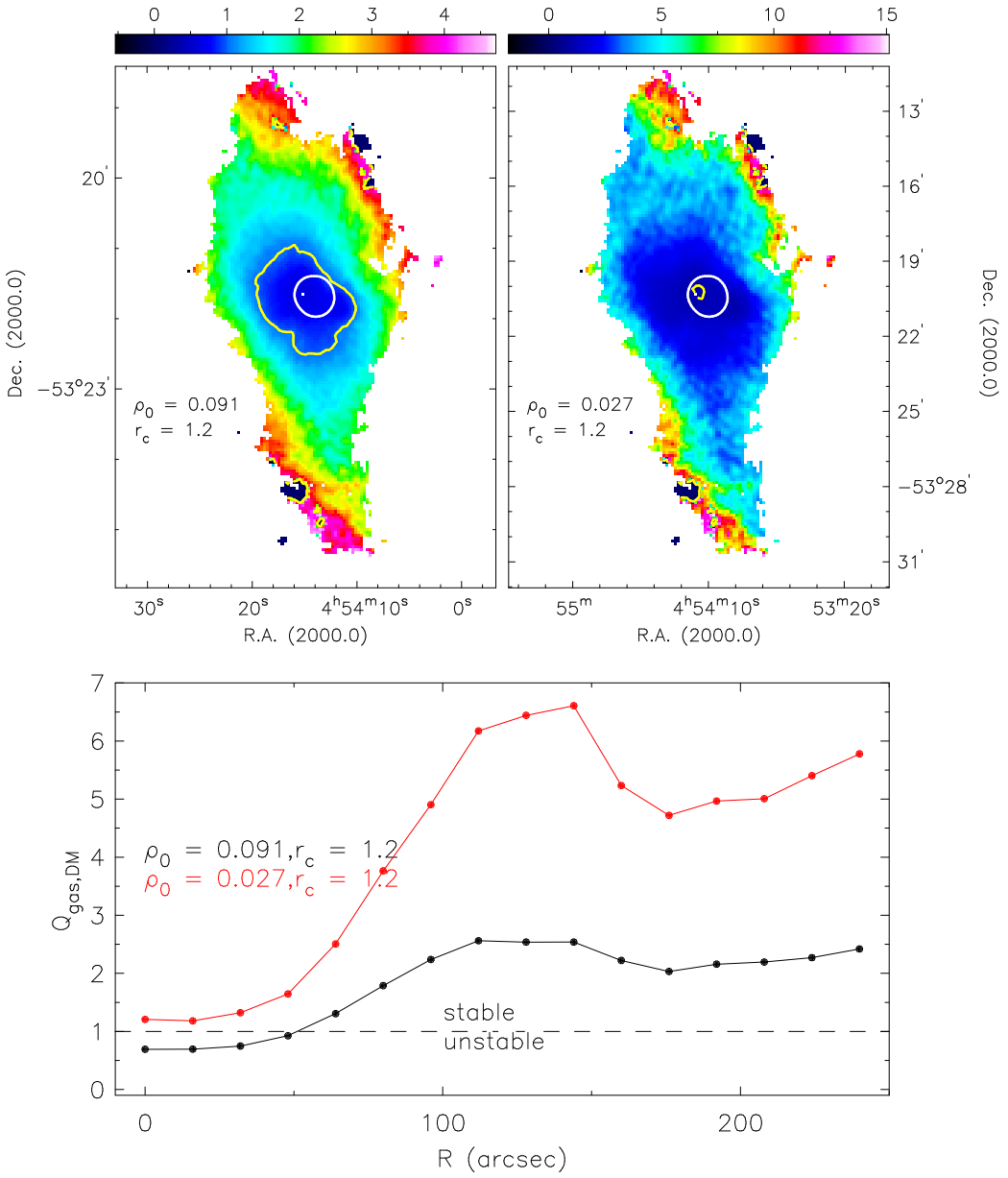

Figure 5.37: **Top panel:** NGC 1705 gas+DM two-fluid instability maps for two different pseudo-isothermal sphere DM halo parameterisations. The colour bar above each panel specifies the intensity scale of each map. The pseudo-isothermal parameters used to generate each map are specified in the lower left corner of each panel. ρ_0 and r_c are in units of $M_\odot$ pc^{-3} and kpc respectively. In each panel the edge of the star-forming core is outlined by an arbitrarily selected solid white $\Sigma_{SFR} = 0.1$ $M_\odot$ pc^{-2} contour while the gravitationally unstable portion of the gas disk is outlined by a solid yellow $Q_{gas+DM} = 1$ contour. **Bottom panel:** Radial profiles of the instability maps.

located with its H I disk ensures that the inner H I disk (where $\rho_{DM}(r)$ is high) contains more dark mass than the outer H I disk (where $\rho_{DM}(r)$ is relatively lower). The resulting radial distribution of Σ_{DM} yields a result different to the one that would be obtained by boosting each line-of-sight Σ_{HI} measurement by a factor of 10, which would yield an instability criterion of the form $Q_{gas,DM} \equiv \alpha_Q \sigma_{gas} \kappa / \pi G(10\ \Sigma_{gas}) < 1$. This criterion would be satisfied throughout the entire H I disk of NGC 2915. An illustrative example of this fact is the radial profile of the NGC 2915 Q_{gas} map for the case in which $\sigma_{gas} = 4.9$ km s^{-1} (middle left panel of Fig. 5.22, Sec. 5.4.4). This profile shows that the largest Q_{gas} parameters are $Q_{gas} \sim 5$. Since $Q_{gas} \propto 1/\Sigma_{HI}$, simply boosting all observed H I surface densities by a factor of 10 will result in the entire H I disk becoming unstable with a maximum Q_{gas} of about 0.5. Such a result is clearly inconsistent with observations. The results of this section demonstrate that if $\sim 30\%$ of the total dark mass of each galaxy is co-located with its H I disk, it can lead to gravitational instabilities of the inner H I disk that are consistent with the observed star formation activity. The additional disk mass does, however, need to be appropriately distributed and cannot simply trace the observed H I distribution.

In their review of cold gas accretion in galaxies, Sancisi et al. (2008) allude to the fact that "it is remarkable that there is such a pronounced spiral structure in the outer regions of spirals where dark matter dominates and even in dwarfs where the dark halo is believed to be predominant everywhere". The question, they therefore say, is "whether these systems have light disks surrounded by massive dark halos or, rather, have heavy and dark disks". The modeling results from this section allow this question to be partly addressed for the cases of NGC 2915 and NGC 1705. It has been shown that only a heavy disk scenario in which the portion of the DM halo that lies within the H I disk is considered allows for an accurate account of the observed star formation in both NGC 2915 *and* NGC 1705. This result, together with the result of Masset & Bureau (2003) that a heavy disk allows for the natural formation of NGC 2915's observed H I spiral structure suggests that certainly NGC 2915 has a heavy H I disk, and very likely NGC 1705 too, with significant amounts of dark mass distributed within them.

5.4.7 Shear-based instability criterion

The last star formation model that is investigated is a rotational shear-based model. It was shown in Sec. 5.4.4 that a simple Toomre Q_{gas} criterion which incorporates only the gravitational potential of the H I disk is inconsistent with the observations of NGC 2915 and NGC 1705, predicting the entire H I disk of each galaxy to be sub-critical. The situation was improved by considering various two-fluid instability models in which the gravitational potential of the stars and dark matter is incorporated. A common aspect of all these models is their characterisation

of the global kinematics of a galaxy–they all use the epicyclic frequency, κ, as a measure of the kinematics. This section investigates a star formation model for which the kinematics are quantified not in terms of the Coriolis force (i.e. κ), but rather the rotational shear.

Introduction

Hunter et al. (1998) suggest that the Coriolis force, incorporated in the Toomre Q_{gas} stability criterion, becomes less important in the presence of rotational shear. It is the time available for clouds to collapse in the presence of rotational shear, they argue, that regulates a galaxy's star formation activity. Hunter et al. (1998) use Oort's A constant,

$$A = 0.5 \left(\frac{V}{r} - \frac{dV}{dr} \right), \tag{5.19}$$

to quantify the rotational shear of the gas. The so-called shear-based parameter for gravitational instability is then

$$S_{gas} = \frac{\alpha_A \sigma_{gas} A}{\pi G \Sigma_{gas}}. \tag{5.20}$$

Based upon the idea that a perturbation must grow by a factor of ~ 100 in the presence of shear for the instability to be significant, Hunter et al. (1998) estimate $\alpha_A \sim 2.5$. This value of A matches the contrast between the surface densities of neutral and molecular inter-stellar media in the presence of rotational shear. It also allows the condition $Q_{gas} \lesssim 1$ to be met over the $V \propto R$ portion of the rotation curve. Regions within the galaxy that have $S_{gas} < 1$ should be forming stars while regions with $S_{gas} > 1$ should be stable against large-scale gravitational collapse.

Hunter et al. (1998) point out that using A to quantify the gas kinematics instead of κ makes very little difference for a flat rotation curve. They estimate the two thresholds to be the same to within 12% for a flat rotation curve. The difference between the two thresholds is most apparent for rising rotation curves where the rotational shear is low. Under such circumstances, S_{gas} can be significantly lower than Q_{gas}. As an illustration of this point, the epicyclic frequencies and rotational shears for NGC 2915 are calculated as functions of R using the parameterisation of the observed rotation curve, and are shown in the bottom-left and bottom-right panels of Fig. 5.38 respectively. The observed rotation curve and its parameterisation are shown in the upper panel of Fig. 5.38. The figure shows that the rotational shear is lower than the epicyclic frequency at all radii. More specifically, the rotational shear is lowest within the steeply rising portion of the rotation curve, being $\sim 5 - 10$ times lower than the epicyclic frequency within $\sim 140''$ from the centre of NGC 2915. In the outer, differentially-rotating disk of NGC 2915, the rotational shear is only a factor of $2 - 3$ lower than the epicyclic frequency. As a further illustration of how star formation intensity can be largely determined by a galaxy's rotation curve, Meurer et al.

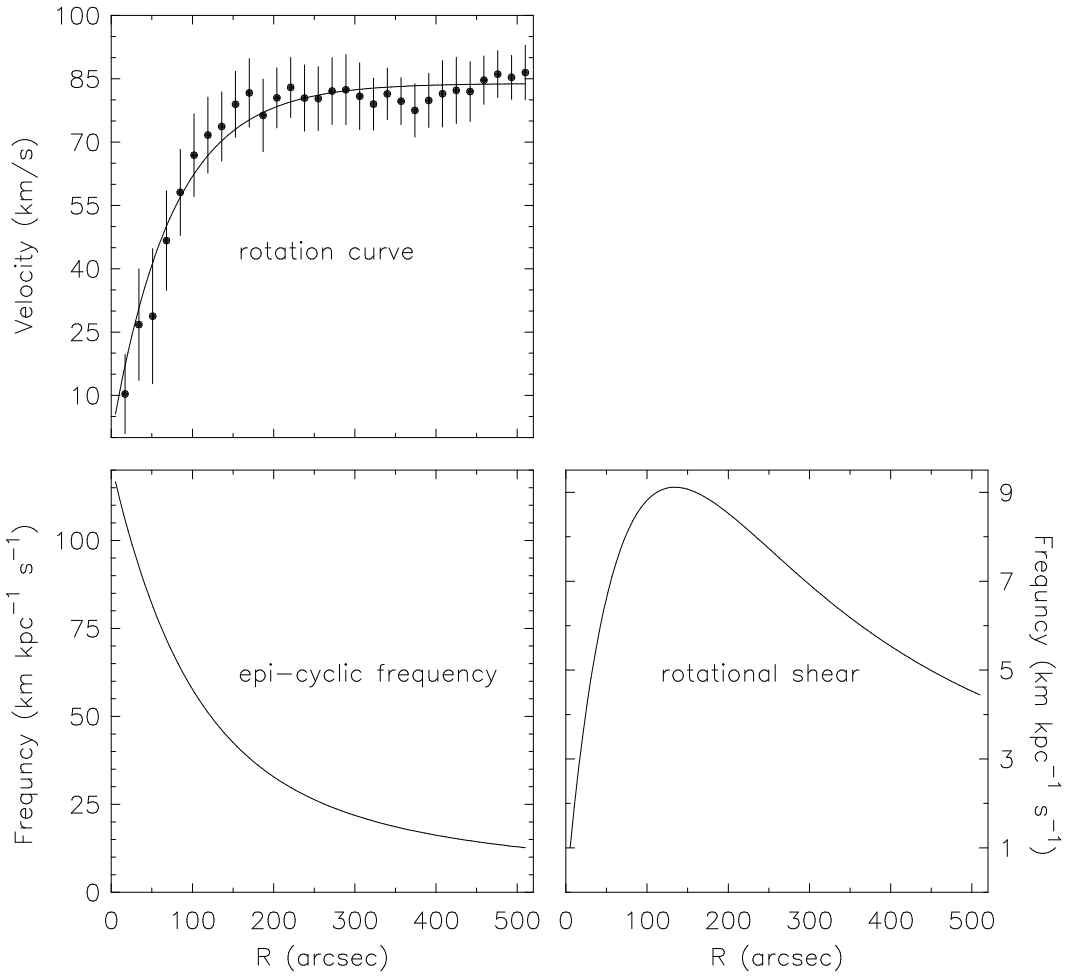

Figure 5.38: **Top panel:** Observed rotation curve of NGC 2915 (black filled circles). Error bars represent the r.m.s. spread of velocities within each ring of the tilted ring model. The solid curve represents the parameterisation of the observed rotation curve, according to Eqn. 5.5. **Bottom left panel:** Epicyclic frequency as a function of radius. **Bottom right panel:** Rotational shear, as quantified using Oort's A constant, as a function of radius.

(1997) show the integrated bolometric surface brightness of a starburst to be consistent with expectations of gravitational instability models applied to the solid body rotation portion of the galaxy.

NGC 2915 and NGC 1705 results and discussion

S_{gas} maps were produced for NGC 2915 and NGC 1705 according to Eqn. 5.20 and are shown in Fig. 5.39 and Fig. 5.40 respectively. H I velocity dispersions of $\sigma_{gas} = 4.9$ km s^{-1} and $\sigma_{gas} = 8.8$ km s^{-1} were used. As for κ in the Toomre Q_{gas} criterion, the shear parameter, A, for each line of sight was approximated as the azimuthally-averaged shear corresponding to the galactocentric radius of the resolution element. The shear radial profile was determined for each galaxy using Eqn. 5.19 together with the parameterisation the galaxy's observed rotation curve.

For both the warm and cold cases, the S_{gas} criterion *correctly describes* star formation activity at the centre of each galaxy's gaseous disk, with the descriptions being most accurate for the cold gas phases. The $S_{gas} = 1$ contour of the shear maps is able to accurately trace the edges of the star-forming cores. By simply using a shear-based characterisation of the global dynamics, the S_{gas} criterion can correctly locate the unstable portions of the disks without the need for extra stellar or dark matter self-gravity.

The distributions of the S_{gas} parameters are shown in the bottom panels of Figs. 5.39 and 5.40. The NGC 2915 S_{gas} distribution exhibits a very sharp increase in the number of bin counts at $S_{gas} \sim 3.58$ ($\log_{10} S_{gas} = 0.55$) for the cold case. Figure 5.41 shows the $S_{gas} = 3.58$ contour for the cold phase NGC 2915 S_{gas} map overlaid on the H I surface density map. The figure shows that the sharp increase in S_{gas} by a factor of ~ 2.3 clearly occurs along the edges of spiral features in the H I distribution. The coincidence of discrete change in the value of S_{gas} with a corresponding change in the properties of the H I distribution emphasises the fact that the H I distribution still plays an important role in determining the SF threshold, regardless of the characterisation of the global kinematics. Yet, as was shown in Sec. 5.4.3, the H I distribution alone does not regulate the star formation activity in NGC 2915 and NGC 1705. In the case of spiral arms, streaming gas motions could actually impede star formation.

Comparison to other dwarfs

Does the shear-based S_{gas} criterion work as well for other dwarf systems as it does for NGC 2915 and NGC 1705? The SFE as a function of S_{gas} for the inner portions of the H I disks of NGC 2915 and NGC 1705 are shown in Fig. 5.42. For comparative purposes the corresponding results for the THINGS sample of Leroy et al. (2008) are shown in Fig. 5.43. The NGC 2915 and NGC 1705 findings are indeed consistent with the results of Leroy et al. (2008) who found the inner disks of their galaxies to be more nearly super-critical in the context of a shear-based star formation threshold than in the context of a Q_{gas} criterion. As is the case for the sample of Leroy et al. (2008), the simple shear criterion performs better than the star+gas two-fluid criterion.

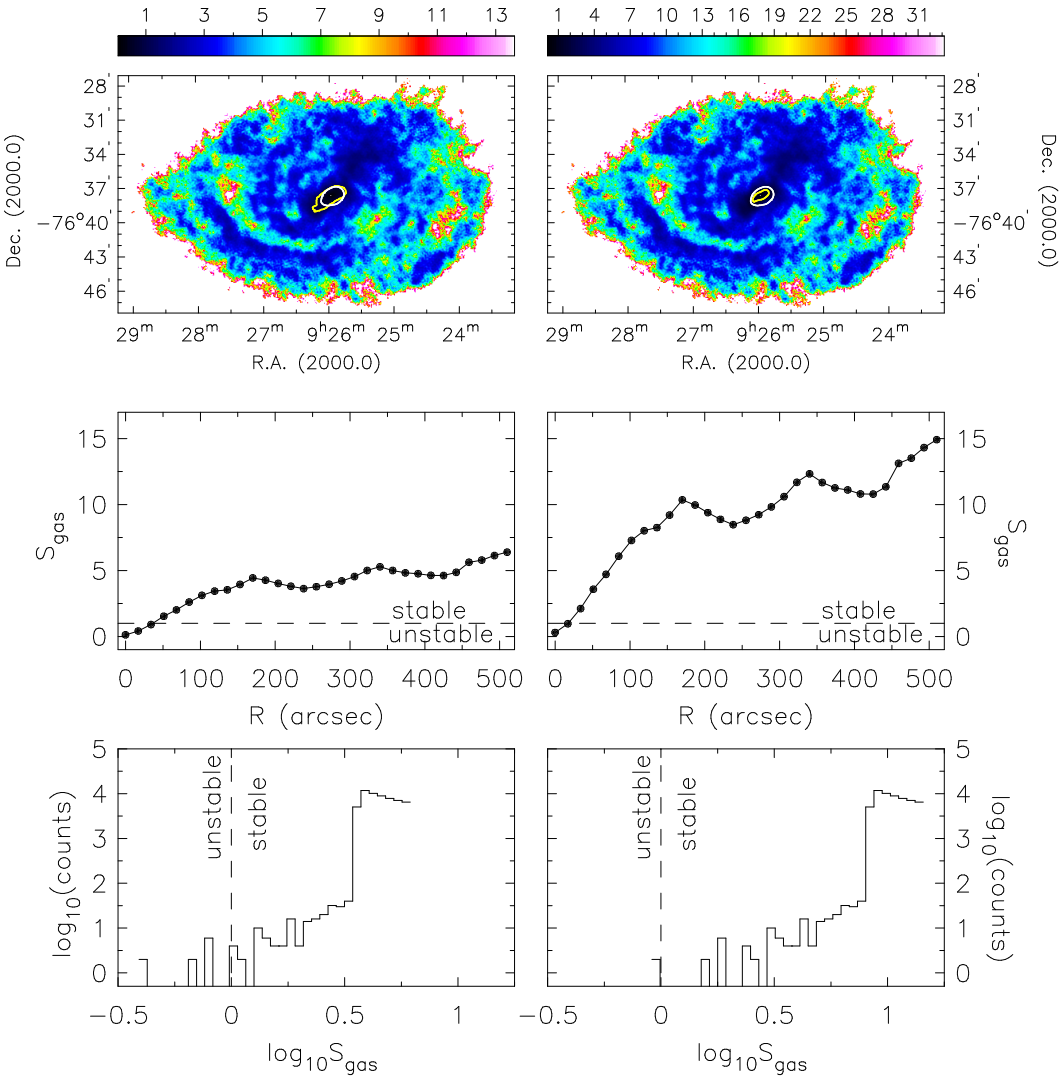

Figure 5.39: **Top row:** S_{gas} instability maps for the H I disk of NGC 2915. **Middle row:** Radial profiles of S_{gas} instability maps. **Bottom row:** Distribution of S_{gas} values. All figures in the left- and right-hand columns correspond to a constant gas velocity dispersion of 4.9 km s^{-1} and 8.8 km s^{-1} respectively. The colour bars above the upper panels specify the S_{gas} intensity scale. The single yellow contour in each map is at a level of $S_{gas} = 1$, and encloses the unstable region of the H I disk. The single white contour in the upper panels, at a level of $\Sigma_{SFR} = 0.0018$ M$_\odot$ yr^{-1} kpc^{-2}, approximates the edge of the star-forming core of NGC 2915.

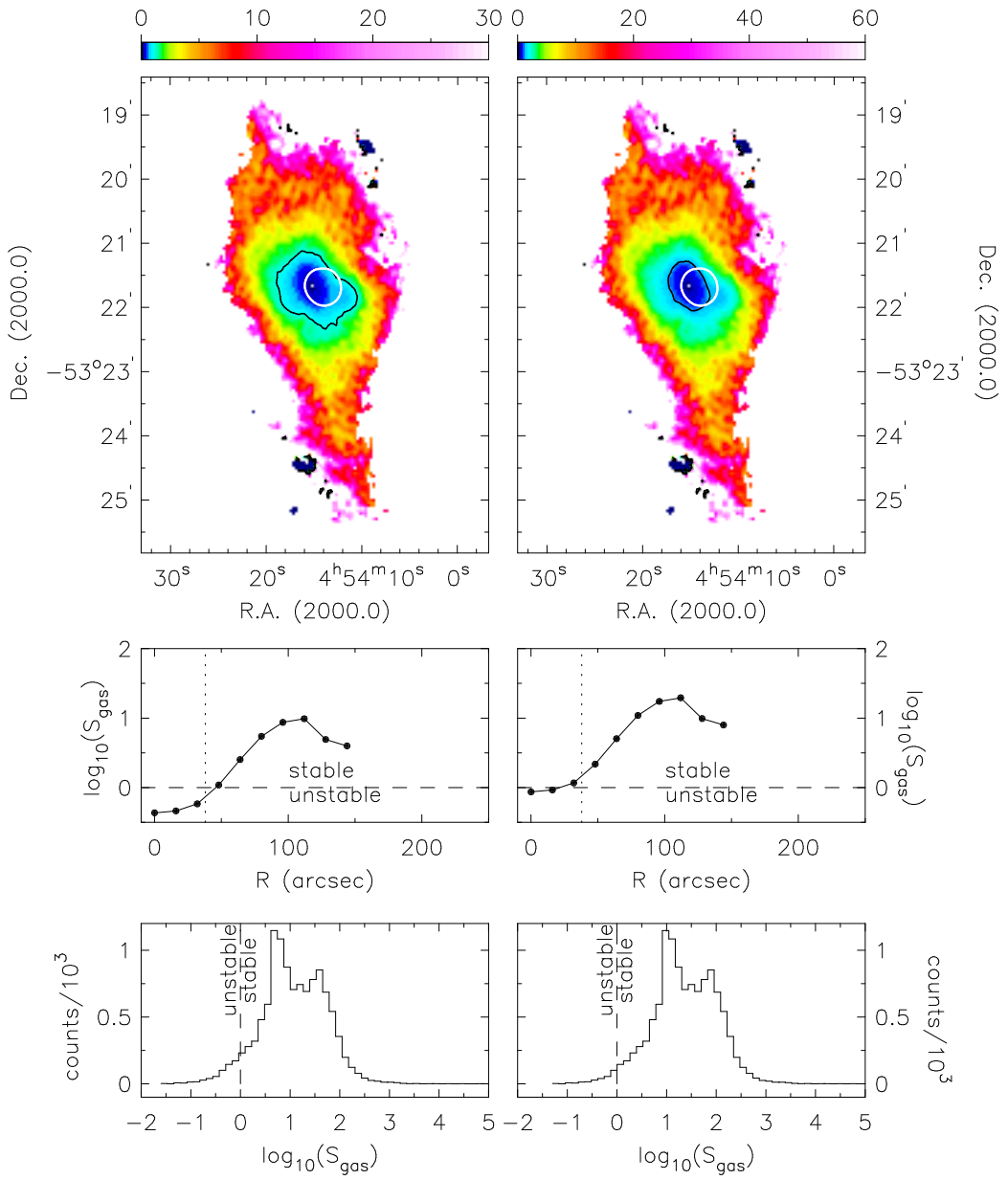

Figure 5.40: **Top row:** S_{gas} instability maps for the H I disk of NGC 1705. **Middle row:** Radial profiles of S_{gas} instability maps. **Bottom row:** Distribution of S_{gas} values. All figures in the left- and right-hand columns correspond to a constant gas velocity dispersion of 4.9 km s^{-1} and 8.8 km s^{-1} respectively. The colour bars above the upper panels specify the S_{gas} intensity scale. The single black contour in each map is at a level of $S_{gas} = 1$, and encloses the unstable region of the H I disk. The single white contour in the upper panels, at a level of $\Sigma_{SFR} = 0.1$ M$_\odot$ yr^{-1} kpc^{-2}, approximates the edge of the star-forming core of NGC 2915.

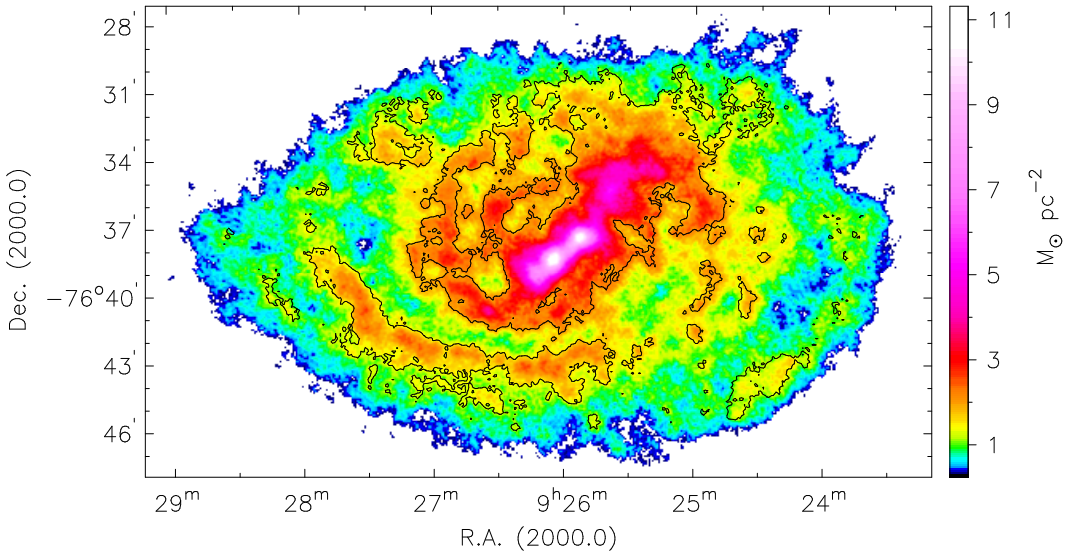

Figure 5.41: H I surface density map of NGC 2915. The black contour *is not* an H I surface density contour, but rather the $S_{gas} = 3.58$ contour from the cold phase S_{gas} map (top left panel of Fig. 5.39). The colour bar represents the logarithmic intensity scale of the H I surface densities.

Finally, our results, like those of Leroy et al. (2008) show no distinct, tight correlation between S_{gas} and the observed SFE. Any of the observed SFEs within the *inner* portions of NGC 2915 or NGC 1705, has a large range of S_{gas} values associated with it (a range of 10, for example, for the high SFEs of NGC 1705). Furthermore, according to this shear-based instability criterion, there are regions of high SFE within the disk that are formally stable against the tendency to gravitationally collapse, instead of being formally unstable. Despite this, however, it has been demonstrated that a shear-based instability model accurately locates the edges of the star-forming disks of NGC 2915 and NGC 1705.

5.4.8 Summary

The second part of this chapter has been dedicated to the investigations of various star formation models. These models incorporate various properties of a galaxy's ISM to determine which regions within the galaxy are unstable against the tendency to gravitationally collapse and hence form high-mass stars on varying galactic length-scales. The success or apparent failure of these models in accurately describing the star-forming regions within a galaxy sheds light on the interplay between the key properties of the ISM that regulate the star formation activity.

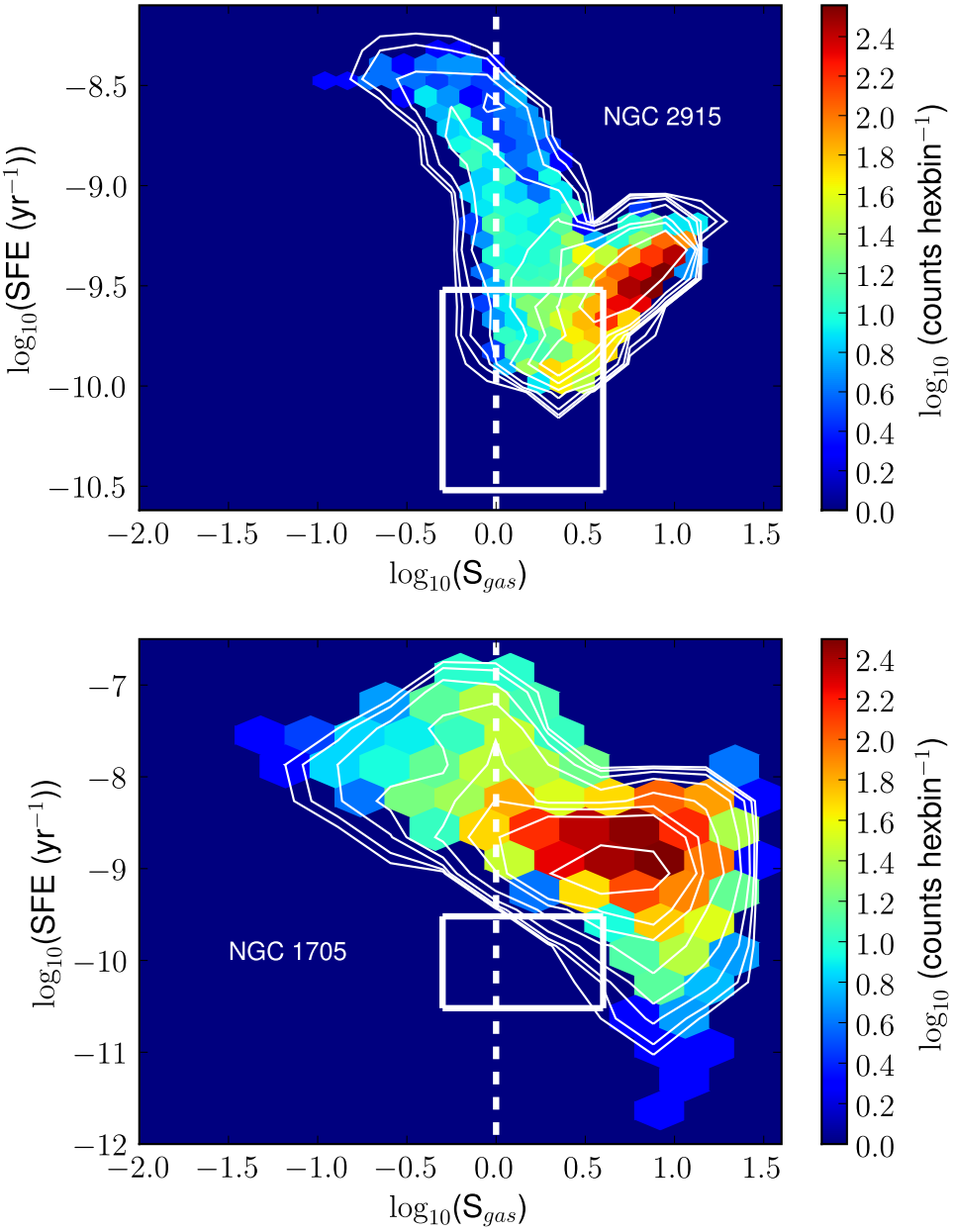

Figure 5.42: Star formation efficiency as a function of S_{gas} for the inner $R \leq 1.2R_{25}$ parts of NGC 2915 and NGC 1705. The colour bar indicates the logarithm of the number of points within each hexagonal bin. The white contours are at levels of $\log_{10}$(0.3, 0.6, 0.9, 1.2, 1.5, 1.8, 2.1, 2.4) for the upper panel, and $\log_{10}$(0.3, 0.6, 0.9, 1.2, 1.5, 1.8, 2.0, 2.4) for the lower panel. The subsets of parameter space leftward and rightward of the white dashed line represent the regions where gravitational instability of the ISM is and is not expected respectively. An H I velocity dispersion of $\sigma_{gas} = 4.9$ km s^{-1} was assumed for both instability maps. The white box in each panel encloses the same region as the black box shown in Fig. 5.43.

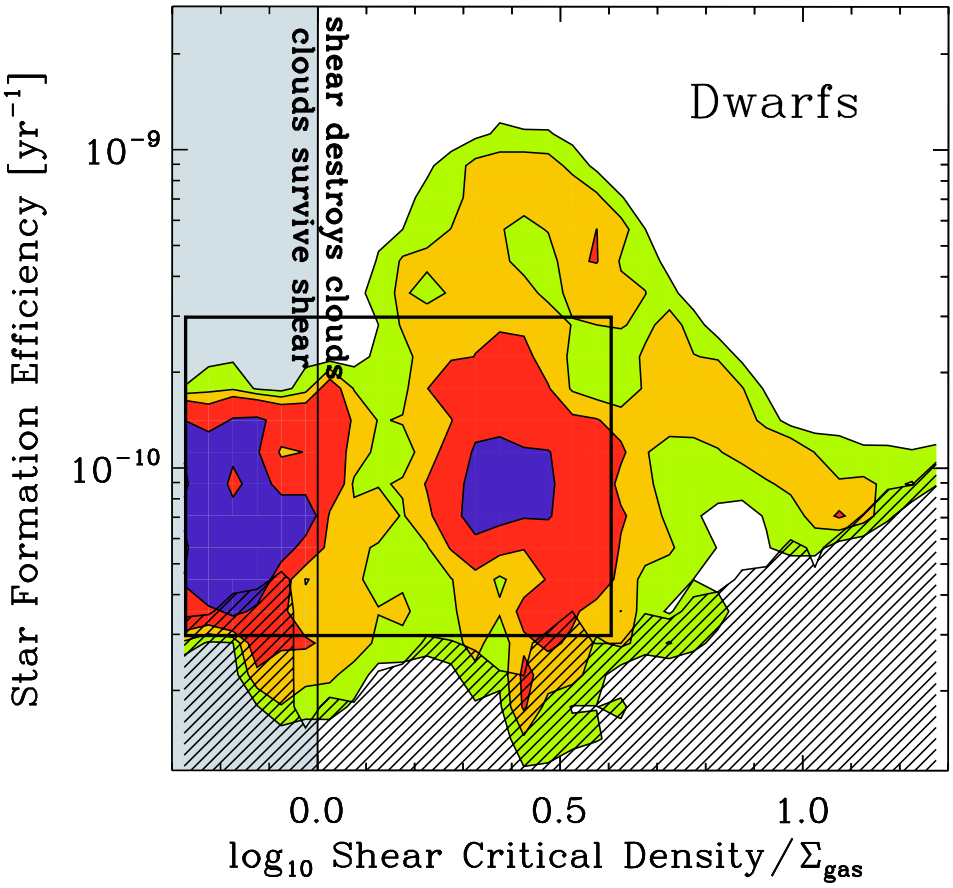

Figure 5.43: Star formation efficiency as a function of S_{gas} for the THINGS sample of dwarf galaxies, taken from Leroy et al. (2008). The figure shows data from 11 dwarf galaxies for individual lines of sight. Equal weight is given to each galaxy and contours include 90%, 75%, 50% and 25% of the data. The hatched region indicates where the THINGS survey is incomplete. The grey area shows where instability of the ISM is expected. The black box encloses the same region as the white boxes shown in Fig. 5.42.

The star formation thresholds in NGC 2915 and NGC 1705 are not purely local phenomena. The observed star formation activity is not found to correlate tightly with H I surface density in either system. Rather, large portions of the inner disks of NGC 2915 and NGC 1705 are described to be super-critical by the Schaye (2004) criterion. Schaye (2004) claims that the formation of a cold H I phase is a necessary condition for gravitational instability of the neutral ISM. Although undoubtedly important, the distribution of H I within NGC 2915 and NGC 1705 alone cannot account for their star-forming cores, thereby implying the formation of a cold H I phase to be an insufficient condition for star formation to occur.

In general, instability models including a characterisation the galaxy's global kinematics more accurately describe the SF activity than the Schaye (2004) model. The Toomre single-fluid Q_{gas} criterion as well as the stars+gas and DM+gas two-fluid criteria ($Q_{gas,*}$ and $Q_{gas,DM}$ respectively) all use the epicyclic frequency at a given galactocentric radius within the galaxy as a measure of its global kinematics. The Q_{gas} criterion incorrectly predicts the entire H I disks of both NGC 2915 and NGC 1705 to be sub-critical. This result is consistent with that of Leroy et al. (2008) who found almost no area of the inner disk for their sample of 23 THINGS galaxies to be formally unstable to gravitational collapse in a Toomre Q_{gas} context. These results suggest that the Toomre Q_{gas} criterion is of limited utility in terms of distinguishing star-forming regions of high and low efficiency.

NGC 2915 and NGC 1705 both contain stellar disks embedded within their H I disks. The stellar potential essentially increases the self-gravity of the gaseous disk, thereby making it more gravitationally unstable. This is expected to play a crucial role in regulating the star formation activity. Despite this expectation, however, the $Q_{gas,*}$ criterion also fails for NGC 2915 whose entire H I disk is predicted to be sub-critical. The model cannot describe NGC 2915's central star formation activity. The situation improves for NGC 1705 for which perturbation length-scales of $\lambda \sim 200$ pc lead to predictions of its inner H I disk being formally gravitationally unstable. A relatively small spread in SFE with $Q_{gas,*}$ is observed for both NGC 2915 and NGC 1705. This result lends itself to a self-regulating star formation scenario in which the gravitational potential associated with newly-formed stars will seed further gravitational collapse of the ISM.

Disk dark matter can account for the observed star formation activity in NGC 2915 and NGC 1705. Both galaxies have been shown in this work to be extremely dark-matter-dominated systems. The fraction of their dark matter that is co-located within the H I disk is treated as boosting the self-gravity of the ISM. If the dark disk mass component of each galaxy is treated as being distributed according to the galaxy's dark matter halo density profile, both NGC 2915 and NGC 1705 have formally unstable inner H I disks, the edges of which accurately trace the observed star-forming cores. This result does not hold for the case in which the distribution of the assumed disk dark matter exactly traces the H I distribution. The presence of disk dark

matter sheds some light on the origin and formation history of NGC 2915's extended H I disk. If pristine H I is accreted onto the outer parts of NGC 2915's H I disk, then, as Masset & Bureau (2003) showed, a heavy disk naturally leads to the formation of the observed H I spiral structure.

The final star formation model investigated in this chapter was a shear-based model which is based on the premise that it is the time available for clouds to collapse in the presence of rotational shear that regulates a galaxy's star formation. Indeed, adopting the rotational shear as a characterisation of the global kinematics allows the S_{gas} criterion to accurately locate the unstable parts of both NGC 2915's and NGC 1705's H I disks without the need for extra stellar or dark matter self-gravity. The same general result was obtained by Leroy et al. (2008) who found the inner disks of their galaxies to be more nearly super-critical in the context of a shear-based S_{gas} criterion than in the context of a Q_{gas} criterion.

In conclusion, despite NGC 2915 and NGC 1705 both being unusual star-forming galaxies, their star-formation activity can be understood in terms of the self-gravity of the ISM which, in turn, is controlled by the combined effects of the gravitational potentials of their various mass components. Alternatively, the star formation activity in each system can be accounted for by correctly characterising its global kinematics. Throughout this chapter, in lieu of published CO data, we have ignored the effects of a possible H_2 component within each galaxy on its star-forming properties. Molecular hydrogen must be present, the observed star formation could not be taking place without it. Based on our measured SFEs, we've estimated the amount of H_2 within each galaxy to be of the order of $\sim 10^7$ $M_\odot$ ($\sim 2-3$ orders of magnitude less than the dynamical mass of each galaxy). Although we cannot reliably implement the effects of this mass component into our star formation models, they are expected to be significant (e.g. Bigiel et al., 2008). Future work will therefore include attempts at constraining the H_2 content of each galaxy so that it may be included in our star formation models.

Chapter 6

Thesis summary

In this thesis new H I synthesis observations of NGC 2915 and NGC 1705 have been used to carry out various detailed analyses of the distribution and kinematics of each system's neutral interstellar medium (ISM). The galaxies were observed as part of the southern hemisphere extension to The H I Nearby Galaxy Survey (THINGS, Walter et al., 2008). The H I data have been combined with high-quality infrared and ultra-violet imaging from the *Spitzer* Nearby Galaxies Survey (SINGS, Kennicutt et al., 2003) and the GALEX Nearby Galaxy Survey (NGS, Gil de Paz et al., 2007). This multi-wavelength approach has allowed for a comprehensive study of: (1) the various mass components of each system, including the dark matter, (2) the H I dynamics and its links to the observed star formation activity, and (3) the unique star-forming properties of each galaxy. The results presented in detail at the ends of chapters 2-5 are summarised below, followed by a list of future prospects.

6.1 Conclusions

The H I mass distribution of NGC 2915 is studied at $\sim 17''$ spatial resolution. The kinematics of the extended H I disk are traced out to ~ 9.3 kpc, more than 5 times the R-band R_{25} radius of the stellar disk. The total H I mass of the system is estimated to be $\sim 6.4 \times 10^8$ $M_\odot$. The H I observations clearly resolve spiral structure within the outer disk. The inner disk is observed to consist of two central H I concentrations, separated by $\sim$ 1.2 kpc and having a mass of $\sim 2.2 \times 10^7$ $M_\odot$. Significantly non-Gaussian line profiles are associated with this complex central H I distribution.

The H I disk of NGC 2915 is used to trace its gravitational potential out to large galactocentric radii. Mass models show that the system is dark-matter-dominated at nearly all radii. The gravitational potential of the stellar disk is unable to account for the steeply-rising inner rotation curve. The mass models suggest that NGC 2915 has a core-like central dark matter distribution with a core density $\rho_0 = 0.17 \pm 0.03$ $M_\odot$ pc^{-3} and a core radius $r_c = 0.9 \pm 0.1$ kpc. At the last measured point on its rotation curve, NGC 2915 has a total mass to blue light ratio $M_{tot}/L_B \sim 140$ $M_\odot/L_\odot$, thereby making it one of the most dark-matter-dominated galaxies known.

Both the inner and the outer portions of NGC 2915's H I disk contain significant non-circular velocity components. An harmonic decomposition of the outer ($200'' \leq R \leq 510''$) H I velocity field has been carried out in order to quantify the non-circular components. The decomposition results are interpreted in the context of non-axisymmetric perturbations to the system's gravitational potential. Evidence is gathered for a globally elongated potential, the projected elongation of which is difficult to determine in the clear presence of an $m = 2$ harmonic term in the H I field. The $m = 2$ component also tarnishes the otherwise strong evidence that is found for the presence of a radial outflow of the order $5 - 17$ km s^{-1} within the outer H I disk.

Full three-dimensional models of the H I data cube have been built to study the central ($R \leq 85''$) H I dynamics of NGC 2915. These models are compared directly to the H I data cube. The central H I energetics are consistent with the energy output of the high-mass stars located at the centre of the galaxy. The models imply the inner H I disk contains radial outflow velocities of ~ 30 km s^{-1}. Furthermore, models consisting of a highly inclined ($i = 85°$) inner disk are most consistent with the observations. The modeling results lend themselves to the scenario in which the galaxy's central gas reservoir is being depleted as the neutral gas is expelled outwards by stellar winds. These complex observed dynamics lead to the new picture that NGC 2915 is not a simple dwarf galaxy. Rather, it is an evolving system with complex interplays occurring between its various mass components.

NGC 1705 is the second dwarf galaxy analysed in this thesis. The distribution and kinematics of the H I disk are studied out to radii of ~ 3.7 kpc, roughly 4 times the B-band R_{25} radius of the stellar disk. The total H I mass of the system is $\sim 1.1 \times 10^8$ $M_\odot$. The central H I distribution is clearly resolved into two concentrations which straddle a luminous star cluster at the centre of the galaxy. A drawn-out H I feature extends for ~ 2.5 kpc from the centre of the galaxy. This feature could be the result of a galactic outflow that is removing mass from the disk of NGC 1705. The galaxy is shown to be dark-matter-dominated at all radii. Treating the dark matter halo as having a core-like distribution at its centre, a core density of $\rho_0 = 0.09 \pm 0.01$ $M_\odot$ pc^{-3} and a core radius of $r_c = 1.2 \pm 0.1$ kpc result in very well-fitted mass models. The stellar potential does not significantly contribute to these mass models. When placed in the context of the dark

matter halo properties of the morphologically diverse sample of THINGS galaxies studied by de Blok et al. (2008), the dark matter cores of NGC 2915 and NGC 1705 are denser and more compact than typical late-type systems.

The final component of this thesis consists of a detailed study of the star-forming properties of both NGC 2915 and NGC 1705. These galaxies are not typical star-forming galaxies - NGC 2915 has a small stellar core embedded in an extended, star-less H I disk; while NGC 1705 is experiencing an intense burst of star formation. The quantitative relationship between the star formation activity and the properties of the ISM provides insight in the processes that regulate the star formation. GALEX far ultra-violet and *Spitzer* 24 μm imaging is used to trace the star formation activity. The ISM distribution and kinematics are measured using the H I synthesis data. A suite of star formation recipes and models are used to understand and describe the star formation activity. Velocity dispersions of the warm and cold phases of the neutral ISM are estimated. A cold phase dispersion $\sigma_{gas} \sim 4.9$ km s^{-1} is required for the star formation models to accurately describe the star formation activity.

Star formation is not a purely local phenomenon in NGC 2915 or NGC 1705. The distribution of H I alone does not regulate the star formation activity. Star formation models require an appropriate characterisation of the global kinematics in order to describe the observations. A single-fluid Toomre (1964) stability criterion is unable to describe the star formation at the centre of each galaxy. Two-fluid stability models that include the gravitational effects of the stellar potential do not offer significantly improved results. Only very specific stars+gas two-fluid stability models successfully describe the star formation activity in NGC 1705, but not NGC 2915.

Star formation models that accurately describe the observations are produced in two ways. The first set of models include the potential of the dark matter. If some of the dark matter within each system is treated as being co-located with the H I disk, the additional self-gravity added to the ISM is enough to overcome the impeding effects of centrifugal forces on the growth of gravitational instabilities. The observed star formation in both NGC 2915 and NGC 1705 can be well-described by these models. The disk dark matter does, however, have to be appropriately distributed. In this work the dark matter surface densities are treated as being distributed in the same way as the dark matter halo volume densities inferred from the mass models. A second set of models that accurately describe the observed star formation include a shear-based characterisation of the global kinematics. The rotational shear is low for the inner disks of both NGC 2915 and NGC 1705. For these models, the self gravity of the gas alone is enough to overcome the inhibiting effects of rotational shear on the growth of gravitational instabilities. Thus, despite being unusual star forming-galaxies, NGC 2915 and NGC 1705 can have their observed star formation activity understood in the context of specific regulatory processes that

are known to work in other star-forming galaxies.

6.2 Future prospects

Although this thesis serves as an extensive multi-wavelength study of NGC 2915 and NGC 1705, it is not an exhaustive study. These galaxies, with all their peculiarities and eccentricities, still contain a wealth of valuable information that needs to be extracted. The results presented in this thesis give a first indication of the important dynamical processes that govern the global properties of each galaxy, and point toward the need for future observations of NGC 2915 and NGC 1705 in order to further understand these unusual systems.

- The inner rotation curve of NGC 2915 needs to be more accurately constrained. It has been shown in this thesis that stellar winds greatly affect the dynamics of the inner H I disk. Using the H I emission as a kinematic tracer of the gravitational potential yields uncertain results at the very centre of the galaxy where the ISM kinematics are extremely non-regular.

  Assuming that the stars are less susceptible than the gas to the effects of non-circular motions, spectroscopic observations of the stellar disk will better constrain the inner rotation curve and hence the properties of the dark matter core of the galaxy. Using spectral fitting techniques, the spectroscopic data can be used to reconstruct the star formation history and chemical evolution of the system. By combining these results with the high-resolution H I data, star formation efficiency and feedback mechanisms in the context of a non-circularly rotating disk can be assessed. The spectroscopic observations will require high enough dispersion to measure both the velocities and velocity dispersions, since stellar populations can also be dynamically supported by random motions. It is proposed that the integral field unit on the Visible MultiObject Spectrograph (VIMOS[¶]) mounted on one of the VLT telescopes be used to spectroscopically sample a large fraction of the stellar disk of NGC 2915. It may also be possible to carry out the spectroscopic observations using the new WiFeS spectrograph (Dopita et al., 2007) on the ANU 2.3 m telescope.

- Detailed modeling of NGC 1705 is required to understand the effects of the intense star formation activity on the kinematics of the ISM. The super star cluster, NGC 1705-1, dictates the central H I kinematics and is powering a galactic outflow. Three-dimensional modeling of the kinematics can help us understand exactly how the outflow and feedback mechanisms operate. Governato et al. (2010) have recently reported on hydrodynamical

[¶]http://www.eso.org/sci/facilities/paranal/instruments/vimos/

simulations in which several million resolution elements are used to resolve dense clumps of the inhomogeneous ISM as small as 10^5 $M_\odot$. The authors show that strong gas outflows at the centres of galaxies caused by supernovae explosions are able to remove sufficient amounts of low-angular-momentum gas. This inhibits the formation of bulges and decreases the central densities of dark matter halos. Their results suggest that dark matter halos with central *core-like* properties can, in fact, arise naturally from simulations, thereby reconciling theory with observations of present-day dwarfs. The results of a detailed study of the gas kinematics of NGC 1705 will provide a strong observational test for this prediction and will help to constrain models of the precise mechanism by which the central dark matter density is decreased.

- Reliable data for the molecular content of NGC 2915 and NGC 1705 are lacking. A quantitative measure of their H_2 mass components will allow for more definitive mass modeling as well as star formation analyses to be carried out. For these reasons, probing the molecular content of these galaxies with the Atacama Large Millimeter Array (ALMA, Wootten & Thompson, 2009) is an exciting unexplored avenue.

- NGC 1705 is an example of the type of galaxy that would have dominated the cosmic scenery of the early universe. The system can be used as a nearby laboratory in which to study galaxy evolutionary processes that occur at high redshifts. The key to developing a comprehensive understanding of the cycle of gas within galaxies such as NGC 2915 and NGC 1705 is to develop a statistically robust characterisation of their properties. The next generation of radio telescopes such as the Karoo Array Telescope (MeerKAT[†]) and the Australian Square Kilometre Array Pathfinder (ASKAP[‡]) will offer astronomers unprecedented views of nearby and distant galaxies. Analyses similar to those presented in this thesis can be carried out for large, distance-limited samples of galaxies. Extremely low-mass systems ($\sim 10^5$ $M_\odot$) can be comprehensively studied in order to understand their direct interaction with the inter-galactic medium, including their connection with the cosmic web. Imaging of very low-column density gas surrounding nearby galaxies will allow us to directly observe how cold gas is accreted from the cosmic web onto their outer disks. This accreted gas serves to replenish the gas reservoir which would otherwise be depleted by star formation on time scales much shorter than a Hubble time. Understanding cold gas accretion is crucial to understanding the processes of galaxy formation and evolution.

  Very promising from a South African perspective is the possibility of carrying out large joint surveys with the MeerKAT and the Southern African Large Telescope (SALT[‖]). The spectroscopic capabilities of SALT make it an ideal instrument with which to study the

[†] http://www.ska.ac.za/meerkat
[‡] http://www.atnf.csiro.au/projects/askap
[‖] http://www.salt.ac.za/

stellar content and kinematics of nearby galaxies. Star formation processes in the outskirts of nearby galaxies can be studied in extremely low H I surface density environments that MeerKAT will sensitively probe. The results of the various proposed MeerKAT and SALT surveys will remain definitive until the next generation of radio and optical telescopes come into operation.

Bibliography

Andersen, D. R., Bershady, M. A., Sparke, L. S., Gallagher, III, J. S., & Wilcots, E. M. 2001, ApJ, 551, L131

Annibali, F., Greggio, L., Tosi, M., Aloisi, A., & Leitherer, C. 2003, AJ, 126, 2752

Baldwin, J. E., Lynden-Bell, D., & Sancisi, R. 1980, MNRAS, 193, 313

Barnes, J. E. 2002, MNRAS, 333, 481

Becker, R., Mebold, U., Reif, K., & van Woerden, H. 1988, A&A, 203, 21

Begeman, K. 1987, HI rotation curves of spiral galaxies (Groningen: Rijksuniversiteit, 1987)

Begeman, K. G., Broeils, A. H., & Sanders, R. H. 1991, MNRAS, 249, 523

Begum, A., Chengalur, J. N., Karachentsev, I. D., Sharina, M. E., & Kaisin, S. S. 2008, MNRAS, 386, 1667

Bell, E. F., & de Jong, R. S. 2001, ApJ, 550, 212

Bell, E. F., McIntosh, D. H., Katz, N., & Weinberg, M. D. 2003, ApJS, 149, 289

Bendo, G. J., Calzetti, D., Engelbracht, C. W., Kennicutt, R. C., Meyer, M. J., Thornley, M. D., Walter, F., Dale, D. A., Li, A., & Murphy, E. J. 2007, MNRAS, 380, 1313

Bigiel, F., Leroy, A., Walter, F., Brinks, E., de Blok, W. J. G., Madore, B., & Thornley, M. D. 2008, AJ, 136, 2846

Binney, J. 1978, MNRAS, 183, 779

Binney, J., & Tremaine, S. 1987, Galactic dynamics

Boomsma, R. 2007, PhD thesis, Kapteyn Astronomical Institute, University of Groningen

Bosma, A. 1978, PhD thesis, Groningen Univ., (1978)

Bournaud, F., & Combes, F. 2003, A&A, 401, 817

Bournaud, F., Combes, F., Jog, C. J., & Puerari, I. 2005, A&A, 438, 507

Bregman, J. N. 1980, ApJ, 237, 280

Briggs, F. H. 1990, ApJ, 352, 15

Brinks, E., & Bajaja, E. 1986, A&A, 169, 14

Broeils, A. H. 1992, PhD thesis, PhD thesis, Univ. Groningen, (1992)

Bureau, M., Freeman, K. C., Pfitzner, D. W., & Meurer, G. R. 1999, AJ, 118, 2158

Calzetti, D., Kennicutt, R. C., Engelbracht, C. W., Leitherer, C., Draine, B. T., Kewley, L., Moustakas, J., Sosey, M., Dale, D. A., Gordon, K. D., Helou, G. X., Hollenbach, D. J., Armus, L., Bendo, G., Bot, C., Buckalew, B., Jarrett, T., Li, A., Meyer, M., Murphy, E. J., Prescott, M., Regan, M. W., Rieke, G. H., Roussel, H., Sheth, K., Smith, J. D. T., Thornley, M. D., & Walter, F. 2007, ApJ, 666, 870

Canzian, B., & Allen, R. J. 1997, ApJ, 479, 723

Casertano, S. 1983, MNRAS, 203, 735

Chu, Y. 2005, in Astronomical Society of the Pacific Conference Series, Vol. 331, Extra-Planar Gas, ed. R. Braun, 297–+

Combes, F. 1999, Ap&SS, 265, 417

Côté, S., Carignan, C., & Freeman, K. C. 2000, AJ, 120, 3027

de Blok, W. J. G., & McGaugh, S. S. 1997a, MNRAS, 290, 533

—. 1997b, MNRAS, 290, 533

de Blok, W. J. G., McGaugh, S. S., & van der Hulst, J. M. 1996, MNRAS, 283, 18

de Blok, W. J. G., & Walter, F. 2006, AJ, 131, 363

de Blok, W. J. G., Walter, F., Brinks, E., Trachternach, C., Oh, S.-H., & Kennicutt, R. C. 2008, AJ, 136, 2648

de Grijs, R. 1998, MNRAS, 299, 595

de Vaucouleurs, G., & de Vaucouleurs, A. 1964, Reference catalogue of bright galaxies, ed. de Vaucouleurs, G. & de Vaucouleurs, A.

de Vaucouleurs, G., de Vaucouleurs, A., Corwin, Jr., H. G., Buta, R. J., Paturel, G., & Fouque, P. 1991, Third Reference Catalogue of Bright Galaxies

Dopita, M., Hart, J., McGregor, P., Oates, P., Bloxham, G., & Jones, D. 2007, Ap&SS, 310, 255

Elmegreen, B. G., & Parravano, A. 1994, ApJ, 435, L121+

Flores, R. A., & Primack, J. R. 1994, ApJ, 427, L1

Fosbury, R. A. E., Bird, M. C., Nicholson, W., & Wall, J. V. 1987, MNRAS, 225, 761

Franx, M., van Gorkom, J. H., & de Zeeuw, T. 1994, ApJ, 436, 642

Galametz, M., Madden, S., Galliano, F., Hony, S., Schuller, F., Beelen, A., Bendo, G., Sauvage, M., Lundgren, A., & Billot, N. 2009, A&A, 508, 645

García-Ruiz, I., Sancisi, R., & Kuijken, K. 2002, A&A, 394, 769

Gentile, G., Salucci, P., Klein, U., & Granato, G. L. 2007, MNRAS, 375, 199

Gil de Paz, A., Boissier, S., Madore, B. F., Seibert, M., Joe, Y. H., Boselli, A., Wyder, T. K., Thilker, D., Bianchi, L., Rey, S.-C., Rich, R. M., Barlow, T. A., Conrow, T., Forster, K., Friedman, P. G., Martin, D. C., Morrissey, P., Neff, S. G., Schiminovich, D., Small, T., Donas, J., Heckman, T. M., Lee, Y.-W., Milliard, B., Szalay, A. S., & Yi, S. 2007, ApJS, 173, 185

Gil de Paz, A., Madore, B. F., & Pevunova, O. 2003, VizieR Online Data Catalog, 214, 70029

Gilmore, G., Wilkinson, M., Kleyna, J., Koch, A., Evans, W., Wyse, R. F. G., & Grebel, E. K. 2007, Nuclear Physics B Proceedings Supplements, 173, 15

Governato, F., Brook, C., Mayer, L., Brooks, A., Rhee, G., Wadsley, J., Jonsson, P., Willman, B., Stinson, G., Quinn, T., & Madau, P. 2010, Nature, 463, 203

Greve, A., Becker, R., Johansson, L. E. B., & McKeith, C. D. 1996, A&A, 312, 391

Haynes, M. P., van Zee, L., Hogg, D. E., Roberts, M. S., & Maddalena, R. J. 1998, AJ, 115, 62

Helmboldt, J. F., Walterbos, R. A. M., Bothun, G. D., O'Neil, K., & de Blok, W. J. G. 2004, ApJ, 613, 914

Hoopes, C. G., Sembach, K. R., Heckman, T. M., Meurer, G. R., Aloisi, A., Calzetti, D., Leitherer, C., & Martin, C. L. 2004, ApJ, 612, 825

Hunter, D. A., Elmegreen, B. G., & Baker, A. L. 1998, ApJ, 493, 595

Józsa, G. I. G., Oosterloo, T. A., Morganti, R., Klein, U., & Erben, T. 2009, A&A, 494, 489

Kamphuis, J. J. 1993, PhD thesis, University of Groningen, (1993)

Kellman, S. A. 1972, ApJ, 175, 353

Kennicutt, R. C., Bendo, G., Engelbracht, C., Gordon, K., Li, A., Rieke, G. H., Rieke, M. J., Smith, J. D., Armus, L., Helou, G., Jarrett, T. H., Roussel, H., Calzetti, D., Leitherer, C., Malhotra, S., Meyer, M., Regan, M. W., Dale, D. A., & Draine. 2003, in Bulletin of the American Astronomical Society, Vol. 35, Bulletin of the American Astronomical Society, 1351–+

Kennicutt, R. C., Hao, C., Calzetti, D., Moustakas, J., Dale, D. A., Bendo, G., Engelbracht, C. W., Johnson, B. D., & Lee, J. C. 2009, ApJ, 703, 1672

Kennicutt, Jr., R. C. 1983, ApJ, 272, 54

—. 1989, ApJ, 344, 685

—. 1998, ApJ, 498, 541

Koribalski, B. S., Staveley-Smith, L., Kilborn, V. A., Ryder, S. D., Kraan-Korteweg, R. C., Ryan-Weber, E. V., Ekers, R. D., Jerjen, H., Henning, P. A., Putman, M. E., Zwaan, M. A., de Blok, W. J. G., & Calabretta, M. R. 2004, AJ, 128, 16

Kregel, M., van der Kruit, P. C., & de Blok, W. J. G. 2004, MNRAS, 352, 768

Kregel, M., van der Kruit, P. C., & de Grijs, R. 2002, MNRAS, 334, 646

Kroupa, P. 2001, MNRAS, 322, 231

Lagache, G., Puget, J., & Dole, H. 2005, ARA&A, 43, 727

Lee, J. C., Gil de Paz, A., Tremonti, C., Kennicutt, R. C., Salim, S., Bothwell, M., Calzetti, D., Dalcanton, J., Dale, D., Engelbracht, C., Funes, S. J. J. G., Johnson, B., Sakai, S., Skillman, E., van Zee, L., Walter, F., & Weisz, D. 2009, ApJ, 706, 599

Leitherer, C., & Heckman, T. M. 1995, ApJS, 96, 9

Leroy, A. K., Walter, F., Brinks, E., Bigiel, F., de Blok, W. J. G., Madore, B., & Thornley, M. D. 2008, AJ, 136, 2782

Mac Low, M.-M., & Ferrara, A. 1999, ApJ, 513, 142

Marchesini, D., D'Onghia, E., Chincarini, G., Firmani, C., Conconi, P., Molinari, E., & Zacchei, A. 2002, ApJ, 575, 801

Marlowe, A. T., Meurer, G. R., & Heckman, T. M. 1999, ApJ, 522, 183

Marquardt, D. W. 1963, SIAM Journal on Applied Mathematics, 11, 431

Martin, C. L. 1996, ApJ, 465, 680

Martin, C. L., & Kennicutt, Jr., R. C. 2001, ApJ, 555, 301

Martin, D. C., Fanson, J., Schiminovich, D., Morrissey, P., Friedman, P. G., Barlow, T. A., Conrow, T., Grange, R., Jelinsky, P. N., Milliard, B., Siegmund, O. H. W., Bianchi, L., Byun, Y., Donas, J., Forster, K., Heckman, T. M., Lee, Y., Madore, B. F., Malina, R. F., Neff, S. G., Rich, R. M., Small, T., Surber, F., Szalay, A. S., Welsh, B., & Wyder, T. K. 2005, ApJ, 619, L1

Masset, F. S., & Bureau, M. 2003, ApJ, 586, 152

Mateo, M. L. 1998, ARA&A, 36, 435

Mauch, T., Murphy, T., Buttery, H. J., Curran, J., Hunstead, R. W., Piestrzynski, B., Robertson, J. G., & Sadler, E. M. 2003, MNRAS, 342, 1117

Melnick, J., Moles, M., & Terlevich, R. 1985, A&A, 149, L24

Meurer, G. R., Blakeslee, J. P., Sirianni, M., Ford, H. C., Illingworth, G. D., Clampin, M., Menanteau, F., Tran, H. D., Kimble, R. A., Hartig, G. F., Ardila, D. R., Bartko, F., Bouwens, R. J., Broadhurst, T. J., & Brown, R. A. 2003, ApJ, 599, L83

Meurer, G. R., Carignan, C., Beaulieu, S. F., & Freeman, K. C. 1996, AJ, 111, 1551

Meurer, G. R., Freeman, K. C., Bland-Hawthorn, J., Jones, M. R., Knezek, P. M., & Allen, R. J. 1999, in Bulletin of the American Astronomical Society, Vol. 31, Bulletin of the American Astronomical Society, 828–+

Meurer, G. R., Freeman, K. C., Dopita, M. A., & Cacciari, C. 1992, AJ, 103, 60

Meurer, G. R., Heckman, T. M., Lehnert, M. D., Leitherer, C., & Lowenthal, J. 1997, AJ, 114, 54

Meurer, G. R., Heckman, T. M., Leitherer, C., Kinney, A., Robert, C., & Garnett, D. R. 1995, AJ, 110, 2665

Meurer, G. R., Mackie, G., & Carignan, C. 1994, AJ, 107, 2021

Meurer, G. R., Staveley-Smith, L., & Killeen, N. E. B. 1998, MNRAS, 300, 705

Meurer, G. R., Wong, O. I., Kim, J. H., Hanish, D. J., Heckman, T. M., Werk, J., Bland-Hawthorn, J., Dopita, M. A., Zwaan, M. A., Koribalski, B., Seibert, M., Thilker, D. A., Ferguson, H. C., Webster, R. L., Putman, M. E., Knezek, P. M., Doyle, M. T., Drinkwater, M. J., Hoopes, C. G., Kilborn, V. A., Meyer, M., Ryan-Weber, E. V., Smith, R. C., & Staveley-Smith, L. 2009, ApJ, 695, 765

Monelli, M., Pulone, L., Corsi, C. E., Castellani, M., Bono, G., Walker, A. R., Brocato, E., Buonanno, R., Caputo, F., Castellani, V., Dall'Ora, M., Marconi, M., Nonino, M., Ripepi, V., & Smith, H. A. 2003, AJ, 126, 218

Moore, B. 1994, Nature, 370, 629

Moore, B., Ghigna, S., Governato, F., Lake, G., Quinn, T., Stadel, J., & Tozzi, P. 1999, ApJ, 524, L19

Mori, M., Ferrara, A., & Madau, P. 2002, ApJ, 571, 40

Navarro, J. F., Frenk, C. S., & White, S. D. M. 1996, ApJ, 462, 563

—. 1997, ApJ, 490, 493

Navarro, J. F., Ludlow, A., Springel, V., Wang, J., Vogelsberger, M., White, S. D. M., Jenkins, A., Frenk, C. S., & Helmi, A. 2010, MNRAS, 402, 21

Noordermeer, E., van der Hulst, J. M., Sancisi, R., Swaters, R. S., & van Albada, T. S. 2007, MNRAS, 376, 1513

Oh, S.-H., de Blok, W. J. G., Walter, F., Brinks, E., & Kennicutt, R. C. 2008, AJ, 136, 2761

Ostriker, E. C., & Binney, J. J. 1989, MNRAS, 237, 785

Papaderos, P., Fricke, K. J., Thuan, T. X., & Loose, H. 1994, A&A, 291, L13

Perlmutter, S., Aldering, G., Goldhaber, G., Knop, R. A., Nugent, P., Castro, P. G., Deustua, S., Fabbro, S., Goobar, A., Groom, D. E., Hook, I. M., Kim, A. G., Kim, M. Y., Lee, J. C., Nunes, N. J., Pain, R., Pennypacker, C. R., Quimby, R., Lidman, C., Ellis, R. S., Irwin, M., McMahon, R. G., Ruiz-Lapuente, P., Walton, N., Schaefer, B., Boyle, B. J., Filippenko, A. V., Matheson, T., Fruchter, A. S., Panagia, N., Newberg, H. J. M., Couch, W. J., & The Supernova Cosmology Project. 1999, ApJ, 517, 565

Rafikov, R. R. 2001, MNRAS, 323, 445

Reach, W. T., Megeath, S. T., Cohen, M., Hora, J., Carey, S., Surace, J., Willner, S. P., Barmby, P., Wilson, G., Glaccum, W., Lowrance, P., Marengo, M., & Fazio, G. G. 2005, PASP, 117, 978

Reshetnikov, V., & Combes, F. 1998, A&A, 337, 9

Richter, O.-G., & Sancisi, R. 1994, A&A, 290, L9

Riess, A. G., Filippenko, A. V., Challis, P., Clocchiatti, A., Diercks, A., Garnavich, P. M., Gilliland, R. L., Hogan, C. J., Jha, S., Kirshner, R. P., Leibundgut, B., Phillips, M. M., Reiss, D., Schmidt, B. P., Schommer, R. A., Smith, R. C., Spyromilio, J., Stubbs, C., Suntzeff, N. B., & Tonry, J. 1998, AJ, 116, 1009

Rix, H.-W., & Zaritsky, D. 1995, ApJ, 447, 82

Rosolowsky, E., & Blitz, L. 2005, ApJ, 623, 826

Rubin, V. C., & Ford, Jr., W. K. 1970, ApJ, 159, 379

Safronov, V. S. 1960, Annales d'Astrophysique, 23, 979

Salim, S., Rich, R. M., Charlot, S., Brinchmann, J., Johnson, B. D., Schiminovich, D., Seibert, M., Mallery, R., Heckman, T. M., Forster, K., Friedman, P. G., Martin, D. C., Morrissey, P., Neff, S. G., Small, T., Wyder, T. K., Bianchi, L., Donas, J., Lee, Y., Madore, B. F., Milliard, B., Szalay, A. S., Welsh, B. Y., & Yi, S. K. 2007, ApJS, 173, 267

Salpeter, E. E. 1955, ApJ, 121, 161

Sanchez-Saavedra, M. L., Battaner, E., & Florido, E. 1990, MNRAS, 246, 458

Sancisi, R. 1976, A&A, 53, 159

Sancisi, R., Fraternali, F., Oosterloo, T., & van der Hulst, T. 2008, A&A Rev., 15, 189

Sandage, A. 1978, AJ, 83, 904

Sandage, A., Binggeli, B., & Tammann, G. A. 1985, AJ, 90, 1759

Sault, R. J., Teuben, P. J., & Wright, M. C. H. 1995, in Astronomical Society of the Pacific Conference Series, Vol. 77, Astronomical Data Analysis Software and Systems IV, ed. R. A. Shaw, H. E. Payne, & J. J. E. Hayes, 433–+

Schaye, J. 2004, ApJ, 609, 667

Schlegel, D. J., Finkbeiner, D. P., & Davis, M. 1998, ApJ, 500, 525

Schmidt, M. 1959, ApJ, 129, 243

Schoenmakers, R. H. M., Franx, M., & de Zeeuw, P. T. 1997, MNRAS, 292, 349

Sersic, J. L., Bajaja, E., & Colomb, R. 1977, A&A, 59, 19

Sersic, J. L., & Donzelli, C. J. 1992, Ap&SS, 193, 87

Shapiro, K. L., Gerssen, J., & van der Marel, R. P. 2003, AJ, 126, 2707

Shapiro, P. R., & Field, G. B. 1976, ApJ, 205, 762

Skillman, E. D. 1987, in NASA Conference Publication, Vol. 2466, NASA Conference Publication, ed. C. J. Lonsdale Persson, 263–266

Skrutskie, M. F., Cutri, R. M., Stiening, R., Weinberg, M. D., Schneider, S., Carpenter, J. M., Beichman, C., Capps, R., Chester, T., Elias, J., Huchra, J., Liebert, J., Lonsdale, C., Monet, D. G., & Price, S. 2006, AJ, 131, 1163

Sofue, Y., & Rubin, V. 2001, ARA&A, 39, 137

Spekkens, K., & Sellwood, J. A. 2007, ApJ, 664, 204

Spergel, D. N., Verde, L., Peiris, H. V., Komatsu, E., Nolta, M. R., Bennett, C. L., Halpern, M., Hinshaw, G., Jarosik, N., Kogut, A., Limon, M., Meyer, S. S., Page, L., Tucker, G. S., Weiland, J. L., Wollack, E., & Wright, E. L. 2003, ApJS, 148, 175

Springel, V., Wang, J., Vogelsberger, M., Ludlow, A., Jenkins, A., Helmi, A., Navarro, J. F., Frenk, C. S., & White, S. D. M. 2008, MNRAS, 391, 1685

Springel, V., White, S. D. M., Jenkins, A., Frenk, C. S., Yoshida, N., Gao, L., Navarro, J., Thacker, R., Croton, D., Helly, J., Peacock, J. A., Cole, S., Thomas, P., Couchman, H., Evrard, A., Colberg, J., & Pearce, F. 2005, Nature, 435, 629

Steer, D. G., Dewdney, P. E., & Ito, M. R. 1984, A&A, 137, 159

Storchi-Bergmann, T., Calzetti, D., & Kinney, A. L. 1994, ApJ, 429, 572

Swaters, R. A. 1999, PhD thesis, , Rijksuniversiteit Groningen, (1999)

Swaters, R. A., Schoenmakers, R. H. M., Sancisi, R., & van Albada, T. S. 1999, MNRAS, 304, 330

Swaters, R. A., van Albada, T. S., van der Hulst, J. M., & Sancisi, R. 2002, A&A, 390, 829

Thuan, T. X., & Martin, G. E. 1981, ApJ, 247, 823

Toomre, A. 1964, ApJ, 139, 1217

Tosi, M., Sabbi, E., Bellazzini, M., Aloisi, A., Greggio, L., Leitherer, C., & Montegriffo, P. 2001, AJ, 122, 1271

Trachternach, C., de Blok, W. J. G., Walter, F., Brinks, E., & Kennicutt, R. C. 2008, AJ, 136, 2720

van Albada, T. S., Bahcall, J. N., Begeman, K., & Sancisi, R. 1985, ApJ, 295, 305

van der Hulst, J. M., Terlouw, J. P., Begeman, K. G., Zwitser, W., & Roelfsema, P. R. 1992, in Astronomical Society of the Pacific Conference Series, Vol. 25, Astronomical Data Analysis Software and Systems I, ed. D. M. Worrall, C. Biemesderfer, & J. Barnes, 131–+

van der Kruit, P. C. 1981, A&A, 99, 298

—. 1988, A&A, 192, 117

van der Kruit, P. C., & Searle, L. 1981, A&A, 95, 105

van der Marel, R. P., & Franx, M. 1993, ApJ, 407, 525

van Eymeren, J., Marcelin, M., Koribalski, B. S., Dettmar, R., Bomans, D. J., Gach, J., & Balard, P. 2009, A&A, 505, 105

Walter, F., & Brinks, E. 1999, AJ, 118, 273

Walter, F., Brinks, E., de Blok, W. J. G., Bigiel, F., Kennicutt, R. C., Thornley, M. D., & Leroy, A. 2008, AJ, 136, 2563

Wang, B., & Silk, J. 1994, ApJ, 427, 759

Weisz, D. R., Skillman, E. D., Cannon, J. M., Dolphin, A. E., Kennicutt, Jr., R. C., Lee, J., & Walter, F. 2008, ApJ, 689, 160

Werk, J. K., Putman, M. E., Meurer, G. R., Thilker, D. A., Allen, R. J., Bland-Hawthorn, J., Kravtsov, A., & Freeman, K. 2010, ApJ, 715, 656

Williams, B. F., Dalcanton, J. J., Stilp, A., Gilbert, K. M., Roškar, R., Seth, A. C., Weisz, D., Dolphin, A., Gogarten, S. M., Skillman, E., & Holtzman, J. 2010, ApJ, 709, 135

Wong, T., Blitz, L., & Bosma, A. 2004, ApJ, 605, 183

Wootten, A., & Thompson, A. R. 2009, IEEE Proceedings, 97, 1463

Wyder, T. K., Martin, D. C., Schiminovich, D., Seibert, M., Budavári, T., Treyer, M. A., Barlow, T. A., Forster, K., Friedman, P. G., Morrissey, P., Neff, S. G., Small, T., Bianchi, L., Donas, J., Heckman, T. M., Lee, Y., Madore, B. F., Milliard, B., Rich, R. M., Szalay, A. S., Welsh, B. Y., & Yi, S. K. 2007, ApJS, 173, 293

Young, L. M., van Zee, L., Lo, K. Y., Dohm-Palmer, R. C., & Beierle, M. E. 2003, ApJ, 592, 111

Zaritsky, D., & Rix, H.-W. 1997, ApJ, 477, 118